2023 NSF/REU

Research Experience for Undergraduates

in

Physics and Astronomy

Student Research Papers

Volume 34

University of Notre Dame

College of Science

REU Director

Umesh Garg, Ph.D.

REU Student Research Papers – Summer 2023
University of Notre Dame – Department of Physics & Astronomy

Phase Analysis of Kagome Superconductors

LILY BAKER

2023 NSF/REU Program
Department of Physics and Astronomy
University of Notre Dame

ADVISOR(S): Prof. Xiaolong Liu

Abstract

Charge density waves (CDWs) can be analyzed using powerful Scanning Tunneling Microscope (STM) images. In this study, we demonstrate an approach to investigate CDWs by registering STM images of the same sample at different bias voltages, followed by an Inverse Fourier Transform and line cuts of the resulting images. This process allows us to create a waterfall plot, revealing the phase shift in the charge density wave. The phase shift provides crucial insights into the positioning of the Charge Density Wave gap relative to the Fermi Level. Our investigation focused on crystal CsV_3Sb_5, and we discovered that the π phase shift occurs at an unexpected sample bias of 280 mV instead of the expected 0 mV.

1 Introduction

Scanning Tunneling Microscopes (STMs) employ a sharp, atomic-scale tip to tunnel electrons through a sample when subjected to a bias voltage. This bias voltage generates an electric field, inducing tunneling current, allowing the visualization of topographical and dI/dV images of the sample. Through such imaging, valuable insights into the structural and quantum properties of crystals can be gained. With atomic-scale resolution, STM images provide crucial information about material surface structures and properties. In this study, we focus on AV_3Sb_5 (A = Cs, K, Rb) crystals, characterized by a Kagome atomic lattice structure. The Kagome lattice, illustrated in Fig. 1, consists of six corner-sharing equilateral triangles forming a hexagonal pattern at the center. Owing to their distinctive electric and superconductive properties, these lattice structures pose a fascinating subject for investigation [2].

A significant phenomenon encountered in materials with Kagome atomic lattice structures is the charge density wave, which represents a periodic modulation in electric charge density. A critical aspect of this study involves the phase shift in the charge density wave, referring to the shift in the position or alignment of this periodic modulation. Understanding the phase shift enables us to gain insights into the location of the shift in the charge density wave gap, offering crucial information about the formation of the charge density wave [1]. In the context of the Kagome atomic lattice structure, the phase change becomes particularly informative regarding the behavior of the system at low temperatures, where multiple coexisting charge density waves are observed. Specifically,

the 1 x 4 charge density wave lattice undergoes a specific phase shift due to unoccupied states in Kagome systems.

The main objective of this project is to develop a simulated charge density wave, facilitating the accurate extraction of the phase from actual STM data with confidence. Furthermore, analyzing the phase shift will provide valuable information about the formation of charge density waves in CsV_3Sb_5. This is particularly significant in advancing our understanding of the charge density wave gap in CsV_3Sb_5. This crystal has an unusual charge density wave and we want to identify any hidden broken symmetries within it. By shedding light on this aspect, our research seeks to contribute to a deeper comprehension of the unique properties of AV_3Sb_5 crystals and their potential applications.

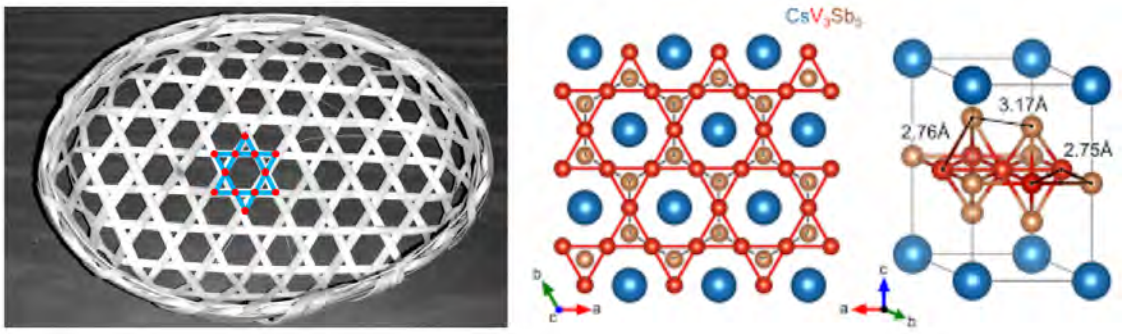

Figure 1: The image on the left shows a Japanese basket weaved in a Kagome style. The atomic lattice structure is highlighted in red and blue. The image on the right is a visualization of the CsV_3Sb_5 lattice where the big blue dots are Cesium atoms, the small red dots are vanadium atoms, and the yellow dots are antimony atoms.

2 Background

2.1 Real Space and Reciprocal Space

In condensed matter physics, real space and reciprocal space are fundamental mathematical frameworks that describe different aspects of the physical world, encompassing the spatial arrangements and properties of materials. Real space refers to the familiar three-dimensional space we encounter in everyday life, where an object's location can be described using Cartesian coordinates such as x, y, and z. On the other hand, reciprocal space, often denoted as q-space, is a mathematical represen-

tation that arises from transformations of real space data, such as through the Fourier Transform. It provides a unique perspective, particularly well-suited for describing the periodicity and wave vectors associated with crystal structures.

Real space representations enable the direct visualization of physical structures and properties. For instance, STM imaging directly captures real space information, displaying surface topographies and atomic arrangements of materials. Additionally, reciprocal space emerges as a valuable tool to analyze crystal structures and understand the underlying wave-like properties of matter. The Fourier Transform, which converts real space data into reciprocal space, reveals the distribution of spatial frequencies within a material.

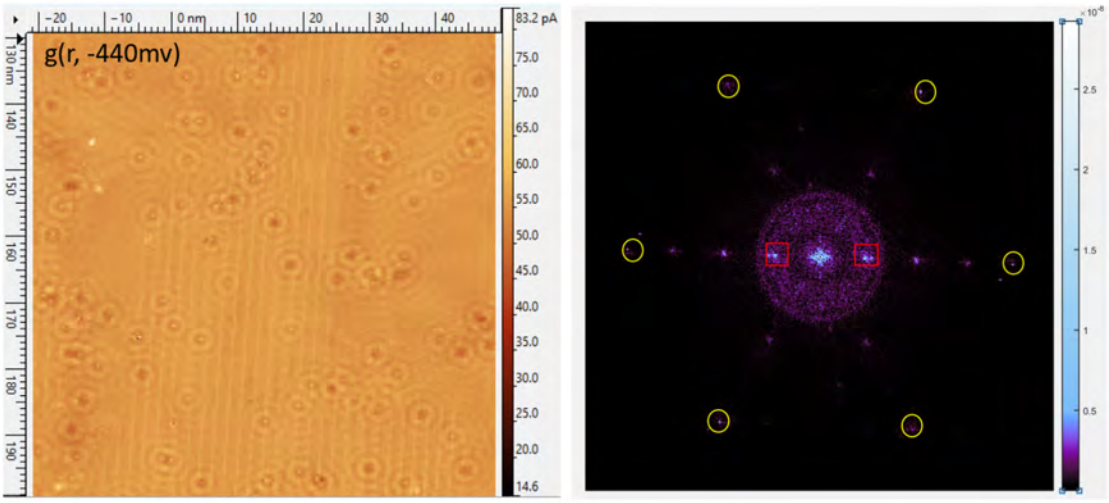

Figure 2: The image on the left is a real-space, g-channel image of CsV_3Sb_5. You can visually see the 1x4 charge density waves in the vertical stripes on the lattice. The image on the right is a Fourier Transform of the real space image on the left. The yellow circles mark the Bragg Peaks and the red squares mark the 1X4 CDW peak.

2.2 Why use STM imaging?

Not all electrons in a crystal participate in the charge density wave, only a small fraction of them being involved. This makes it hard to detect changes in the electron bands using usual tools, so we use STM to study the CDW states. Using STM, we have discovered that the CDW pattern changes in a spatial way when the energy used for imaging is adjusted. The CDW behaves differently

depending on how much electric charge is in the material because the crystal wants to find the lowest energy state. Due to this, the role of Fermi surface nesting in the crystal can be found with STM [3].

3 Methods

3.1 Image Correction

CsV_3Sb_5 has a triangular lattice structure. After taking the Fourier transformation of an STM image, an ideal triangular lattice has six Bragg peaks in a symmetrical, hexagonal shape. Through the acquisition of STM images of CsV_3Sb_5, distortions that come from piezo-electric drift occur that break the lattice symmetry. The Lawler-Fujita (LF) algorithm sharpens and defines the Bragg peaks in the Fourier transform [4]. This is done by using a two-dimensional "lock-in" technique to acquire the spacial phase and to make the lattice perfectly periodic. After applying the LF algorithm, the Shear correction is then preformed on the STM data. The Shear correction makes the Bragg peaks in q-space symmetrical so that the lattice will be symmetrical in real space. The ideal triangular lattice will have Bragg peaks that are an angle of $\pi/3$ radians apart, and the Shear correction makes this so [1].

Following the performance of these corrections on the STM data, the next step is to do a multi-image registration on all of the STM images that are to be analyzed. The multi-image registration corrects for the drifting that occurs when a sample is being scanned by the STM by registering the different images taken during a data set into the same field of view [1]. After performing all of these corrections on the STM images, they are ready to be used for further analysis. See further analysis in results section 4.1.

3.2 Waterfall Plot

After registering the images to ensure proper alignment and compensate for any drift, we performed the Inverse Fourier Transform on the registered images. This mathematical operation converts a

signal from its frequency components (obtained through Fourier Transform) back to its original waveform in real space. To identify the 1 x 4 CDW point in the Fourier transform, we located the peak situated 1/4 of the distance from a Bragg peak. This specific peak, representing the 1 x 4 CDW, was selected as a reference for the subsequent inverse Fourier transform. Figure 2 illustrates the position of the 1 x 4 CDW point, marked by a red square. Following the Inverse Fourier Transform, we proceeded with the analysis by taking line cuts from each registered image. These line cuts provided one-dimensional profiles along a specific direction, enabling a closer examination of the signal's variation.

To visualize the occurrence of the phase shift relative to the bias voltage, the line cuts from different images were stacked to form a waterfall plot. This plot is presented in Figure 4, effectively highlighting the location of the phase shift in the charge density wave. We expect the phase shift to happen at a zero bias voltage because of the change from a negative to positive voltage.

3.3 Simulated Charge Density Wave

A simulated charge density wave with a known phase and amplitude can be used to confirm that NDSTM, which is the STM image processing software developed in MATLAB that was used in this study to analyze CsV_3Sb_5 data, can faithfully extract the phase and amplitude from real STM data. It can also be used to make sure that the LF and shear correction algorithms are working correctly in NDSTM. The simulated charge density wave was made with a phase slip, which is a defect in the charge density wave order. Phase slips occur when the periodic arrangement of charges is disrupted, leading to a localized region with a different charge density wave phase compared to the surrounding regions. This disruption typically occurs due to thermal fluctuations, defects in the material, or interactions with external perturbations and are present in all charge density waves.

An important thing aspect in extracting the phase from the charge density wave is making sure that the filter size is correct. If the filter size is too small, the phase is not smooth as shown in Figure 5(a). If the filter size is too large, then it will warp the phase extraction as shown in Figure 5(c).

Making a simulated charge density wave with variables such as phase and amplitude that can

easily be changed can be used to simulate real data. This can be helpful in limiting the amount of actual data runs done on the STM which saves the liquid helium needed to run the machine.

4 Results

4.1 Real Data

To show that the LF and shear correction algorithms accurately and the multi-image registration was done correctly, I compiled six different images of at different bias voltages. I then found two specific defects that were present on the top left corner and bottom right corner and I cropped the different images in the same location. This shows that the images are all correctly registered because all of the atoms align with the same pixels in each image. We need the images to be correctly registered because even a one-atom difference in the images could give us an inaccurate π phase shift. The accurate registration of the images is shown in Figure 3. The waterfall plot of these registered images is shown in Figure 4. This plot shows that there is a pi phase shift between -280 mV and -240mV. This shows that the charge density wave has lowered the Fermi level and gives us further motivation to study the unconventional behavior of the material due to the CDW.

4.2 Simulated Charge Density Wave

The LF and Shear Correction algorithms were applied to a simulated charge density wave (Fig. 5) containing a phase slip and a phase function $\phi(x)$ mimicking the 1x4 charge density wave. The objective was to assess whether these algorithms accurately remove artificially introduced noise from the simulated charge density wave and enable precise extraction of phase and amplitude information. The simulated charge density wave is shown in Fig. 5(d). The amplitude of the simulated charge density wave was accurately extracted as shown by the line cut shown in Fig 5(e). The amplitude lineally increases through the simulated CDW and the line cut shows a lineally increasing amplitude over distance.

Upon implementing the LF and Shear corrections on the simulated charge density wave, we

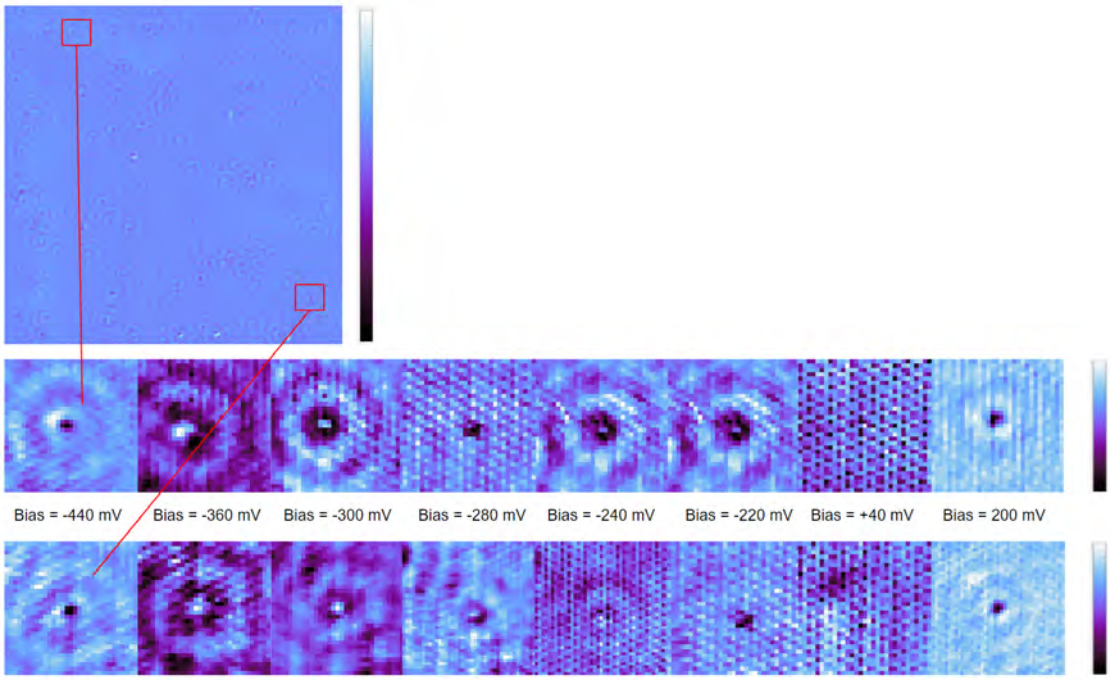

Figure 3: The red boxes on the large topographic image point to specific defects that are tracked throughout subsequent bias voltages. They are cropped in the same location, so the figure shows that all of the 8 images in this data run are registered to each other.

successfully obtained accurate phase and amplitude data from the simulated lattice, as depicted in Fig. 5. Notably, a phase shift of $\pi/3$ was deliberately included at the midpoint on the x-axis to evaluate the algorithms' performance. As evident in Fig. 5(b), the phase is represented by a red color denoting 0 phase shift for the first half of the image, transitioning to a yellow color indicating $\pi/3$ phase shift for the second half. This shows that NDSTM can accurately extract phase information from data.

5 Conclusion

In this study, we successfully demonstrated an effective method for extracting the phase from a charge density wave on a periodic Kagome lattice. The development and validation of a simulated charge density wave allowed us to establish the accuracy and reliability of our phase extraction software. As a result, we gained the confidence to apply the software to actual STM images, enabling us to extract the phase with precision and accuracy.

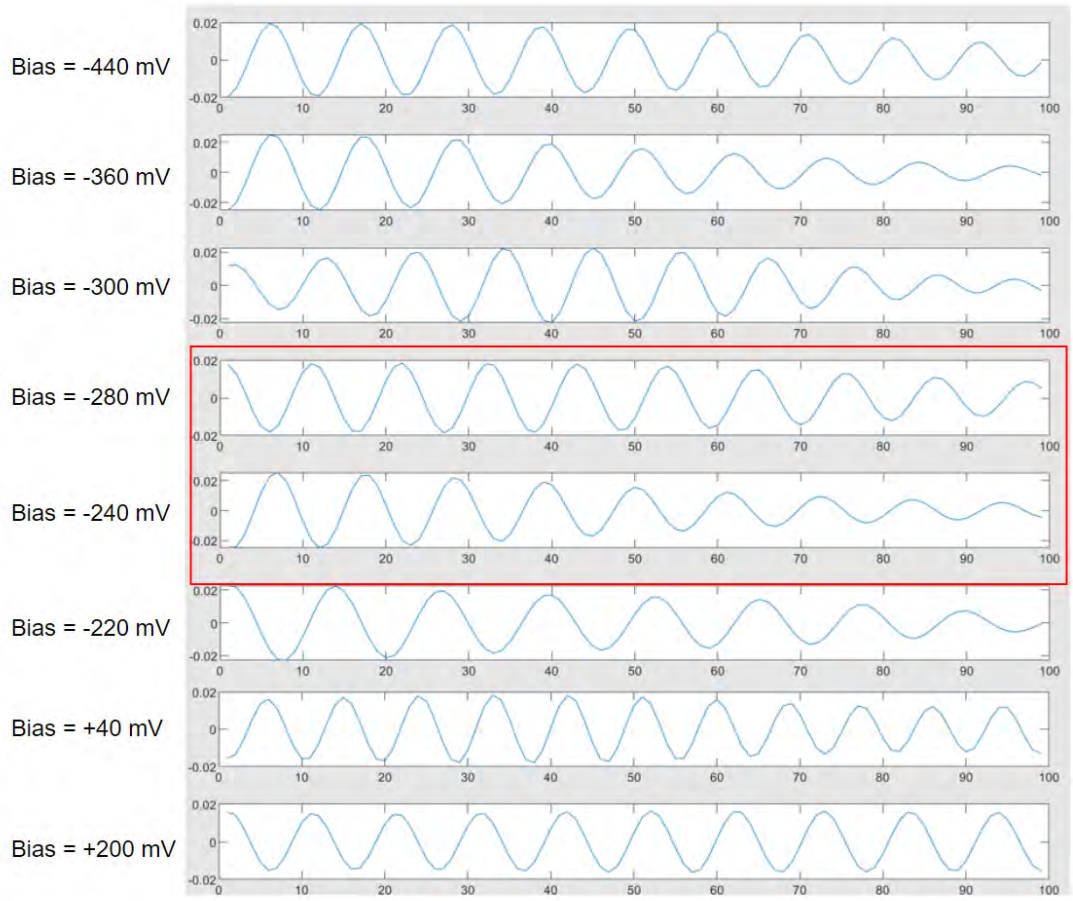

Figure 4: This is a waterfall plot of the line cuts taken from the inverse Fourier transformations of the CsV_3Sb_5 data that was registered above. There is a π phase shift shown between -280 mV and -240 mV

Looking ahead, future efforts in this project would focus on enhancing the efficiency of ND-STM. By streamlining the data analysis procedures, we can obtain results more rapidly and efficiently, facilitating more extensive investigations of Kagome lattice structures and opening doors to exploring larger data sets. The methods and insights obtained here have the potential to advance our comprehension of complex quantum materials and contribute to broader applications in condensed matter physics and related fields.

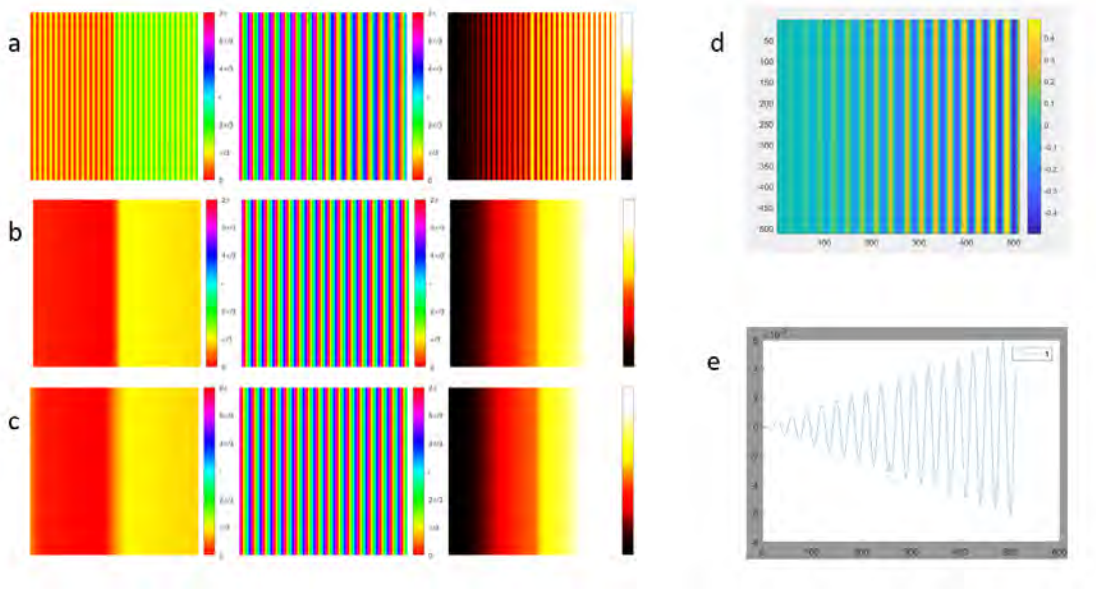

Figure 5: a) Shows a phase extraction with a filter size of 5 that is too small. b) shows a phase extraction with a correct filter size of 10. c) shows a phase extraction with a filter size that is too large. d) shows the simulated lattice. e) is the line cut of the simulated lattice that shows a linearlly increasing amplitude.

6 Acknowledgements

I would like to thank my advisor Dr. Xiaolong Liu, and graduate students Matt Toole and Nileema Sharma for their help this summer. I would also like to thank Dr. Umesh Garg and Kristen Amsler for directing and running the Notre Dame REU program.

References

[1] Xiaolong Liu and Yi Xue Chong and Rahul Sharma and J. C. Séamus Davis, Science 372, 1447-1452 (2021). https://www.science.org/doi/abs/10.1126/science.abd4607

[2] Ortiz, B. Wilson, S. D. (2020). CsV3Sb5: A ZPhysical Review Letters, 125(24). https://doi.org/10.1103/physrevlett.

[3] Spera, M., Scarfato, A., Pásztor, Á., Giannini, E., Bowler, D. R., Renner, C. (2020). Insight into the Charge Density Wave Gap from Contrast Inversion in Topographic STM Images. Physical Review Letters, 125(26). https://doi.org/10.1103/physrevlett.125.267603

[4] Lawler, M., Fujita, K., Lee, J. et al. Nature 466, 347–351 (2010). https://doi.org/10.1038/nature09169

Lorentz Angle Calculations: Coding for New Geometry in the Phase-II CMS

Lucia Baquerizo

2023 NSF/REU Program

Department of Physics and Astronomy

University of Notre Dame

Advisor: Professor Michael Hildreth, PhD

1 Abstract

The Phase-II upgrades to the Large Hadron Collider (LHC) will increase the radiation and particle density by approximately an order of magnitude, necessitating an upgrade to the Compact Muon Solenoid (CMS) detectors to withstand these new conditions. The Phase-II upgrade to the CMS also optimizes the geometry of the CMS Outer Tracker. Several layers of the pixel-strip (PS) tracker modules are tilted with respect to the beam line to minimize the path length through the detector. This varying tilt angle affects particle trajectory calculations by changing the drift of the ionization points, or hits on the detector, since the electrons from the ionizing hit drift to form clusters under the influence of the magnetic field. The purpose of this project was to properly incorporate the Lorentz angle into the simulation by adjusting the drift calculations. The calculations involving varying tilt angle were also analyzed. We concluded that the drift calculations do take the varying tilt angle into account by observing the change in the Lorentz angle under changing parameters, and by comparing the Lorentz angle to the various tilt angles. Therefore, this aspect of the new geometry will not be an issue when running the Phase-II CMS.

2 Introduction

The Large Hadron Collider (LHC) operated by CERN in Geneva, Switzerland, is undergoing a major upgrade to increase its ability to detect statistically rare events and processes. This upgrade is known as the Phase-II upgrade, and the new configuration of the LHC is the High Luminosity Large Hadron Collider (HL-LHC). This upgrade will increase the energy of the proton collisions to a center-of-mass energy of 14 TeV, such that the peak instantaneous luminosity will reach $5 - 7.5 \times 10^{34} cm^{-2} s^{-1}$ with an average number of pileup events of 140-200 per branch crossing [1]. As a result, the Compact Muon Solenoid (CMS)

experiment will be able to collect an integrated luminosity of 250 fb^{-1} per year with the goal of 3000 fb^{-1} in about a dozen years after the upgrade [1], [2].

The CMS is one of four detectors—ATLAS, ALICE, CMS, and LHCb—each of which sits at one of the four collision points of the LHC. The CMS is a general-purpose detector that collects data from the particles emitted at the collision point, such that the data can be analyzed to recreate trajectories of the particles from the event. Reconstructing the particle trajectories enables analysis of the collision point and of less stable, shorter-lived particles, with the goal of investigating into the bounds of the Standard Model. The 14,000 ton detector is essentially a solenoid magnet and layers of sensors around a central proton beam line, as seen in Figs. 1 and 2 [3]. The detectors are arranged in a cylindrical or barrel shape around the beam line, and as disks or caps at the ends of the barrel. The magnetic field runs parallel to the beam line. The CMS specifically measures the energy and momentum of the particles emitted from the proton beam collision. The Electromagnetic Calorimeter (ECAL) measures the energies of electrons and photons, and the Hadron Calorimeter (HCAL) measures the energies of hadrons. The detector layers shown in Fig. 2 are used to measure the particle momentum. These detectors are separated into the Inner Tracker and Outer Tracker—i.e. whether it is inside or outside the magnet [4].

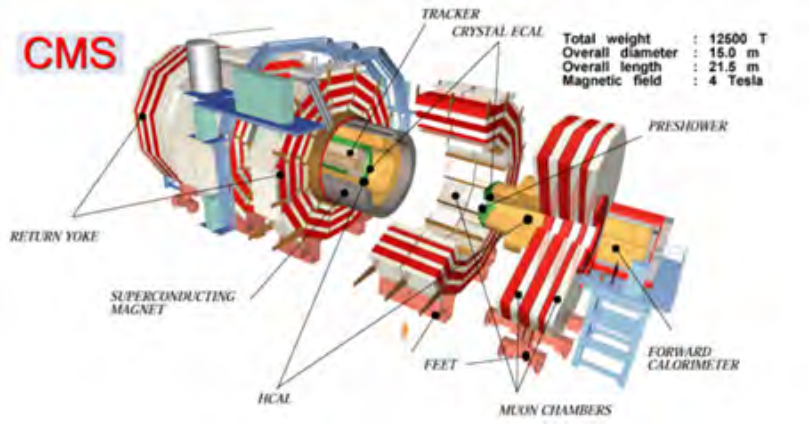

Figure 1: An illustration of the CMS. The general structure is visible and the calorimeters are indicated [4].

The CMS uses solid-state tracking detectors (SSTDs) made of silicon, that convert the ionization left by the passing of a charged particle into an electrical signal, which is sent to computers at high-speed for processing. The particle-detector interaction results in a

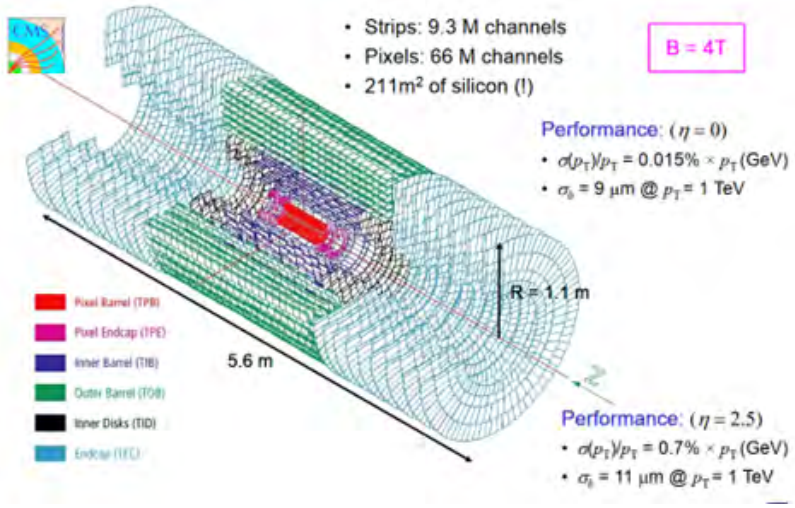

Figure 2: An illustration of the CMS, focusing on the different layers of sensors [5].

loss of momentum and energy on the part of the particle, and the power dissipation in the electronics requires a powerful cooling system [5].

The increased radiation and particle density that is part of the Phase-II upgrade is a problem for the current CMS trackers, which are already running in higher radiation conditions than they were designed for. As a result, the entire CMS detector system must be redesigned and replaced. The new detectors will have higher granularity and radiation hardness, an increased ability to handle higher data rate, and longer trigger latency in order to ensure there is no decrease in performance in comparison to the current detector's tracking capabilities [6].

In the Phase-II upgrade to the CMS, the Inner Tracker is made of pixel detector modules, and the Outer Tracker's three inner layers are made of pixel-strip (PS) modules, each of which is a pixelated sensor under a microstrip sensor, and the Outer Tracker's outer layers are made of micro-strip (2S) modules, each of which is one microstrip sensor on top of another [7]. The two-sensor module setup in the Outer Tracker allows for the L1 Trigger system, which only accepts data from high-momentum particles, eliminating information from small or slow-moving charged particles, and raising the probability of detecting muons. Tracks showing the trajectory of the particle through the detector are developed from hits via a multi-step process. When a charged particle interacts with the detector, the

particle ionizes a set of points on the detector. The excited electrons drift under the influence of the magnetic field to form clusters on the surface of the detector as depicted in Fig. 3. In a two-sensor module system, hits from the same particle passing through both sensors can be linked to form a stub. As seen in Fig. 4, this method of stub formation process allows low-momentum particles to be rejected. This is because a larger curvature in the particle's path implies greater deflection from the Lorentz force, which means the momentum of the particle perpendicular to the detector is low. Conversely, a muon moving at a high velocity would have a mostly straight path through the detector. Stubs from adjacent layers in the detector are combined to form tracklets, which are used to form a track for a particle through the entire detector as depicted in Fig. 5. Rebuilding the trajectories of the various particles detected by the sensors allows for study of the collision, such as to identify previously unknown short-lived particles [8].

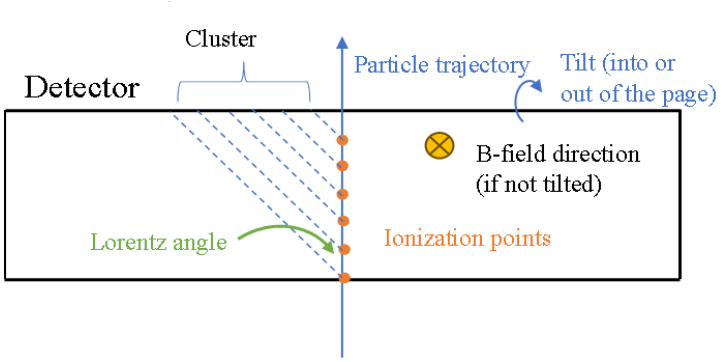

Figure 3: An illustration of an ionizing particle forming a cluster on a detector.

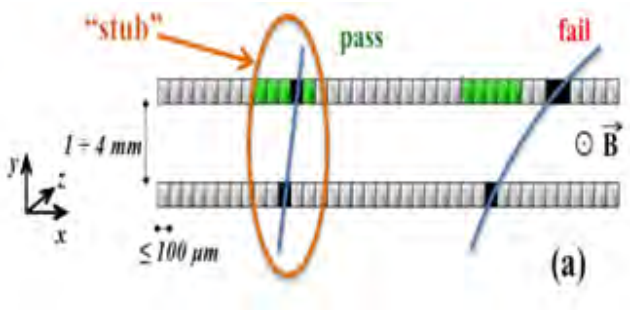

Figure 4: An illustration of stub formation, showing that only high momentum particles are accepted for stub formation and further processing [7].

Since the entire CMS tracker is to be redesigned and replaced, another project was undertaken: to optimize some of the detector geometry. Modules in the three PS barrel

Figure 5: An illustration of the detector hits being converted to tracks [5].

layers of the Outer Tracker were progressively tilted as η increased or decreased, as shown in Figs. 6 and 7. This was done both to minimize the number of modules and to have better trigger performance by minimizing the path length through the detector material [6].

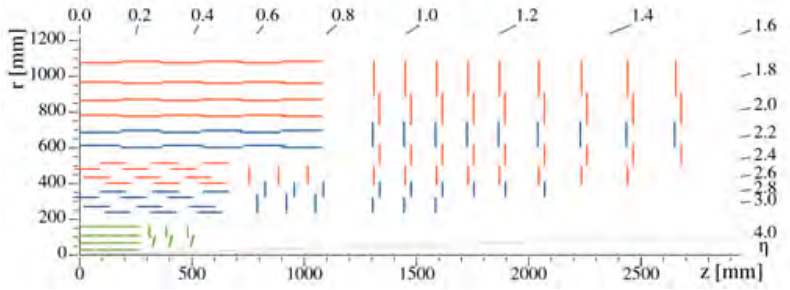

Figure 6: Phase 1 CMS Detector [3]. This is a side view showing about one-fourth of the Outer Tracker, oriented suth that the beam line is parallel to the z-axis shown.

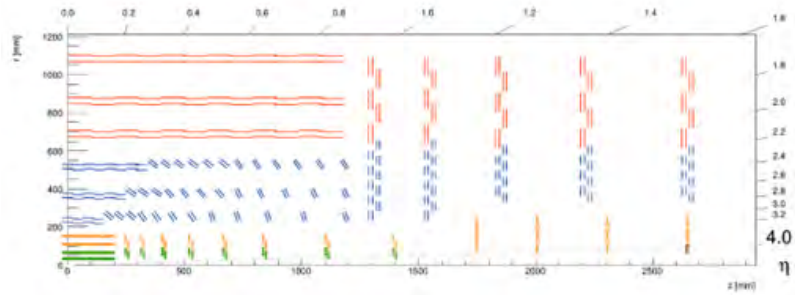

Figure 7: Phase 2 CMS Detector[7]. The view and orientation are the same as in Fig 6.

However, changing the detector alignment has the potential to impact the L1 Trigger system. Specifically, this raised concerns on whether the Lorentz angle, or the angle at which the ionization from the particle is deflected by the magnetic field during cluster formation, was properly included in the simulation of particles through the CMS [9], [10]. If not included, there is the possibility that hits could be recorded in the wrong position, or stub predictions made incorrectly. Thus, the initial purpose of this project was to correct

the calculations based on the Lorentz angle, as well as properly incorporating the tilt angle in the code and calculations in the hit and stub formation. Our final objective was to verify the effect of the tilt angle on the calculations for the Lorentz angle, hit formation, and stub formation.

3 Materials and Methods

The CMS Software (CMSSW) was used and analyzed in this project [11]–[13]. Groups of muons, either 3, 10, or 500, were simulated as generated from the interaction point, passing through the CMS, and interacting with the sensors. This project dealt exclusively with the Phase-II L1trigger code, with commands added to the Phase2TrackerDigitizerAlgorithm.cc file and thus the data analyzed was restricted to sensors in the Outer Tracker. The main steps that were taken to investigate the effect of the Lorentz Angle and the tilt angle began with interacting with set values for the Lorentz angle from the database. The code reads a set value for the Lorentz angle from the database, or rather, the tangent of the Lorentz angle. In a config file, we set the tangent of the Lorentz angle per Tesla to be 0.3 for both the barrel and the endcap. This value is at least an order of magnitude higher than the original value and served to make the relations we were investigating more noticeable. We investigated how the code treated the orientation of sensors. We were able to access the tilt angle associated with each detector, and associate hit information with the tilt angle and specific detector, as shown in Fig. 8

The various ways in which the code represented the magnetic field were also analyzed. Information on the drift direction, ionization points, and cluster and stub formation were analyzed with the magnetic field on (as normal) and without the magnetic field.

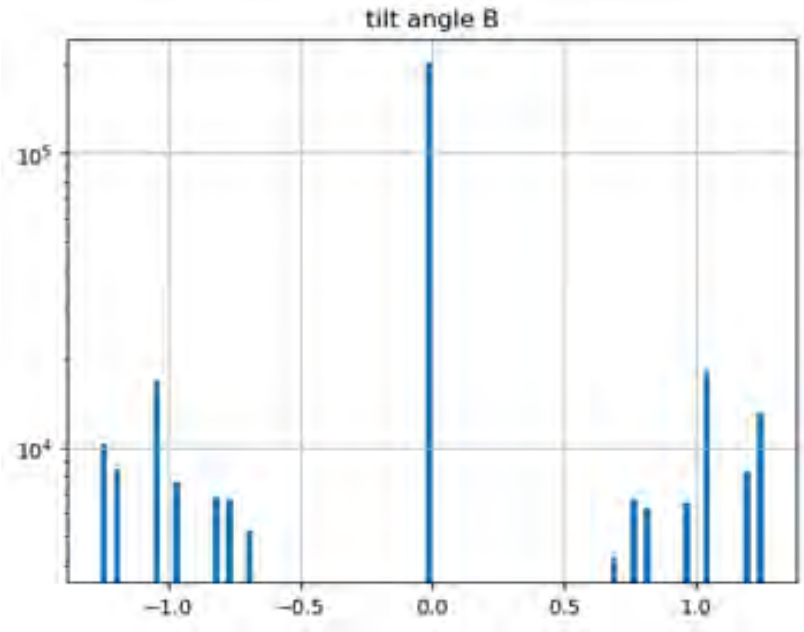

Figure 8: A histogram showing the different tilt angles (radians) and their frequency in log scale. The data for this was taken from a 500 muon simulation.

4 Results and Discussion

Various stages of hit processing, from the ionization points, to cluster formation, and stub formation, were analyzed in the presence of the normal magnetic field and without the magnetic field. Analyzing the cluster positions in the presence and absence of the magnetic field gave the first indication that calculations involving the Lorentz angle and the tilt angle were in fact yielding the expected results. There was a consistent difference between the two data sets, indicating that the magnetic field and Lorentz angle were being processed correctly. To analyze the effect of the tilt angle on the Lorentz angle, we compared the ionization points and corresponding points making up the cluster under identical magnetic field conditions. The Lorentz angle was calculated for each ionization-cluster set. Each tilt angle was found to have a distinct, associated Lorentz angle as shown in Fig. 9.

We note that the configuration of the tangent of the Lorentz angle per Tesla was at least an order of magnitude higher than would be in actual conditions, to make the differences more noticeable. In addition, there were instances of particles passing through a corner of the detector. This created some noise, which was eliminated from the graphs.

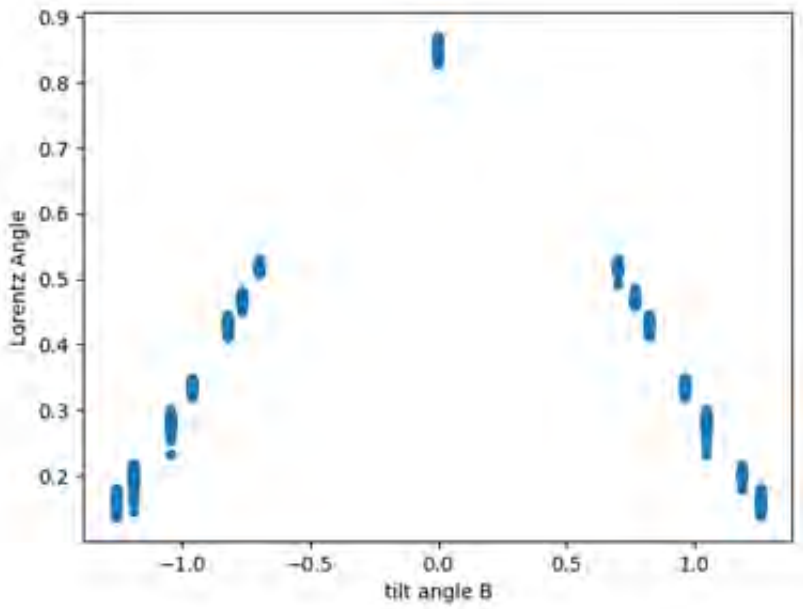

Figure 9: A graph of the Lorentz Angle vs the tilt angle.

5 Conclusions

Contrary to expectations, the simulation code and calculations were determined to be accurate in the scope of this investigation. Both the effect of the magnetic field and pre-set Lorentz angle on cluster formation were consistent with predicted results as seen in Fig. 9. The relation between the tilt angle, the Lorentz angle, and the drift were also consistent with expectations. The addition of a tilt angle on some of the Outer Tracker modules did not cause issues with the simulation and analysis. This aspect of the CMS Phase-II upgrade should proceed without issue.

6 References

[1] A. Cassese, "The CMS pixel detector for the High Luminosity LHC," Nucl Instrum Methods Phys Res A, vol. 1045, p. 167620, Jan. 2023, doi: 10.1016/J.NIMA.2022.167620.

[2] G. Apollinari et al., "High-Luminosity Large Hadron Collider (HL-LHC). Technical Design Report V. 0.1," Jan. 2017, doi: 10.23731/CYRM-2017-004.

[3] D. Contardo and A. Ball, “The Phase-2 Upgrade of the CMS Tracker,” Jun. 2017. doi: 10.17181/CERN.QZ28.FLHW.

[4] “Detector — CMS Experiment.” https://cms.cern/detector (accessed Aug. 01, 2023).

[5] M. Hildreth, “Introduction to Charged Particle Tracking,” in 2010 Hadron Collider Physics Summer School, Fermilab, 2010.

[6] A. Rossi, “The CMS Tracker for the High Luminosity LHC,” Nucl Instrum Methods Phys Res A, vol. 1048, p. 167950, Mar. 2023, doi: 10.1016/J.NIMA.2022.167950.

[7] S. R. Chowdhury, “The Phase-2 Upgrade of the CMS Outer Tracker,” Nucl Instrum Methods Phys Res A, vol. 979, p. 164432, Nov. 2020, doi: 10.1016/J.NIMA.2020.164432.

[8] A. Ryd, “Tracklet-based L1 Tracking,” Oct. 2014.

[9] P. Schütze, “Measurement of the Lorentz Angle in CMS Pixel Detector Modules Setup, Simulation and Analysis status,” in 5th BTTB, Barcelona, 2017.

[10] A. M. Nurnberg and T. Schneider, “Lorentz angle measurements as part of the sensor R&D; for the CMS Tracker upgrade.” Sep. 10, 2012. Accessed: Aug. 01, 2023. [Online]. Available: https://cds.cern.ch/record/1478135

[11] “CMS Offline Software.” http://cms-sw.github.io/ (accessed Aug. 02, 2023).

[12] “WorkBook ¡ CMSPublic ¡ TWiki.” https://twiki.cern.ch/twiki/bin/view/CMSPublic/WorkBook (accessed Aug. 02, 2023).

[13] “/CMSSW_13_3_X_2023-08-02-2300/.” https://cmssdt.cern.ch/lxr/source (accessed Aug. 02, 2023).

Dissociative Electron Attachment to Ethanol: Resonance Energies and Fragmention Pathways

AYSIA BITTINGER

2023 NSF/REU Program
Department of Physics and Astronomy
University of Notre Dame

ADVISOR(S): Dr. Sylwia Ptasinska, Dr. Ian Carmichael

Abstract

Dissociative electron attachment (DEA) is a key process by which low-energy electrons (1 to 15 eV) cause significant damage to DNA. To understand DEA to a complex arrangement of biomolecules like DNA, we must first understand DEA to simple, individual molecules. This project studies DEA to the simple alcohol, ethanol, because of its medical and clean energy applications. A comparison is made between experimental resonance energies and theoretical fragmentation pathways with corresponding thermodynamic thresholds to understand the mechanisms behind DEA to ethanol. This comparison yielded results similar to other studies regarding the OH^- fragment. However, results regarding the remaining fragments were less consistent with other literature. Further research into these discrepancies is required to discover the most accurate resonance energies of these fragments.

1 Introduction

Low-energy electrons (LEEs) from 1 to 15 eV are produced from interactions between molecules and ionizing radiation or in plasma discharges [1]. For example, during radiation therapy, high energy radiation ionizes molecules in the patient's body, producing secondary LEEs that can cause damage to biomolecules [2]. They are also abundant in cellular systems, the atmosphere, and electronic, electrochemical, and photovoltaic devices [1]. These LEE interactions can result in the dissociation of the target molecule through neutral dissociation, dissociative ionization, and dissociative electron attachment (DEA) [1]. This project focuses on uncovering the mechanisms behind DEA to molecules. DEA occurs when a LEE attaches to a molecule, excites it into a temporarily charged state–also called a transient negative ion (TNI)–and finally breaks the molecule apart into a negatively charged fragment and one or more neutral fragments [3].

1.1 Background Knowledge on DEA

Since 2000, when it was reported that LEEs (below the ionizing energy for DNA) can cause single and double strand breaks in DNA [4], DEA to biomolecules has been studied in hopes of discovering what mechanisms cause such damage to DNA. DEA is also a process used for breaking specific bonds in molecules with the same functional group (atom or a group of atoms in a molecule that, when included, gives molecules similar chemical properties) [5]. Prabhudesai et al. proposed

that functional group dependent bond cleavage (or breakage) could be utilized on larger or more complex molecules, and may even help in modeling LEE-induced damage to DNA [5]. Thus, a few aspects of DEA are usually studied: 1) the resonance energy, or energy where DEA to a molecule maximally produces fragments [5–10], 2) the scattering angles of fragments [11; 12], and 3) the thermodynamic threshold (TDT), or minimum energy required for DEA to occur, of different fragmentation pathways [6–8; 10].

1.2 Ethanol Applications

Results from studying the process of DEA to a simple alcohol like ethanol (CH_3CH_2OH) could help us understand mechanisms behind DEA to more complex alcohols and organic compounds that are related to DNA [8; 9]. Through a better understanding of DEA to DNA constituents, models of LEE-induced damage to DNA could be improved [4]. Furthermore, ethanol is a renewable bio-fuel. It does not contain benzene (a carcinogen) or butadiene (a teratogen), both of which are found in gasoline. Due to its simple structure, there are also fewer complex substances released into the atmosphere when ethanol is combusted [13]. This study of ethanol's resonant energy peaks could contribute to calculating ethanol's differential cross sections for elastic LEE scattering, which is useful in the design of efficient ethanol-combustion based engines [14]. In order to understand DEA to ethanol, this project has three main goals: 1) experimentally discover the resonance energies of detected fragments from DEA to ethanol, 2) calculate the TDT of fragmentation pathways to infer which are most energetically favorable, and 3) compare the theoretical threshold energies and experimental resonant energies.

2 Methods

The DEA experiment setup consists of an electron and gas source, vacuum chamber, and quadrapole mass spectrometer. Electrons are produced from a heated filament via thermionic emission under vacuum conditions, and an accelerating voltage gives them a particular energy between 1 and 15 eV. The gas is also introduced to the vacuum chamber with a precise needle valve ($\pm$0.01 mbar). In

the vacuum chamber DEA occurs, and a quadrapole mass spectrometer with a secondary electron multiplier (SEM) detector detects the fragments produced based on their mass. Depending on the type of experiment, the quadrapole system will allow all fragments to be detected (mass spectrum) or isolate a specific mass (ion yield).

2.1 Calibration and Preliminary Mass Spectra

The ion yield (number of anions detected as a function of incident electron energy) of O^- from CO_2 was used to calibrate the DEA setup because it has well-studied resonance peaks. The calibration scan of CO_2 had a resonance peak that was 0.9 eV lower than Rapp et al.'s measurements [15]. Therefore, a correction factor of 0.9 eV is added to each ion yield. Then, mass spectra (number of counts as a function of mass) were measured at multiple energies between 1 and 15 eV to detect the mass of fragments produced from DEA to ethanol. The masses 13, 15, 16, 17, 19, 35, 43, and 45 amu were detected.

2.2 Ion Counts as a Function of Incident Electron Energy

For each mass detected in the mass spectra, an ion yield was completed for ethanol from 1 to 15 eV. These scans were measured for varying lengths of time depending on the strength of the signal detected. Then, ion yields of a deuterated ethanol sample, where the H in the hydroxyl group is replaced by a deuterium (CH_3CH_3OD), were measured. The masses we decided to scan for were dependent on how the inserted deuterium would effect the mass of detected fragment. For example, the 17 amu fragment (presumably OH^-), would most likely have a mass of 18 amu from the deuterated sample.

2.3 Ab initio Calculations

Computational chemistry uses a variety of theoretical methods to evaluate molecular electron structures and energetics. The Gaussian 16 program was used which requires the starting positions of the atoms in the molecule, its charge and its spin multiplicity, and a prescribed computational method.

This project is using the W1BD composite method to calculate the TDTs of fragmentation pathways. The W1BD method optimizes the input coordinates by quickly finding the atomic configuration of lowest electronic energy, then further improves this energy by a series of more thorough calculations. Although computationally expensive, it was used to achieve the most accurate energies possible [16]. This information will allow us to infer which bonds are most likely to break, based upon which pathway is more energetically favorable.

3 Results and Discussion

The following subsections present ion yields of notable fragments from both regular and deuterated ethanol (CH_3CH_2OD). Note, every ion yield shows an increase in signal around 13 eV. This is background noise and is not regarded as a resonance peak. Also note, a fragment with its corresponding mass in amu is denoted with a capital M and mass number.

3.1 Mass 16 Fragment

The initial scan of M16 had several resonances at 4.1, 6.9, and 9.3 eV. The second scan had peaks at 6.6 and 9.3 eV, but showed a significantly reduced signal at 4.1 eV, indicating this may have been from contamination (O^- not from DEA). Hence, a background scan (chamber pressure $< 5.00 \cdot 10^{-10}$ mbar) was measured to check for other contamination, however no signal was detected. Finally, a similar scan was obtained for the deuterated sample of ethanol (CH_3CH_2OD), with peaks at 6.7 and 9.2 eV (Figure 1). These two peaks are inconsistent with other singular resonances found at

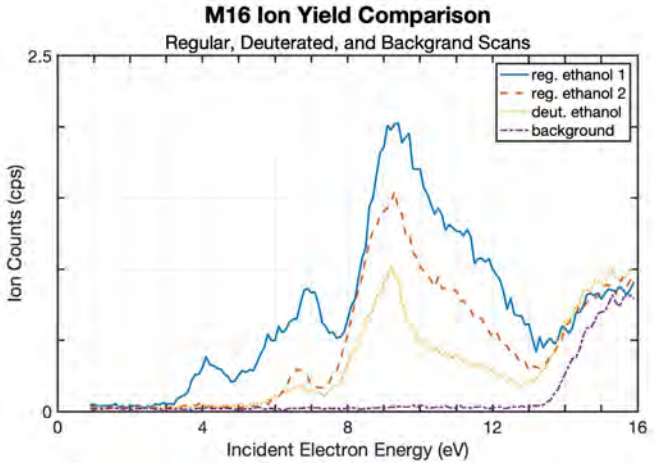

Figure 1: Multiple ion yields of the 16 amu fragment. Two scans of regular ethanol (CH_3CH_2OH) are shown in solid blue and dashed orange. A scan of deuterated ethanol (CH_3CH_2OD) is shown in dotted yellow. A background scan of the vacuum chamber ($< 5.00 \cdot 10^-10$ mbar) is shown in dash-dotted purple. The two most prominent resonances are at 6.7 and 9.2 eV.

5.8 [6] and 6.2 eV [7]. It is also inconsistent with Ibanescu et al. who did not observe an M16 resonance [10]. Thus, causes of these inconsistencies with other papers regarding this fragment requires further investigation.

The M16 fragment is assumed to be O^-, and a few pathways have been proposed for its formation [6; 7]. We calculated the pathway proposed by Orzol et al. [6]

$$e^- + CH_3CH_2OH \rightarrow [CH_3CH_2OH]^{-\#} \rightarrow CH_3CH_2 + O^- + H \quad (1)$$

to have a TDT of 7.06 eV (consistent with Orzol et al.'s 7.05 eV). This is energetically unfavorable since the experimental detection of O^- begins before 7.06 eV. Thus, Orzol et al. [6] also suggests the pathway

$$e^- + CH_3CH_2OH \rightarrow [CH_3CH_2OH]^{-\#} \rightarrow CH_3CH_3 + O^- \quad (2)$$

The TDT calculated for pathway (2) is 2.69 eV, which is very similar to the TDT of 2.68 eV reported by Orzol et al. [6]. This pathway is more energetically favorable, as its TDT is below where the O^- fragment begins to be produced in Figure 1.

3.2 Mass 17 Fragment

The ion yield of M17 from regular ethanol and M18 from deuterated ethanol (CH_3CH_2OD) both yielded resonances at 8.6 eV with no other significant peaks (Figure 2). This resonance peak is fairly consistent with other articles that detected peaks at 8.2 eV [6], 8.5 eV [7], and 9.1 eV [10]. Since the hydroxyl group has a mass of 17 and 18 amu in the regular and deuterated ethanol, respectively, this indicates cleavage of the C-O bond resulting in the OH^- fragment. This pathway can be described as

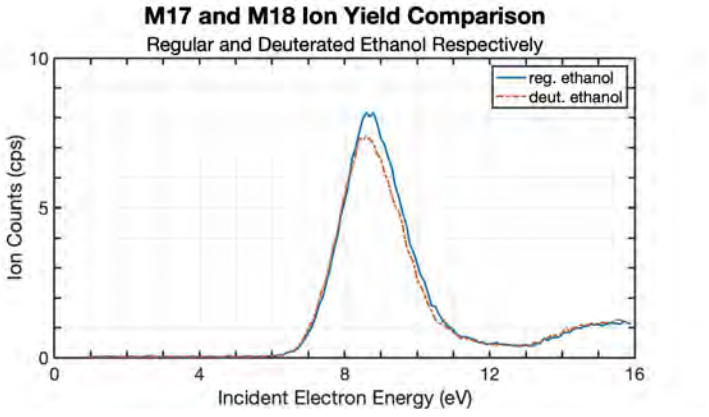

Figure 2: An ion yield of the 17 amu fragment from regular ethanol (CH_3CH_2OH) in solid blue and the 18 amu fragment from deuterated ethanol (CH_3CH_2OD) in dash-dotted orange is shown. A resonance at 8.6 eV was detected in both scans.

$$e^- + CH_3CH_2OH \rightarrow [CH_3CH_2OH]^{-\#} \rightarrow CH_3CH_2 + OH^- \quad (3)$$

This fragmentation pathway has a TDT of 2.2 eV. This value is consistent with Orzol et al. [6], which found the TDT to be 2.4 eV. Since the peak yield of OH^- (8.6 eV) is significantly higher (6.2 eV greater) than the TDT for pathway (3), Orzol et al. proposed the excess energy could cause further H loss of the neutral fragment. Thus, we calculated the pathway

$$e^- + CH_3CH_2OH \rightarrow [CH_3CH_2OH]^{-\#} \rightarrow CH_2CH_2 + H + OH^- \quad (4)$$

which yielded a TDT of 3.76 eV. This is also in agreement with Orzol et al.'s respective 3.82 eV [6]. Therefore, this is also an energetically plausible fragmentation pathway.

3.3 Mass 45 Fragment

A relatively weak resonance at 2.5 eV was detected for M45 from regular ethanol (Figure 3). Other studies have detected comparable resonances at 2 [6], 2.88 [8], and 2.8 eV [10]. However, Orzol et al. also detected resonances at 5 eV and 8.2 eV [6]. Moreover, Ibanescu et al. detected resonances at 6.35, 7.85, and 9.15 eV [8], and then 6.3, 7.85, and 9.1 eV [10].

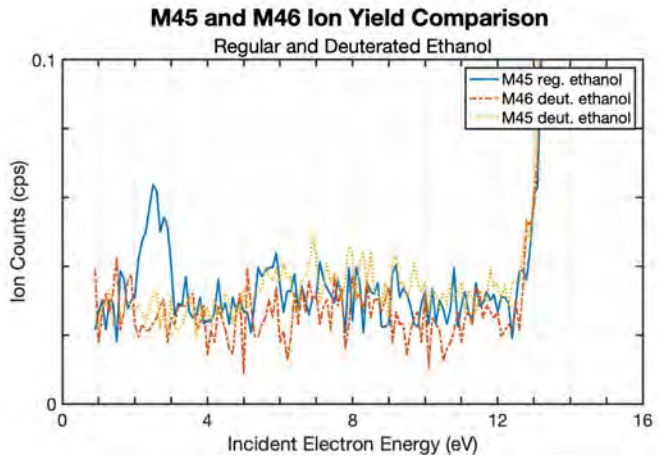

Figure 3: Ion yield of 45 amu mass from both regular ethanol (CH_3CH_2OH) in solid blue and deuterated ethanol (CH_3CH_2OD) in dotted yellow. An ion yield of the 46 amu fragment from deuterated ethanol is also shown in dash-dotted orange. Only the solid blue resonance at 2.5 eV was detected.

Our ion yields showed no such indication of other resonances. In fact, the M45 and M46 ion yields of the deuterated sample (CH_3CH_2OD) showed no resonant peaks. The detection of M45 from deuterated sample would indicate the O-D bond (O-H bond in regular ethanol) cleavage. If M46 was detected, then we could infer a C-H bond was breaking. However, the lack of signal from both scans (Figure 3) could indicate in regular ethanol both the O-H and C-H bond cleavages occur, but when one instance is isolated, the fragment's signal is too weak for detection. Therefore, this

fragment still requires scans of other deuterated samples and longer scanning periods to understand which H-bond is being broken during this process.

Orzol et al. concluded M45 could only result from the pathway

$$e^- + CH_3CH_2OH \rightarrow [CH_3CH_2OH]^{-\#} \rightarrow [CH_3CH_2O]^- + H \quad (5)$$

with a TDT of 2.55 eV [6]. However, this TDT is above their lowest energy feature (2 eV), which makes the pathway energetically improbable. Our calculations produced a comparable TDT at 2.83 eV for pathway (5), which is also above our ion yield peak. Thus, we completed TDT calculations for cleavage of the C-H bonds.

$$e^- + CH_3CH_2OH \rightarrow [CH_3CH_2OH]^{-\#} \rightarrow [CH_2CH_2OH]^- + H \quad (6)$$

$$e^- + CH_3CH_2OH \rightarrow [CH_3CH_2OH]^{-\#} \rightarrow [CH_3CHOH]^- + H \quad (7)$$

Pathway (6) has a TDT of 3.74 eV and pathway (7) has a TDT of 4.35 eV. It is relevant to note that for pathways (5) and (6), it is more energetically favorable to produce $[CH_3CH_2O]^-$ and $[CH_2CH_2OH]^-$. However, in pathway (7), the H fragment has a higher electron affinity than the CH_3CHO fragment. Therefore, it is more energetically favorable for DEA to ethanol to produce the H^- fragment via the complementary channel to pathway (7). This is interesting to note since the detection of the H^- fragment has been reported in other articles [5; 9].

4 Conclusion

This study of experimental resonant peaks and theoretical fragmentation pathways showed consistencies with other literature, but also opened new questions. The ion yield for the M17 fragment showed a resonance consistent with other literature [6; 7; 10]. The M18 scan of the deuterated ethanol (CH_3CH_2OD) also highly suggests the C-O bond cleavage produces this fragment. Furthermore, the ab initio calculations supported pathway (4) as a plausible fragmentation pathway [6]. Both the M16 and M45 fragment resonances were inconsistent with other studies. Only one

resonance peak is detected for M16 in other literature [6; 7], but we detected two. The M45 scan had a resonance at 2.5 eV which agrees with other peaks around 2 eV found in other articles [6; 8; 10]. However, the 2.5 eV resonance was not detected in subsequent scans of the deuterated sample. Moreover, many M45 peaks reported in other papers [6; 8; 10] were not detected by our scans. Therefore, further analysis of the M16 and M45 fragments is required to understand these discrepancies and their relationship to the proposed fragmentation pathways.

The results of this project could advance clean energy research through the development of ethanol-combustion based engines. It will also aid in the understanding of DEA to simple alcohols, which can be applied to research in DEA to DNA constituents, ultimately contributing to modelling DEA-induced damage to DNA. LEE interactions not only have applications in clean energy and medicine, but also in atmospheric sciences and electronics. Thus, this study of DEA and the mechanisms behind it allow us to gain a deeper knowledge of how to improve a variety of technologies.

References

[1] S. Ptasinska, M. Varella, M. Khakoo, D. Slaughter, and S. Denifl, Eur. Phys. J. D **76**, 10.1140/epjd/s10053-022-00482-8 (2022).

[2] L. Sanche, Eur. Phys. J. D **35**, 367 (2005).

[3] L. G. Christophorou and J. K. Olthoff, *Fundamental Electron Interactions with Plasma Processing Gases*, Physics of Atoms and Molecules (Kluwer Academic / Plenum Publishers, New York, 2004).

[4] B. Boudaïffa, P. Cloutier, D. Hunting, M. Huels, and L. Sanche, Science **287**, 1658 (2000).

[5] V. S. Prabhudesai, A. H. Kelkar, D. Nandi, and E. Krishnakumar, Phys. Rev. Lett. **95**, 143202 (2005).

[6] M. Orzol, I. Martin, J. Kocisek, I. Dabkowska, J. Langer, and E. Illenberger, Phys. Chem. Chem. Phys. **9**, 3424 (2007).

[7] X.-D. Wang, C.-J. Xuan, W.-L. Feng, and S. X. Tian, J. Chem. Phys. **142**, 064316 (2015), https://pubs.aip.org/aip/jcp/article-pdf/doi/10.1063/1.4907940/14034124/064316_1_online.pdf .

[8] B. C. Ibănescu, O. May, A. Monney, and M. Allan, Phys. Chem. Chem. Phys. **9**, 3163 (2007).

[9] V. S. Prabhudesai, D. Nandi, A. H. Kelkar, and E. Krishnakumar, J. Chem. Phys. **128**, 154309 (2008), https://pubs.aip.org/aip/jcp/article-pdf/doi/10.1063/1.2899330/15410364/154309_1_online.pdf .

[10] B. C. Ibanescu and M. Allan, J. Phys.: Conf. Ser. **194**, 052037 (2009).

[11] A. G. Falkowski, M. A. P. Lima, and F. Kossoski, J. Chem. Phys. **152**, 244302 (2020), https://pubs.aip.org/aip/jcp/article-pdf/doi/10.1063/5.0008428/13897132/244302_1_online.pdf .

[12] M. A. Khakoo, J. Blumer, K. Keane, C. Campbell, H. Silva, M. C. A. Lopes, C. Winstead, V. McKoy, R. F. da Costa, L. G. Ferreira, M. A. P. Lima, and M. H. F. Bettega, Phys. Rev. A **77**, 042705 (2008).

[13] J. B. Heywood, *Internal Combustion Engine Fundamentals*, 1st ed. (McGraw-Hill Education, 1989).

[14] M. C. A. Lopes, D. G. M. Silva, M. H. F. Bettega, R. F. da Costa, M. A. P. Lima, M. A. Khakoo, C. Winstead, and V. McKoy, J. Phys.: Conf. Ser. **388**, 012014 (2012).

[15] D. Rapp and D. D. Briglia, J. Chem. Phys. **43**, 1480 (2004), https://pubs.aip.org/aip/jcp/article-pdf/43/5/1480/11049504/1480_1_online.pdf .

[16] E. C. Barnes, G. A. Petersson, J. A. J. Montgomery, M. J. Frisch, and J. M. L. Martin, J. Chem. Theory Comput. **5**, 2687 (2009), pMID: 26631782, https://doi.org/10.1021/ct900260g .

Improving the Efficiency of Modeling Half-life Curves with ^{33}Cl

MILLER CHRISTEN

2023 NSF/REU Program
Department of Physics and Astronomy
University of Notre Dame

ADVISOR(S): Prof. Maxime Brodeur

Abstract

Efficient modeling of the half-life of ^{33}Cl directly impacts the evaluation of the standard model of physics and the precision of the unitary CKM matrix. This paper discusses parameter estimating methods, particularly a new implementation of "sum-fit" modeling, to achieve more accurate and precise half-life measurements. Improved measurements could lead to a better extraction of other critical variables, advancing our comprehension of the standard model and its implications. By ensuring reliable half-life measurements, these models help maintain the integrity of our current understanding of elementary particles.

1 Introduction

Precision measurements have led to considerable advances in the understanding of nuclear astrophysics, nuclear structure, and probing beyond the Standard Model of physics. More specifically, precision beta decay measurements contributes on testing the unitarity of the Cabibbo-Kobayashi-Maskawa (CKM) quark-mixing matrix [1], which describes the strength of flavor-changing weak interactions and quantifies the mismatch of quantum states of quarks between their free propagation and their involvement in weak interactions. Isolating the top row elements of this matrix, (V_{ud}, V_{us}, V_{ub}), allows the most precise unitarity test, with V_{ud} holding the largest weight. The determination of the V_{ud} value can be extracted from four different types of beta decays: superallowed pure Fermi transitions, superallowed mixed transitions, pion decay, and neutron decay.

While a precise value of V_{ud} has been determined using superallowed pure Fermi transitions, it is crucial to ensure its accuracy. Hence, a research program at the University of Notre Dame Nuclear Science Laboratory focusses on confirming this value using superallowed mixed transitions between mirror nuclei. Two nuclei are said to be mirrors from one another when the number of protons in one is equal to the number of neutrons in the other. A superallowed transition conserves angular momentum, isospin, and parity without changing the spin of the nucleons involved [2]. To extract V_{ud} from such transitions, the Ft-value must be determined, which is reliant on measurements of half-life, branching ratio, and decay transition energy, Q_{EC}. An in-depth explanation of the Ft-equation and its variables can be found in Ref. [3]. In addition, one also needs to determine the Fermi-to-Gamow Teller mixing ratio for transitions between mirror nuclei, which will be measured

using the St.Benedict facility currently under construction at the Nuclear Science Laboratory of Notre Dame.

The fractional uncertainty of the experimental quantities as well as the theoretical corrections entering the Ft-value are shown in Figure 1. It can be seen that in several cases the literature half-life is found to be imprecise or coming from a series of conflicting measurements. Furthermore, the relative half-life of ^{33}Cl is among the highest in the lighter transitions, and also serves as a large source of uncertainty in the Ft-value of that transition. It is important to ensure that the various quantities entering in the determination of the Ft-values are precise and accurate. This motivated performing a precision half-life measurement of ^{33}Cl alongside planned future measurements of the mixing ratio.

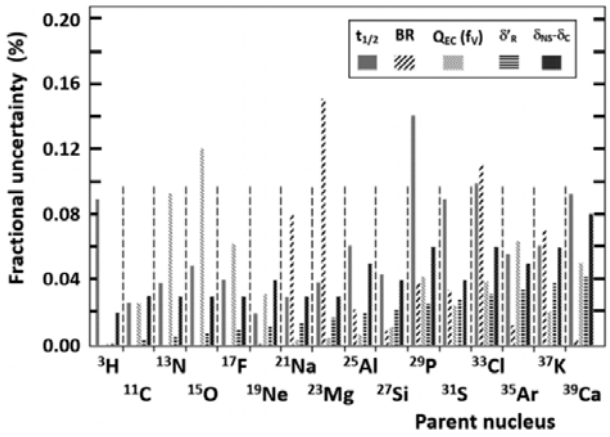

Figure 1: Fractional uncertainties in the corrected Ft-value of various superallowed mixed transitions.

2 Background

For the lifetime measurement, a radioactive ion beam (RIB) of ^{33}Cl is produced and separated using the twin solenoid facility TwinSol at the NSL. A stable primary beam of ^{32}S is first generated using an FeS cathode in a cesium sputtering ion source and accelerated using a FN tandem accelerator set to a terminal voltage of 9.0 MV. In the tandem, the negatively charged ions are accelerated toward a thin carbon stripper foil placed at the center of the tandem which removes multiple electrons. The

now positively charged ion is accelerated even more as it heads downstream of the center, which is how it gains the majority of its energy. Following the accelerator, a dipole magnet separated the charge states and only selected the ^{32}S ions, which were sent to the RIB production target, a gas cell containing 800 Torr of deuterium gas.

After its production, the ^{33}Cl beam was separated from the primary beam using the TwinSol facility, and was then implanted on a gold foil attached to a rotating arm and placed in the NSL β-decay counting station [4]. The foil is typically implanted for a duration equal to three half-lives of the isotope of interest. Then it is rotated in front of a plastic scintillator backed by a photomultiplier tube (PMT) and the betas emitted from the decay of ^{33}Cl are counted for at least 25 half-lives [5; 6]. The ^{33}Cl half-life measurement comprised a series of 57 runs, the standard runs being composed of 20 cycles each with 650s counting periods. In each of these runs, the potential of the PMT, the discriminator threshold voltage, the irradiation duration, the counting duration, and the material of the target were varied to probe for possible systematic effects that would affect the measurement.

3 Methods

3.1 Raw Data Sorting

Events registered at the counting station are saved in "list-mode" data files. Each event appears as a new line in a list with three time stamps: a pre-scaled time, the 100 Hz clock time, and the time for which the system has been "live". The pre-scaled time is used to define the total length of our counting cycles, and the "live" time correspond to the times for which the system is not busy (or dead) processing an event. For the fitting of half-lives, these three column files are then sorted using two methods of grouping. The first method groups events by their occurrence given a "pre-scaled time", while the second sorts given "clocktime". The resulting data files display cycle number, prescaled time, number of counts given the time used to sort, clocktime, and live time.

3.2 Binning Process

While the two different data sorts should theoretically result in the same total number of counts per run, a cross-checking was done to ensure consistency in counts and distribution of counts. This process begins with a rebin of the data to reduce and equate the size of the data sets for the two sorts. Rebinning data, sometimes referred to as data bucketing, allows for faster fitting and interpretation, as shown in the next section. This method can also improve accuracy of predicting models by diminishing noise while preserving the original data distribution. Over the 57 runs, bins were cut from an initial average of 16,250 down to 500.

The residual difference for an individual run can be seen in Figure 2. While the residuals, defined as the difference between the binning of the two sorting methods, are not always zero, this does not present a systematic trend that would lead to different half-lives. It was verified that the distribution of counts/events was consistent between both sorting methods before this processed data was used in the following fitting process.

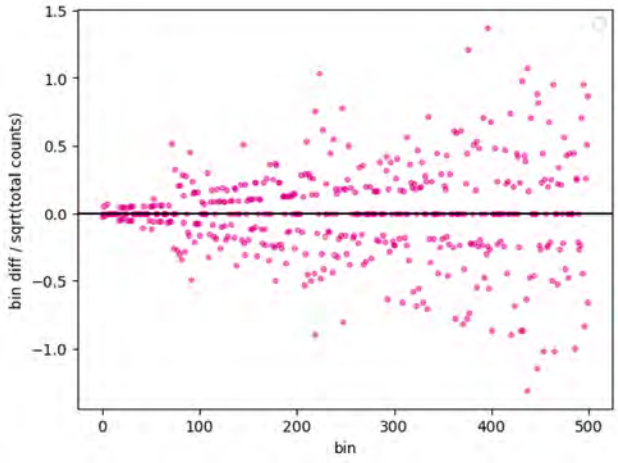

Figure 2: Residuals of count distribution given prescaled time and clocktime are shown for sample run 51.

3.3 Maximum Likelihood Fitting

Maximum likelihood estimation (MLE) is a powerful statistical method used for parameter estimation in scientific data analysis. It aims to find the parameter values that maximize the likelihood

of observing the given data while considering the probability distribution of the data points' uncertainties. Compared to the least-squares method, using maximum likelihood offers versatility in parent distributions (non-Gaussian), which is important for fitting half-life curves as these are made with discrete binned data and the counts in these bins will follow a Poisson parent distribution.

A variant of MLE, used for data for half-life measurements, known as the "sum-fit" method, was implemented in the model-fitting for decay-curves of ^{33}Cl. This method further defines maximum likelihood regression of Poisson-scatter data by using summed individual probabilities and distorting the statistical weights to also account for dead-time losses.

4 Results

Implementation of the "sum-fit" method was done in Python as opposed to previous executions using Mathematica. The termination of the algorithm, happening when relative change in all parameters is less than a certain percentage, is allowed to push past 0.01% to convergence and at an enhanced computational speed, ensuring accurate and efficient parameter estimates. As seen in Figure 3, a side-by-side comparison of the new and previous executions display the tighter-fit curve of the former. Using run 43 as an example, the root mean squared error (RMSE) of the Python model was 21.12 in comparison to the Mathematica model's RMSE of 237.39, the new fit showing a 0.027% improvement in correctness of predicted values. A similar increase in accuracy was found across all runs. With this new implementation, modeling decay curves can provide an enhanced description of raw data in future half-life measurements, as it has convincingly demonstrated in the case of ^{33}Cl.

A final fitting was done for the half-life of ^{33}Cl over the summed data of 54 runs, 3 runs having been discarded, as shown in Figure 4. The first two runs were excluded due to a long activation time that led to a large amount of background contaminants and run 22 due to the PMT base not being properly connected. Based on the conducted experiment described earlier in this paper, the half-life estimation was found to be 2.535 ± 0.005 s. A contaminant of 30P was found to be present, likely responsible for the deviation from the standing measurement of ^{33}Cl half-life to be 2.5038 s.

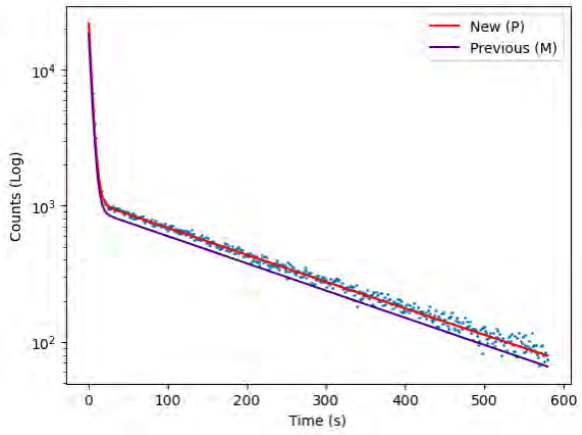

Figure 3: Comparing ^{33}Cl half-life modeling curves using parameter estimates generated by Mathematica and Python 'sum-fit' algorithms. Notably, the Python implementation exhibits a 0.03% improvement in accuracy.

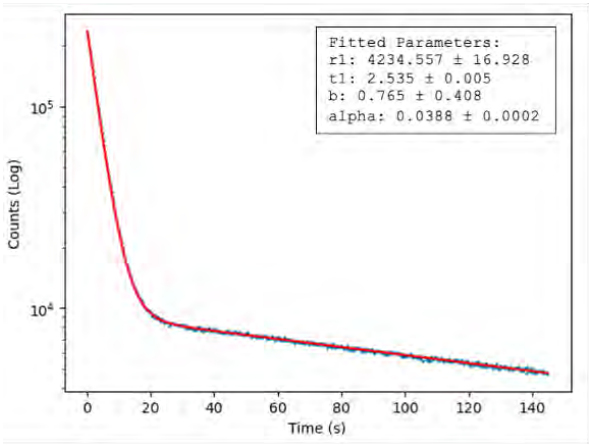

Figure 4: Modeling the half-life of ^{33}Cl, using the summed data of 54 runs, with a contaminant of ^{30}P present.

Nevertheless, this observation does not undermine the enhanced efficiency of the utilized modeling program.

5 Conclusion

The objective of cross-checking and fitting ^{33}Cl was to enhance the efficiency of modeling half-life decay, achieved through the implementation of the "sum-fit" method, which not only allows for faster analysis of half-life data but also ensures a tighter and more accurate curve-fit. Furthermore, this new implementation is easily accessible and comprehensible for future users. The half-life measurement of ^{33}Cl conducted at the NSL of the University of Notre Dame was among several crucial measurements aimed at augmenting global data. In order to further improve the extraction of V_{ud}, more precise measurements are also required of the other leading uncertainties in the Ft value, in addition to the continued increase of half-life precision. These measurements will play a significant role in confirming the true unitarity of the CKM matrix, with the potential to unveil a new generation of quarks or particles in case of any deviations.

Acknowledgements

I want to share my gratitude to my advisor, Maxime Brodeur, and his research group, for their support and warm welcome throughout this program. Additionally, I would like to thank Dr. Umesh Garg and Kristen Amsler for orchestrating such an enriching and memorable experience.

References

[1] V. Koslowsky, E. Hagberg, J. Hardy, G. Savard, H. Schmeing, K. Sharma, and X. Sun, Nuclear Instruments and Methods in Physics Research Section A: Accelerators, Spectrometers, Detectors and Associated Equipment **401**, 289–298 (1997).

[2] O. Naviliat-Cuncic, Mirror transitions within and beyond the sm (2021).

[3] N. Severijns, L. Hayen, V. De Leebeeck, S. Vanlangendonck, K. Bodek, D. Rozpedzik, and I. S. Towner, Phys. Rev. C **107**, 015502 (2023).

[4] M. Brodeur, C. Nicoloff, T. Ahn, J. Allen, D. W. Bardayan, F. D. Becchetti, Y. K. Gupta, M. R. Hall, O. Hall, J. Hu, J. M. Kelly, J. J. Kolata, J. Long, P. O'Malley, and B. E. Schultz, Phys. Rev. C **93**, 025503 (2016).

[5] A. A. Valverde, M. Brodeur, T. Ahn, J. Allen, D. W. Bardayan, F. D. Becchetti, D. Blankstein, G. Brown, D. P. Burdette, B. Frentz, G. Gilardy, M. R. Hall, S. King, J. J. Kolata, J. Long, K. T. Macon, A. Nelson, P. D. O'Malley, M. Skulski, S. Y. Strauss, and B. Vande Kolk, Phys. Rev. C **97**, 035503 (2018).

[6] J. Long, M. Brodeur, M. Baines, D. W. Bardayan, F. D. Becchetti, D. Blankstein, C. Boomershine, D. P. Burdette, A. M. Clark, B. Frentz, S. L. Henderson, J. M. Kelly, J. J. Kolata, B. Liu, K. T. Macon, P. D. O'Malley, A. Pardo, C. Seymour, S. Y. Strauss, and B. Vande Kolk, Phys. Rev. C **101**, 015501 (2020).

Galactic Archeology in M15: Origins of Neutron-Capture Elements and Globular Clusters

BENJAMIN COCO

2023 NSF/REU Program
Department of Physics and Astronomy
University of Notre Dame

ADVISOR(S): Professor Evan Kirby

Abstract

M15 is one of the brightest and densest globular clusters in the night sky and is one of a few clusters with a significant star-to-star dispersion in the abundances of neutron-capture elements. The goal of the project has been to use stellar spectroscopy in M15 by using high-resolution spectra collected from the Keck/HIRES spectrograph. Continuing the project from the 2022 REU session, my work this summer focused on expanding the analysis from last year's project to more stars and more elements, as well as examining the differences between first and second-generation stars as determined by magnesium abundance. Our hypothesis was that the high dispersion of the neutron-capture elements in the first generation decreases to a very low dispersion in the second generation of stars. If confirmed, M15 would be the second globular cluster to show a relation between the neutron-capture and light elements. These results would imply that the timescale for neutron-capture nucleosynthesis is probably too short to be explained by binary neutron star mergers. So far, our results in M15 do not support the hypothesis, which means that the neutron-capture elements have a diversity of production pathways in globular clusters.

1 Introduction

Galactic archaeology is the study of the formation and history of our galaxy. By observing and collecting data on various astronomical bodies, conclusions can be made about how the Milky Way came to be as we know it. The work conducted this summer with the guidance of my advisor, Professor Evan Kirby, was to examine the chemical abundances within Messier 15, also known as M15. M15 is a globular cluster in the Pegasus constellation and was actually the first globular cluster shown to host a planetary nebula.

Globular clusters are bright regions on the outer edges of galaxies that have high concentrations of stars within a small region of space but are still bound gravitationally to the galaxy it is orbiting.[GBC19]

One of the primary avenues of research in galactic archaeology is to determine the chemical abundances of stars and search for any illuminating patterns.[Rod11] One particularly compelling pattern was found in M92 seen in figure 2, which showed a high dispersion of the neutron capture elements in the first generation of stars that decreased by the time the second generation formed. This de-

crease in dispersion suggests that a single source of the neutron-capture occurred concurrently with the formation of the first generation, but M92 became well-mixed and homogenized before the formation of the second generation. The timescale between a generation of stars is on the magnitude of 'only' a few million years. However, Binary Neutron Star Mergers, the only confirmed source of neutron capture elements, occur on a timescale of 100 million years which is far too long for one to have created the elements for the second generation of stars. In a recently submitted paper to the Astrophysical Journal, Professor Kirby used this relationship in M92 to show that there must be a rare source of neutron-capture elements—particularly the heaviest neutron-capture elements.

We hypothesized that M15 would show a similar relationship between the two generations of the stars, which would confirm and present the second instance to the literature of a second origin of the neutron-capture elements being necessary. All of the data used is archival data collected from the W. M. Keck Observatory in Maunakea, Hawai'i, using its HIRES spectrograph.

2 Background

2.1 Spectroscopy

Spectroscopy is the study of how light interacts with matter. Light is electromagnetic radiation and has both particle-like and wave-like properties, which are the only ones pertinent to this project. The electromagnetic spectrum, in order of decreasing wavelength and increasing energy, covers Radio Waves, Infrared Rays, Visible Waves, Ultraviolet Rays, X-rays, and Gamma Rays. The visible range is between roughly 400 nm and 750 nm, which is approximately the spectral range of the data used for this project.

There are two main kinds of stellar spectroscopy: Absorption and Emission. We used absorption spectroscopy. It uses the absorption lines from the energy absorbed by electrons from photons. An absorption line appears as the absence of light at a particular wavelength, as can be seen in Figure 1.

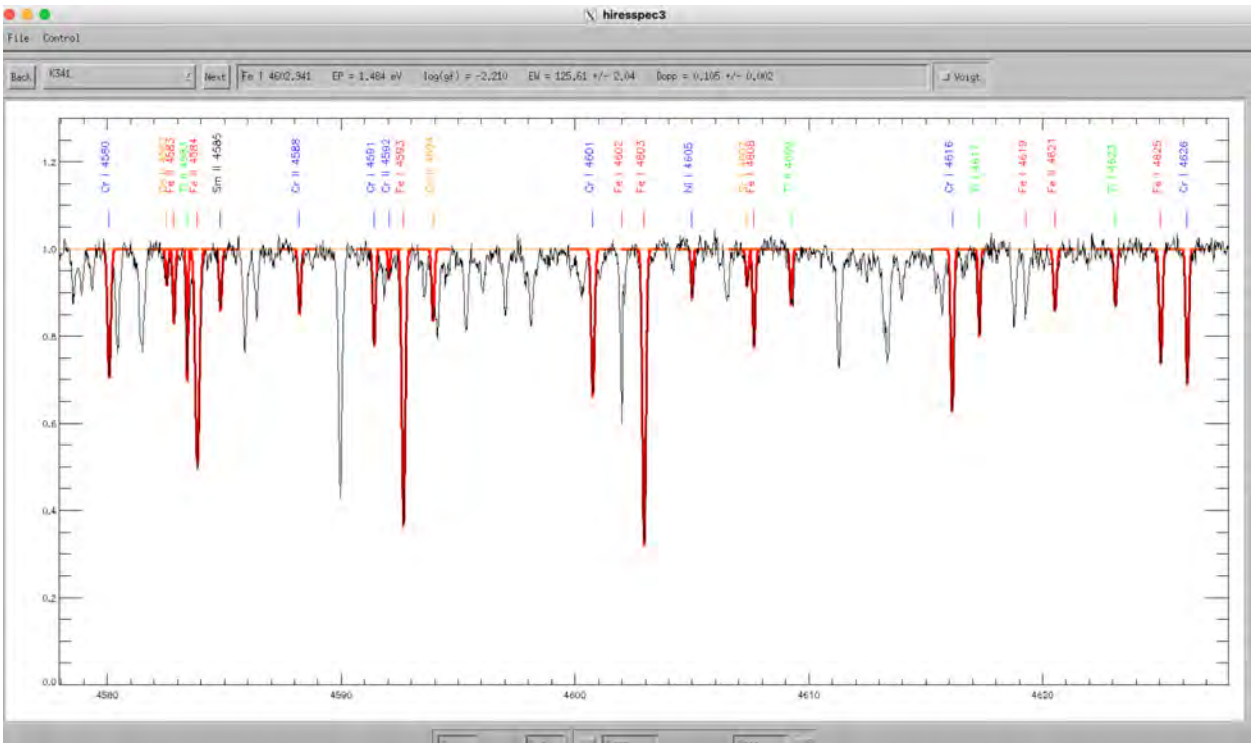

Figure 1: Representation of IDL Data fitting

We used archival data from HIRES. The spectra are high-resolution, which enables us to cleanly separate absorption lines from each other.

2.2 R-process

In the Big Bang, in addition to our universe beginning, the first elements were created: Hydrogen, Helium, and trace amounts of Lithium. Over time the 'dust' and gas that existed in the interstellar medium experienced enough gravitational attraction that they began to form protostars. As more and more mass became compacted, the protostars became denser and denser until the cores were hot enough for nuclear fusion to begin.

Over the lifetime of stars, the fusion process naturally produces elements through Iron, the 26th element. Iron is the most stable element that can be formed by Fusion and the tipping point at which energy is lost when fusing elements. However, the periodic table does not stop at Iron, the highest naturally occurring element is Uranium which is the 92nd element which means there must

be a source that produces the elements past Iron.[FB18]

There are at least three types of processes that produce neutron-capture elements: the p-process, the s-process, and the r-process. The r-process is the process relevant to the work this summer. The r stands for rapid. The timescale is over 100 captures per second, and it is one of the sources of the heaviest elements. For decades, there had been several hypothesized sources of the r-process in space, but there were no confirmed sources. In 2017 LIGO detected gravitational waves from GW170817, a neutron star merger [PPa17]. The decay of nuclei that were neutron-rich [AT23] showed that the r-process had to be occurring and was the first confirmed source of the neutron-capture elements. Neutron star mergers occur on a time scale of 100 million years.

3 Methods

3.1 Using IDL to calculate the abundances

The process of analyzing the data and determining the elemental abundances begins by fitting the curves seen in Figure 1. The red curves are the absorption lines of different elements. The name of the element is marked above each curve. The absorption lines correspond to specific wavelengths, and the lines for each element are the same across all the stars used in this project. These curves are used to create Equivalent Widths, which is the width of a rectangle with a height of 1 that has the same area as the curve of the absorption line.

The equivalent widths are used to calculate the abundances of the elements. This is done by taking the average of the values for each element. Iron (Fe) has a very high number of absorption lines in the optical spectrum, and if one measurement is slightly off, it will be balanced out with all of the other measurements for Iron. However, there are certain elements, such as Barium and Europium, which have only a few lines present in the entire spectrum, and as a result, the statistical and systematic errors increase significantly if the measurements aren't as accurate as they should be.

After the curves have been fit, the software MOOG, which calculates the emergent spectrum of a star, is used to convert the equivalent widths into abundances. This is done by creating parameter files that input each star's temperature, surface gravity, microturbulent velocity, metallicity, and ratio of Alpha elements to Iron. Alpha elements are the even numbered with atomic numbers between 8 (oxygen) and 22 (titanium). The Metallicity used was $[\mathrm{Fe/H}] = -2.4$, and the Alpha to Iron ratio was $[\alpha/\mathrm{Fe}] = 0.4$. The microturbulent velocity was calculated by multiplying the surface gravity by 0.23 and subtracting that product from 2.13 [Kir+09]. Stars with temperatures above 5000 K aren't used because they have absorption lines too weak to be useful for measuring abundances.

After running MOOG, we produced graphs and plotted the elements in relation to each other with Python matplotlib.

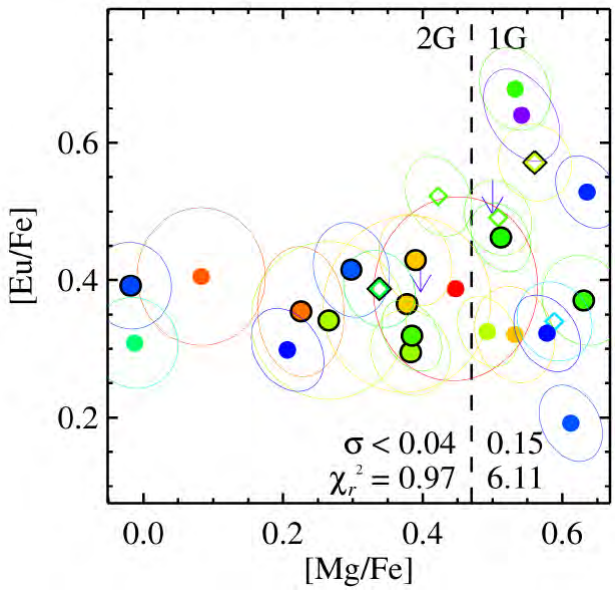

Figure 2: Magnesium and Europium relation in M92

3.2 Python Coding

A Python dictionary with all the solar elemental abundances was imported, and the packages used were Astropy, Numpy, Pandas, and Matplotlib. After using a code to read the MOOG output files of each star and produce the average abundance for each element in each star, the first graphs were

produced. The desired Max Standard Deviation is 0.2 dex for each element measured for each star. Each element was in relation to the abundance of Hydrogen (H) for that star using the equation 1. Because this is a log measurement, the 12 represents 10^{12}, which is equal to 1 trillion and puts the abundance values in parts per trillion. After using MOOG to calculate the abundance measurements, Python was used to subtract the corresponding stellar values of the element to produce values in the form of the equation 2, where $\odot$ represents the sun. The code has three inputs (x, y, Starlist) where x and y are two different elements that correspond to the x and y values to be plotted, and Starlist is the list of stars that those abundance measurements will be taken from to plot.

$$\text{A(Element)} = 12 + \log(\frac{\text{Number density of Element}}{\text{Number density of Hydrogen}}) \tag{1}$$

$$[\text{A/B}] \equiv 12 + \log[n(\text{A})/n(\text{B})] - \log[n(\text{A})/n(\text{B})]_{\odot} \tag{2}$$

The final step for plotting the elements is to put the elements in relation to Iron which is done by subtracting the values for the abundance of Iron from the abundance values for the other measurements. The form of [Element/Fe] is the final form of the graphs and corresponds to [Element/Fe] = [Element/H] - [Fe/H]. The line from the code used to plot the elements is below: 3.

```
plt.errorbar(abund[x]-abundFe, abund[y]-abundFe,xerr=stddev[x],yerr=stddev[y])
```
(3)

The graphs are similar to the one shown in Figure 2, but are not yet separated between the first and second generation of stars.

4 Current Results

The graph shown in Figure 2 shows a high dispersion of Europium, reminiscent of the dispersion of neutron-capture elements in M92. This strong decrease in the dispersion in M92 indicates that there has to be an event between the two generations of stars that would produce the neutron-capture

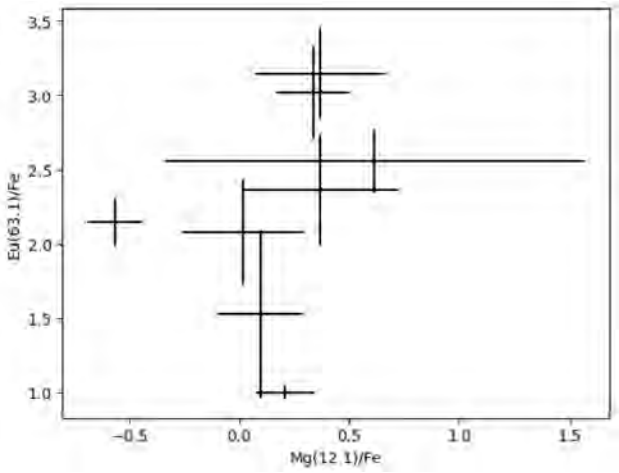

Figure 3: Magnesium and Europium relation in M15

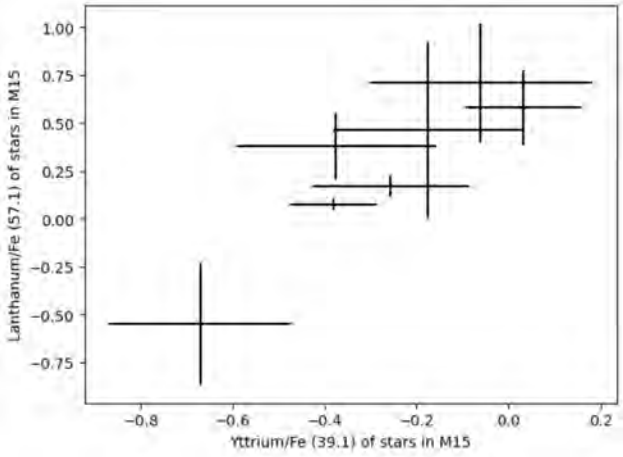

Figure 4: Yttrium vs Lanthanum relation in M15

elements. Because the difference between generations of stars is only a few million years, this shows that there must be a source other than neutron star mergers since the time scale is much too short for a merger to have produced the elements. We don't speculate what the source is, but the literature has many promising potential sources, such as supernovae. [MMa92]

The graph in Figure 3 plots Magnesium and Euriopium measurements for some of the stars in M15 and the same relationship is not seen. Currently, our results are showing that the elements in M15 formed differently from M92 and that the process for neutron capture elements is not homogeneous across Globular Clusters. The graph in Figure 4 shows that there is a correlation between

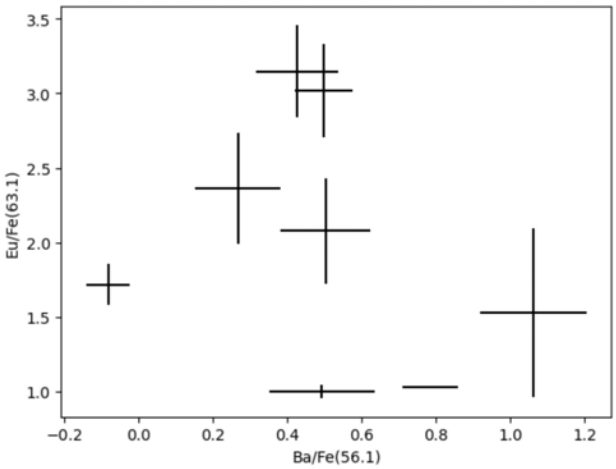

Figure 5: Barium vs Europium relation in M15

Yttrium and Lanthanum, which is important because this one-to-one relationship supports that the neutron-capture elements came from the same source. The graph in Figure 5 is interesting because it indicates that some of the concentrations of the elements were produced from the s-process.

5 Conclusion

We began this project hoping to see the same relation between the neutron-capture elements in M15 that was seen in M92. However, currently, our results do not show the relationship in M15. Based on our current results, we tentatively conclude that the neutron-capture elements formed differently between the two Globular Clusters, which would indicate that the formation of neutron-capture elements in a Globular Cluster is unique to that Globular Cluster and not homogeneous across all clusters. While different than our initial hypothesis, this is an interesting finding that has weight in how globular clusters will be studied in the future.

Following this REU, Professor Kirby and I will continue to work on M15. Once we finish adjusting the data for the redshift in the stars, we will be able to include more stars and have enough data points to be to know which of our conclusions is confirmed.

6 Acknowledgements

I would like to thank my advisor, Professor Evan Kirby, for selecting and directing this project and for his continual support throughout the program this summer; without him and his support, the project wouldn't exist. I would like to thank last year's REU student Alice Cai for beginning the project and Natalie Edmisten and Aaron McNeely for their help in obtaining measurements last year. I would like to thank Ian McHugh and Aaron McNeely for their help this summer in measuring the stars and adjusting the data to account for the redshift in the stars. I would also like to thank Dr. Umesh Garg and Kristen Amsler for directing and coordinating this excellent experience. Furthermore, thank you to the Notre Dame Physics Department, and the general Notre Dame community for hosting me. Finally, I would like to thank the NSF for their funding.

References

[AT23] A. Arcones and FK. Thielemann. "Origin of the elements". In: *Astron Astrophys Rev* 31.1 (2023).

[FB18] Anna Frebel and Timothy C. Beers. "The formation of the heaviest elements". In: *Physics Today* 71.1 (2018), pp. 30–37.

[GBC19] R. Gratton, A. Bragaglia, and E. et al. Carretta. "What is a globular cluster? An observational perspective". In: *Astron Astrophys Rev* 27.1 (2019).

[Kir+09] Evan N. Kirby et al. "Multi-element Abundance Measurements from Medium-resolution Spectra. I. The Sculptor Dwarf Spheroidal Galaxy". In: *ApJ* 705.1 (Nov. 2009), pp. 328–346. DOI: 10.1088/0004-637X/705/1/328. arXiv: 0909.3092 [astro-ph.GA].

[MMa92] B Meyer, G. Matthews, and et al. "r-Process nucleosynthesis in the high-entropy supernova bubbler". In: *APJ* 399.2 (1992).

[PPa17] D'Avanzo Pian E., S. P. Benetti, and et al. "Spectroscopic identification of r-process nucleosynthesis in a double neutron-star merger". In: *Nature* 551 (2017).

[Rod11] Ian. Roderer. "Primordial r-process Dispersion in Metal-Poor Globular Clusters". In: *ApJL,* 732.1 (2011).

Measurement and Analysis of the ^{17}F(p, p') reaction

SYDNEY COIL

2023 NSF/REU Program
Department of Physics and Astronomy
University of Notre Dame

ADVISOR(S): Dr. Daniel Bardayan

Abstract

X-ray bursts are one of the most frequent transient events observed in the universe. They repeat irregularly with periods from a few hours to months and lead to the synthesis of numerous heavy elements in the rp-process. This process is poorly understood due to the numerous reactions on exotic nuclei. The *rp*-process is thought to be triggered by the ^{14}O(α,p)^{17}F reaction, and understanding the rate of this reaction will aid in interpreting x-ray burst light curves. Because of the difficulty of studying the forward reaction, recent attempts have been made to study the time reversed reaction, ^{17}F(p,α)^{14}O. Since these studies only probe astrophysical branches to the ground state of ^{17}F, the ^{17}F(p,p') reaction was studied at the Nuclear Science Laboratory (NSL) at the University of Notre Dame to look for the population of excited states. The data will be presented and preliminary results discussed.

1 Introduction

1.1 Astrophysical Background

Type-I x-ray bursts occur in accreting neutron star binary systems [1]. The rapidly rising temperatures in this type of astrophysical explosion causes a breakout from the hot CNO cycle, eventually leading to the rapid proton capture process, or *rp*-process for short. The ^{14}O(α,p)^{17}F reaction is understood to be the reaction that begins the *rp*-process [2], and is also among one of the top reactions that contributes to x-ray burst light curves [3; 4], and therefore to more completely understand the physics occuring in these stellar explosions, it is necessary to understand the ^{14}O(α,p)^{17}F reaction.

1.2 Previous Studies

Despite this importance, the ^{14}O(α,p)^{17}F reaction is poorly understood owing to the difficulty in studying it since an ^{14}O beam and a helium target are difficult to create and maintain. One of the most productive avenues instead is to study the reverse reaction, ^{17}F(p,α)^{14}O [5]. ^{17}F beams are available at high intensities, and hydrogen targets can be produced in the form of solid foils as opposed to trying to produce targets of helium. This reaction has been studied many times previously. In 1999, Argonne National Laboratory surveyed the ^{17}F(p,α)^{14}O reaction at beam energies between 70 and 90 MeV. This study found three resonances at excitation energies $E_x = 7.60 \pm 0.05$

MeV, 7.37 ± 0.06 MeV, and 7.16 ± 0.15 MeV [6]. These resonances created an experimentally determined cross section that differed from the expected cross section, leading to a need for further measurement.

In 2001, the same reaction was studied at Oak Ridge National Laboratory, in addition to the ^{17}F(p,p) reaction [5] as a way to address the uncertainties in the ^{17}F(p,α)^{14}O cross sections from the previous study. This measurement found four resonances that corresponded with observed states in ^{18}Ne: $E_x \approx$ 6.15 MeV, 7.07 MeV, 7.35 MeV, and 7.60 MeV. This measurement also studied the ^{17}F(p,p) reaction and surveyed beam energies between 40.1 and 68.2 MeV using two primary targets. For higher energy measurements, a 100 μg/cm^2 target was used, and for lower energy measurements, target thickness ranged from 200-300 μg/cm^2. Total cross section plots were produced for this reaction for center of mass angles between $\theta = 128° - 159°$.

The ^{17}F(p,α)^{14}O reaction was studied seven years ago in the Notre Dame Nuclear Science Lab [7]. This study attempted to measure the reaction with a beam energy between 40 and 52 MeV, but the results were inconclusive because of relatively poor beam qualities. This earlier study used TwinSol, which has now been upgraded (to TriSol) and would have benefited greatly from recent upgrades. Figure 1 shows the cross section measurements done to date for the ^{17}F(p,α)^{14}O reaction.

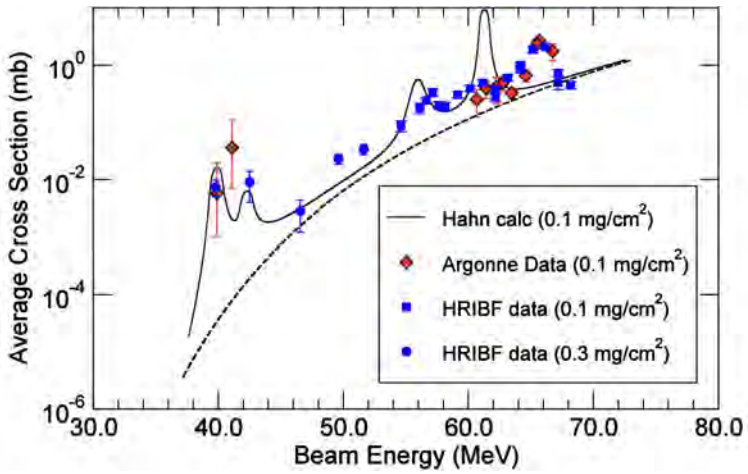

Figure 1: This figure shows a cross section vs. beam energy plot for the ^{17}F(p,α)^{14}O reaction, and includes all surveys done to date. This figure was taken from Reference [7].

1.3 Motivation

Although it has been studied multiple times, significant discrepancies in the measurement of the ^{17}F(p,p') reaction still remain. This reaction is important to study as it allows a probe into the excited states of ^{17}F, which may be populated during the ^{14}O(α,p)^{17}F reaction. Furthermore, in studying the ^{17}F(p,α)^{14}O reaction, it is not possible to create an excited state beam, making it necessary to study the ^{17}F(p,p') reaction to gain any insight into the ^{17}F excited states. The rest of this paper will focus on this reaction.

2 Instrumentation

2.1 *TriSol* system

As mentioned in Subsection 1.3, the *TwinSol* system was upgraded to the *TriSol* system prior to the next measurement. This upgrade included a fifteen degree bending magnet and the third superconducting solenoid, shown in Figure 2

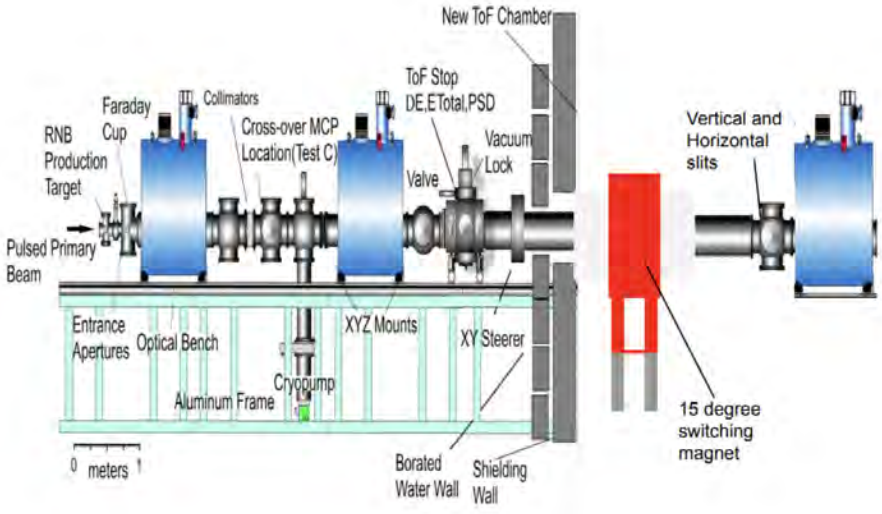

Figure 2: A schematic of the *TriSol* system.

To commission this system, the switching magnet's field needed to be characterized as it has

been altered to accept larger envelope secondary beams. This allowed for more accurate modeling of the beam optics with the LISE++ simulation [8], as shown in Figure 3. This simulation shows computationally that the third solenoid acts as a focusing device.

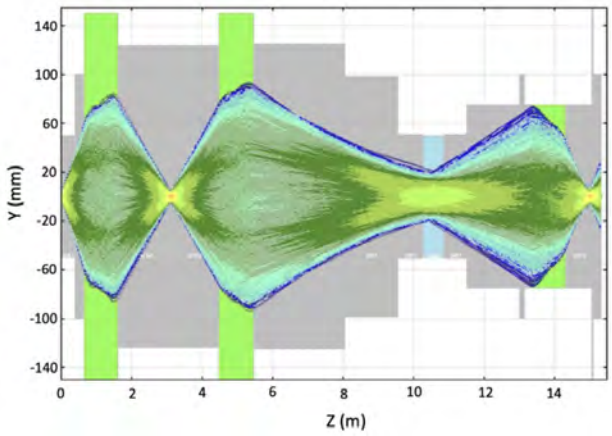

Figure 3: A ray tracing diagram showing the optics of the *TriSol* system. The leftmost green area indicates the first solenoid, the middle green area indicates the second solenoid, the blue area indicates the switching magnet, and the rightmost green area indicates the third solenoid. The y axis shows the height from the center of the beamline in milimeters and the x axis shows the distance downstream of the front of Sol 1 in meters.

Despite the computational confirmation that *TriSol* would work as intended, it was still necessary to provide experimental evidence of *TriSol's* focusing and separation capabilities. A test reaction of ^{3}He(^{6}Li,n)^{8}B was run through *TriSol*, and a position-sensitive detector was placed both before and after the third solenoid in order to determine the change in spot size and beam purity. As shown in Figure 4, the beam spot for the species of interest before the third solenoid was approximately 30 mm in diameter. After the third solenoid, the beam spot for the species of interest was approximately 7 mm, leading to a four-fold spot size reduction. Although everything in the beam line was focused to a similar scale, the contaminants came in off-axis due to the prior focusing of the first two solenoids and the bending magnet. This showed that it was necessary to use vertical and horizontal slits upstream of the third solenoid to block both the scattered beam contaminants and the reaction contaminants.

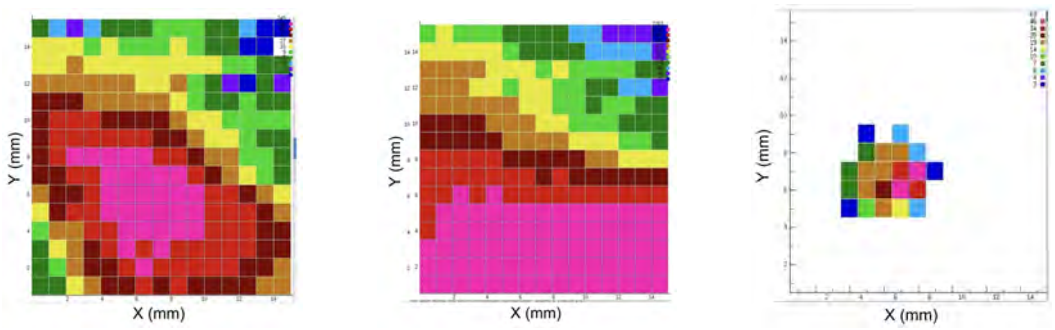

Figure 4: A comparison of the beam spot sizes before and after the third solenoid. The left figure shows the species of interest before the third solenoid, the middle figure shows the scattered beam contaminant before the third solenoid, and the right figure shows the species of interest after the third solenoid. Each square represents approximately 2 mm.

2.2 Detector Array

The detector array used for measuring the ^{17}F(p,p') reaction was a circular array of Micron Semiconductor style YY1 silicon strip detectors. Each segment included a thin detector (approximately 50 microns thick) for measurements of the change in energy of the particle and a thick detector (approximately 1000 microns thick) for total energy measurements. Silicon was used as the material of choice for these detectors because unlike many other semiconductor detectors, silicon does not have to be cryogenically cooled for accurate energy resolution [9]. Furthermore, silicon detectors can be made into very thin detectors relatively cheaply, making it an advantageous material to use. The detectors needed to be tested for thickness via depletion testing. In this method, one places a radioactive source (in this instance, a ^{228}Th sample) in front of the detector. One then increases the bias on the detector until the signal from the alpha particle is no longer increasing in voltage, meaning that the detector is fully depleted.

3 Results

The beam of interest was a ^{17}F beam produced by a ^{16}O(d,n) reaction directly before Sol 1. The ^{17}F beam energy was 53.5 MeV and contained both the +8 and +9 charge states. The primary beam contaminant was unreacted ^{16}O beam in two charge states.

First, the resultant histograms were binned by energy to see if there was a way to distinguish

between the ^{17}F species and the ^{16}O species. An example of these histograms is shown in Figure 5. While the peaks are separated and distinguishable, the ratio between the two peaks is unfavorable and shows that the beam is significantly contaminated with unreacted beam.

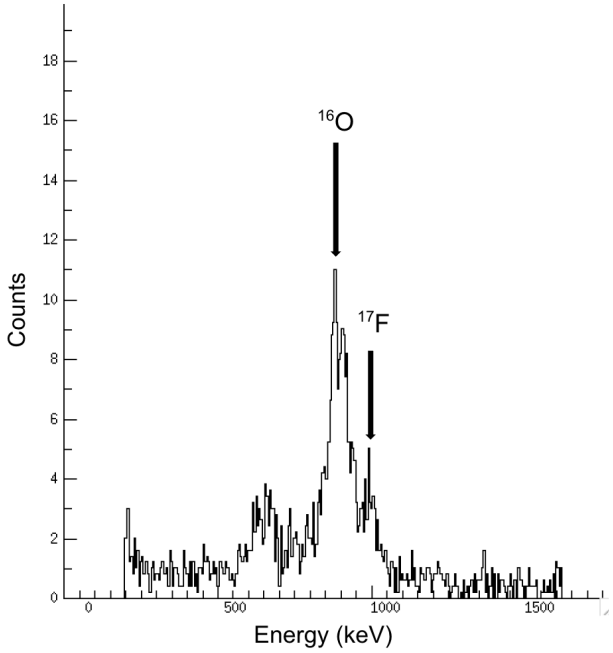

Figure 5: A histogram for the eighth strip on detector 1 on the array in units of 0.1 keV. The ^{16}O peak is located at roughly 800 and the ^{17}F peak is located at roughly 1000.

To distinguish between protons scattered from the 17F beam and the other constituents, a timing technique known as Time-of-flight was employed. This technique records the amount of time it takes for the scattered particles to travel from the target to the detector, making it easier to separate two species of different energies as shown in Figure 6. This figure shows that although the fluorine and oxygen groups are close together, it is possible to gate between the two to reduce the amount of oxygen included in the energy histogram.

After gating the two-dimensional histogram to minimize the amount of ^{16}O included in the one-dimensional energy histogram, the energy histogram changes as seen in Figure 7. The primary oxygen peak, located at ~800, is greatly reduced in the timing-corrected energy histogram. Integrating the ^{16}O and ^{17}F peaks gives a ratio of 1.69 ^{16}O counts for every ^{17}F count. Gating more tightly around the ^{17}F does lower the ratio of ^{16}O to ^{17}F, but at the loss of ^{17}F statistics, and there-

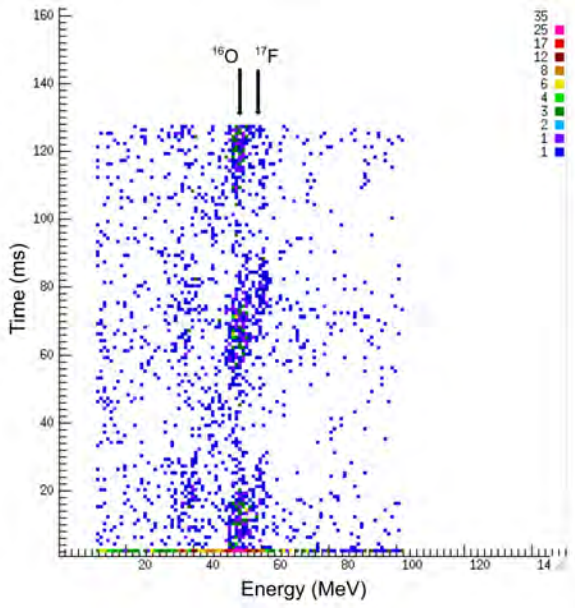

Figure 6: A two-dimensional histogram showing energy on the x axis and timing on the y axis. This plot is taken from the fourth strip on the first detector. The ^{16}O groups are located between 40-50 and the ^{17}F groups are located between 50-60.

fore it was determined that this gating method was the best for ensuring an appropriate ratio while maintaining usable statistics. Figure 7 shows two composite histograms of all events captured over all strips, leading to higher statistics in those histograms as compared to Figure 5.

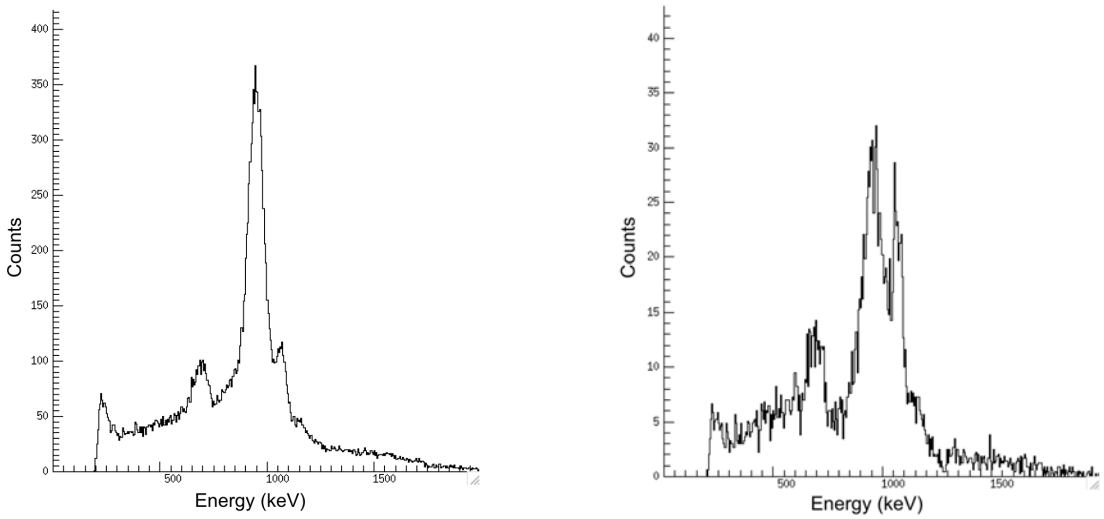

Figure 7: A comparison of the raw energy histogram on the left and the timing-corrected energy histogram on the right.

4 Conclusion

The ^{17}F(p,p') reaction gives important insight into the ^{14}O(α,p)^{17}F reaction, which is among the reactions that contribute the most to observational x-ray light curves. To more completely understand the physics occurring during Type-I x-ray bursts, it is therefore important to study the ^{17}F(p,p') reaction. Despite the previous work on this reaction, there is still a need to investigate further for more precise data.

References

[1] S. Starrfield, J. Truran, W. Sparks, and G. Kutter, The Astrophysical Journal **176** (1972).

[2] R. K. Wallace and S. E. Woosley, Astrophys. J., Suppl. Ser.; (United States) **45:2**, 10.1086/190717 (1981).

[3] R. H. Cyburt, A. M. Amthor, A. Heger, E. Johnson, L. Keek, Z. Meisel, H. Schatz, and K. Smith, The Astrophysical Journal **830**, 55 (2016).

[4] Z. Meisel, G. Merz, and S. Medvid, The Astrophysical Journal **872**, 84 (2019).

[5] J. Blackmon, D. Bardayan, W. Bradfield-Smith, A. Champagne, A. Chen, T. Davinson, K. Hahn, R. Kozub, Z. Ma, P. Parker, G. Rajbaidya, R. Runkle, C. Rowland, A. Shotter, M. Smith, K. Swartz, D. Visser, and P. Woods, Nuclear Physics A **688**, 142 (2001), nuclei in the Cosmos.

[6] B. Harss, J. P. Greene, D. Henderson, R. V. F. Janssens, C. L. Jiang, J. Nolen, R. C. Pardo, K. E. Rehm, J. P. Schiffer, R. H. Siemssen, A. A. Sonzogni, J. Uusitalo, I. Wiedenhöver, M. Paul, T. F. Wang, F. Borasi, R. E. Segel, J. C. Blackmon, M. S. Smith, A. Chen, and P. Parker, Phys. Rev. Lett. **82**, 3964 (1999).

[7] D. W. Bardayan, T. Ahn, J. Allen, F. D. Becchetti, J. C. Blackmon, M. Brodeur, B. Frentz, Y. K. Gupta, M. R. Hall, O. Hall, S. Henderson, J. Hu, J. M. Kelly, J. J. Kolata, A. Long,

J. Long, K. Macon, C. Nicoloff, P. D. O'Malley, K. Ostdiek, S. D. Pain, J. Riggins, B. E. Schultz, M. Smith, S. Strauss, and R. O. Torres-Isea, Journal of Physics: Conference Series **730**, 012004 (2016).

[8] O. Tarasov, Astrophys. J., Suppl. Ser.; (United States) (2023).

[9] W. R. Leo, *Techniques for nuclear and particle physics experiments* (1987).

Synthesis and Characterization of Hexagonal Boron Nitride Nanosheets

JOSIAH J. DEONARINE

2023 NSF/REU Program
Department of Physics and Astronomy
University of Notre Dame

ADVISOR(S): Dr. David Beke, Prof. Laszlo Forro

Abstract

Light emitting defects within hexagonal boron nitride (hBN) are a promising source of qubits to be used in quantum sensing and information technology. However, efficient synthesis of thin layer hBN nanosheets remains a difficulty in investigating hBN defects. We investigate liquid exfoliation and hydrothermal synthesis as possible methods of synthesizing hBN nanosheets through Raman, photoluminescence, and ultraviolet/visible light spectroscopy. Our results show that liquid exfoliation can produce hBN nanosheets between 0.35nm-20 nm. We also show some viable hydrothermal synthesis reactions, between boric acid and various nitrogen sources, that can produce hBN nanosheets.

Introduction

The field of quantum information technology has been exploding in innovation and development in recent times. Quantum information technologies utilize the two state quantum mechanical systems, or qubits, within materials which are incredibly sensitive to weak signals that conventional solutions cannot sense. A variety of materials have been studied for qubits with the most well studied being the visible light emitting defects in diamond and silicon carbide, which have high stability and sensitivity. However, diamond and silicon carbide are three dimensional materials which are not great at interfacing and integrating with other materials. Thus, defects within two dimensional materials have been proposed as more effective sites for housing quantum spin mechanical defects [1].

Hexagonal boron nitride (hBN) is a two dimensional Van der Waals material that has been shown to house several types of defects including visible light emitting defects or color centers [2]. One of the key issues in exploring the color centers within the material is obtaining hBN monolayer and bilayer nanosheets where defects can be created and found. We explore two methods to synthesize hBN nanosheets: top-down or liquid phase exfoliation and bottom-up or hydrothermal synthesis. The top-down exfoliation method takes advantage of the Van der Waals nature of the material by stripping down the top layers of the bulk hBN from the top using a

polar solvent [4]. The bottom up method is a reaction between a nitrogen source and a boron source and due to reactants for hydrothermal synthesis having atoms such as carbon in them, defects are likely to occur. Following synthesis, the product was characterized using Raman, photoluminescence, and UV/Vis light spectroscopy with the size of the nanosheets determined using atomic force microscopy.

Methods

Liquid Phase Exfoliation

250 ml of solution consisting of isopropyl alcohol (IPA) and deionized water (DI water) in a 3:7 ratio was created. Bulk hBN from Sigma-Aldrich was dispersed in a beaker containing the solution. The solution was sonicated by a sonicator for eight hours, with 20 mls of solution being removed for three time intervals, 2, 4, and 8 hours then stored in centrifuge tubes. A separate 250 ml solution of IPA and DI water in a 3:7 ratio was created and 5g of sodium cholate was dissolved in the solution in accordance with. Bulk hBN was dispersed in the solution and DI water was added to each of the centrifuge tubes to obtain a uniform weight, then the solutions were centrifuged at 14,000 rpm for 30 minutes.

Hydrothermal Synthesis

Hydrothermal synthesis uses high pressure and heat to synthesize hBN nanosheets from a boron (boric acid) and nitrogen source. We performed hydrothermal synthesis using six 15 ml and one 150 ml Teflon lined hydrothermal reactors. There were three batches of reactions done which are shown in the reactions column in tables 1-3. The first batch replicated Wang et al's study, where halide salts were used to catalyze the reaction between boron nitride and NH3, and expands on it by testing new halide salts [5]. The second batch replicated and expanded the results from Chen et al, where reactions between melamine and boric acid was done, with our

investigation testing for different concentrations of melamine, boric acid, and ammonia [7]. The third batch replicated the reactions from batch 1 and 2, that showed evidence of hBN from Raman spectroscopy, and varies the amounts of reactants and the time of reaction. Each reaction product was stored in centrifuge tubes and was later centrifuged at 14,000 rpm for 2 hours. The supernatant from each reaction was then removed and stored in a separate centrifuge tube.

Raman Spectroscopy

A confocal microscope Raman spectrophotometer from Witec Solutions was used to characterize the synthesized hBN nanosheets. Laser wavelengths of 532nm (green) with a power ranging from 10 - 300 μW was shone on sample, that was drop casted on a silicon dioxide glass coverslip or on an aluminum foil covered microscope slide. Laser power was increased in order to increase the response of the Raman active modes. The primary substrate was SiO2 glass coverslip, but aluminum foil was used when SiO2 glass influence on the material was too strong. Typical accumulation times were from 5 seconds for 10 accumulations, for lower signal:noise ratio but quicker analysis, and 20 seconds for up to 100 accumulations, for higher signal:noise ratio.

Photoluminescence Spectroscopy

Photoluminescence spectroscopy was performed on the Witec Solutions Raman Spectrophotometer by using the “Spectral Stitching” mode in the software. The typical range of stitching was from 540 nm to 900 nm to isolate the photoluminescence spectrum from the Raman spectrum. Bulk hBN shows that the zero phonon line of hBN is centered at 573 nm and the absorbing phonon side band is centered at around ~600 nm.

Ultraviolet/Visible spectroscopy

Ultraviolet/visible (UV/Vis) spectroscopy was done using the Jasco V-670 spectrometer in pass through mode. 1ml of product was diluted in 10 ml of DI water then around 3 ml of the solution was pipetted into a quartz cuvette.

Atomic force microscopy

Atomic force microscopy (AFM) was performed using the Park XE7 AFM. Product was drop casted onto a square of mica then the mica was secured to a metal disk using a double sided tape. Atomic force microscopy uses a thin needle that runs along the sample to measure the height of the sample.

Results and Discussion

Top-down synthesis

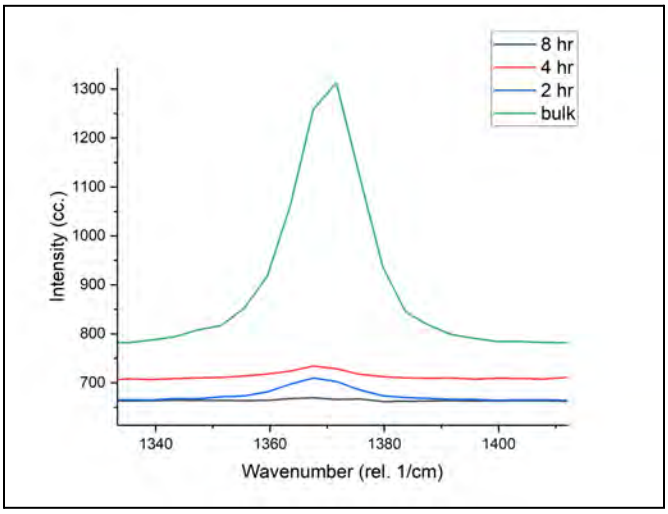

Figure-1. Raman Spectroscopy comparison between bulk hBN and exfoliated hBN sonicated at different times.

Figure-1 shows a comparison of Raman spectroscopy of the bulk hBN and exfoliated hBN samples. Compared to the Raman peak of the bulk hBN, the exfoliated hBN show a significant reduction in the intensity of the peak along with a downshift of the peak from 1372

1/cm to 1368 1/cm. This result was consistent with Gorbachev et al's findings where the intensity of the peak decreased with decreasing number of layers of hBN and that the peak was downshifted for multilayers and upshifted for monolayers [3]. To confirm that our results were accurate, we performed AFM measurements on the product, the results of which are shown in figure-2.

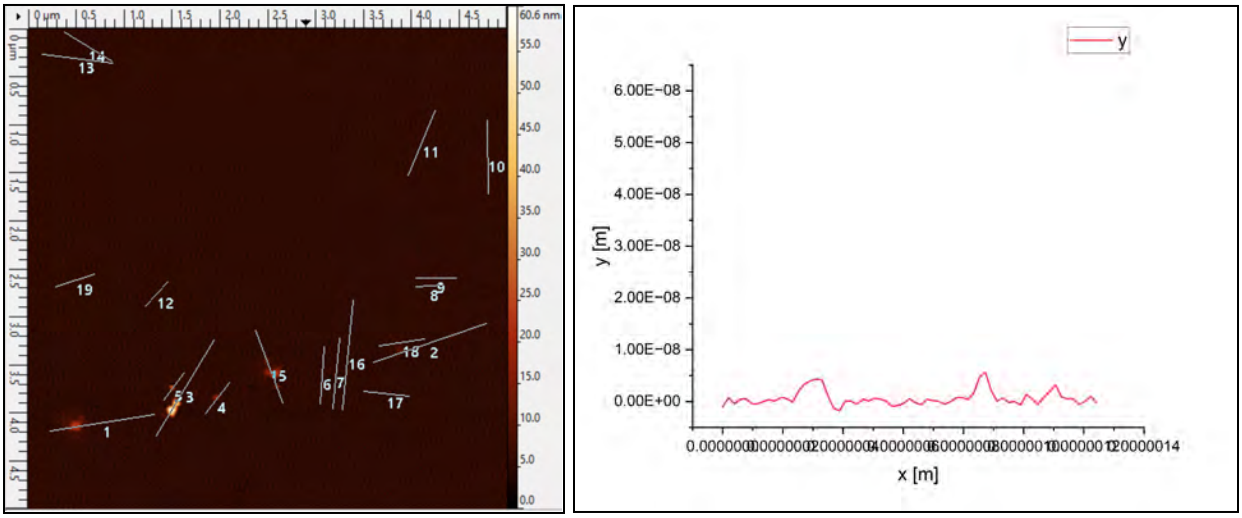

Figure-2. A. AFM image of 2hr exfoliated hBN. b. Graph of the size of hBN nanosheets from analysis of the AFM image.

Figure-2 a shows an AFM image of the 2hr exfoliated hBN product and figure-2 b shows a graph of the size of one of the areas measured in figure-2 a. The brighter areas show increasing size of the particle. Analysis of the AFM image shows that the smaller nanosheets (<20 nm) are clustered around the larger nanosheets (>20 nm). Small nanosheets ranged from 0.35 nm to 20 nm while the theoretical thickness of an hBN nanosheet is 0.0906 nm [6]. Most experimental results measured the thickness to be 0.4 nm with up to 1 nm of uplift due to solvent contamination since hBN interacts strongly with polar solvents [3].

Photoluminesence spectroscopy of the exfoliated samples showed a zero phonon line centered at 573 nm, which was consistent with the bulk hBN, while phonon side band showed

variance from the bulk hBN. UV/vis spectroscopy did not properly characterize the exfoliated species as they show similar uv absorbance at 300nm.

Bottom-up Synthesis

Table-1. Batch 1

Reaction	Reactants, Amount	hBN peak?	Other peaks present
1	Ethanol, 4ml DI Water, 2ml Boric Acid, 0.2g Urea, 0.39g NH3-H2O, 4ml	weak	strong boric acid
2	Boric acid, 0.5 g NH3-H2O, 4ml H2O, 6ml	weak	strong boric acid
3	Boric acid, 0.5 g NH3-H2O, 4ml H2O, 6ml NaCl, 0.06g	no	
4	Boric Acid, 0.5g NH3-H2O, 4ml H2O, 6ml NaCl, 0.06g	no	strong boric acid
5	Boric acid, 0.5 g NH3-H2O, 4ml H2O, 6ml LiF, 0.03g	no	strong boric acid
6	Boric Acid, 0.5g NH3-H2O, 4ml H2O, 6ml NaCl, 0.04g	no	

Table-2. Batch 2

Reaction	Reactants, Amount	hBN peak?	Other peaks present

1	Boric Acid, 100mg Melamine, 24mg DI water, 10ml	no	Strong boric acid Strong melamine
2	Boric acid, 100 mg Melamine, 24 mg NH3-H2O, 4ml H2O, 6ml	no	Strong boric acid
3	Boric acid, 705mg Melamine, 24mg H2O, 10ml	no	Strong boric acid
4	Boric Acid, 500 mg NH3-H2O, 4ml H2O, 6ml	weak	Strong boric acid
5	Boric Acid, 500mg Melamine, 120 mg H2O, 10ml	weak	Strong boric acid Medium melamine
6	Boric acid, 500mg Melamine, 120mg NH3-H2O, 9ml H2O, 6ml	no	Strong boric acid Strong melamine

Table-3. Batch 3

Reaction	Reactants, Amount	Reaction Time	hBN peak?	Other peaks present
1	Boric Acid, 0.1g Melamine, 0.03g H2O, 10ml	24 hrs	weak	medium boric acid
2	Boric Acid, 0.1g Melamine, 0.03g H2O, 10ml	48 hrs	no	medium boric acid
3	Boric Acid, 0.8g Melamine, 0.8g	24 hrs	no	Weak boric acid

	H2O, 10ml Nh3-H2O, 5ml			
4	Boric Acid, 0.8g Melamine, 0.8g H2O, 10ml Nh3-H2O, 5ml	48 hrs	weak	Medium boric acid
5	Boric Acid, 0.8g Melamine, 0.2g H2O, 15ml	24 hrs	no	Weak boric acid
6	Boric Acid, 0.8g Melamine, 0.2g H2O, 15ml	48 hrs	no	Weak boric acid
7	Boric Acid, 80g Melamine, 20g H2O, 150ml	48hrs	weak	Medium boric acid

Hydrothermal synthesis of hBN nanosheets have shown mixed results as summarized in tables 4-6. Most reactions do not show the characteristic ~1372 1/cm Raman peak and the reactions that do show a very weak peak that is indicative of a low concentration of hBN material. Reactions that worked were ones that were with NH3, Urea, and melamine at amounts of 30 mg or more.

The hydrothermal synthesis reactions had photoluminesence spectra that was distinct from the photoluminesence spectrum of the bulk hBN samples. While the bulk hBN had a zero phonon line (ZPL) at 573 nm, most of the spectra ZPL was at around 553nm. Phonon side band activity was extremely varied by sample and by location in the sample. UV/Visible spectroscopy on all samples showed absorption lower than 300nm, however it is not characteristic of any specific reactant or the end product.

Conclusion and Further Work

Color centers within hBN nanosheets are a promising source of quantum information technologies, however, one of the difficulties in studying are the thin hBN nanosheets (<1nm).

We use two methods to obtain hBN nanosheets: liquid exfoliation and hydrothermal synthesis. Liquid exfoliation yielded nanosheets that were less than 1 nm in size as confirmed by Raman spectroscopy and AFM measurements. Hydrothermal synthesis showed that nitrogen sources like NH3-H2O and melamine were capable of producing hBN though at a low yield. Halide assisted synthesis was unsuccessful however, which may be due to the extremely low yield of the technique (<0.2%).

Further work needs to be done on further purification and characterization of the hydrothermal synthesis products to isolate the hBN. hBN is an infrared spectroscopy active species and confirmation of the product as hBN could be done. Due to carbon being present in the nitrogen sources we expect the hBN produced by the hydrothermal synthesis to have defects caused by the carbon, which can be explored by photolumesence spectroscopy and electron spin spectroscopy.

References

1. Vaidya, Sumukh, Xingyu Gao, Saakshi Dikshit, Igor Aharonovich, and Tongcang Li. 2023. arXiv.
2. Abdi, Mehdi, Jyh-Pin Chou, Adam Gali, and Martin B. Plenio. 2018. *ACS Photonics* 5 (5): 1967–76.
3. Gorbachev, Roman V., Ibtsam Riaz, Rahul R. Nair, Rashid Jalil, Liam Britnell, Branson D. Belle, Ernie W. Hill, et al. 2011. *Small* 7 (4): 465–68.
4. Mittal, Neha, Garima Kedawat, Kanika, Sarika Gupta, and Bipin Kumar Gupta. 2020. *ChemistrySelect* 5 (40): 12564–69.
5. Wang, Haixu, Ning Wang, Tianshu Cheng, Xuejuan Wan, Rong Sun, and Ching-Ping Wong. 2019. *Particle & Particle Systems Characterization* 36 (10): 1900278.
6. Yan, J.W., L.H. Tong, R.J. Luo, and D. Gao. 2019. *International Journal of Mechanical Sciences* 164 (December): 105163.
7. Chen, Yongliang, Xiaoxue Xu, Chi Li, Avi Bendavid, Mika T. Westerhausen, Carlo Bradac, Milos Toth, Igor Aharonovich, and Toan Trong Tran. *Small* 17, no. 17 (2021): 2008062. y

Mechanism of flat band formation and heterostructure fabrication for twisted bilayer graphene

ZHENG FANG

2023 NSF/REU Program
Department of Physics and Astronomy
University of Notre Dame

ADVISOR(S): Prof. Stepanov

Abstract

As one of the most promising stackings in the new trending research field of van der Waals heterostructures, the magic-angle twisted bilayer graphene(MATBG) exhibits abundant exotic strong correlated properties like correlated insulators,orbital magnetism and topology. In this paper, concise derivation of Hamiltonian and core thoughts therein are firstly delivered to explain flat energy band formation in MATBG which dominates its characteristics physical natures. The energy band diagram drawn by MATLAB explicitly demonstrates the flat band at magic-angle. Then hands-on fabrication process of hBN-graphene heterostructure is exhaustively reported under thorough supervision with atomic force microscope(AFM) and optical microtechnology, which has indicated great quality of produced samples. Besides, the target heterostructure is successfully made with the modified transfer procedure in the absence of polycarbonate(PPC).

1 Introduction

Many novel states and phase transitions can be induced in twisted Van der Waals heterostructures under the conditions of applied electric and magnetic fields, such as the strong correlation effect [1], unconventional superconductivity [2] etc. which have already been reported. Researchers have discovered that the structure known as magic-angle twisted bilayer graphene (MATBG) has a flat electronic energy band in which electronic interactions are significantly enhanced. MATBG functions as an extraordinary material platform that can switch between insulating and superconducting states through the in situ tuning of their electron density. It is therefore an ideal material for the study of strongly correlated phenomena, unconventional superconductivity and anomalous Hall Effect to answer unsettled questions.

This paper begins with an elaboration on physical structure and fundamental properties of MATBG, then the intrinsic derivation of the reasons for the formation of its flat energy band which is the source of all its unusual characteristics has been reported at the first part. It basicly supplemented Bistritzer and MacDonald's theoretical work [3] with some details, organized the ideas to make the derivation of Hamiltonian quantities explicit. Plus, the application of simulation software(MATLAB and Python) makes the explanation especially vivid and pellucid. Then the author succeed implementing concrete fabrication of hBN/graphene/hBN heterostructure with precise

exfoliation and modified non-solution-based transfer method without polycarbonate(PPC), which showcases the core steps of the preparation process for encapsulated twisted bilayer graphene(tBLG) devices. Optical microtechnology and utilization of atomic force microscope(AFM) enables deeper exploration and examination of samples.

1.1 Van der Waals heterostructures

A van der Waals heterostructure(vdW HSs) consists of vertically stacked two-dimensional(2D) crystal building blocks held together by the van der Waals forces between the layers. 2D crystals are a new family of promising materials, with graphene being just the first and most well known example of this large class. Sharing low dimensionality as a common feature, 2D crystals display a plethora of physical properties, ranging from the insulating to the superconducting, having a high potential for many technological and fundamental applications. The emergence of van der Waals epitaxy, in particular the ability to separate and manipulate two-dimensional materials, opens up greater opportunities for 2D crystals integration in heterostructures. Dissimilar materials can be combined into heterostructures without any of the limitations that apply in epitaxy. Even the orientation can be varied, giving rise to new degrees of freedom such as interlayer twist.

1.2 Magic-angle twisted bilayer graphenes

Adding this novel twist degree of angle freedom to the vdW HS stacked by two sheets of graphene, the result twisted bilayer graphene amazingly enables tuning and control of the strength of electron-electron interactions. Especially when two layers of graphene are twisted by a specific angle of about 1.1°(the first 'magic' angle), its electronic band structure exhibits flat bands near zero Fermi energy, resulting in correlated insulating states at half-filling. Upon electrostatic doping of the material away from these correlated insulating states, tunable zero-resistance states with a critical temperature of up to 1.7 kelvin have been observed. The temperature-carrier-density phase diagram of twisted bilayer graphene is similar to that of a classical unconventional superconductor copper oxides. Moreover, exotic states of matter and phase transitions like quantum anomalous Hall effect

and strong correlation-induced topological phase have also been discovered successively on it.

2 Introduction and theoretical derivation of flat band in MATBG

Superconductivity and the fractional quantum Hall effect are commonly found in condensed matter systems and other systems with high density states. One way to generate dense states is to have a "flat" band, which has a weak dispersion in momentum space. The recent advance as the development of twisted van der Waals heterostructure offer new approaches to the realization of flat bands. In addition to the inherent advantage of basic 2D material, where the chemical potential of the electrons can be continuously tuned by electric field effects without introducing disorder, it also has a moiré pattern regulation mechanism. Moiré pattern is the geometrical design that results when a set of straight or curved lines is superposed onto another set. Over two decades elapsed before scientists observed that moiré patterns can dramatically alter electronic properties beyond aesthetic characteristics. Because of the disparate orientation of the two graphene lattices in TBG, moiré superlattice occurs as shown in Fig. 1(a), which is drew by author with python through building up coordination systems.

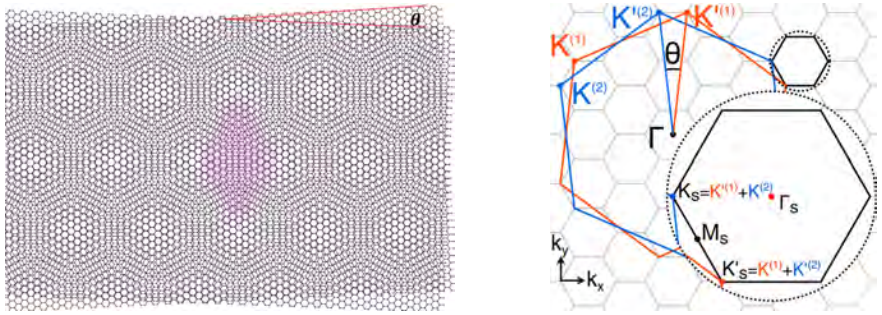

(a) Moiré pattern (b) Moiré Brillouin zone

Figure 1: (a) Schematic of tBLG and its superlattice unit cell.$\lambda_{\mathrm{SL}} = a/\left[2\sin\left(\frac{\theta}{2}\right)\right]$ is the moiré period.(a) is the lattice constant of graphene), the pink diamond shaped area highlighted is the unit cell area. (b) The red and blue hexagons correspondingly indicate the pristine Brillouin zone of graphene layers 1 and 2. As demonstrated in k space, the band structure is folded into the equivalent mini Brillouin zone.

Starting from a single layer, assume an homogeneous nonzero hopping term, $-t$, only between

nearest neighbors(NN), which takes into account the possibility of an electron hopping from an atom to its NN, and a diagonal term ε_{p_Z} reflecting the atomic energy of an electron in the pz orbital(remaining electron delocalized in a pz orbital) in the absence of any other nuclei. Furthermore, to model twisted bilayer system, besides retaining the approximations for each individual layer, we need to consider interlayer hopping, in a transversal tight-binding approximation between NN. First, we split the total hamiltonian in three terms, where H_1 represents the first layer(α), H_2 for the second(β), $H_\perp$ for the hopping.

$$H = H_1(-\frac{\theta}{2}) + H_2(\frac{\theta}{2}) + H_\perp \tag{1}$$

In the tight-binding approximation, the wave functions read as

$$|\psi_{\boldsymbol{k}}\rangle = \sum_{\alpha,i} c_\alpha^{(i)}(\boldsymbol{k})\,|\psi_{\boldsymbol{k},\alpha}^{(i)}\rangle \tag{2}$$

Additionally, within the continuum low-energy model and within a **K** expansion, we can obtain the following non-null matrix elements for the interlayer hopping(detailed simplification process reference to Bistritzer and MacDonald's work [3]):

$$\langle\psi^{(1)}_{K+\boldsymbol{q}_1,\alpha}|H_\perp|\psi^{(2)}_{K^\theta+\boldsymbol{q}_2^\theta,\beta}\rangle = T^{\alpha,\beta}_{K+\boldsymbol{q}_1,K^\theta+\boldsymbol{q}_2^\theta} = T^{\alpha,\beta}_{\boldsymbol{q}_b}\delta_{\boldsymbol{q}_2^\theta-\boldsymbol{q}_1,\boldsymbol{q}_b} + T^{\alpha,\beta}_{\boldsymbol{q}_{tr}}\delta_{\boldsymbol{q}_2^\theta-\boldsymbol{q}_1,\boldsymbol{q}_{tr}} + T^{\alpha,\beta}_{\boldsymbol{q}_{tl}}\delta_{\boldsymbol{q}_2^\theta-\boldsymbol{q}_1,\boldsymbol{q}_{tl}} \tag{3}$$

Figure 2: Momentum-space geometrical picture

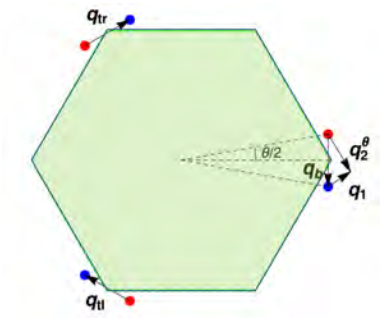

Fig. 2 provides clear momentum-space geometrical picture for the interlayer hopping on a tBLG. layer 1 is rotated by $-\frac{\theta}{2}$ and layer 2 by $\frac{\theta}{2}$. By means of geometric relations, we can easily obtain: $\boldsymbol{q}_b = \frac{8\pi\sin(\theta/2)}{3\sqrt{3}d}(0,-1)$, $\boldsymbol{q}_{tr} = \frac{8\pi\sin(\theta/2)}{3\sqrt{3}d}\left(\sqrt{3}/2, 1/2\right)$, $\boldsymbol{q}_{tl} = \frac{8\pi\sin(\theta/2)}{3\sqrt{3}d}\left(-\sqrt{3}/2, 1/2\right)$. Small deviations near the K-point are considered($\left|q_1\right|, \left|q_2^\theta\right| \ll |K|$). To satisfy the Kronecker condition for fomula(5) in MacDonald's paper;$G^\theta_{m,n} = G_{k,l} = 0, b_2^\theta, -b_1^\theta$, that is, the "conservation of momentum process" shown in the in-

set. By substituting the values of $G^{\theta}_{m,n}$ in (5) by MacDonald, then you can get the values of the three 2×2 matrices for the right side of equation (3) above.

$\|\mathrm{K}+\boldsymbol{q},1\rangle$	$\|\mathrm{K}^{\theta}+\boldsymbol{q}+\boldsymbol{q}_b,2\rangle$	$\|\mathrm{K}^{\theta}+\boldsymbol{q}+\boldsymbol{q}_{tr},2\rangle$	$\|\mathrm{K}^{\theta}+\boldsymbol{q}+\boldsymbol{q}_{tl},2\rangle$	
$H^{K}_{SLG}(\boldsymbol{q},-\theta/2)$	$T^{\dagger}_{qb}$	$T^{\dagger}_{qtr}$	$T^{\dagger}_{tl}$	$\|\mathrm{K}+\boldsymbol{q},1\rangle$
$T^{\dagger}_{qb}$	$H^{K}_{SLG}(\boldsymbol{q}+\boldsymbol{q}_b,\theta/2)$			$\|\mathrm{K}^{\theta}+\boldsymbol{q}+\boldsymbol{q}_b,2\rangle$
$T^{\dagger}_{qtr}$		$H^{K}_{SLG}(\boldsymbol{q}+\boldsymbol{q}_{tl},\theta/2)$		$\|\mathrm{K}^{\theta}+\boldsymbol{q}+\boldsymbol{q}_{tr},2\rangle$
$T^{\dagger}_{tl}$			$H^{K}_{SLG}(\boldsymbol{q}+\boldsymbol{q}_{tl},\theta/2)$	$\|\mathrm{K}^{\theta}+\boldsymbol{q}+\boldsymbol{q}_{tl},2\rangle$

Table 1: tBLG Hamiltonian matrix elements for NN with subscripts shown. Because each substrate omits the sublattice indicator, the above Hamiltonian is actually an 8×8 matrix.

This is obviously the case where only the nearest neighbors are considered, and we have to count other K points thus leading to an expansion of our base. Therefore, it can be concluded with $|K+\boldsymbol{q}+m_1\boldsymbol{b}^m_1+m_2\boldsymbol{b}^m_2,2\rangle$ and $|K^{\theta}+\boldsymbol{q}+\boldsymbol{q}_b+m_1\boldsymbol{b}^m_1+m_2\boldsymbol{b}^m_2,1\rangle$. When the base expands, the Hamiltonian matrix add diagonal elements besides their non-diagonal leapfrog terms with respect to the nearest neighbors. For calculability, we set value '3' for truncation term that means $-tr < m_1, m_2 < tr$, since m can take 7 values from -3 to 3. Hence there are 2×49 basis vectors with 2 on behalf of two layers, and finally we should multiply by 2 because each matrix is 2×2, which form a 196×196 ultimate hamiltonian used for energy band simulation. In MATLAB code, I input 5.944 eV·Å as Fermi velocity of graphene; $\sqrt{3} \cdot 1.42$Å for lattice constant; 110 meV for interlayer jump energy. Then, the program obtained eigenvalues of Hamiltonian and drew the electronic spectrum diagram as Fig. 3, which unambiguously verified the flat band at the first magic-angle.

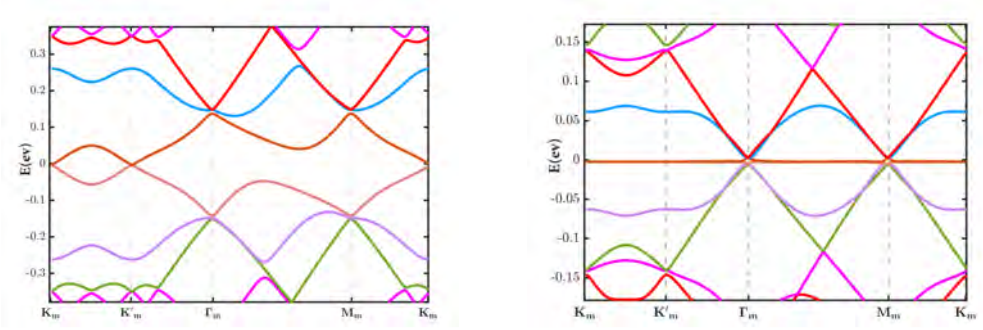

Figure 3: Left happens at $\theta = 2$; By contrast, the right-hand side proves that when θ is equal to the first magic-angle 1.1°, flat bands of size less than 15meV do occur.

3 hBN-graphene heterostructure fabrication and results

Among all the fabrication methods for MATBG, the tear-and-stack technique is the most commonly used one to achieve twisted homobilayers as TBG, which selectively pick up(tear) one part of a 2D flake, and next, stack it onto the other part of the same flake, which should also be rotated for a magic-angle in this case. During the summer program, I was committed to carry out fabrication of 2D vdW HSs, in particular the hBN/graphene/hBN located on the SiO_2/Si substrate, which substantially a process akin to the preparation of tBLGs. It takes two stages to accomplish it. The first step is to exfoliate plenty of decent monolayer graphene flakes on SiO_2/Si that are usually free standing without other impurities around it and manage to insure them relatively regular shape and flat undulating surfaces with no rolls or folds. The further step is a typical non-solution-based transfer process which stack the layers we have already produced together to construct objective heterostructure.

The mechanical exfoliation technique we used is basically the process where monolayers of carbon are peeled from graphite crystals using a primitive "Scotch" tape. We repeatedly peeled the tape against itself numerous times, the graphitic layer becomes thinner and thinner and consequently single-layer graphene crystal suitable for laboratory research with small-scale but high-precision needs. Some obtained exfoliated samples are shown here in Fig. 4.

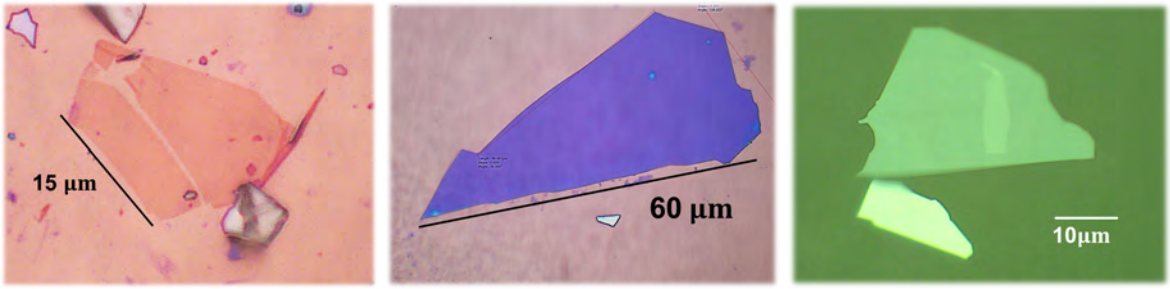

(a) Monolayer graphene (b) hBN (c) graphene/hBN/PDMS

Figure 4: Flakes (a) and (b) were observed under optical microscope. Stack in (c) is exactly the product of the second procedure demonstrated in Fig. 6. The lightest-colored area in the center is the graphene at the top. The slightly darker green area around it is another hBN.

Moreover, AFM was used to carry out further checks by scan, mainly to verify the sample

flakes shows smooth and flat surfaces and are of satisfactory thickness(about 0.8 for monolayer graphene on SiO_2, dozens of nanometers for hBN). Its parameter values for set point, drive, gain etc. were continuously adjusted to achieve optimal performance under the non-contact mode. The following Fig. 5 shows altitude variations of some sample cross-sections along a certain line and offers supplementary demonstration in 3D image.

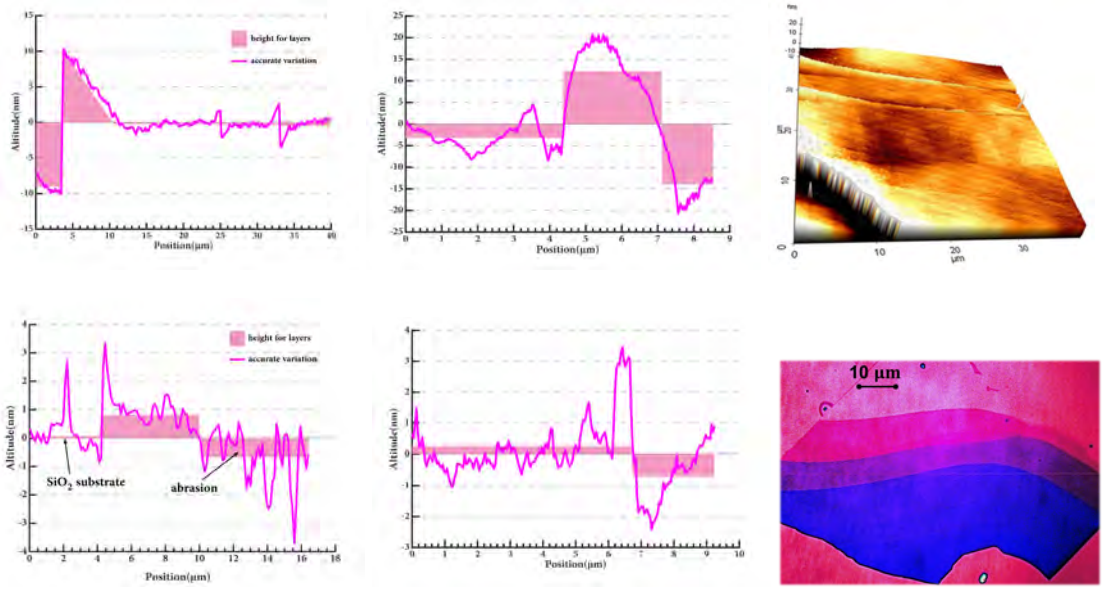

Figure 5: The upper left two figures indicate profiles of two hBN flakes and the two below are for monolayer graphene flakes. In order to exclude the influence of noise fluctuations in the instrument and the abnormal protrusion of impurities, further algorithmic processing was undertook to roughly determine stratification of flakes shown with light-pink areas. (Note that the lowest surfaces are the substrates, not of flakes, except for the case marked above) The two scan images on the right side presents a sample of hBN with a stepped architecture respectively under optical microscope and AFM so as to test AFM accuracy and give readers a better view of relationship between optical color and thickness of hBN.

The thicknesses of two graphenes turned out to be 0.970 and 0.764μm. Examined with $N = \frac{(thickness_{measured} - 0.4)}{0.335}$ [4], they are proved to be monolayer. Plus for hBN, it shows suitable layers of proper thickness.

Then we adopted a non-solution-based transfer method to avoid solution contamination during the construction of 2D vdW HSs. In principle, both of these two polymers, polycarbonate(PPC) and polydimethylsiloxane(PDMS) ought to be simultaneously applied to build complicated vdW

HSs. The elaborate h-BN/graphene/hBN heterostructure fabrication process we generally followed is illustrated in Fig. 6.

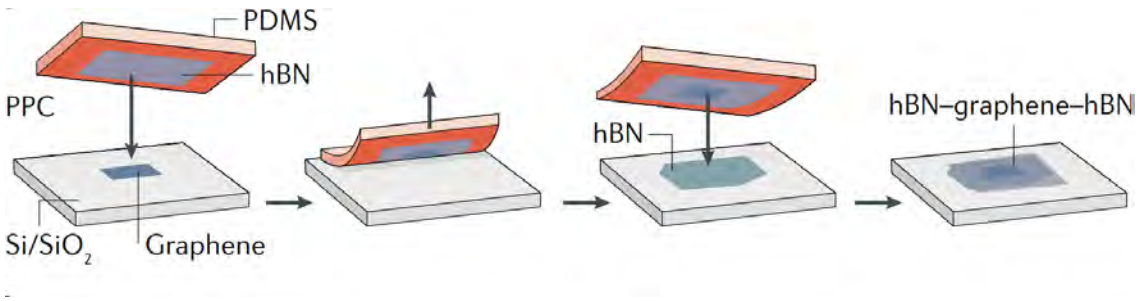

Figure 6: Graphite and hBN flakes are separately exfoliated on SiO_2 substrates A PPC polymer on a PDMS elastomer stamp are then used to peel an hBN flake directly off the substrate under an optical microscope. Next, the hBN is positioned over a graphene flake and brought into contact with it while the whole system is heated to promote adhesion between the flakes. The two flakes develop a strong vdW adhesion so the graphene is peeled off its substrate as PDMS is removed. Encapsulating hBN layer can then be added onto the stack following the same procedure. Finally the complete stack of flakes is deposited on SiO_2.

The only change from the practice stated in the above procedures is that we utilized only PDMS in the first step, due to the lack of PPC availability. Since PC is more capable of picking up target 2D flakes while PDMS better serves as a temporary substrate holding 2D flakes, our experiments were much more challenging and several attempts ended in failure where the hBN entirely fell down from PDMS to SiO_2. As a result of our experience, we have found that appropriate heat(around 50°C) to SiO_2 sample, larger hBN size and smaller graphene size can enormously increase success rate. Ultimately, we accomplished the transfer without PPC and attained acceptable results as Fig. 7. Both the optical microscope and AFM scan reflect the relatively high quality of the manufactured hBN-graphene heterostructure on SiO_2 and declare a satisfactory completion of the whole process.

4 Conclusion

This paper initially starts with a pithy overview of magic-angle twisted bilayer graphenes and delivered a skeletal outline for math derivation of its Hamiltonian based on the modal in Bistritzer and MacDonald's work. The energy band diagrams with truncation of 3 in approximation have been perfectly plotted with MATLAB, verfying the flat band at the magic-angle. Besides the theoretical

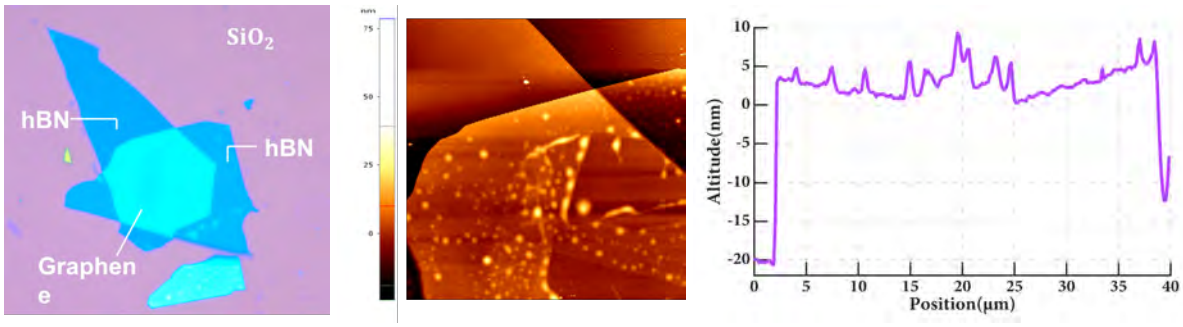

Figure 7: Left two images of hBN/graphene/hBN located on SiO_2 are respectively taken with optical microscope and AFM which indicates small amount of curling on the surface and bubbles beneath. The right displays the profile along the SiO_2/hBN/graphene/hBN/SiO_2 as proof of its structure.

work, the author also dedicated to practical manufacturing. Considering that construction of 2D twisted homobilayer systems like tBLGs makes the fabrication of Van der Waals heterostructures an important subject, the author implemented the preparation of hBN/graphene/hBN vdW HS and successfully obtained decent hBN/graphene/hBN stack in the absence of robust assist from the PC during transfer process. Additionally, with applying atomic force microscope, the configuration of flakes made in each stage were detected and fineness of the product were reliably verified, which allows fully encapsulated tBLG devices processing for further research to seek more facts about MATBGs.

References

[1] Y. Cao, V. Fatemi, and e. a. Demir, Nature **556**, 80 (2018).

[2] Y. Cao and e. a. Fatemi, Nature **556**, 43 (2018).

[3] R. Bistritzer and A. H. MacDonald, Proceedings of the National Academy of Sciences **108**, 12233 (2011).

[4] C. J. Shearer and S. et al., Nanotechnology **27**, 125704 (2016).

Spurious isospin symmetry breaking in the IMSRG

ALEXANDER FARREN

2023 NSF/REU Program
Department of Physics and Astronomy
University of Notre Dame

ADVISOR(S): Prof. Ragnar S. Stroberg

Abstract

Sources of spurious isospin symmetry breaking (ISB) in both post-Hartree-Fock IMSRG (2) and (3) truncations for a ^{14}O Minnesota reference were traced back to a problematic nested commutator $\left[\eta(s), \left[\eta(s), \hat{T}^2(0)\right]\right]$. The latter was reduced to an analytic sum which agreed with computational results. Asymmetric definitions of the reference state, $\hat{H}^{\mathrm{od}}(s)$ and $\eta(s)$ were found to spoil the isospin symmetry of the problematic term. Replacing an energy denominator generator $\eta(s) \sim 1/\Delta$ with the imaginary time generator remedied the latter source of ISB.

1 Introduction

1.1 Mise-en-scène

Since the 1950's, we have been developing and refining the Standard Model of particle physics by challenging theoretical predictions with increasingly precise experimental data. One such prediction is the unitarity of the Cabibbo-Kobayashi-Maskawa (CKM) matrix. The CKM matrix details the discrepancy between the weak and mass eigenstate representations of quark flavour change. In particular, the matrix element V_{ud} is of interest due to its major role in the unitarity condition

$$|V_{\mathrm{ud}}|^2 + |V_{\mathrm{us}}|^2 + |V_{\mathrm{ub}}|^2 = 0.9985(05) \overset{!}{=} 1$$

where $|V_{\mathrm{ud}}|^2 \approx 0.97373(31)$ [1; 2]. If we consider $0^+ \to 0^+$ superallowed β Fermi decays, we can relate V_{ud} to precisely measurable coupling constants G_F and G_V as $V_{\mathrm{ud}} = G_V/G_F$. We want to compare prediction to experiment while minimizing both sides' uncertainty.

There is a theoretical correction δ_C, to what was originally thought to be G_V, related to *isospin symmetry breaking* (ISB). Protons and neutrons are different with respect to the Coulomb interaction and pion exchange. This means the symmetry under isospin rotation (going from a proton to a neutron or vice versa) is broken. The probability for an initial nuclear state $|\psi_{\mathrm{i}}\rangle$ to transition to a final state with raised or lowered isospin $|\psi_{\mathrm{f}}\rangle$, e.g. via β decay, is

$$|M_{\mathrm{fi}}|^2 = \left| \langle \psi_{\mathrm{f}}| \hat{T}_{\pm} |\psi_{\mathrm{i}}\rangle \right|^2 = 2(1 - \delta_{\mathrm{C}})$$

Improving the reliability of IMSRG computational methods in quantifying this δ_C correction was the motivation for this research.

1.2 What was the issue?

Current computational methods for finding δ_C are limited by the very nature of *ab initio* many-body nuclear physics, which deals with nuclei from first principles, i.e. quantum mechanically. Both analytical and numerical approximations must be made to treat the many-body problem with computers. One approach to solving such systems is the similarity renormalisation group (SRG) formalism. A variant of the SRG is the in-medium SRG (IMSRG), the focus of this paper, with which we hope to create a robust computational treatment of various nuclei in order to calculate δ_C.

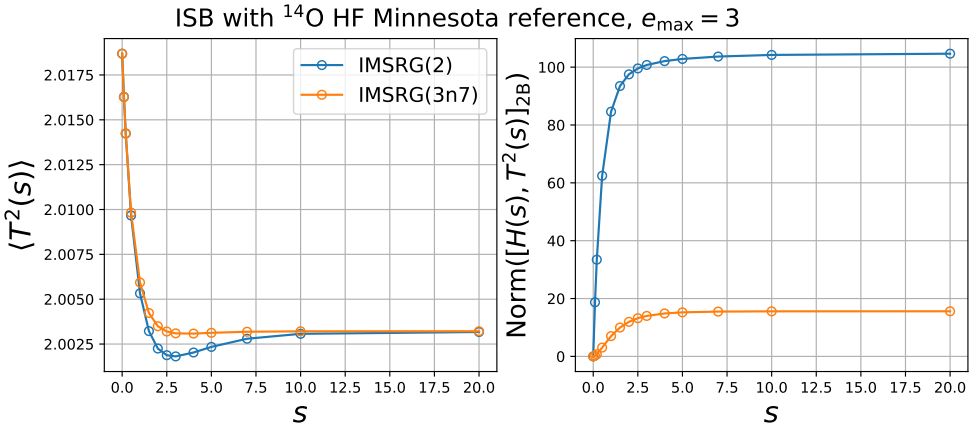

Figure 1: Isospin symmetry is broken under S. Stroberg's IMSRG flow of ^{14}O HF Minnesota potential reference state. (Left) The isospin $\langle \hat{T}^2(s) \rangle$ should trend to 2 as $s \to \infty$ and (Right) the two-body part of the commutator $\left[\hat{H}(s), \hat{T}^2(s)\right]$ should be identically 0. Presented at [3], reproduced here.

Since $\langle \hat{T}^2 \rangle$ is misbehaved, by looking at Figure 1, and $\hat{T}^2 \sim (\hat{T}_+\hat{T}_- + \hat{T}_-\hat{T}_+)$ it was evident that the code at the start of the project could not accurately handle calculations regarding $\langle \hat{T}_\pm \rangle$ and thus δ_C. Since δ_C is of the order 1%[1], we should try to have a firm understanding of all sources of isospin symmetry breaking in the IMSRG, and try to control them. Throughout this paper, we will seek to understand specifically sources of *spurious* ISB, which is just ISB arising even though it is not predicted (due to approximation errors in the Hamiltonian, for example).

2 Background

2.1 Quantum many body theory

We will work in the particle-hole formulation of second-quantised operators and Slater wavefunctions [4, Ch.3]. First we define the *vacuum state* $|0\rangle$ and field operators $a_\lambda,\ a_\lambda^\dagger$ such that

$$a_\lambda|0\rangle = 0 \qquad \frac{1}{\sqrt{\Pi_\lambda n_\lambda!}} a_{\lambda_N}^\dagger \cdots a_{\lambda_1}^\dagger |0\rangle = |\lambda_1 ... \lambda_N\rangle \tag{1}$$

where $|\lambda_1 ... \lambda_N\rangle$ are N-fermion Slater determinants. We say that the *creation operator* $a_\lambda^\dagger$ creates a particle in the single-particle state λ while the *annihilation operator* a_λ destroys it.

Consider a symmetric one-body operator $\hat{\mathcal{O}}_1$ with 1-B equivalent $\hat{o}$. We can write the *second quantisation representation* of $\hat{\mathcal{O}}_1$, expanded in an arbitrary basis,

$$\hat{\mathcal{O}}_1 = \sum_{\mu\nu} \langle\mu|\,\hat{o}|\nu\rangle a_\mu^\dagger a_\nu \ \text{, and similarly} \quad \hat{\mathcal{O}}_2 = \frac{1}{2}\sum_{\alpha\beta\gamma\delta} \langle\alpha\beta|\,\hat{o}|\gamma\delta\rangle a_\alpha^\dagger a_\beta^\dagger a_\gamma a_\delta \tag{2}$$

We can *normal-order* the field operators with respect to a *reference state* $|\Phi_0\rangle$

$$\{a_\mu^\dagger a_\lambda\} \equiv a_\mu^\dagger a_\lambda - \langle\Phi_0|\, a_\mu^\dagger a_\lambda |\Phi_0\rangle \implies \langle\Phi_0|\,\{a_\mu^\dagger a_\lambda\}|\Phi_0\rangle = 0 \tag{3}$$

We can rewrite a Hamiltonian with 1- and 2-body interactions as

$$\hat{H} = \sum_i \hat{h}_i + \sum_{ij} \hat{v}_{ij} = E_0 + \sum_{pq} f_{ab}\{a_p^\dagger a_q\} + \frac{1}{4}\sum_{pqrs} \Gamma_{pqrs}\{a_p^\dagger a_q^\dagger a_r a_s\} + ...$$

where $E_0 = \langle\Phi_0|\,\hat{H}\,|\Phi_0\rangle$ is the reference state energy and $f_{ab} \equiv \langle a|\,\hat{f}\,|b\rangle - \langle b|\,\hat{f}\,|a\rangle$ are anti-symmetrised matrix elements which can be found using (2) & (3) .

2.2 Isospin

Heisenberg introduced isospin t in 1932 because the proton and neutron are interchangeable with respect to mass and interaction with the nuclear force. Both nucleons have isospin $t = 1/2$ [5].

$$\mathrm{n}^0 \uparrow (t_z = +\tfrac{1}{2}) \text{ isospin up} \qquad \mathrm{p}^+ \downarrow (t_z = -\tfrac{1}{2}) \text{ isospin down}$$

Isospin has familiar angular momentum properties; $\hat{T}^2|t\rangle = t(t+1)|t\rangle, \hat{T}_\pm|t,\ t_z\rangle \sim |t,\ t_z \pm 1\rangle$...

2.3 IMSRG formalism

We want to use a unitary similarity transformation (hence the name *similarity* renormalisation group) so that

$$\hat{H}(s) \equiv \hat{U}(s) H(s=0) \hat{U}^{\dagger}(s) \tag{4}$$

which is parametrised by the *flow parameter* s. We choose a reference state $|\Phi_0\rangle$ which is our initial guess of the exact ground state energy eigenket $|\psi\rangle$. Alternatively, we could think of the exact states transforming as

$$|\psi(s)\rangle \equiv \hat{U}^{\dagger}(s)|\Phi_0\rangle$$

We are transforming a non-vacuum, so a medium reference state (hence the name *in-medium* as opposed to in-vacuo). Consistency requires

$$\langle\Phi_0|\, \hat{H}(s)|\Phi_0\rangle = \langle\Phi_0|\, \hat{U}(s)\hat{H}(0)\hat{U}^{\dagger}(s)|\Phi_0\rangle = \langle\psi|\, \hat{H}(0)|\psi\rangle = E$$

We can freely impose the following condition on the unitary operator $\hat{U}(s)$

$$\frac{d}{ds}\hat{U}(s) \equiv \eta(s)\hat{U}(s) \overset{\text{unitarity}}{\Rightarrow} \frac{d}{ds}\hat{U}^{\dagger}(s) = -\hat{U}^{\dagger}(s)\eta(s) \tag{5}$$

such that we obtain the *flow equation* for the transformed Hamiltonian

$$\frac{d}{ds}\hat{H}(s) = \left[\eta(s), \hat{H}(s)\right] \tag{6}$$

One choice of transformation is the *Magnus formulation* $\hat{U}(s) \equiv e^{\Omega(s)}$ [6]. Unitarity of $\hat{U}(s)$ implies that the *Magnus operator* $\Omega(s)$ is anti-hermitian. We choose $\eta(s)$ so that $\hat{H}(s) \equiv \hat{H}^{\mathrm{d}} + \hat{H}^{\mathrm{od}} \overset{s\to\infty}{\to} \hat{H}^{\mathrm{d}}$ where $\hat{H}^{\mathrm{d}}(s\to\infty)$ is 'diagonal' in the reference state $|\Phi_0\rangle$. This is convenient, because it becomes easy to read off E via $\lim_{s\to\infty}\langle\Phi_0|\, \hat{H}(s)|\Phi_0\rangle = \langle\Phi_0|\, \hat{H}^{\mathrm{d}}(s\to\infty)|\Phi_0\rangle = E$. For all non-trivial particle hole pairs, $\hat{H}^{\mathrm{d}}$ satisfies $\langle\Phi_0|\, \hat{H}^{\mathrm{d}}(s\to\infty)|\Phi^{ab\ldots}_{ij\ldots}\rangle = 0$. Operators $\hat{\mathcal{O}}(0)$ evolve as $\hat{\mathcal{O}}(s) \equiv \hat{U}(s)\hat{\mathcal{O}}(0)\hat{U}^{\dagger}(s)$ and so

$$\hat{\mathcal{O}}(s) = e^{\Omega(s)}\hat{\mathcal{O}}(0)e^{-\Omega(s)} = \hat{\mathcal{O}}(s) = \hat{\mathcal{O}}(0) + \frac{1}{1!}\left[\Omega(s), \hat{\mathcal{O}}(0)\right] + \frac{1}{2!}\left[\Omega(s), \left[\Omega(s), \hat{\mathcal{O}}(0)\right]\right] + \ldots \tag{7}$$

The number after IMSRG indicates after which term we truncate the normal-ordered operators

$$\hat{H} = \overbrace{E_0 + \sum_{pq} f_{ab}\{a_p^{\dagger}a_q\} + \frac{1}{4}\sum_{pqrs}\Gamma_{pqrs}\{a_p^{\dagger}a_q^{\dagger}a_r a_s\}}^{\text{IMSRG (2)}} + \underbrace{\ldots}_{\text{IMSRG (3)+}}$$

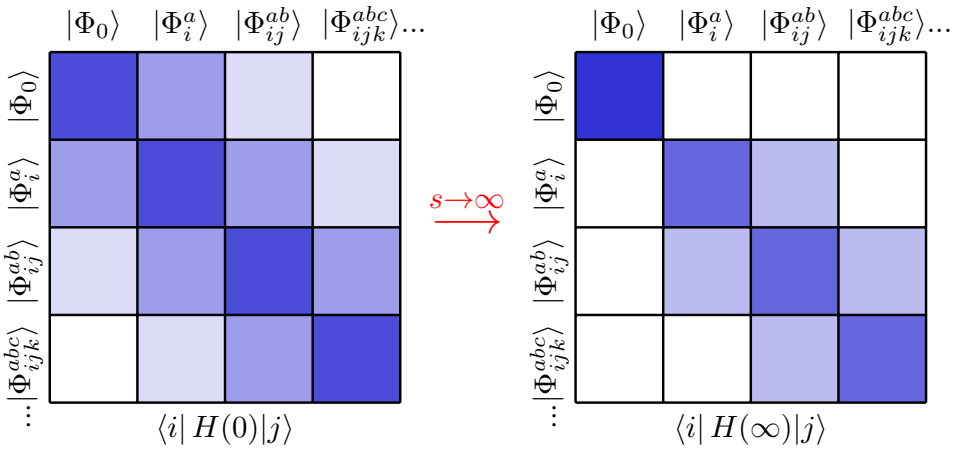

Figure 2: As $s \to \infty$, the Hamiltonian becomes block-diagonal, i.e. the reference state decouples from any particle-hole excitation. There are no restrictions on the block connecting excitations.

3 Hunting for spurious ISB

As mentioned in the introduction, we seek a framework with which to compute δ_C. In particular, it should reliably handle calculations involving $\langle \hat{T}^2 \rangle$ and thus $\langle \hat{T}_\pm \rangle$. This means that if there were no *a priori* sources of ISB, i.e. we introduce a nuclear potential faithful to the description of the shell model while including *no* Coulombic interaction and *no* pion-exchange physics, isospin symmetry should be observed.

A candidate for such a nuclear potential is the Minnesota potential, which is the sum of two Gaussians. However, as detailed in Figure 1, even with the improved approximation scheme going from IMSRG(2) to IMSRG(3n7), there was still ISB for a ^{14}O HF reference state. After extending the IMSRG truncation to IMSRG(3), the error ($\lim_{s\to\infty}\langle \hat{T}^2(s)\rangle - 2$) actually grew instead of being reduced (Figure 3). In parallel, Jonathan Riess was working on whether the $e_{\max}$ truncation was responsible for this error. He found that it did not account for most of the error.

Continuing with the same ^{14}O reference, after finding that the error did not significantly depend on the energy level spacing $\hbar\omega$ either, the importance of orbital population was investigated. It was found that for certain orbital spaces, i.e. depending on which shells are included in the model space of the nucleus, there was a much greater lack of convergence to 2 (Figure 3). At the IMSRG(2) approximation, when the model space was reduced to the $0p_{3/2}$, $0p_{1/2}$ and $0d_{5/2}$ energy shells, the error was acute relative to the full $e_{\max} = 3$ model space for ^{14}O.

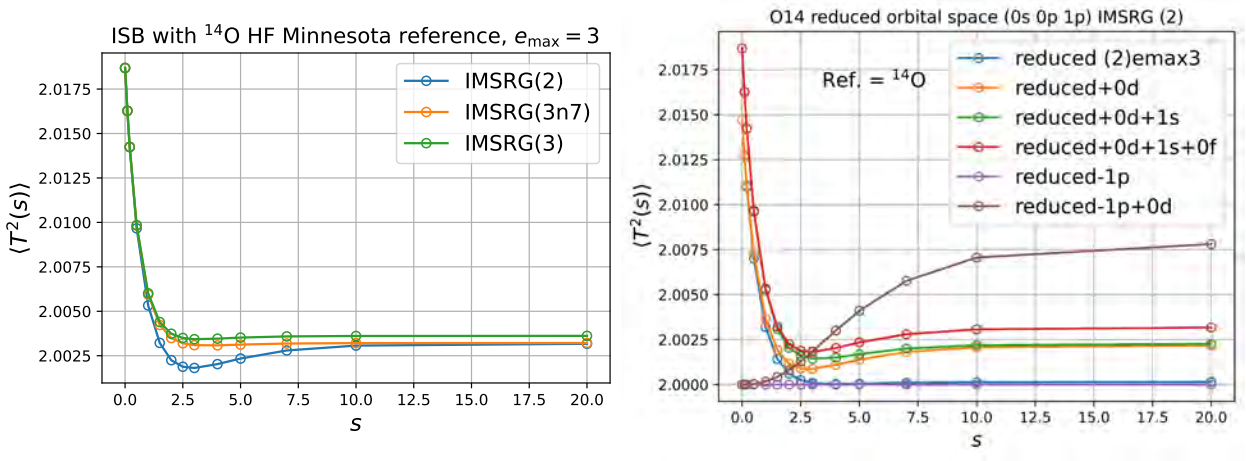

Figure 3: (Left) IMSRG truncation is relaxed yet the error does not decrease (Right) Different orbital spaces display different convergence behaviours.

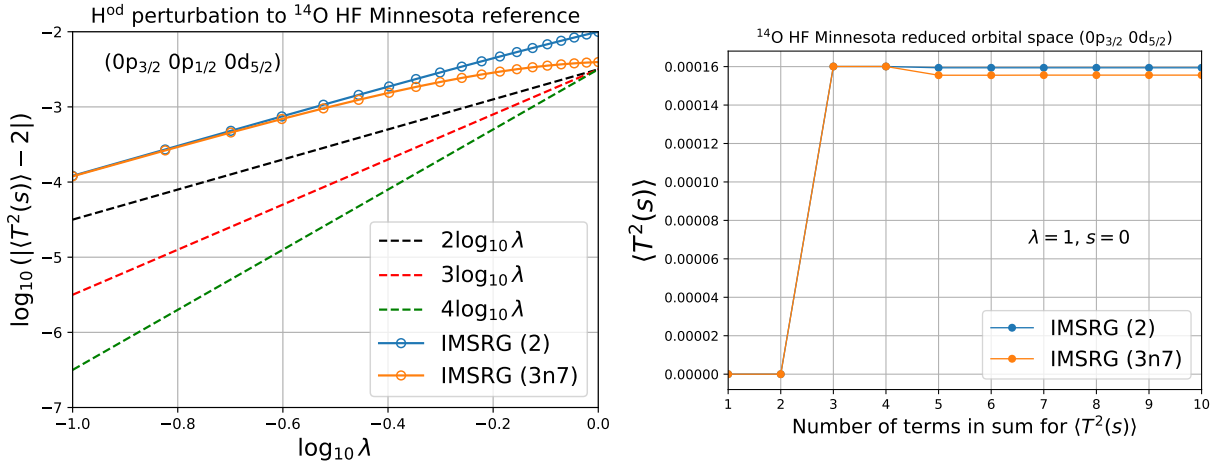

Figure 4: (Left) Log-log plot indicating that error source scales as λ^2, so with two factors of $\hat{H}^{\text{od}}$. (Right) Cumulative sum shows that problematic term indeed has two factors of $\hat{H}^{\text{od}}$.

Hoping to track what caused the error in the unrestricted case, an investigation into the source of error in the $0p_{3/2}$, $0p_{1/2}$, $0d_{5/2}$ (0p0d5) model space was warranted. To pinpoint the source of error even further, a perturbative scheme was employed by redefining $\hat{H}(s) \equiv \hat{H}^{\text{d}} + \lambda \hat{H}^{\text{od}}$ and then tracking the error as a function of λ. Figure 4 tells us that the error is proportional to λ^2, even as the IMSRG truncation is relaxed, and the cumulative sum (7) in the Magnus evolution of $\langle \hat{T}^2 \rangle$ indicated that the source of isospin symmetry breaking was the third term in the sum; the nested commutator

$$\langle [\Omega(s), [\Omega(s), \hat{T}^2(0)]] \rangle \tag{8}$$

The two plots in Figure 4 both point to the zero-body part of this commutator because we were using the White generator $\eta(s) \equiv \hat{H}^{\text{od}}/\Delta$, for some suitable energy denominator Δ. This is because the nested commutator (8) behaves like λ^2, since $\Omega(s \to \infty) \sim \eta$ to leading order in η and we treat $\lambda \hat{H}^{\text{od}} \sim \eta$ as a (small) perturbation. *The hunt is over.*

We will now evaluate this commutator analytically using Hugenholtz and ASG diagrams [4] in order to further understand why this commutator was problematic. We make the approximation $\Omega(s \to \infty) \approx \eta$ and expand (8) explicitly

$$\langle \left[\eta(s), \left[\eta(s), \hat{T}^2(0)\right]\right] \rangle = \langle \Phi_0 | \left(\eta^2(s)\hat{T}^2(0) - 2\eta(s)\hat{T}^2(0)\eta(s) + \hat{T}^2(0)\eta^2(s)\right) | \Phi_0 \rangle$$

where $|\Phi_0\rangle$ is the ^{14}O HF Minnesota reference state. When the 1B and 3B parts of $\Omega \approx \eta$ were set to zero, the error vanished. This meant we should only consider topologies which yield a non-zero 0B and involve the 2B part of η, which we call $\eta_{2\text{B}}$. According to the normal-ordered commutator rules for an MB operator $\hat{A}$ and an NB operator $\hat{B}$ [7, pg. 562],

$$\left[\hat{A}^{[M]}, \hat{B}^{[N]}\right] = \sum_{k=|M-N|}^{M+N-1} \hat{C}^{[k]} \tag{9}$$

which gives a sum of different kB operators $\hat{C}^{[k]}$. Since the outer commutator in (8) must be between $\eta_{2\text{B}}$ and the inner commutator, we need only consider the cases of $\hat{T}^2$ which give a non-zero $\left[\eta_{2\text{B}}, \hat{T}^2\right]_{2\text{B}}$ since we are looking for an overall 0B term. This leaves only $\hat{T}^2_{1\text{B}}$ and $\hat{T}^2_{2B}$. Because $\hat{H}^{\text{od}}$ only connects the reference state with excited states, so does $\eta_{2\text{B}}$. This means the only two-body diagrams [4] it can produce are

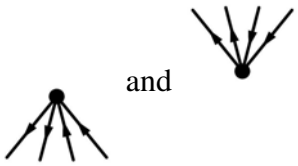

and

Because of this, both the $\eta^2\hat{T}^2$ and $\hat{T}^2\eta^2$ terms from the commutator can't be fully contracted down to a 0B term given $\hat{T}^2_{1\text{B}}$ or $\hat{T}^2_{2\text{B}}$ at either end of the diagram. Equation (8) reduces down to

$$\begin{aligned}\langle \left[\Omega(s), \left[\Omega(s), \hat{T}^2(0)\right]\right] \rangle &= -2 \langle \Phi_0 | \eta(s)\hat{T}^2(0)\eta(s) | \Phi_0 \rangle \\ &= -2 \langle \Phi_0 | \eta_{2\text{B}}(s)\hat{T}^2_{1\text{B}}(0)\eta_{2\text{B}}(s) | \Phi_0 \rangle - 2 \langle \Phi_0 | \eta_{2\text{B}}(s)\hat{T}^2_{2\text{B}}(0)\eta_{2\text{B}}(s) | \Phi_0 \rangle\end{aligned} \tag{10}$$

These terms correspond to the two Hugenholtz skeletons in Figure 5, and can now be evaluated.

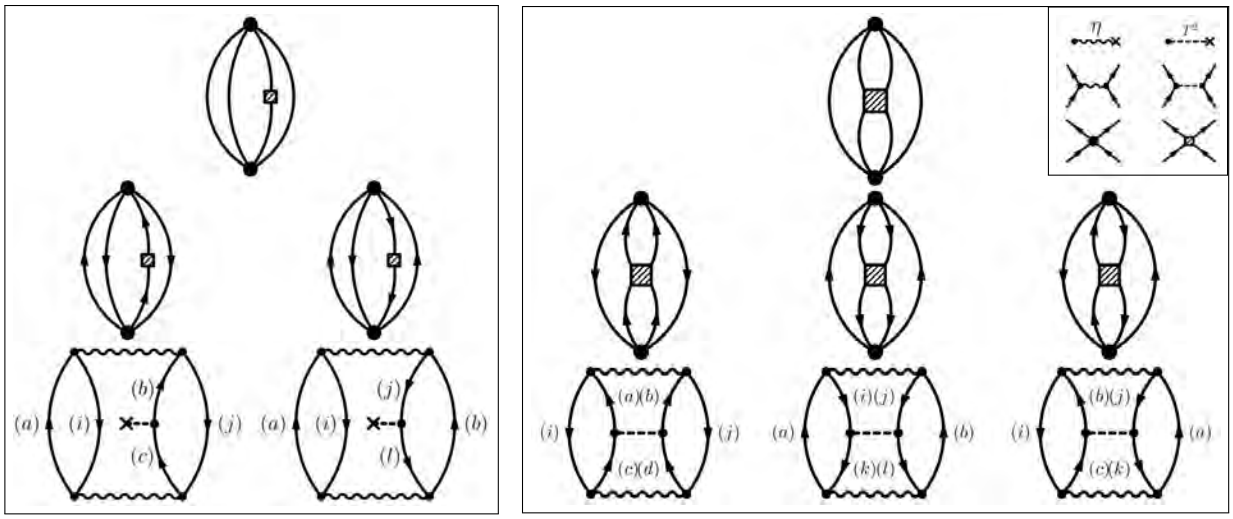

Figure 5: Diagrammatic notation for the $\hat{T}^2_{1B}$ term (left) and $\hat{T}^2_{2B}$ term (right) in (10) . Hugenholtz skeletons are expanded into directed Hugenholtz diagrams each of which are then expanded into anti-symmetrised Goldstone diagrams (ASG). These can finally be interpreted according to rules laid out in Ref. [4].

Adding all 5 ASG diagrams yields

$$\langle\left[\eta(s),\left[\eta(s),\hat{T}^2(0)\right]\right]\rangle_- = -2\sum_{abij}\Big[\eta_{ijab}\Big(\overbrace{\frac{1}{2}\eta_{abij}(n_{\bar{j}}-n_{\bar{b}})}^{\hat{T}^2_{1B}}+\overbrace{\frac{1}{4}\eta_{\bar{a}\bar{b}ij}\overline{n}_{\bar{a}}\overline{n}_{\bar{b}}}^{\hat{T}^2_{2B}\text{ p ladder}}+\overbrace{\frac{1}{4}\eta_{ab\bar{i}\bar{j}}n_{\bar{i}}n_{\bar{j}}}^{\hat{T}^2_{2B}\text{ h ladder}}$$
$$\overbrace{-\eta_{a\bar{b}i\bar{j}}\overline{n}_{\bar{b}}n_{\bar{j}}}^{\hat{T}^2_{2B}\text{ ring}}\Big)+\eta_{ija\bar{j}}\eta_{ab\bar{i}\bar{b}}\overline{n}_{\bar{j}}n_{\bar{b}}\Big]$$

where $\overline{\mu}$ is the orbital μ with t_z flipped. The above expression only comes from the isospin-flipping matrix elements of $\hat{T}^2$, since $\left[\eta(s),\hat{T}_z(0)\right]=0$. The occupation number $n_{\bar{b}}$ and hole number $\overline{n}_{\bar{j}}$ (highlighted) vanish for a symmetric reference, for which j and $\bar{j}$ are both hole states and b and $\bar{b}$ are both particle states. For the RHS to vanish, we should then have a symmetric reference and $\eta(s)$. (If $\eta_{abij}=\eta_{\bar{a}bij}=\eta_{a\bar{b}ij}=\eta_{ab\bar{i}j}=...$, then the sum trivially vanishes.) If η is not isospin-symmetric, the expression does not vanish. If the reference is asymmetric, this could be another source of ISB. Møller-Plesset and Epstein-Nesbet partitionings of Δ for $\hat{\eta}(s)=\hat{H}^{\text{od}}/\Delta$ both lead to spurious ISB. When the imaginary generator was substituted, the error vanished for a symmetric reference and $\hat{H}^{\text{od}}$ (and thus η). The sum above was reindex in terms of orbital quantum numbers and isospin-basis elements for a symmetric reference, e.g. in terms of $\langle T=1,T_z=1\big|\,\eta|T=1,T_z=1\rangle$,..., and was found to agree with the computed commutator.

4 Conclusion

Through the problematic commutator term (10) , three possible sources of spurious ISB were identified; an isospin-asymmetric reference and an isospin-asymmetric generator $\eta(s)$, via $\hat{H}^{\text{od}}$ and via $1/\Delta$. A possible extension to this research would be to determine whether isospin-mixing or isospin-conserving terms in the ASG diagram sum contribute more to ISB and to understand why. By mastering sources of spurious ISB, we will be one step closer to calculating δ_{C} precisely.

5 Acknowledgements

I would like to thank my supervisor, Prof. Ragnar S. Stroberg, for his constant guidance and support throughout this summer REU project, Dr. Bĭngchéng Hé, without whom I would not have been able to even run the IMSRG code and Jonathan Riess for his constant skepticism which pushed my knowledge to its limits at times.

Thanks also to Prof. Umsesh Garg and Ms. Kristen Amsler, who gave two dozen REU students a great summer. This work was funded by the Naughton Foundation, to whom I am very grateful.

References

[1] J. C. Hardy and I. S. Towner, Phys. Rev. C **102**, 045501 (2020).

[2] R. W. et al. (Particle Data Group), Progress of Theoretical and Experimental Physics **2022**, 083C01 (2022).

[3] S. Stroberg, TRIUMF Progress in Ab Initio Nuclear Theory, University of Notre Dame (Feb 28 2023).

[4] I. Shavitt and R. Bartlett, *Many-Body Methods in Chemistry and Physics: MBPT and Coupled-Cluster Theory* (2009).

[5] K. S, *Introductory Nuclear Physics* (Wiley India, 2008).

[6] T. D. Morris, N. M. Parzuchowski, and S. K. Bogner, Physical Review C **92**, 10.1103/physrevc.92.034331 (2015).

[7] M. Hjorth-Jensen, M. Lombardo, and U. van Kolck, *An Advanced Course in Computational Nuclear Physics: Bridging the Scales from Quarks to Neutron Stars* (2017).

Reproduction of the Band Structure of Twisted Bilayer Graphene

MIN GUO

July 2023

2023 NSF/REU Program
Department of Physics and Astronomy
University of Notre Dame

Advisor: Prof. Yi-Ting Hsu

Abstract

This project aims to replicate the band structure of twisted bilayer graphene (tBLG) using Bistritzer and MacDonald's model for the Hamiltonian of tBLG's electrons known as the "Dirac Continuum model." This model focuses solely on the band structure near the Dirac point K in the momentum space. To achieve this, I divide the effective Hamiltonian for electrons in tBLG into two parts: the interlayer component and the intralayer component, and then proceed to calculate each part individually. Once the Hamiltonian is obtained, I generate band structure plots along a chosen path for various twist angles. The plots reveal the emergence of flat bands at a twist angle of 1.05°, which aligns with experimental results.

1 Introduction

Twisted Bilayer graphene (tBLG) consists of two layers of graphene stacked atop each other. One layer is twisted by a small angle relative to the other one, forming a Moire pattern. Depending on the twist angle, the crystalline exhibits various electronic properties. Extensive research effort has been devoted to studying those properties. In 2011, Bistriszer and MacDonald published a Continuum Dirac model for energy bands in tBLG, which gained wide academic recognition. [1] My project aims to reproduce the band structure using Bistriszer and MacDonald's model. It explicates the details in the derivation of this model. Section II explains the geometry of the crystalline. Section III is the mathematical derivation of the model. Section IV constructs the matrix of the Hamiltonian for plotting.

2 Defining the Parameters

We regard the top layer as the reference layer with zero twist angle. The top layer's structure is the same as the monolayer graphene. It is periodic because it remains invariant under the translation along a set of lattice vectors $\{\mathbf{R}\}$

$$\{\mathbf{R}\} = \{n_1\mathbf{a_1} + n_2\mathbf{a_2} \mid (n_1, n_2) \in \mathbb{Z} \times \mathbb{Z}\}$$

$\mathbf{a_1}$, and $\mathbf{a_2}$ are called primitive vectors. $\mathbf{a_1} = \left(\frac{1}{2}, \frac{\sqrt{3}}{2}\right) d, \quad \mathbf{a_2} = \left(\frac{-1}{2}, \frac{\sqrt{3}}{2}\right) d.$

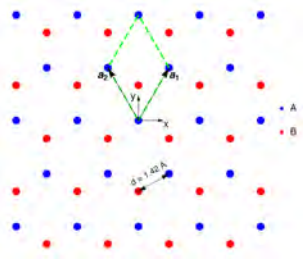

Figure 1, Graphene in real space.

The individual atom in graphene is parametrized as $\mathbf{R_i} + \delta$. i is the index of the cell. δ denotes the atom's relative position inside the cell. By applying a Fourier transform, we get the reciprocal space, also known as the momentum space of graphene. The reciprocal lattice also possesses honeycomb periodicity. Its primitive vectors are $\mathbf{b_1}$, and $\mathbf{b_2}$. They are obtained through the following relation:

$$\mathbf{a_i} \cdot \mathbf{b_j} = \delta_{i,\ j} \cdot 2\pi$$

Therefore, we get $\mathbf{b_1} = \left(\frac{\sqrt{3}}{2}, \frac{1}{2}\right) \frac{4\pi}{\sqrt{3}d}, \quad \mathbf{b_2} = \left(-\frac{\sqrt{3}}{2}, \frac{1}{2}\right) \frac{4\pi}{\sqrt{3}d}$. The set of reciprocal vectors are $\{\mathbf{G}\} = \{n_1\mathbf{b}_1 + n_2\mathbf{b}_2 \mid (n_1, n_2) \in \mathbb{Z} \times \mathbb{Z}\}$.

The bottom layer of tBLG is twisted by an angle θ relative to the top layer and then moved by a translation vector $\mathbf{d}$ relative to the top layer. The bottom layer's lattice vectors are $\mathbf{R}' = M_\theta(\mathbf{R}+\delta)+\mathbf{d}$. δ is the vector connecting two atoms in a unit cell; M_θ is the a unitary operator that rotates a vector by θ; $\mathbf{d}$ is the translation vector that can take any arbitrary value. Obviously, the two primitive lattice vectors for the lower layer in real space are $\mathbf{a_1'} = M_\theta(\mathbf{a_1})$ and $\mathbf{a_2'} = M_\theta(\mathbf{a_2})$. The corresponding lattice vector set is $\{\mathbf{R}'\} = \{\mathbf{d} + \delta' + n_1\mathbf{a_1'} + n_2\mathbf{a_2'} \mid (n_1, n_2) \in \mathbb{Z} \times \mathbb{Z}\}$.[2]

As the real space of the bottom layer is rotated, so is its momentum space. I propose its momentum space's primitive vectors are $\mathbf{b_1'} = M_\theta(\mathbf{b_1})$ and $\mathbf{b_2'} = M_\theta(\mathbf{b_2})$. My proof is the following.

We know

$$\langle M_\theta(\mathbf{a_j}) \mid M_\theta(\mathbf{b_i})\rangle = \langle M_\theta^\dagger(M(\mathbf{a_j})) \mid \mathbf{b_i}\rangle$$
$$\mathrm{M}_\theta^\dagger = M_{-\theta}$$

Therefore

$$\langle M_\theta(\mathbf{a_j}) \mid M_\theta(\mathbf{b_i})\rangle = \langle M_{-\theta}(M_\theta(\mathbf{a_j})) \mid \mathbf{b_i}\rangle = \langle \mathbf{a_j} \mid \mathbf{b_i}\rangle = 2\pi\delta_{ij} \quad \text{Q.E.D.}$$

3 Derivation of the Hamiltonian

The Hamiltonian of the tBLG consists of two terms: the intralayer hopping and the interlayer hopping. The intralayer terms are identical to the monolayer graphene Hamiltonian. Since our model is concerned only with the energy bands near the Dirac K points in the reciprocal space, we simplify the monolayer Hamiltonian by Taylor expansion about the $\mathbf{K}$ point. Measuring from the $\mathbf{K}$ point, we can write the wave vector as $|\mathbf{k}| \ll |\mathbf{K}|$. The first nonzero term of the Tayler series is the following.

$$h_\theta(\mathbf{k}) = -v|\mathbf{k}| \begin{bmatrix} 0 & e^{i(\theta_k-\theta)} \\ e^{-i(\theta_k-\theta)} & 0 \end{bmatrix} \quad (1)$$

To simplify our formula, I define the top layer to be rotated by -$\theta/2$ with respect to the reference frame and the bottom layer by $\theta/2$.

We proceed to the interlayer terms. In the reciprocal space, interlayer hopping is the process where an electron at momentum $\mathbf{K} + \mathbf{k}$ and sublattice α on a layer transfers to the **K' + q'** momentum state at sublattice β on the other layer. (We abbreviate the momenta as **k** and **q'**) Accordingly, the matrix elements of the Hamiltonian is defined as

$$T^{\alpha\beta}_{k,q'} = \langle \psi^1_{k\alpha} | H_T | \psi^2_{q'\beta} \rangle \quad (2)$$

$\psi^i_{k\alpha}$ is electron state at sublattice α and momentum $\mathbf{K} + \mathbf{k}$ on layer i.

$$\psi^1_{k\alpha} = \tfrac{1}{\sqrt{N}} \textstyle\sum_R e^{i\mathbf{k}(\mathbf{R}_i+\delta_\alpha)} |\mathbf{R}_i + \delta_\alpha\rangle \quad (3)$$
$$\psi^2_{q'\alpha} = \tfrac{1}{\sqrt{N}} \textstyle\sum_{R'} e^{i\mathbf{q'}(\mathbf{R}'_i+\delta'_\beta)} |\mathbf{R}'_i + \delta'_\beta\rangle \quad (4)$$

The **R** and **R'** sum over all unit cells in their respective layer. N is the number of cells in a layer. Substitute (3) and (4) into (2), and we get

$$T^{\alpha\beta}_{k,q'} = \tfrac{1}{N} \textstyle\sum_R \sum_{R'} e^{-i(\mathbf{k})(\mathbf{R}_i+\delta_\alpha)+i(\mathbf{q'})(\mathbf{R}'_i+\delta'_\beta)} \langle \mathbf{R}_i + \delta_\alpha | H_T | \mathbf{R}'_i + \delta'_\beta \rangle \quad (5)$$

The term $\langle \mathbf{R}_i + \delta_\alpha | H_T | \mathbf{R}'_i + \delta'_\beta \rangle$ is the tunneling strength of electron transfer between the two atomic orbitals. It is a function of the position difference between them. We Fourier Transform this function into the reciprocal space and get

$$\langle \mathbf{R}_i + \delta_\alpha | H_T | \mathbf{R}'_i + \delta'_\beta \rangle = t(\mathbf{R}_i + \delta_\alpha - \mathbf{R}'_i + \delta'_\beta) = \textstyle\sum_p \frac{t_p}{A} e^{i\mathbf{p}\cdot(\mathbf{R}_i+\delta_\alpha-M(\mathbf{R}_i)-\delta'_\beta-\delta'+\mathbf{d})}$$

Where t_q is a coefficient that depends on the momentum $\mathbf{q}$ and A is the total area of structure. By rearranging (5), we get

$$T^{\alpha\beta}_{k,q'} = \frac{1}{NA}\sum_R \sum_{R'} \sum_p t_p e^{i(\mathbf{p\text{-}K\text{-}k})\mathbf{R}_i)+i(\mathbf{q'\text{-}p})M(\mathbf{R})} e^{i(\mathbf{p\text{-}k}\delta_\alpha)(\mathbf{q'\text{-}p}(\delta'_\beta-\delta'+\mathbf{d})} \quad (6)$$

The complex function inside the sum $\sum_R e^{i(\mathbf{p\text{-}k})\cdot\mathbf{R}_i)}$ in (6)is periodic. As we sum it over all possible $\mathbf{R}$, the positive terms cancel the negative ones and the sum vanishes. It is not the case only if the function inside is constant for all $\mathbf{R}$, which requires that the exponent $(\mathbf{p\text{-}k})\cdot\mathbf{R}_i) = n\cdot 2\pi$ By the definition of the reciprocal lattice vectors, we know $\mathbf{R}\cdot(\mathbf{p\text{-}k}) = n\cdot 2\pi$ when $(\mathbf{p\text{-}k})\in\mathbf{G}$. Since there are N cells, the sum equals N for $(\mathbf{p\text{-}k})\in\mathbf{G}$. By the same token, $\sum_{R'}(\mathbf{q'\text{-}p})M(\mathbf{R}) = N$ only for $(\mathbf{q'\text{-}p})\in\mathbf{G'}$. It entails that the matrix element is non-vanishing only if two equations are satisfied:

$$\mathbf{p}-\mathbf{k} = \mathbf{G}_i \rightarrow \mathbf{p} = \mathbf{G}_i + \mathbf{k} \quad (7)$$

$$\mathbf{q'}-\mathbf{p} = \mathbf{G'}_j \rightarrow \mathbf{p} = -\mathbf{G'}_j + \mathbf{q} \quad (8)$$

Redefining $\mathbf{G'_j}$ as $-\mathbf{G'_j}$, we arrive at

$$\langle\psi^1_{k\alpha}|H_T|\psi^2_{q'\beta}\rangle = \frac{N}{A}\sum_G\sum_{G'} t_{k+G_i}\delta_{k+G_i,q'+G'_j} e^{i(\mathbf{G_i}\cdot\delta_\alpha-\mathbf{G'_j}\cdot(\delta'_\beta-\delta')-\mathbf{G'_j}\cdot\mathbf{d})} \quad (9)$$

(9) is the analytic expression of the matrix element, but it is an infinite sum. We have to truncate it to make it computationally possible. Experiments confirm that t_q decays rapidly with $|\mathbf{q}|$, so we only need to keep the largest t value in our approximation. The largest t value occur when $\mathbf{k}+\mathbf{G}$ is closest to the origin. So, $\mathbf{G} = 0, -\mathbf{b}_1$, or $\mathbf{b}_2$. Due to the rapid decay of t, all other terms are negligible. In all three cases, $t \approx t_K$, where $\mathbf{K}$ is the Dirac point on the top layer. Our model only considers momenta near the Dirac points, meaning $\mathbf{k}$ and $\mathbf{q'}$ are very small. So, the

$\delta_{k+G_i,q'+G'_j}$ term in equation (9) uniquely determines the possible values of **G'**. By expanding the sum in (9), we get

$$T^{\alpha\beta}_{k,q'} =$$
$$\frac{t_K}{A_{u.c.}}\left(\delta_{k,q'} + e^{i(\mathbf{b}_2\cdot(\delta_a-\delta_b+\delta)-\mathbf{b}'_2\cdot\mathbf{d})}\delta_{k+\mathbf{b}_2,q'+\mathbf{b}'_2} + e^{i(-\mathbf{b}_1\cdot(\delta_a-\delta_b+\delta)+\mathbf{b}'_1\cdot\mathbf{d})}\delta_{k-\mathbf{b}_1,q'+\mathbf{b}'_1}\right) \quad (10)$$

Here, the three Kronecker deltas in the equation suggest that hopping occurs if and only if the difference between **q'** and **k** take the following values:

$$\mathbf{q}' - \mathbf{k} = \mathbf{K} - \mathbf{K}', \quad \mathbf{K} - \mathbf{K}' + \mathbf{b}_2 - \mathbf{b}'_2, \text{or} \quad \mathbf{K} - \mathbf{K}' - \mathbf{b}_1 + \mathbf{b}'_1$$

We define $\mathbf{K} - \mathbf{K}' = q_b$, $\mathbf{K} - \mathbf{K}' + \mathbf{b}_2 - \mathbf{b}'_2 = q_{tr}$, and $\mathbf{K} - \mathbf{K}' - \mathbf{b}_1 + \mathbf{b}'_1 = q_{tl}$.

There are two possible lattice sites in a cell, 0 and δ, so

$$T_{k,q'} = \begin{bmatrix} T^{0,0}_{k,q'} & T^{0,\delta}_{k,q'} \\ T^{\delta,0}_{k,q'} & T^{\delta,\delta}_{k,q'} \end{bmatrix} \quad (11)$$

Combining (11) and (12) gives us

$$T_{k,q'} = \frac{t_K}{A_{\text{u.c.}}}\left(T_b\delta_{k,q'} + T_{tr}\delta_{k+\mathbf{b}_2,q'+\mathbf{b}'_2} + T_{tl}\delta_{k-\mathbf{b}_1,q'-\mathbf{b}'_1}\right) \quad (12)$$
$$T_b = \begin{bmatrix} 1 & 1 \\ 1 & 1 \end{bmatrix}, \quad T_{tr} = e^{-i\mathbf{b}'_2\cdot\mathbf{d}}\begin{bmatrix} e^{i\frac{2}{3}\pi} & 1 \\ e^{-i\frac{2}{3}\pi} & e^{i\frac{2}{3}\pi} \end{bmatrix}, \quad T_{tl} = e^{i\mathbf{b}'_1\cdot\mathbf{d}}\begin{bmatrix} e^{-i\frac{2}{3}\pi} & 1 \\ e^{i\frac{2}{3}\pi} & e^{-i\frac{2}{3}\pi} \end{bmatrix}$$

4 Building the Matrix

After deriving the matrix elements of the Hamiltonian, we proceed to the construction of the matrix for band computation. The first step is to define the basis of our matrix. Suppose that we would like to know the Hamiltonian matrix H(**k**)

for an electron at state $\mathbf{k}$ on the top layer. We certainly need to include ψ^1_k in our basis. $\psi^2_{k+q_b}$. $\psi^2_{k+q_{tr}}$, $\psi^2_{k+q_{tl}}$ should also be part of the basis because they are the states that our electron could possibly hop to. By the same reasoning, a state on the bottom layer will force us to add two new states on the top layer to our basis, and so on. If this process goes infinitely, it will give all basis states of H($\mathbf{k}$). Drawing the momenta of several iterations of basis states on an x-y momentum space, we find that they exhibit a hexagonal periodicity. (Fig 2) Its primitive vectors are $\mathbf{b_1^m} = q_b - q_{tl}$ and $\mathbf{b_2^m} = q_{tr} - q_b$. All basis states of on the top layer are in the form of $\psi^1_{k+n_1 b_1^m + n_2 b_2^m}$ while the ones on the bottom layer are $\psi^2_{k+q_b+n_1 b_1^m + n_2 b_2^m}$. The translational symmetry in the momentum states leads to the periodicity of the Hamiltonian. H($\mathbf{k}$) and H($\mathbf{k} + n_1\mathbf{b_1^m} + n_2\mathbf{b_2^m}$) have exactly the same set of bases. As a result, H($\mathbf{k}$) = H($\mathbf{k} + n_1\mathbf{b_1^m} + n_2\mathbf{b_2^m}$). The set of basis states of H($\mathbf{k}$) can be rewritten as

$$\{Basis\} = \{\psi^1_{k+n_1 b_1^m + n_2 b_2^m} | n_1, n_2 \in \mathbb{Z}\} \cup \{\psi^2_{k+q_b+n_1' b_1^m + n_2' b_2^m} | n_1', n_2' \in \mathbb{Z}\} \quad (13)$$

Another consequence of the translational symmetry in the momentum states is the Hamiltonian's periodicity. Equation (13) implies H($\mathbf{k}$) and H($\mathbf{k} + n_1\mathbf{b_1^m} + n_2\mathbf{b_2^m}$) have the same set of bases. Accordingly, $H(\mathbf{k})$ = H($\mathbf{k} + n_1\mathbf{b_1^m} + n_2\mathbf{b_2^m}$).

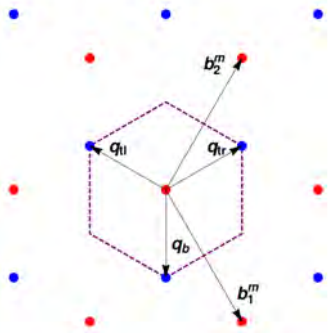

Figure 2, Basis states on the reciprocal space. The dashed lines demarcates the Moire Unit cell. The points represent momentum states in the reciprocal space.

$\{Basis\}$ is infinite, so truncating the momentum space becomes necessary. Our truncation method is to limit the range of values that n_1, n_2, n_1', and n_2' can take. It is reasonable to fear that truncation would lead to inaccuracy in our energy bands. [2] This worry is unnecessary because as we increase the size of the momentum space, the energy bands converge extremely rapidly. When our matrix's dimensionality reaches 36, further increases in the size of the basis no longer result in any significant changes in the energy band.

Having defined the basis, we can populate the matrix using what we derived earlier. Truncating the momentum space to only include the states in the first Moire unit cell and setting $\mathbf{d} = 0$, we get the following Hamiltonian:

$$H(\mathbf{k}) = \begin{bmatrix} h_{-\theta/2}(\mathbf{k}) & \frac{t_K}{A_{u.c.}} T_q & \frac{t_K}{A_{u.c.}} T_{tr} & A_{u.c.} T_{tl} \\ \frac{t_K}{A_{u.c.}} T_q\dagger & h_{\theta/2}(\mathbf{k}) & 0 & 0 \\ \frac{t_K}{A_{u.c.}} T_{tr}\dagger & 0 & h_{\theta/2}(\mathbf{k}) & 0 \\ \frac{t_K}{A_{u.c.}} T_{tl}\dagger & 0 & 0 & h_{\theta/2}(\mathbf{k}) \end{bmatrix} \quad (15)$$

Here, the basis is $(\psi_k^1, \psi_{k+q_b}^2.\ \psi_{k+q_{tr}}^2, \psi_{k+q_{tl}}^2)$. It is also worth noting that previous researchers have computationally shown that the energy bands do not depend on $\mathbf{d}$; thus, we can always set $\mathbf{d} = 0$ for simplicity. [2]

In my band structure plot (Fig 3), we took more bases into consideration for higher accuracy. I limit the values of n_1, n_2, n_1', and n_2' to be between -1 ad 1, resulting in a 36-dimensional matrix. As shown in Fig 6, flat bands appear at $\theta \approx 1.05°$, which matches the flat bands in Bistriszer and MacDonald's original paper.

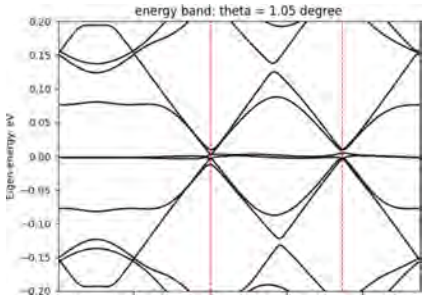

Figure 3, Energy bands of the tBLG at $\theta = 1.05°$. Path: $q_b : -q_b : -q_{tl} : q_b$.

5 Conclusion and Discussion

This report presents a comprehensive reproduction of the model for tBLG's effective Hamiltonian. It goes beyond previous reproductions by providing readers with more detailed information. However, some intriguing questions regarding tBLG remain unresolved. For example, how will the Hamiltonian change as we apply an external E-field or B-field to it? Future research based on this model may provide insights into these problems.

6 References

1. Bistritzer, R., amp; MacDonald, A. H. 2011. Moiré bands in twisted double-layer graphene. Proceedings of the National Academy of Sciences, 108(30), 12233–12237. https://doi.org/10.1073/pnas.1108174108

(Since my report is a reproduction of reference 1, the reader should assume that any idea in my report, if not specified otherwise, is drawn from this paper)

2. Santos Catarina, G. F. (2017). Twisted Bilayer Graphene — Electronic and Optical Properties.

3. https://github.com/MinGuo2023 (Source code for plotting)

Understanding Von Karman Instability in Granular Media

SHAENA HARASTY

August 2023

2023 NSF REU program
Dept. of Physics and Astronomy
University of Notre Dame

Advised by Professor Dervis Vural

1 Abstract

In the growing field of fluid dynamics, well known phenomenon in classical fluids are yet to be applied to granular fluid flow. Granular mediums are ubiquitous in the post-industrial world; yet, the physics determining their flow is still incomplete. One such phenomenon is von Karman instability, which creates an oscillating wake of eddies trailing behind a moving obstruction. Here, we attempt to further understand the processes that create von Karman vortex streets in a granular media using a computer simulation. We study the development of such instability depending on grain size, obstruction size, flow velocity, and simulated force between particles. Further research is still required to complete our understanding of von Karman vortex street generation in granular fluids.

2 Introduction

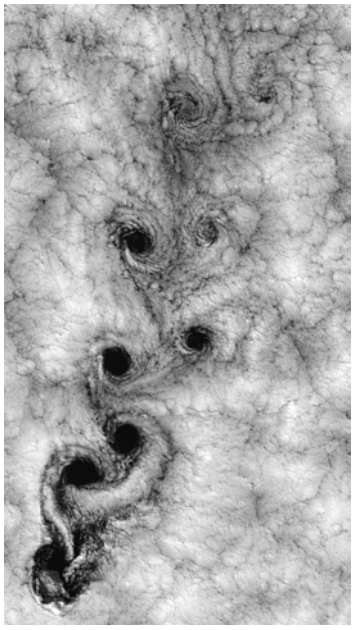

Figure 1: Von Karman Vortex Streets that developed in the atmosphere around the Juan Fernández Islands off the Chilean coast[Cah]

Granular media is defined as a multitude of distinct particles. Examples include sand, powders, grains, or even bouncy balls. The specific inter-particle interactions depend on the specific material and scale. Although each constituent element may be solid, liquid, or gas, granular media does not act specifically like any of them. [Cal] Some scientists have suggested defining granular materials as their own state of matter for that reason. Granular materials are extremely common, especially in our post-industrial world. Much of the raw materials, food products, and pharmaceuticals produced globally are granular mediums for at least part of their production, if not entirely. [Mas] However, no continuum model exists for predicting the flow of these materials. Understanding, and eventually predicting, the behavior of granular mediums will help improve efficiency in the industries that rely on them.

One phenomena of particular interest is known as von Karman instability, also known as von Karman vortex streets. Von Karman instability describes the production of vortexes behind a blockage as fluid flows around the blockage. Vortex production oscillates from two opposing sides of the blockage. As flow is blocked, an area of lower pressure forms behind the object. One side of the flow will fill this area, creating an eddy. As that eddy continues to move behind the object, another area of low pressure forms that now becomes filled by the opposite side of flow. This process continues

and a 'street' of eddies can be seen behind the blockage. A natural occurrence of this can be seen in Figure 1.

This blockage could be a skyscraper or chimney that blocks the flow of wind. It could be part of the machinery along a production line of grain. In the case of biophysics research, the blockage may be a lizard or worm attempting to navigate a sandy environment. Regardless of the specific situation, von Karman vortex streets represent a dissipation of energy, and is therefore undesirable. When the oscillation of vortex production matches the natural resonance of the blockage, vortex induced vibration (VIV) occurs. VIV can cause damage, fatigue, and structural failure; thus motivating research in the area to prevent such damage. This can affect bridges, power transmission lines, marine risers, and more. [Wat] Additional research into VIV is needed to determine if the vibrational energy can be transformed into any usable forms of energy as well.

Here, I discuss some of the various facets of fluid dynamics, biomechanics, and engineering that are needed to understand to these phenomena. More research is needed by the entire scientific community in order to fully comprehend all the details of this complex and cutting-edge field of physics.

3

3.1 Navier-Stokes equations

The entire discipline of fluid dynamics is based on the Navier-Stokes equations.

$$\rho \frac{D\,\acute{u}}{Dt} = -\nabla p - (\nabla \cdot \bar{\tau}) + \Sigma \rho_s F_s \tag{1}$$

$$\nabla \cdot \vec{u} = 0 \tag{2}$$

Equation (1) is known as the momentum equation and is derived from Newton's second law. On the left-hand side, the density ρ is multiplied by the full space and time derivative of velocity $\vec{u}$. This is clearly equivalent to Newton's $m \frac{dv}{dt}$. Where Newton's second law would describe the external forces on the right-hand side, fluid mechanics necessitates a few additional terms. ∇p describes the pressure gradient in the fluid medium. $(\nabla \cdot \bar{\tau})$ describes the divergence of the stress tensor. The remainder of the external forces are summarized in $\Sigma \rho_s F_s$. Equation (2) is known as the continuity equation. By stating that the divergence of the fluid velocity must be equal to zero, there cannot be any sources or sinks of velocity within the boundaries. This is equivalent to stating mass conservation for the standard second law. [Bro]

Although the Navier-Stokes equations have been proven solvable for 2 spatial dimensions, the

Navier-Stokes equations have yet to be proven solvable for all cases in three spatial dimensions and in one time dimension. It is one of seven unsolved equations presented by the Clay Mathematics Institute for the Millennium Prize. The first person to prove the Navier-Stokes equation or give a valid counter-example will win a 1,000,000 dollar reward. [Ins] Due to the difficulties in solving these flow equations, there exists a subfield known as computational fluid dynamics that focuses on how different numerical and computational techniques can be used to predict flow patterns around cars, planes, and boats. Programs known as CFD solvers are used in engineering and industry. The other primary technique for determining flow behavior is via simulation.

Since this paper focuses on granular media, the simplest way to model such behavior is by using a simulation. By definition, granular media is constituted of several discrete particles rather than one continuous and deformable mass, which lends itself nicely to computer simulations. Additionally, no solvers exist for granular flow at this poin in time.

3.2 Boundary conditions

In order to solve the Navier-Stokes equation for any system, one must start with a specific set of boundary conditions. Some conditions are particular to unique systems, such as the specific symmetry of the system. However, some conditions must remain true for all systems due to the nature of fluids. These conditions include

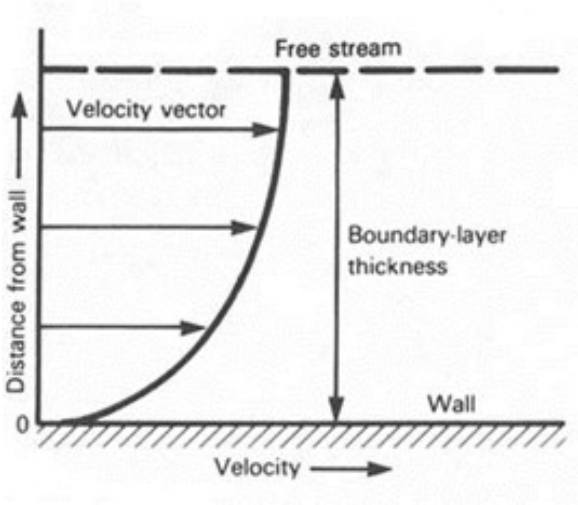

Figure 2: Example of a boundary layer development in a flow velocity profile [Rei]

$$U_{fluid,parallel}|_{x=wall} = U_{wall} \quad (3)$$

$$U_{fluid,perpendicular}|_{x=wall} = 0 \quad (4)$$

$$\bar{\tau}|_{x=wall} = 0 \quad (5)$$

$$\bar{\tau}_{jk}(\text{fluid}_1)|_{x=boundary} = \bar{\tau}_{jk}(\text{fluid}_2)|_{x=boundary} \quad (6)$$

$$U_{parallel}(\text{fluid}_1)|_{x=boundary} = U_{parallel}(\text{fluid}_2)|_{x=boundary} \quad (7)$$

Equations (3) and (4) describe the no slip wall condition. Fluid that is in direct contact with the wall is stuck to the surface and therefore unable to gain any perpendicular or parallel velocity with respect to the wall. Flow must be continuous at all points, creating a boundary layer between the wall and fully developed flow. The development of a boundary layer can be seen in the velocity

profile of Figure 2. Equations (5) and (6) describe conditions for stress continuity. Since there is no stress along the wall, the stress tensor of the fluid at that point must also be zero. Additionally, all elements of the stress tensor must be equal at the boundary of two fluids if more than one fluid exists in the system. Equation (7) describes velocity continuity, meaning that if more than one fluid exists in the system, the two fluids must move at the same velocity at their boundary. [Bro] These conditions are known to be true in all fluid mechanics problems. However, the validity of these conditions is less understood in regards to granular media. While it is intuitive to assume that the conditions would largely be the same, it is more difficult to notate these conditions when considering several discrete particles rather than a continuous fluid.

3.3 Reynolds Number and Strouhal Number

Since the Navier-Stokes equations are often too laborious to solve, the field of fluid mechanics relies heavily on dimensionless numbers in order to predict the macrostate of the system. The two most important dimensionless numbers for this analysis are Reynolds number (Re) and Strouhal Number (St).

$$\mathrm{Re} = \frac{\rho U L}{\mu} \tag{8}$$

$$\mathrm{St} = \frac{f}{L} \tag{9}$$

Where ρ describes the fluid density, U describes the fluid velocity, L describes the characteristic length of the system, μ describes the fluid viscosity, and f is the frequency of vortex shedding in von Karman instability. Reynolds number can be understood as the ratio of internal forces and viscous forces. Knowing the Reynolds number allows us to predict whether flow will be laminar or turbulent. Low RE implies a laminar flow with high RE indicates a turbulent follow. Re can be any number greater than zero. Strouhal number is used to predict the dominance of oscillations around a blockage. St ranges from zero to one. At $\mathrm{St} \approx 1$, oscillations dominate the flow. When $\mathrm{St} \approx 0$, the flow is dominated by the direction of the initial velocity. At intermediate values of $\mathrm{St} \approx .2$, eddy shedding begins to occur and the von Karman vortex street phenomena can be observed. There is a well-known relation between Reynolds number and Strouhal number in classical fluids, which can be seen in Figure 3.

Dimensionless numbers from fluid mechanics can be used to further understand animal locomotion as well. By using the frequency of movement as f and the length of movement as L, strouhal number has many relevant applications to biomechanics One study found that Rainbow trout *Oncorhynchus mykiss* modify the frequency of their tail beat in order to maintain $\mathrm{St} \approx .2$, even when conditions were changed that forced them to change their swim patterns. [Nud+] In similar stud-

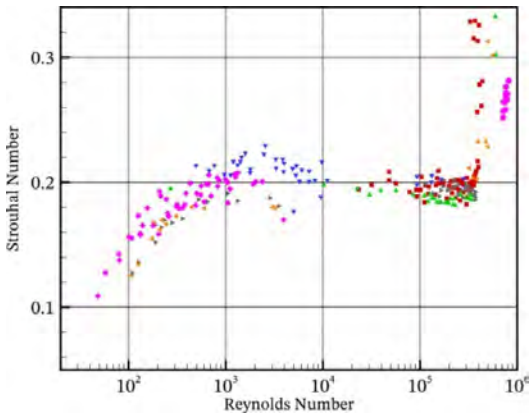

Figure 3: The standard relationship between Re and St in classical fluids [Kat]

ies of bird flight, researchers found that in dual medium specialists (birds that can fly in both air and water with decent efficiency) adapt their flight patterns depending on the medium to roughly St ≈ .2. [LZT] This research points to the existence of some optimal St for forward movement, which needs to be further studied.

3.4 Granular Media

Granular media describes a wide range of different materials with an equal range of unique properties. The most important distinction between granular media and classical fluids is the presence of frictional forces between discrete particles in granular media. Where classical fluids experience some amount of internal friction via viscosity, the particles remain stuck together. In granular media, there are far more dissipative forces since particles can have more kinetic interactions.

Similarly, where classical fluids have a definable stress tensor that is continuous throughout the mass, granular media does not have as simple of a solution. Coulomb was the first scientist to investigate the internal forces between granular particles. He studied the collapse of piles of particles using the maximal stable angle θ_m and the minimum angle of repose θ_r. The difference between these two values is known as the Bagnold angle is used to measure the dependence of state history for a given material. This occurs due to the non-uniform distribution of force throughout the system. Force chains describe networks of particles that can rest on each other. Once shear stress reaches a critical value, the force chains begin to slide and the pile returns to its angle of repose. Several models have been proposed to model this phenomenon with more rigorous mathematics, but most have yet to be experimentally verified. [DW]

Another important divergence of granular media compared to classical fluids is their ability to jam. Granular systems undergo jamming, which is often conceptualized as a thermodynamic phase change of the system. Within a jammed state, not all particles are completely confined. Some

particles can still move within cages formed by immobile/jammed neighbors. Jamming can be predicted using the Lubachevsky-Stillinger algorithm (LSA). [LS]

4 Methods

All simulations were completed using GFlow v4.0, a code repository created by a previous student of Professor Vural named Nathaniel Rupprecht. Gflow simulates two dimensional granular flow through a pipe with a circular obstruction. Individual particles are modelled as dissipative harmonic spheres, meaning that they can withstand a small amount of deformation before exerting an outward force modelled by equation (10).

$$\mathbf{F}^{\text{net}}_{1,2} = \max\{0, k_s(R_1 + R_2 - r) + \gamma_d v_n\} \cdot \hat{\mathbf{r}} \tag{10}$$

The constants k_s and γ_d represent the coefficients for repulsive force and dissipative force respectively. The maximum of force is used to ensure collisions always result in repulsive, not attractive. Force acts along the r^ direction, where r^ is along the line that connects to two centers of the particles.

Particles were generated using the probability distribution of equation (11) such that grains are generated with an equal distribution between [r, 1.2r]. Packing fraction, equation (12), is kept at 0.875 to prevent jamming of particles.

$$p_{r_a,r_b}(r') = \frac{r_a r_b}{r_b - r_a}(r')^{-2} \tag{11}$$

$$\phi = \sum_{i=1}^{N} \pi r_i^2 / V = 0.875 \tag{12}$$

A stationary circular object of radius 1 is placed at the origin with infinite mass. Once initialized, the simulation fills the system with a random distribution of particles all moving to the right with initial velocity v_d. Data is collected immediately after the transient period. [RV] An example of a working simulation can be seen below in Figure 4.

5 Results & Conclusions

Grains are colored based on their initial y value when entering the boundary. Resonance was found to occur between $2.3 < v_d < 3.1$. Past $v_d > 4$ the particles no longer oscillate since the cavity behind the disk becomes too large. When the dissipative energy is relatively high, $\gamma_d = 1, 0.75, 0.5, 0.25$, the Fourier period pattern is stable at $v_d < 3.2$. Within this range, particles oscillate within the cavity instead of forming spatiotemporal eddy streets behind the obstruction.

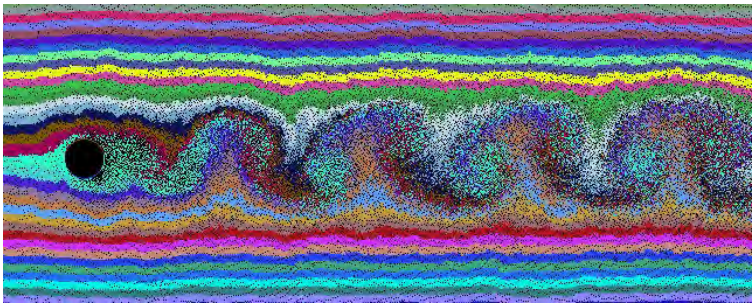

Figure 4: Formation of eddies behind a circular blockage. Successful run of the program showing that it is possible to see von Karman Instability in granular media [RV]

For lower γ_d, the period velocity curve is much lower and decreases instead of increases as before. As the dissipation is decreased, the system transitions to vortex-shedding behavior as one would expect from a classical fluid. This is the expected behavior, as the dissipative force is the defining characteristic of granular flow. [RV] All of these results were already determined by Nathaniel Rupprecht and Professor Vural before my arrival at the REU.

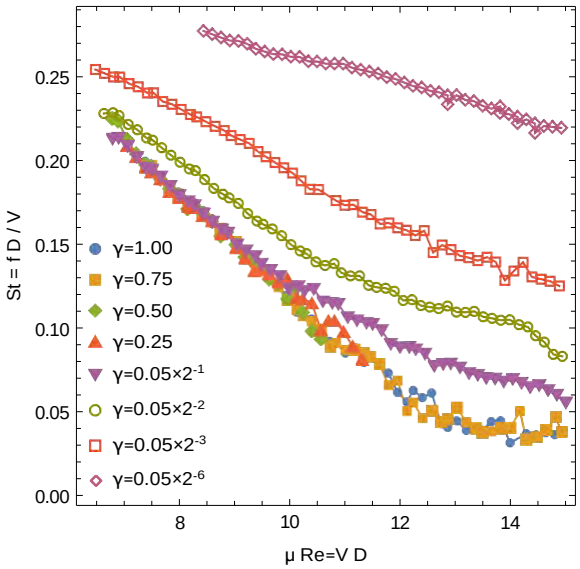

Figure 5: Relationship between Re and St according to the simulation.[RV] However, this looks very different then the well known relationship in classical fluids seen in Figure 3.

While attending the REU, I intended to continue to use Gflow to investigate the simulation in more detail as parameters are adjusted, specifically to determine when classical fluid behavior reemerges from the system. Additionally, I intended to further investigate the discrepancies between the relationship between Strouhal number and Reynolds number in classical fluids and the relationship determined by the simulation. The discrepancies between Figure 3 and Figure 5 are vast and we are unsure as to why. Professor Vural and I also intended to attempt to implement different force models into the simulation so that the particle interaction behavior would more closely model real granular media. Due to continuing medical issues throughout the summer that became espe-

cially intense in the second half of the program, I was unable to achieve these programming goals. However, I still learned a huge amount in the first 6 weeks and I hope that has been reflected in the background sections of this paper. This project made me realize how much is still not understood within the fields of fluid mechanics and biomechanics, and I believe that all subsections of this paper could benefit from more investigation from the entire scientific community.

6 Acknowledgements

Thank you to Professor Dervis Can Vural, as well as his graduate students Catagay Eskin and Martin Heidelman, for their assistance throughout the program. Thank you to the National Science Foundation for the REU grant funding and The University of Notre Dame's College of Sciences for facilitating the program. I would like to acknowledge Nathaniel Rupprecht as the primary author of the GFlow code. I would like to thank Professor Umesh Garg and Mrs. Kristen Amsler for being such wonderful directors of the ND REU. Lastly, I understand that this paper is atypical for the REU program, and I would like to thank Professor Vural, Professor Garg, and Mrs. Amsler for their continued support throughout the program while I struggled with several medical issues this summer.

References

[1] Robert S. Brodkey. *The Phenomena of Fluid Motions*. url: Dover%20Publications%201967.

[2] Robert Cahalan. *Kármán vortex street caused by wind flowing around the Juan Fernández Islands off the Chilean coast. NASA/GSFC*. url: http://earthobservatory.nasa.gov/Newsroom/NewImages/images.php3?img_id=3328.

[3] University of California Santa Barbara. *Granular Material. Complex Systems*. url: https://web.physics.ucsb.edu/~complex/research/granular.html.

[4] E. DeGiuli and M. Wyart. *Friction law and hysteresis in granular materials*. url: https://www.pnas.org/doi/10.1073/pnas.1706105114.

[5] Clay Mathematics Institute. *Navier-Stokes Equation. Unsolved*. url: https://www.claymath.org/millennium/navier-stokes-equation/.

[6] Nikolaos D. Katopodes. *Free-Surface Flow Environmental Fluid Mechanics. Chapter 5 - Viscous Fluid Flow*. url: https://www.sciencedirect.com/science/article/abs/pii/B9780128154892000058.

[7] Anthony B Lapsansky, Daniel Zatz, and Bret W Tobalske. *Alcids 'fly' at efficient Strouhal numbers in both air and water but vary stroke velocity and angle*. url: https://elifesciences.org/articles/55774#:~:text=Strouhal%20numbers%20of%20four%20species%20of%20alcid%20in%20aerial%20and%20aquatic%20flight.&text=St%20for%20aerial%20flights%20based,2%2C%20dark%20red%20points)..

[8] Boris D. Lubaehevsky and Frank H. Stillinger. *Geometric Properties of Random Disk Packings*. url: https://citeseerx.ist.psu.edu/document?repid=rep1&type=pdf&doi=222d563eb9dbd66d320c695385feae9cc2dfeeda.

[9] Kamrin Group at Massechuets Institute of Technology. *Theory and Modeling of Granular Media*. url: http://web.mit.edu/kkamrin/www/granular.html.

[10] Robert L. Nudds et al. *Rainbow trout provide the first experimental evidence for adherence to a distinct Strouhal number during animal oscillatory propulsion*. url: https://journals.biologists.com/jeb/article/217/13/2244/12227/Rainbow-trout-provide-the-first-experimental.

[11] Brad Reisfeld. *Fluids and Fluid Flow. Boundary Layers*. url: https://www.engr.colostate.edu/CBE101/topics/fluids_and_fluid_flow.html.

[12] Nathaniel Rupprecht and Dervis Can Vural. *Vortex streets in granular fluids*. url: https://www.overleaf.com/project/624b2ef12b2437d84a108d21.

[13] University of Waterloo. *Computational Fluid Dynamics and Turbulence Modelling Laboratory. Vortex-Induced Vibration*. url: https://uwaterloo.ca/computational-fluid-dynamics-turbulence-modeling-laboratory/research/vortex-induced-vibration-viv.

Upper limits on Companions to Kepler's Circumbinary Planets

CARLOS JURADO

2023 NSF/REU Program
Department of Physics and Astronomy
University of Notre Dame

ADVISOR(S): Prof. Lauren Weiss

Abstract

A circumbinary planetary system is a system in which a planet(s) orbit around two stars, instead of one. These systems are of great interest because they test our understanding of stellar and planetary formation. Kepler-34 is a system that contains two solar type stars at the center and a gas giant at a distance of 1.1 AU. We analyze a decade of radial velocity data from Kepler-34 with the Keck HIRES spectrograph and explore the possibility of distant stellar companions in the system from long-term trends in the RV data. We place conservative upper limits for the possible stellar companions to be of M-type stars located further than 15 AU from the stellar binary.

1 Introduction

Circumbinary planets (CBPs) are planets that orbit around a stellar binary system and the detection of such planets have been made primarily with the transit method. The transit method measures the periodic dip in flux from a star as the planet crosses the star along our line of sight and is most sensitive to detecting planets (or stellar objects) with shorter orbits because this increases the likelihood of a transit. The Kepler space telescope was launched in 2009 to continuously monitor more than 150,000 stars in the search of exoplanets via the transit method [1]. Out of the 12 known transiting circumbinary planet systems, 9 have been discovered from the Kepler mission, all of which with distinct stellar and planetary properties, highlighting the diversity of these multi-body systems. We highlight some of the significant properties of 2 Kepler circumbinary systems in Table 1 that are significance to this paper.

Due to the low mass of the CBPs in these Kepler systems, the center of mass, also known as the barycenter, of the three body system is roughly at the stellar binaries barycenter and each star approximately follows a Keplerian orbits due only to the mass of the other star. The parameters for the Keplerian orbits can be obtained from radial velocity (RV) measurements of each star over a sequence of dates that are on the same order as the period of the binary stars. Long term RVs, spanning over a decade, have been obtained for the Kepler-34 system and with these measurements, we are interested in searching for long term variations from the two-body Keplerian orbits. The

[1] https://www.nasa.gov/mission_pages/kepler/overview/index.html

Properties	Kepler-34	Kepler-35
Stellar Binary Orbital Properties		
Mass of Star A (M_{sun})	1.0479	0.8877
Mass of Star B (M_{sun})	1.0208	0.8094
SMA (AU)	0.22882	0.17617
Eccentricity	0.52087	0.1421
Planet Orbital Properties		
Mass of Planet ($M_{jupiter}$)	0.220	0.127
SMA (AU)	1.0896	0.60347
Eccentricity	0.182	0.042

Table 1: Stellar and Planetary orbital parameters for Kepler-34 and Kepler-35 [1]. The semimajor axis (SMA) is defined as half the distance of the major axis of the elliptical orbit. The eccentricity is a measures the deviation of the orbit from circular.

presence of a trend in the RVs over time would indicate a high-mass companion located further outwards in this system driving these variations. Even in the case that no significant trend is detected in the RVs, we can still apply an upper limit mass constraint on possible companions to Kepler's circumbinary systems.

2 Methods

Stellar spectra of Kepler-34 were obtained with the High Resolution Echelle Spectrometer (HIRES) on the Keck telescope. In total, we obtain 294 RVs across 6 dates for Kepler-34. The majority of RVs were measured from spectra taken in 2011 and were crucial for fitting the Keplerian orbital parameters for the binary star system. Spectra obtained from observations in 2019 and 2021 are utilized to determine deviations in the RV measurements from the model, possibly due to a hidden high-mass companion. We utilized the broadening function technique to calculate the radial velocity measurements of each star and model RV curves from the stellar orbital parameters with `Radvel` [2].

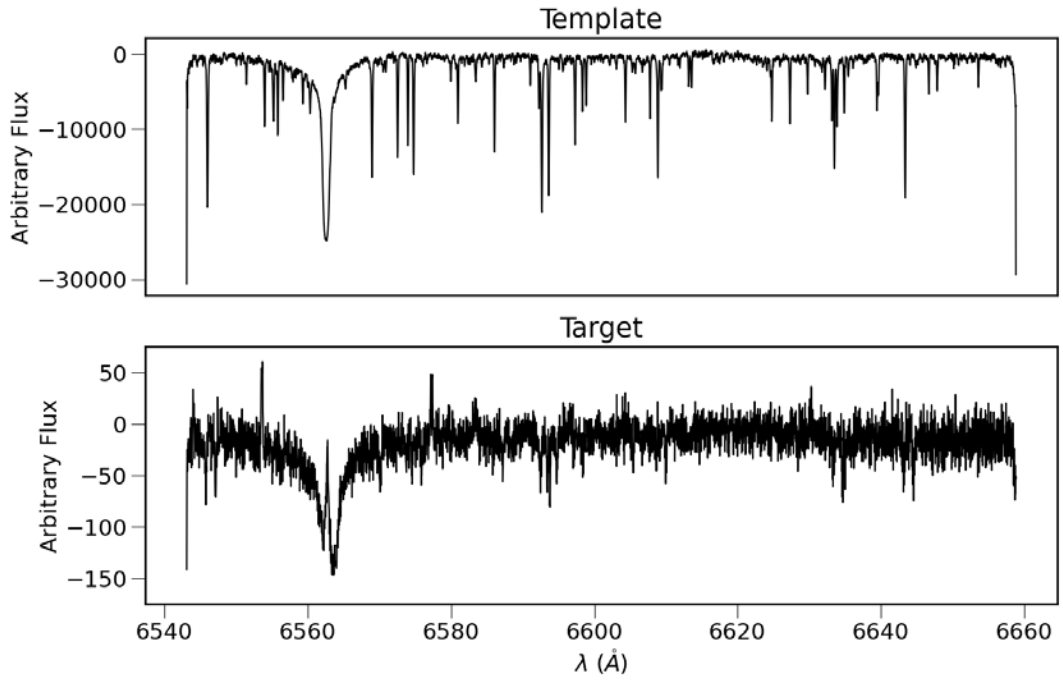

Figure 1: Stellar spectra of the template spectrum (top panel) and target spectrum (bottom panel) in the 6545 - 6658 $\mathring{A}$ band. In the template spectra, the prominent absorption line (centered at 6563 $\mathring{A}$) is the H-alpha line. In the target spectrum, the H-alpha line appears twice because the target spectrum is the combined spectrum of both stars.

2.1 Measuring Radial Velocities

The Broadening Function (BF) technique is an algorithm to determine the radial velocity of each star from its spectrum. The algorithm requires a template spectrum that is typically from a sharp-lined single star and compares it to the spectrum that we are interested in. Our template spectrum is of HD182488, a star of similar spectral classification to Kepler-34. In Figure 1, we compare the spectra for our template star and Kepler-34 in the wavelength band near the prominent H-alpha absorption line (centered at 6563 $\mathring{A}$). Our target spectrum displays two sets of absorption lines due to each star and are broadened due to Doppler-effect line broadening and various other rotational effects. The BF algorithm determines the function that is convolved with the template spectrum to create the observed double-lined spectrum. The result of this algorithm is information on the radial velocities of the individual stars of the binary.

We utilize `SAPHIRES` (Stellar Analysis in Python for HIgh REsolution Spectroscopy), a python

package that models the radial velocities of double-lined binary systems [3]. In Figure 2, we show an output file for one of our spectra from SAPHIRES. The two vertical peaks corresponds to the radial velocity measurement of each star. The peaks are broadened, as opposed to delta functions due to various natural broadening effects and instrumentation noises. We fit each peak with a Gaussian profile to extract the RV measurement. For each date, these are 49 RV measurements with some measurements suffering from high noise due to atmospheric absorption of the incoming light or cosmic rays, causing a mismatch in the template spectrum and the double-lined binary spectrum. We perform an iterative sigma clipping algorithm (with $\sigma = 3$) to remove these outliers and utilize the remaining RVs for parameter fittings. Despite these efforts, the RV measurements from the 2019 data suffer severely from these effects and obtaining a reliable RV measurement was difficult compared to the other RV measurements. Although we report the measured RV values on this date in Figure 3, we exclude this point in our RV modeling when determining the long-term RV trend to maintain a more conservative upper mass limit.

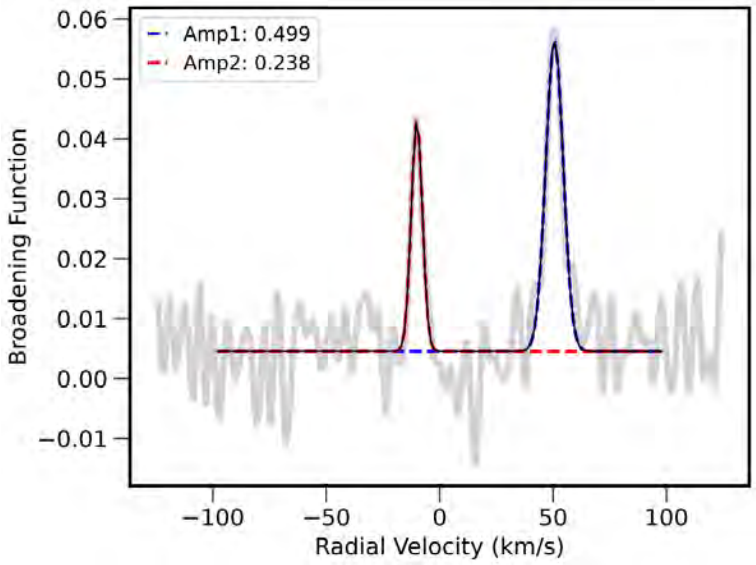

Figure 2: Broadening Function of the spectrum of both stars in the Kepler-34 system at a time of BJD = 2455806.862. Gaussian profiles are fitted to the peaks in the Broadening Function at the radial velocities associated with star A (red) and star B (blue).

2.2 RV Modeling

We utilize `Radvel`, a python package for modeling Keplerian orbits with RVs to fit the RVs with the orbital parameters. Welsh *et al.* [1] has obtained precise measurements of the stellar and planetary orbital parameters for Kepler-34 by combining stellar spectra, transit timing variations, and photo-dynamical modeling of the systems. We adopt these values to generate our Keplerian orbits, rv_{model}, with three free parameter: γ, $\dot{\gamma}$, and t_{per}. γ corrects for the vertical offset between the RV measurements and Keplerian orbit model due to the systemic velocity of the binary star system and instrumental corrections, $\dot{\gamma}$ is a parameter that we introduce to determine long-term trends in the RVs introduced by a higher mass companion and t_{per} is the time of periastron passage of the binary. The values for each parameter are fitted with an optimizing algorithm to maximize the log likelihood function

$$\ln\, p\left(rv_{obs} \mid t, rv_{model}, \sigma\right) = -\frac{1}{2}\sum\left[\frac{\left(rv_{obs} - rv_{model}\right)^2}{\sigma^2} + \ln(2\pi\sigma^2)\right] \tag{1}$$

where rv_{obs} are the obtained RV measurements for each date, rv_{model} are the RV values determined from the model, and σ is the standard deviation for each measurement. We estimate the uncertainty in our parameters with `emcee`, a Python package for implementing MCMC algorithms [4].

3 Results

In this section, we display the results of our optimization and MCMC algorithms for the Kepler-34. In particular, we discuss the implications that $\dot{\gamma}$ has on the constraints for a high-mass companion in the systems.

We obtain the values of: $\gamma = -2.55717^{+0.200}_{-0.190}\, \dot{\gamma} = -0.00032^{+0.00012}_{-0.00012}, t_{per} = 2455007.12735^{+0.01412}_{-0.01475}$ for our free parameters. In Figure 3, we display the RV Curve for Kepler-34, fitted with our best-fit parameters. Noticeably, the RV measurements in 2011 are strongly in agreement with the model. The RV measurement in 2019 was unreliable because the BF algorithm suffered from a low S/N ratio. We removed this data point for the determination of $\dot{\gamma}$ to obtain a conservative upper limit

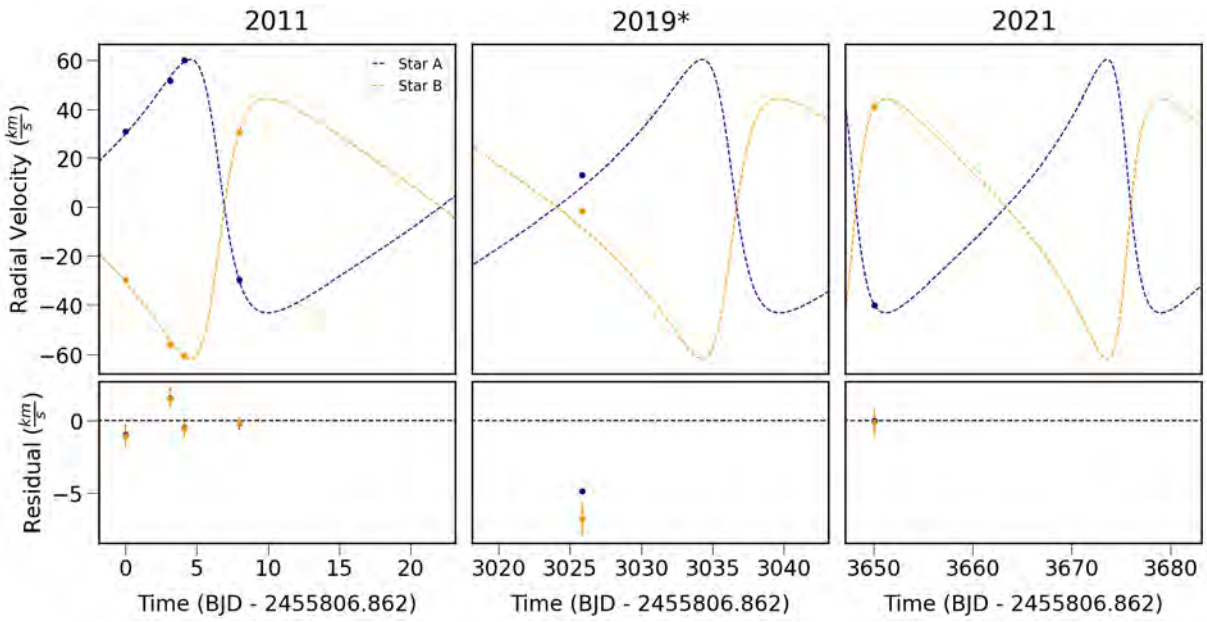

Figure 3: In the top panels, we show radial velocities obtained with Keck HIRES for Kepler-34 spanning over a decade (solid points). The 1σ error bars are typically smaller than the point size. Our best fit model of the RVs (dashed curve), from which we determine values for γ, $\dot{\gamma}$, and t_{per}. The bottom panels show the residuals.

mass constraint but leave the data point in Figure 3 for completion.

A significant detection of $\dot{\gamma}$ would correspond to a companion in the system with degeneracy between the semi-major axis and mass. A non-detection of $\dot{\gamma}$ can be used to place upper limits of putative, hidden companions. As a proof of concept, we assume a companion on a co-planar, circular orbit around the barycenter of the binary stars. Then, the mass of that companion can be calculated by dividing the gravitational force by its acceleration of the binary stars, yielding:

$$M_c = \frac{\dot{\gamma} a_c^2}{G} \tag{2}$$

where a_c is the semi-major axis of the companion object and G is the gravitational constant. We are restricted to companions on orbital periods much greater than the span of the RV measurements (i.e., $a_c > 15AU$). Possible companions with orbital periods on a scale of a decade will average the direction of the RV change and so, $\dot{\gamma}$ would not be representative of the true companion mass. In Figure 4, we illustrate the conservative upper limit for the mass of a companion in the Kepler-34

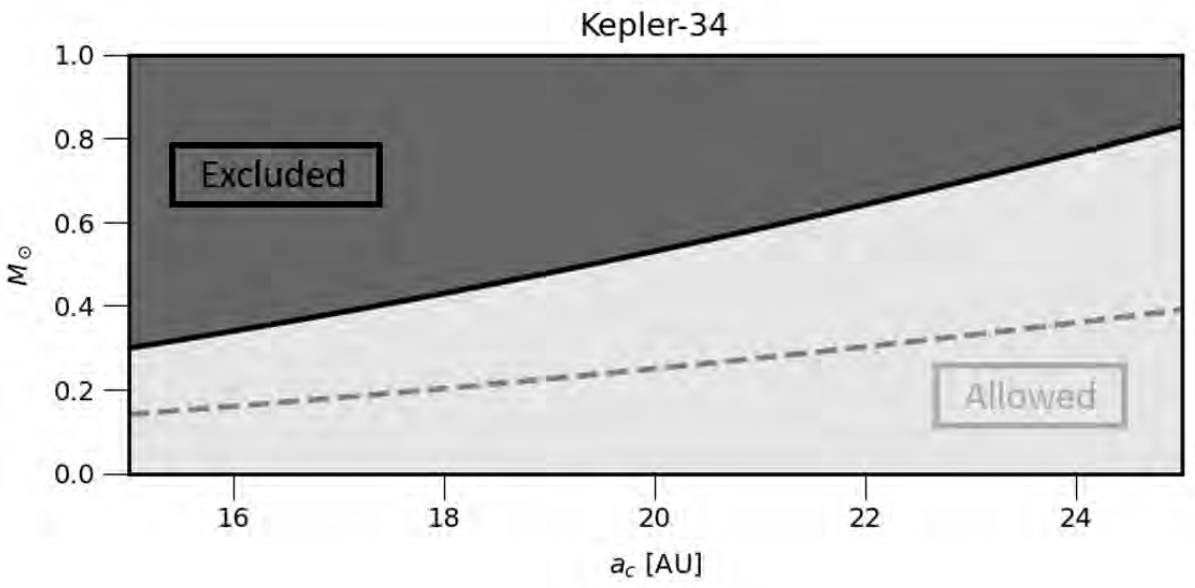

Figure 4: Upper limits on a proposed coplanar companion in the Kepler-34 system as a function of companion mass and semi-major axis. The dashed grey curve is obtained from the mean value of $\dot{\gamma}$ and the light grey region is the $\pm 3\sigma$ interval. The dark grey region corresponds to masses above our 3σ upper limit.

system, derived from $\dot{\gamma}$. The mass limit obtained from the mean value of $\dot{\gamma}$ is shown as a dashed grey curve, while the shaded grey region represents the $\pm 3\sigma$ interval. Stellar companions with masses exceeding 0.6 solar masses and situated within a semi-major axis of less than 21.5 AU are not possible in the Kepler-34 system. M-type stars are characterized as red, low-temperature stars with masses ranging between 0.08 and 0.6 solar masses [5]. Therefore, M-type stars are considered feasible candidates for being companions to the binary stars under consideration. Other objects of planetary mass may exist in the system but detecting their presence from only radial velocity measurements requires extreme precision. In fact, only recently has Standing *et al.* [6] detected the first new planet from radial velocity measurements (as opposed to the transit or transit timing techniques) in a circumbinary system.

4 Conclusion

By monitoring the RV curves of Kepler-34 over a decade, we were able to provide upper limit mass constraints on hidden companions in the system. We determine the RV long-term trend to have a slope of $\dot{\gamma} = -0.00032^{+0.00012}_{-0.00012}$. That is, we've limited the possible companions in the Kepler-34 system to low mass M-type stars located further than 15 AU from the stellar binary. A follow up with HIRES to increase the number of precise RV measurements in the latter half of the decade would provide us with a more accurate value for $\dot{\gamma}$ and further limit the possible parameter space for stellar companions. We leave it for a further work to explore the parameter space with n-body simulations and stability criteria.

5 Acknowledgments

I would like to thank Dr. Lauren Weiss for her guidance during this project and the astroweiss group for their support. I would also like to thank Dr. Garg and Ms. Amsler for organizing the Notre Dame REU program and the experience. This work was supported by NSF grant PHY-2050527.

References

[1] W. F. Welsh, J. A. Orosz, J. A. Carter, D. C. Fabrycky, E. B. Ford, J. J. Lissauer, A. Prša, S. N. Quinn, D. Ragozzine, D. R. Short, G. Torres, J. N. Winn, L. R. Doyle, T. Barclay, N. Batalha, S. Bloemen, E. Brugamyer, L. A. Buchhave, C. Caldwell, D. A. Caldwell, J. L. Christiansen, D. R. Ciardi, W. D. Cochran, M. Endl, J. J. Fortney, I. Gautier, Thomas N., R. L. Gilliland, M. R. Haas, J. R. Hall, M. J. Holman, A. W. Howard, S. B. Howell, H. Isaacson, J. M. Jenkins, T. C. Klaus, D. W. Latham, J. Li, G. W. Marcy, T. Mazeh, E. V. Quintana, P. Robertson, A. Shporer, J. H. Steffen, G. Windmiller, D. G. Koch, and W. J. Borucki, **481**, 475 (2012), arXiv:1204.3955 [astro-ph.EP] .

[2] B. J. Fulton, E. A. Petigura, S. Blunt, and E. Sinukoff, **130**, 044504 (2018), arXiv:1801.01947 [astro-ph.IM] .

[3] B. M. Tofflemire, tofflemire/saphires: Zenodo archive (2019).

[4] D. Foreman-Mackey, D. W. Hogg, D. Lang, and J. Goodman, **125**, 306 (2013), arXiv:1202.3665 [astro-ph.IM] .

[5] B. W. Carroll and D. A. Ostlie, *An Introduction to Modern Astrophysics*, 2nd ed., edited by S. F. P. Addison-Wesley (2007).

[6] M. R. Standing, L. Sairam, D. V. Martin, A. H. M. J. Triaud, A. C. M. Correia, G. A. L. Coleman, T. A. Baycroft, V. Kunovac, I. Boisse, A. C. Cameron, G. Dransfield, J. P. Faria, M. Gillon, N. C. Hara, C. Hellier, J. Howard, E. Lane, R. Mardling, P. F. L. Maxted, N. J. Miller, R. P. Nelson, J. A. Orosz, F. Pepe, A. Santerne, D. Sebastian, S. Udry, and W. F. Welsh, Nature Astronomy **7**, 702 (2023), arXiv:2301.10794 [astro-ph.EP] .

Manipulating DUNE Beam Parameters to Optimize Tau Neutrino Events

ERIC LEON

2023 NSF/REU Program
Department of Physics and Astronomy
University of Notre Dame

ADVISOR(S): Dr. Laura Fields

Abstract

The Deep Underground Neutrino Experiment (DUNE) at Fermilab is one of the most anticipated experiments in neutrino physics in the world [1]. DUNE will employ the Long-Baseline Neutrino Facility (LBNF) as its revolutionary neutrino beam to aid in its goals to detect and better understand neutrino properties. This study identified potential modifications to the LBNF that optimize the tau neutrino event rate by approximately 5%, thereby creating an improved data set to aid scientists in studying tau neutrinos. The LBNF engineering team will be able to utilize these modifications to build a more efficient beam to study tau neutrinos.

1 Introduction

Neutrinos are the least understood known particle in our current standard model. However, as the least understood particles, studying neutrinos provides a great potential leap in our understanding of the nature of the universe. DUNE is an upcoming flagship experiment at Fermilab whose primary objectives will be to study neutrinos, specifically by investigating why there is more matter than antimatter in the universe and what gives neutrinos their mass, as well as testing the three-neutrino model and beyond three-neutrino models [2]. This study took an interest in tau neutrinos. Tau neutrinos can help answer the questions that give credence to DUNE's objectives, and as the least observed particle, they have great potential for new discoveries. As of 2020, less than 20 confirmed tau neutrino events were recorded by the DONuT [3] and OPERA [4] experiments combined. Part of the DUNE mission is to increase this data set dramatically. This project looked at ranges of physical beam parameters to optimize the tau neutrino event rate to an order of approximately 1000 per year. To fully understand what DUNE is looking for and why it is so well-equipped to do so, one must first understand the neutrino and how our combined human ingenuity built over 60 years of neutrino research has led to one of its newest inventions.

1.1 Understanding the Neutrino

The neutrino belongs to a group of particles in the standard model called the Leptons. As shown in Figure 1, there are three types, or flavors, of neutrinos. Each flavor corresponds to either the electron, muon, or tau lepton. These particles are copiously produced in our universe. For example,

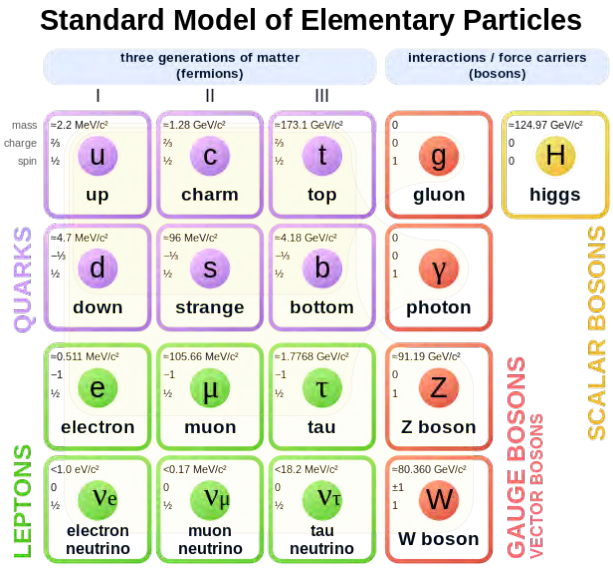

Figure 1: The standard model of particle physics, MissMJ et al [5]

electron neutrinos are mass-produced in the sun as a result of nuclear interactions. To demonstrate such an example, let us look at the decay of a neutron into a proton.

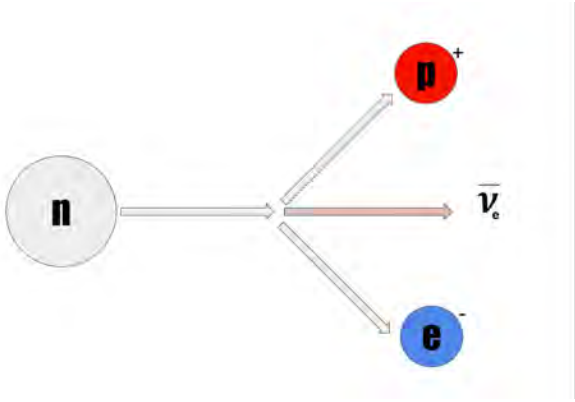

Figure 2: Simplified diagram of neutron to proton decay

Note that in Figure 2, charge is conserved with a net neutral charge on the left side of the interaction and a net neutral charge on the right side as the proton and electron charges cancel out.[i] The neutrino was first proposed as a solution to conserve energy and momentum in an interaction

[i]It should also be noted that in the standard model, interactions are mediated by particles called bosons (not depicted in the visual). Weak Force interactions are governed by charged W bosons and neutral Z bosons. This particular reaction requires a mediating W^- boson. Since this weak force interaction requires a W boson, it is considered a charged current (CC) event. If a weak interaction required the uncharged Z boson, it would be known as a neutral current (NC) event. For further details, see [6].

like this. After it was finally detected, it was observed to be a product of weak force interactions and obeys a conservation law known as lepton number conservation. The electron is assigned a lepton number of $+1$, and the antineutrino (denoted by the bar over the ν) is assigned a lepton number of -1, and thus cancel out, and lepton number is conserved. This example is only one of a practically infinite series of possible particle interactions, but it effectively demonstrates the role of neutrinos in weak force interactions.

There is more to say about the innate properties of the neutrino. The more massive a particle is, the less stable it will likely be. Muons are less stable than electrons, and tau leptons are the least stable of all. Unstable, high-energy states tend to decay into lower-energy configurations. Therefore, tau neutrinos are rarely found due to their unstable mass. This has caused very little progress to be made in our knowledge of these particles, thus providing a motivation behind studying them with DUNE.

The final relevant point to make about neutrinos reduces to a word that has gained much attention in particle theory, which is neutrino "oscillation." Much can be said about this phenomenon, but the general premise is that the three flavors of neutrinos are mixtures of three different mass states, commonly notated as ν_1, ν_2, and ν_3. These mass states evolve with time, effectively meaning that over a certain distance, a muon neutrino ν_μ, for example, could oscillate to become a tau neutrino ν_τ. This was my oscillation of interest in my research, but any other conceivable switch between flavors can occur. DUNE will search for more clarity on this phenomenon, such as what order the mass states actually occupy from lowest to highest. Understanding this will lead to an increased understanding of the mechanism that gives the neutrino its mass. Even though these curious properties have been a substantial hurdle to overcome in experiments, DUNE has employed several strategies to give scientists the best possible chance to observe and perform analysis on these particles.

1.2 Understanding DUNE

DUNE is what is known as a long-baseline experiment, which means that neutrinos have enough room after being created to go through oscillations even at their near-light speeds. Figure 3 provides

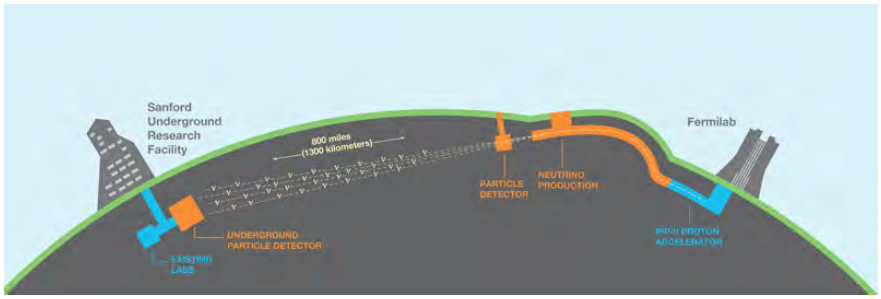

Figure 3: Visual of DUNE experiment, DUNE at LBNF [7]

a helpful visual for how DUNE is to be constructed. The particle beam will direct neutrinos to a set of detectors at the SURF (Sanford Underground Research Facility) in South Dakota about 1300 km from Fermilab. While detection is a difficult endeavor, producing neutrinos is straightforward. Figure 4 gives a general layout of the neutrino production beam. Protons are accelerated to have

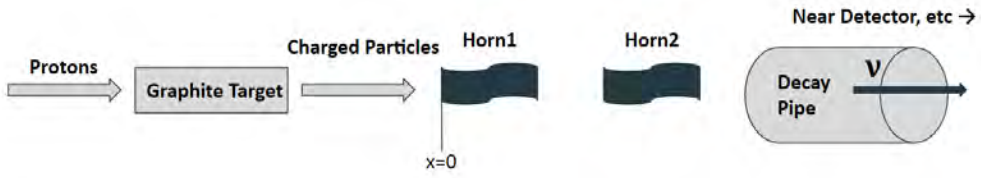

Figure 4: Neutrino Beam Configuration at LBNF (not to scale). $x = 0$ represents the relative point where the distance parameters are measured from

an energy of 120 GeV and collide with a graphite target. This collision creates many particles of different energies, but the focus was on those most likely to produce tau neutrinos. While the particles are charged and can still interact electromagnetically, magnetic horns direct them into a focused beam and are led down an empty tube called a decay pipe. Here, the charged particles decay, leading to the production of neutrinos. The charged particles that did not decay are filtered out with shielding, and the neutrinos go through a near detector at Fermilab to measure the composition of the beam before they have a chance to oscillate. Muon neutrinos with an energy of $> 3\,GeV$ [8]

can potentially oscillate to tau neutrinos and will then be received by the far detector at SURF to see the result of the oscillation.[ii]

2 Methods

The best method available to test the outcomes of these experiments is through simulation. The particle beam simulation (called G4LBNF) employs a Monte Carlo method to model particles going through the apparatus as described in figure 4.

The simulation is built using the Geant4 software [10], into which the geometries and materials of DUNE were imported, thus modeling how particles would interact with the experiment. Configuration files were required by the Geant4 simulation in order to customize the orientation of the LBNF components. A configuration to increase tau-neutrino flux was written previously, and it is upon this original file that this study began. It was required to write new configuration files with the desired geometries in order to isolate beam components and observe how changing certain parameters contributed to the final tau neutrino flux.

```
 9 #
10 /LBNE/det/Use1p2MW True
11 /LBNE/det/RemoveDecayPipeSnout True
12 #/LBNE/det/InstallShield False
13 /LBNE/det/InstallBaffle False
14 /LBNE/det/InstallUpstreamHorizontalTarget False
15 /LBNE/det/GraphiteTargetFinWidth 10.0 mm
16 /LBNE/det/GraphiteTargetLength 1.5 m
17 /LBNE/det/Horn2LongPosition 17.5 m
18 /LBNE/det/TargetLengthOutsideHorn .5 m
19 #
20 /LBNE/det/seHornCurrent 230 kA
21 #
```

Figure 5: Example of a neutrino beam configuration file

Figure 5 shows a portion of a configuration file. The numbers at the end of lines 15-20 represent the physical parameters that could be manipulated across a desired range.

[ii] The far detector at SURF is a Liquid-Argon Time Projection Chamber (LArTPC), the details about how these work will not be discussed here, but further details can be found in Diwan et al. [9]

The beam parameters of interest were as follows, (1) the target position with respect to the beginning of Horn 1 was changed from 0.5 m to 2.7 m. (2) The width of the graphite target was observed between 5 mm to 21 mm. (3) The horn current was tested between 200 kA and 300 kA. (4) The initial proton momentum ran from 60 $GeVc^{-1}$ to 130 $GeVc^{-1}$. (5) The Horn 2 longitudinal position, which is measured from the beginning of Horn 1 to Horn 2 was run from 8 m to 20 m. (6) Horn 1 length rescale, which was a global scaling factor lengthening Horn 1 was run from 0.5 to 2.1 (7) Horn 1 radial rescale, which was a global scaling factor that scaled the radius of the horn ran from 0.5 to 2.1 as well. Identical processes happened with the (8) Horn 2 length rescale and (9) Horn 2 radial rescale. These parameters were chosen based on the fact that they can be simply isolated and studied independently of one another.

In order to verify if the parameter change increased the tau neutrino flux, each G4LBNF simulation was run, and tau neutrino events were plotted as a function of the parameter range. If a modified parameter caused more tau neutrino events than the original beam configuration, it could be considered a potential improvement on the original beam design.

3 Results and Discussion

The following plots demonstrate which parameters had room for improvement to optimize the tau neutrino events as compared to the original configuration.

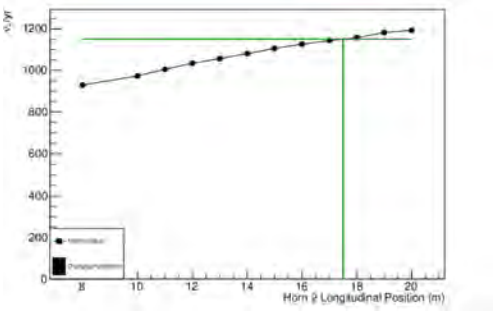

	Horn2LongitudinalPosition (m)	taus/yr
0	8	929.720826
1	10	973.316354
2	11	1005.193432
3	12	1034.344020
4	13	1056.694437
5	14	1080.394040
6	15	1105.710451
7	16	1126.692847
8	17	1143.000366
9	18	1157.745810
10	19	1181.880094
11	20	1192.823272

Figure 6: Plot for Horn 2 longitudinal position marked from the beginning of Horn 1 ($x = 0$) with the corresponding data table. The intersecting straight lines on the plot indicate the position and tau neutrino event rate of the original configuration. Everything $>$ 17.5 m is a more optimized configuration of the original design

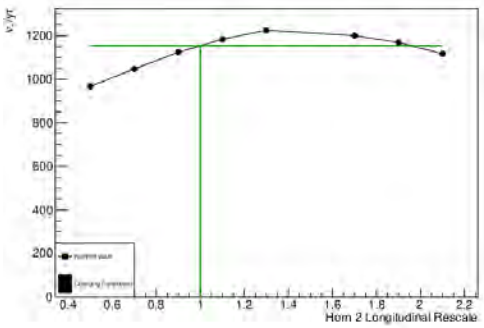

	Horn2LongRescale	taus/yr
0	0.5	967.427592
1	0.7	1047.153627
2	0.9	1123.245424
3	1.1	1182.690657
4	1.3	1224.189208
5	1.7	1199.462197
6	1.9	1168.216495
7	2.1	1115.950054

	Horn2LongitudinalRescale	taus/yr
0	1.3	1211.862811
1	1.5	1224.906579

Figure 7: Tau neutrino events per year vs. Horn 2 longitudinal rescale. Optimization appears at approximately 1.3 times the original length of Horn 2. Note that after a separate simulation shown below the original plot and table, the value 1.5 yielded more tau neutrinos than 1.3, but the value mirrors the 1.3 value of the previous simulation and thus can likely be attributed to a statistical artifact rather than an improved scaling factor. The final optimization configuration used 1.5.

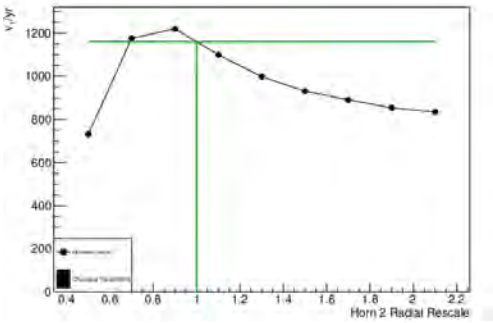

	Horn2RadialRescale	taus/yr
0	0.5	731.441989
1	0.7	1175.324719
2	0.9	1219.494011
3	1.1	1099.649114
4	1.3	998.198955
5	1.5	930.783450
6	1.7	890.665393
7	1.9	853.457881
8	2.1	834.552254

Horn2RadialRescale	taus/yr
0.9	1205.103154
1.0	1160.561734

Figure 8: Tau neutrino events per year vs Horn 2 radial rescale. Optimization occurs at about 0.9 times the original radius of Horn 2. Note that the original simulation did not include the point at scale = 1, but a follow-up simulation shown below the original plot and table found the point at 1 yielded approximately 4% fewer tau neutrinos than at 0.9.

Figures 6,7, and 8 suggest that an optimized tau neutrino beam should have the Horn 2 position be $\approx 20\,m$ from the beginning of Horn 1, and Horn 2 should be ≈ 1.5 times as long and ≈ 0.9 times as wide as its previous design. It was of interest to know if the potential improvements could be combined together to form one optimized configuration.

Figure 9 shows that the optimized beam configuration yielded a nominal difference in tau-neutrino flux compared to the original file. It is conceivable that the changes, when used all together,

(a) Original File (b) Optimized File

Figure 9: Comparison of original and optimized files

do not work together to dramatically increase the tau neutrino flux.

While the changes implemented together did not create the highest-optimized beam, the two independent changes that yielded the highest tau-neutrino flux were the Horn 2 Radial Rescale to 0.9, which yielded 1219 tau-neutrinos, and the Horn 2 Longitudinal Rescale to 1.5, which yielded about 1225 tau-neutrinos. These changes added approximately 60 tau-neutrinos to the original flux, which represents an increase of approximately 5% from the original configuration.

4 Conclusion

By manipulating Horn 2 to be 50% longer or 10% narrower, the DUNE far detector could potentially detect about 5% more tau neutrinos than it would have otherwise. This is a significant amount as this 5% represents roughly 60 neutrinos per year, and as of 2020, the tau-neutrino detection global total was around 20. When DUNE is built with these and future considerations, scientists will have a higher chance of accomplishing the goals of DUNE and thus improve our general knowledge of neutrinos and contribute to answering our deepest questions on the nature of the universe.

References

[1] B. Abi, R. Acciarri, M. A. Acero, G. Adamov, D. Adams, M. Adinolfi, Z. Ahmad, L. Fields, and J. A. et al., Deep underground neutrino experiment (dune), far detector technical design report, volume ii: Dune physics (2020), arXiv:2002.03005 [hep-ex] .

[2] P. Huber, K. Scholberg, E. Worcester, J. Asaadi, A. B. Balantekin, N. Bowden, P. Coloma, P. B. Denton, L. Fields, and A. de Gouvêa et al., Snowmass neutrino frontier report (2022), arXiv:2211.08641 [hep-ex] .

[3] K. Kodama, N. Ushida, C. Andreopoulos, N. Saoulidou, G. Tzanakos, P. Yager, and B. et al. (DONuT Collaboration), Phys. Rev. D **78**, 052002 (2008).

[4] N. Agafonova, A. Alexandrov, A. Anokhina, S. Aoki, A. Ariga, T. Ariga, A. Bertolin, and B. et al. (OPERA Collaboration), Phys. Rev. Lett. **120**, 211801 (2018).

[5] MissMj and Cush, Wikipedia (2023).

[6] J. Holdsworth, Beta negative decay (2007), available on "List of Feynman Diagrams" on Wikipedia next to "Beta Decay".

[7] Fermilab, DUNE at LBNF.

[8] P. Machado, H. Schulz, and J. Turner (DUNE Collaboration), Tau neutrinos at DUNE: New strategies, new opportunities (2020).

[9] M. Diwan, M. Potekhin, B. Viren, X. Qian, and C. Zhang, Journal of Physics: Conference Series **762**, 012033 (2016).

[10] CERN, Geant4, available at https://geant4.web.cern.ch.

Improving St. George Through Pressure Regulation of the HIPPO Gas Jet Target

WHIT LEWIS

2023 NSF/REU Program
Department of Physics and Astronomy
University of Notre Dame

ADVISOR(S): Prof. Manoel Couder

Abstract

The St. George recoil separator at the University of Notre Dame's Nuclear Science laboratory is employed with the study of reactions of astrophysical interest, specifically radiative capture reactions. St. George's High Pressure Point like gas jet target (HIPPO) is used to provide a constant diameter point-like target to the system. The thickness of the target observed by the beam depends on the injection pressure applied to the nozzle of HIPPO. Improvement to the pressure regulation of HIPPO has been studied and conclusions regarding the possible significant improvement of thickness stability of the gas target have been reached. Furthermore, recommendations regarding the permanent implementation of a more robust mass flow system and the possible benefits of implementing such a system are discussed.

1 Introduction

The Strong Gradient Electromagnetic Online Recoil separator for capture Gamma-Ray Experiment (St. George) at Notre Dame's ISNAP laboratory is an apparatus for study of reactions of astrophysical importance with the ability to separate reaction products from the beam. The energy as well as velocity are then measured, which allows for identification of the masses of the ions in the system and specifically that of the reaction products which can then be used to calculate the reaction rate. St. George takes advantage of inverse kinematics, in which a heavier ion is fired at a lighter target, to study lower energy astrophysical reactions by reducing the influence of the radiation background. ST. George's ion beam is made by the 5U Santa Anna accelerator, this beam bombards the High Pressure Point-like gas target. Following a reaction, the products (recoils) are then filtered by a series of dipole magnets as well as a Wien filter to allow for only the product of interest to enter the detector. The reaction rate is directly dependent upon the beam current, beam intensity, as well as the density of the gas target. St. George operates on relatively well understood principles to give high precision outputs of reaction rates [1]. To increase this precision further work is being done to decrease the thickness variability of the gas target. This work involves implementing a mass flow controller to decrease gas jet pressure fluctuation, producing a jet with more stable thickness.

2 Background

HIPPO uses a 3mm diameter converging diverging nozzle in conjunction with the differential pumping setup to create a localized supersonic jet of helium gas that serves as the target for the heavy ion beam. This setup provides a point like gas target with a thickness in the millimeter range that is well localized due to the differential pumping setup that forces the pressures to quickly descend back to the low vacuum of the surrounding beamline. This allows for a consistent target as the beam is largely unaffected by gas diffused into the surrounding beamline as well as the heating or bending of the gas jet. A further advantage of employing the supersonic gas jet is the small variance, aside from density, of the properties of the jet relative to inlet pressure [2]. Though there is little effect on the shape of the target with pressure, density of the target is dependent on injection pressure. Target thickness observed by the beam is therefore also dependent upon the nozzle injection pressure. Variance in the injection pressure varies the thickness of the target causing the reaction yield to have a tail since the cross section (which in this case is calculated from the measured yield) is dependent of the concentration of nuclei in the target. Though the reaction is first observed at the same energy regardless of target thickness variance, the variance in target thickness causes the reaction to occur across a wider spread of energies giving less resolution in the measurement of the resonance width. Assuming a uniformly flat cross section, the yield of the reaction is directly proportional to target thickness. Thus any improvement in the variation of the target thickness directly corresponds to the same improvement in variation of the yield. [3]

3 Methods

In setting out to improve HIPPO, a proof of concept test to ensure that pressures would be within the allowable range when adding flow regulation was performed. This test involved utilizing an existing needle valve to provide a constriction of flow to demonstrate that the variances in system pressure could be damped by restricting the orifice size. As this test proved successful, we chose to proceed with regulating injection pressure by use of of a mass flow controller. This was chosen

due to its ability to respond to the fluctuating pressures generated by the compressor due to its ability to give a nearly constant density output. Following this choice a proof-of-concept setup to ensure the mass flow controllers ability to regulate effectively at low pressures as well as low pressure differentials across the valve assembly was assembled. This setup involved building both the mounting plate that would later be used to mount the mass flow controller to HIPPO as well as the bypass assembly providing the ability to not utilize the mass flow controller. This setup proved that even after adjusting for the orifice correction (which due to the density difference between helium and nitrogen is a multiplier of 2.64 times), that the existing mass flow controller's throughput of 264 SCCM was inadequate to accommodate the 15 SLPM throughput of the HIPPO jet once adjusted for the orifice factor (unadjusted throughput for HIPPO is 40 SLPM or 2405 mBar m^3/h). This value is around thirty time smaller than the throughput of HIPPO which was found with the following orifice factors and equation for the Brooks 5851e mass flow controller:

$$\begin{aligned} Q_{Nitrogen} &= \text{ Nitrogen equivalent flow rate} \\ Q_{Gas} &= \text{ desired flow rate} \\ \text{(Orifice conversion of Helium)} &= .378 \\ Q_{Nitrogen} &= Q_{Gas} * \text{Orifice conversion of Helium} \end{aligned} \tag{1}$$

Despite this initial error, the mass flow controller proved successful in regulating the flow in sub atmosphere pressure ranges as well as with low pressure differential across the controller. Due to this success, we acquired a larger 80 SLPM Brook 5851e mass flow controller to be substituted for the existing controller. The new controller was then tested on the test stand to prove that it was able to adequately regulate flow at the volumes and pressures necessary. At this point some electrical abnormalities were noted, mostly regarding the zeroing, linearity of the flow control based upon input voltage, and span of flows reachable but these abnormalities were determined to not completely hinder operation. The setup was then mounted to HIPPO using the mounting plate. The existing piping was modified to incorporate this setup including relocating the needle valve to

provide the ability to isolate this segment of the system as well as a pressure sensor to give more accurate injection pressure readings. This full setup was then leak checked and a number of tests were run with various before mass flow pressures ranging from 500 to 1700 mBar as well as a range of injection pressures from 400 to 1300 mBar, both while utilizing the mass flow controller and utilizing the bypass. During this time adjustments to the settings of the mass flow controller were made to allow it to better suit the needs of injection pressure as well as improve stability. During this time data was taken using the DAQ to output pressures of gauges inside the re-circulation loop of HIPPO which was then processed using python. Results of initial tests were then used to guide further adjustment and testing. As these tests were winding down the mass flow controller experienced an electrical failure which despite extensive troubleshooting was unable to be solved, effectively ending this stage of the project.

4 Results

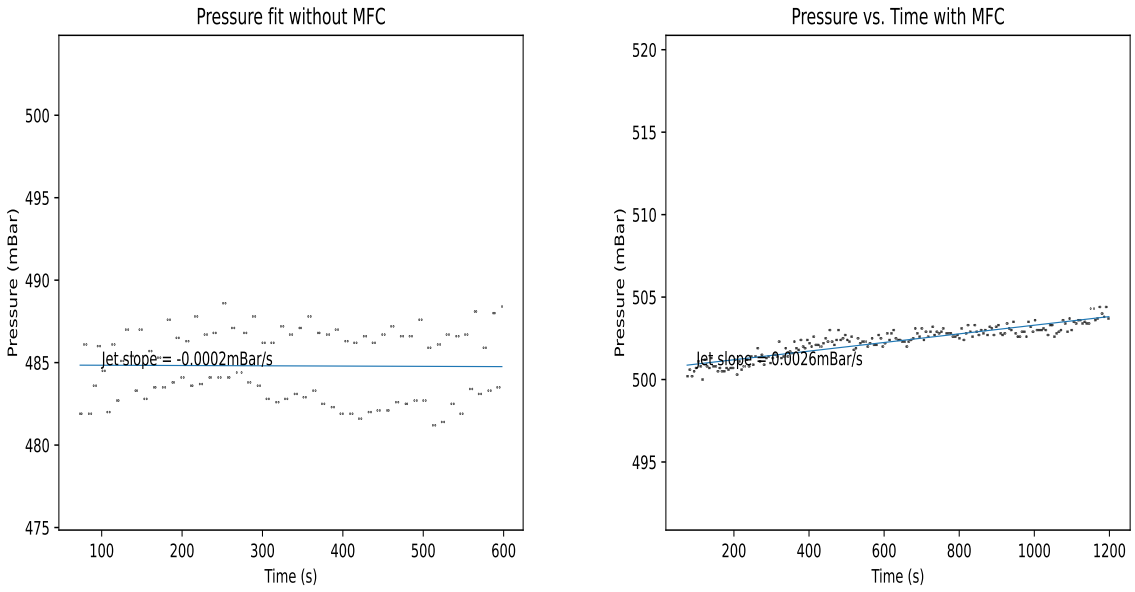

Figure 1: Scatter plot and fit of Injection gas pressures with and without the mass flow controller at pressures around 500 mBar

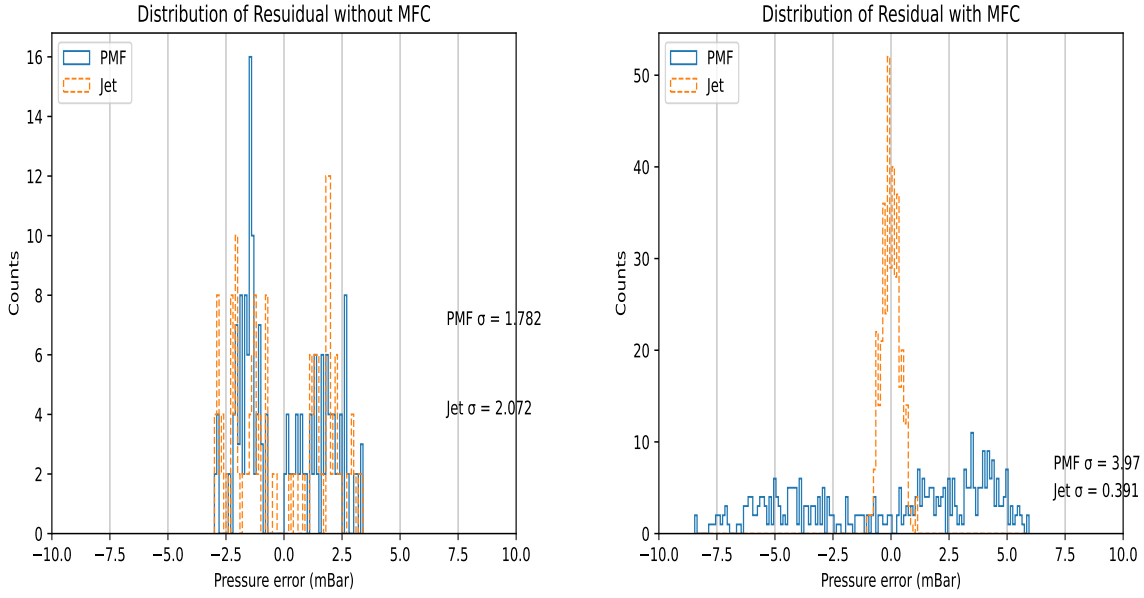

Figure 2: Histograms of the residual of the data in figure 1 with and without mass flow controller at 500 mBar incorporating pressure data from the Pre Mass-Flow Controller sensor (PMF) as well as injection pressure in which the residual is plotted to remove effects of heating and contamination.

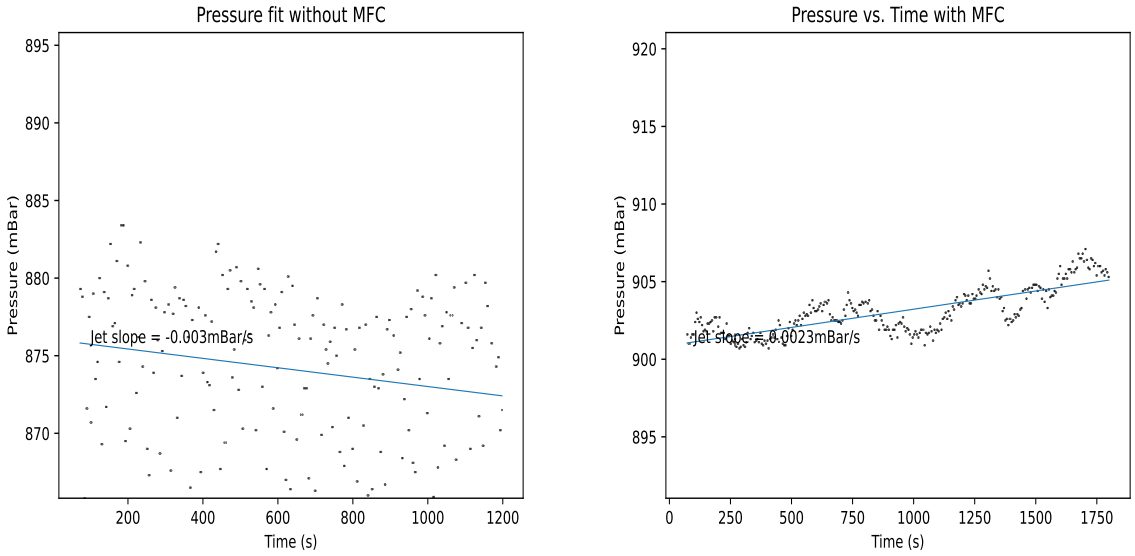

Figure 3: Scatter plot and fit of Injection gas pressures with and without the mass flow controller at pressures around 900 mBar.

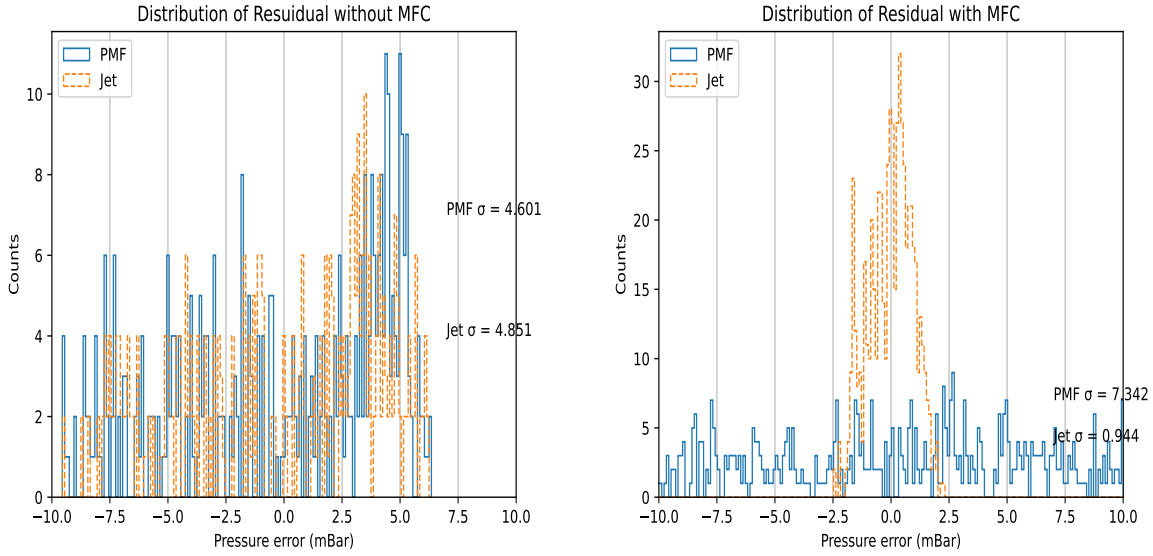

Figure 4: Histograms of the residual of the data in figure 1 with and without mass flow controller at 900 mBar incorporating pressure data from the Pre Mass-Flow Controller sensor (PMF) as well as injection pressure in which the residual is plotted to remove effects of heating and contamination.

Figures 1-4 clearly show a significant improvement of the distribution of injection pressure when the mass flow controller is in use despite the marked increase in the distribution of pressures before the mass flow controller that occurs due to the increase in the back pressure seen by the

pumps. At both pressures shown as well as pressures in the range of 500 – 900 mBar there is large improvement in the spread of the pressures. At 500 mBar without the mass flow controller the pressures occupy a range of 7.4 mBar compared to 4.4 mbar with the mass flow controller. This trend is also followed by the data in figure 3 in which the spread of pressures decreased from a width of 20.7 mBar to 6.4 mbar.

Jet Pressure avg (mBar)	PMF Pressure avg (mBar)	Ratio (PMF/Jet)	Jet σ (of residual)	PMF σ (of residual)	Jet Range (mBar)
1238.387	1339.693	1.082	7.335	7.433	34.0
1204.664	1307.516	1.085	7.075	6.961	34.0
910.601	1403.331	1.541	1.408	5.458	6.6
894.363	1408.15	1.574	1.354	5.397	8.0
899.391	1458.809	1.622	1.22	6.143	9.1
953.901	1698.083	1.78	2.22	6.861	10.8
957.847	1708.765	1.784	2.95	7.167	11.5
903.105	1668.276	1.847	0.943	7.381	6.4
910.172	1700.611	1.868	0.943	5.665	4.8
496.194	1022.238	2.06	0.376	3.643	1.9
502.413	1063.679	2.117	0.385	3.954	4.4
449.841	1313.351	2.92	2.95	9.708	30.6

Figure 5: The table above shows Pre Mass-Flow pressure vs Injection pressure ratios at various pressures as well as giving the injection pressure standard deviation width of the spread of pressures for each run.

This table shows that the standard deviation of the injection pressure is related to the ratio of the pressures that are seen before and after the mass flow controller. When the natural increase that occurs in standard deviation of the jet with greater injection pressures is considered it appears that the optimal ratio to minimize variance in pressures is in the range of 1.8 – 2.0 depending on the target injection pressure though there is too little data to make a conclusive statement.

5 Conclusion

Despite the untimely failure of the mass flow controller being used for this project, the data collected serves as a proof of concept for the future permanent implementation of a mass flow controller to regulate injection pressure. This is shown by the roughly eighty percent decrease in the standard deviation of the injection pressures residual. Given the assumption of a uniformly flat cross section it is likely that the standard deviation of the reaction yield could be decreased by a similar percentage. At minimum implementation would lead to a 40.5% decrease in yield uncertainty at 500 mBar and 69.1% decrease in yield uncertainty at 900 mBar following the decrease in the overall range of the injection pressures given the above assumption. In a permanent implementation of this setup with a properly calibrated mass flow controller it is likely that the variance of the pressure could be decreased even further reducing the uncertainty of the thickness of the gas target.

6 Acknowledgements

I would like to thank to professor Manoel Couder for serving as an excellent mentor for this work as well as the St. George research group. I would further like to thank the University of Notre Dame department of Physics, as well as the Notre Dame ISNAP laboratory, and the National Science Foundation for their support of the REU program. I would also like to thank professor Umesh Garg for coordinating the program. This research is supported by the National Science Foundation (NSF) under Grant No. PHY-2011890 and PHY-2050527.

References

[1] M. Couder, G. P. A. Berg, J. Görres, P. J. LeBlanc, L. O. Lamm, E. Stech, M. Wiescher, and J. Hinnefeld, Nucl. Instrum. Methods Phys. Res. A **587**, 35 (2008).

[2] A. Kontos, D. Schürmann, C. Akers, M. Couder, J. Görres, D. Robertson, E. Stech, R. Talwar, and M. Wiescher, Nucl. Instrum. Methods Phys. Res. A **664**, 272 (2012).

3] C. Iliadis, Nuclear physics of stars (Wiley-VCH Verlag, 2007) Chap. 4.8.

The St. Benedict Cooler-Buncher Commissioning

JIAJU LI

2023 NSF/REU Program
Department of Physics and Astronomy
University of Notre Dame

ADVISOR(S): Prof. Maxime Brodeur

Abstract

The St. Benedict project is under construction at the Nuclear Science Laboratory of the University of Notre Dame. This experimental device aims to test the Standard Model through the accurate determination of V_{ud}, the largest element of the Cabibbo-Kabayashi-Maskawa (CKM) matrix, which is used for the unitarity test of that matrix. St. Benedict is comprised of several major components that are required to perform such determination, including a radio-frequency quadrupole (RFQ) ion cooler buncher for cooling radioactive ion beams and creating ion bunches. As part of this project, we finalized the commissioning of this device.

1 Introduction

Probing for physics beyond the SM has been the focus of many researchers because it does not include several features such as gravity and dark matter and while not being able to explain the matter-antimatter asymmetry. One probing mechanism is the unitary test of the CKM matrix[1], which describes the relation between quark weak states and regular eigenstates. Non-unitarity of the matrix could lead to new physics like extra quark generation or could be simply caused by problematic experimental data or theoretical corrections. Consequently, all matrix elements, particularly the largest one, V_{ud}, need to be precise and accurate. There are four ways of extracting this element including pion decay, neutron decay, and superallowed pure Fermi beta decay, but at Notre Dame, we focus on the measurement of superallowed transitions between mirror nuclei. Recently, the Superallowed Transition Beta-Neutrino Decay Ion Coincidence Trap (St. Benedict) is under construction at the Nuclear Science Laboratory of ND, with for aim to improve the accuracy of the V_{ud} element via its determination in superallowed transitions between mirror nuclei[2].

2 St. Benedict

2.1 Motivation

The SM has been successful in explaining many physical experiments, but there are still many phenomena that it does not explain. The limitation of the SM may be probed by testing the unitarity of the CKM matrix. The most precise of such tests consists of taking the sum of the squares of three

first-row elements and seeing if it equals one. Our device, St. Benedict, is expected to obtain V_{ud} from superallowed transitions between mirror nuclei for more transitions than the current ensemble of 5[2].

Obtaining V_{ud} in these transitions relies on the determination of the Fermi-to-Gamow Teller mixing ratio, which at St. Benedict will be determined from the measurement of the beta-neutrino angular correlation parameter $\alpha_{\beta\nu}$. This parameter will be obtained from fitting the time of flight distribution of the daughter nuclei after a beta decay inside a Paul trap[2].

2.2 Components

St. Benedict consists of four main components: a gas catcher, an extraction system, a cooler-buncher, and a Paul trap. The radioactive ion beams (RIBs) received by St. Benedict are produced by the dual solenoid system *TwinSol* at the NSL[2].

The RIB will be produced by impinging a primary beam on a gas target and separating it using *TwinSol* after which it will pass through a 15° switching magnet before entering St. Benedict. The first part of St. Benedict, the gas catcher, is used to thermalize ions. The ions lose their energy by passing through a degrader and a thin window before getting thermalized via collisions with helium atoms at a pressure of about 0.1 atm[2]. Then, they are transported to the extraction system that includes two differentially-pumped chambers, the first uses an RF carpet, where the ion surfing method is used, and the second an RFQ ion guide. Prior measurements reveal that the transport efficiency of the RF carpet can reach about 100% under proper settings and about 50% of such ions can be transmitted successfully via the ion guide[2]. The role of the cooler-buncher, which my project mainly focuses on, is transforming the continuous RIBs into cooled bunches. This is achieved in a radiofrequency quadrupole divided into two regions, respectively for cooling and bunching. After the cooler-buncher, the ions are transported to the Paul trap where the measurement of $\alpha_{\beta\nu}$ takes place[2].

2.3 RFQ Cooler-Buncher Overview

The RFQ cooler-buncher is a crucial component that creates ion bunches, which allows measurement in the Paul trap. By having collisions with helium atoms, beams with energies of ∼200 eV can be cooled. The application of an electric field created by a potential decreasing gradually along the axis drags the ions down to a potential well where they accumulate. At the same time, the ions are confined radially using time-varying radiofrequency potential applied on four electrode poles. After some accumulation time, the potentials are changed abruptly and the accumulated ions are released rapidly as a bunch that is sent to the Paul trap. Additionally, the shapes of electrodes on the upstream side and downstream side have been specially devised, in order to maximize transport efficiency.

The RFQ rods are divided into several sections including electrode A, which is flared to better accept the beam, plus two regions, the cooling region with electrodes B, C, D, and E and the bunching region with electrodes from F to K, which can be explicitly seen in the potential scheme shown in Figure 1[1].

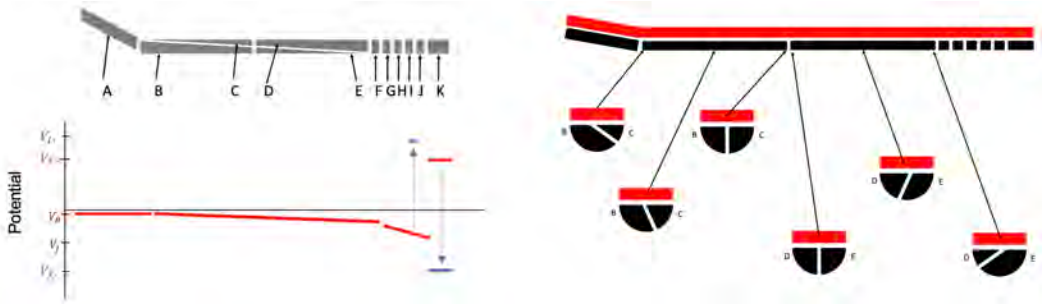

Figure 1: Left: Electrodes A-K of the cooler-buncher and their segmentation potential scheme for the accumulation and ejection of ions; Right: Schematic showing the crosscut running along electrodes B-E

The accumulation and ejection of ions use two potential schemes. During accumulation, the potential seen by the ions decreases gradually from electrodes B, C, D, and, E, and then changes in slope when they encounter electrodes from F to J, while the potential of electrode K is higher to form a well. The gradual reduction of potential, in the cooling section, is achieved via the crosscut shown in Figure 2. In the bunching section, on the other hand, each electrode is segmented

orthogonal to the beam axis. With appropriate potentials applied on these electrodes, the ions can be pulled forward slowly, cooling, and then accumulate around electrode J due to the blocking by the high potential of electrode K. For the ejection, all the potentials are maintained except for the potentials of electrode I and K. Suddenly, the potential of electrode K will decrease far lower than that of J and the potential of electrode I will be raised much higher so that all the accumulated ions can be released as a single bunch for measurement[1]. This is the working principle of the RFQ cooler-buncher. Each 50 ms time cycle includes an accumulation time (typically $t_{\mathrm{acc}} = 5\mu s$) when the beam gate is open, a holding time for ions accumulation (100μs), and an opening time for releasing the ions (200μs). To acquire more reliable data, such time cycles can be repeated several thousand times during one single scan.

3 Cooler-Buncher Commissioning

3.1 Off-line setup

The off-line commissioning of the cooler-buncher was performed with the installation of an off-line ion source on the injection side of it, and a Micro Channel Plate (MCP) on the ejection side to diagnose the ion beam. We used a potassium thermionic ion source to produce ions with a filament current of 1.51 A and we applied a potential of 200 V on that source. Potentials of the subsequent electrodes, including anode and lens, were kept at 193.5 V and 0 V separately[1]. Potential scans done this summer indicates that the ideal potential settings for MCP front plate, back plate, and anode are -2000 V, 0 V, and 200 V respectively. The signal from the anode of the MCP was sent to an SR430 multichannel scaler that also receives the trigger signal for the extraction and bin each event producing a TOF spectra. Based on the aforementioned setup, the aim of the commissioning was to determine the parameter setting for which the bunch contains the highest count, has the narrowest time width, and has the lowest levels of water and background contamination.

3.2 Commissioning Results

Through our tests, we proved that the RFQ cooler-buncher works well on cooling ions and producing bunches. A typical TOF spectra is given in Figure 2 from which we can see a high potassium peak located at about 4.3 μs and a much lower water peak at about 3 μs with nearly no background. This figure also indicates the TOF of $^{85}Rb^{+}$, which is only present for high RF amplitudes.

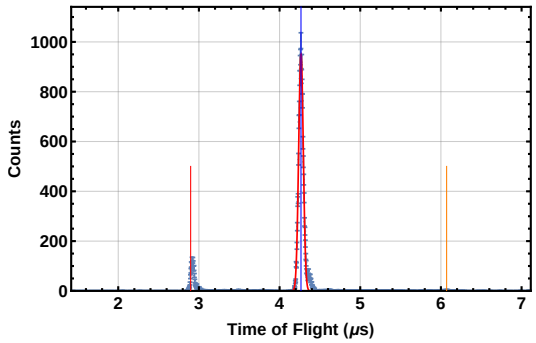

Figure 2: Typical TOF spectra with a Gaussian fit of the $^{39}K^{+}$ peak. The red and orange lines indicate water and possible $^{85}Rb^{+}$ peaks respectively.

As first scan, we varied the potential of the MCP pre-amplifier bias to investigate whether an increase in the potential results in spurious effects such as increased pile-up and double counting after due to pulses. As shown in Figure 3, we get the highest total number of counts when the pre-amplifier bias is at 12 V, the recommended voltage. The linear increase in the number of counts and constant FWHM observed indicates that increasing the potential does not cause such spurious effects.

Then, scans of the potential of the well depth V_{trap} were done to determine whether we could get potassium peaks with more counts and narrower widths. Figures 4 indicate that the FWHM drops quickly until $V_{\text{trap}} = 8$V and more slowly afterward. At the same time, the number of ions remains constant until 10 V before starting to drop. This drop is seen for $t_{\text{acc}} = 2$ and 5μs, which indicates that this drop is not due to an increase in pileup. Hence, we chose $V_{\text{trap}} = 8$V as the optimal setting for the subsequent tests.

Afterward, we did scans of the potential difference between adjacent segments of the bunching

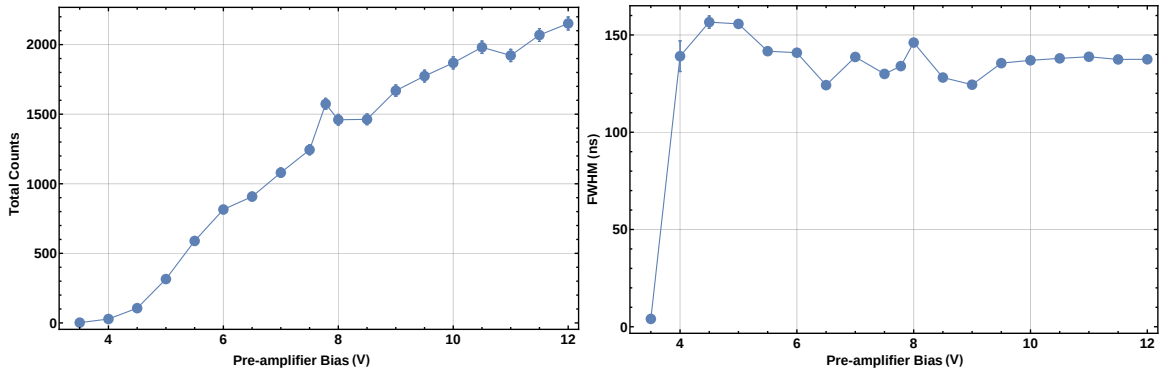

Figure 3: Total number of ions (left) and FWHM (right) as a function of the pre-amplifier bias

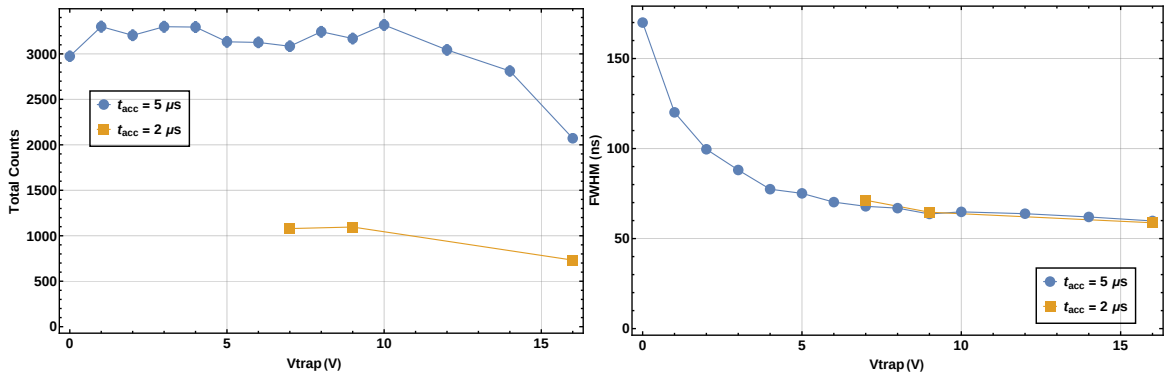

Figure 4: Total number of ions (left) and FWHM (right) as a function of the depth of the potential well V_{trap} for 2 and 5 μs accumulation time

section V_{bunching} and the electric field strength of the cooling section E_{drag}. The total number of ions as a function of these parameters is shown in Figure 5. An increase in V_{bunching} for both $V_{\text{trap}} = 4$ and 8V results in a rapid drop in counts for $V_{\text{bunching}} > 2$V and very little changes in counts with E_{drag} where seen. According to those scans, the best V_{bunching} and E_{drag} are 1.3 V and 0.2 V/m respectively. Additionally, not much effect of the two parameters on the FWHM was observed.

Next, we scanned the positive kick (from electrode I) $V_{\text{kick+}}$ and the negative kick (from electrode K) $V_{\text{kick−}}$ by maintaining identical values for both parameters first and then changing them one at a time. The results of the first scan are shown in Figure 6. As it can be seen, the stronger the kicking voltage, the narrower the ion bunch is. At the same time, the total number of ions extracted slowly increases until about $V_{\text{kick}} = 180$V. A similar behavior was observed when varying $V_{\text{kick−}}$ and $V_{\text{kick+}}$ independently.

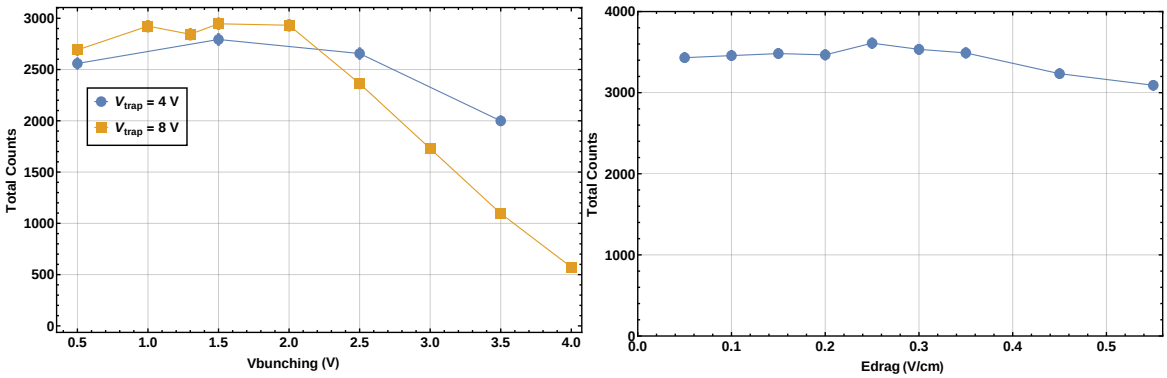

Figure 5: Left: Total number of ions for increasing potential difference between electrodes of the bunching section for two different potential well depth; Right: Total number of counts for the increasing electric field in the cooling section

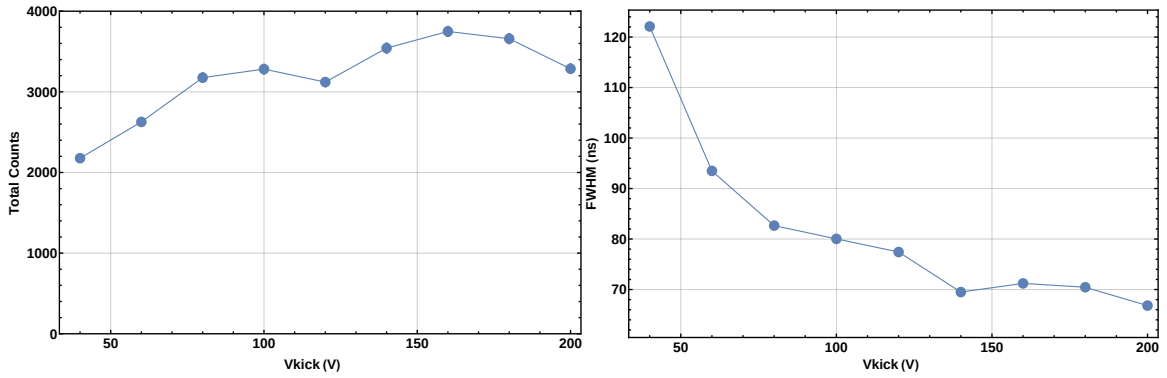

Figure 6: Total number of ions (left) and FWHM (right) for the increasing kicking voltage

After, setting the holding time at 1 μs, we scanned the pressure for two modes, DC (direct current) and bunching. As Figure 7 indicates, ions are insufficiently cooled when $p < 4 \times 10^{-3}$ torr to produce an ion bunch and when $p > 3.5 \times 10^{-2}$ torr the total number of ions per bunch does not change. A similar behavior is seen for the DC beam except some still get through at low pressure.

For the same purpose, scans of the gain of the injection-side of the RF generator were done with a 100 μs holding time under 6.46×10^{-2} torr pressure (shown in Figure 7). Generally, as the gain increases, the number of total counts increases and remains constant afterward. The efficiencies derived by taking the ratio in counts for bunching and DC show that we can reach over 90%, and the optimal setting for this was 18%, with the highest number of total counts and comparatively great bunching efficiency.

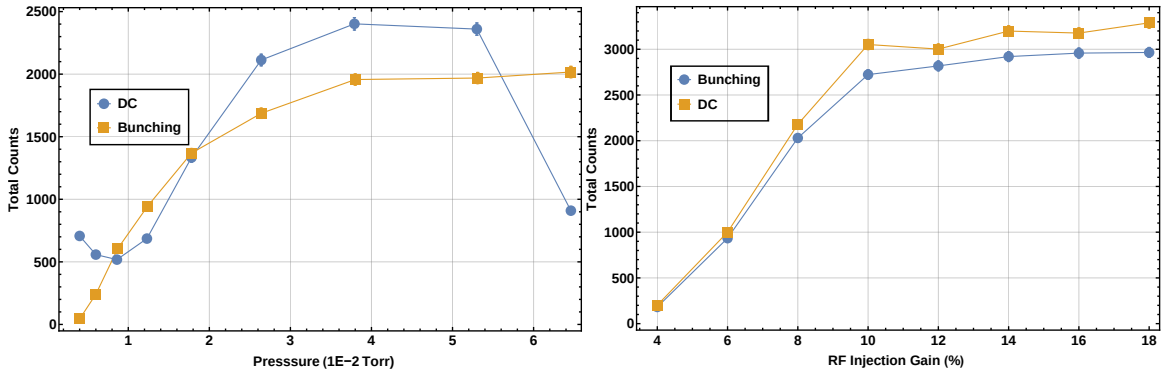

Figure 7: Total number of ions for the increasing gas line pressure (left) and RF injection gain (right)

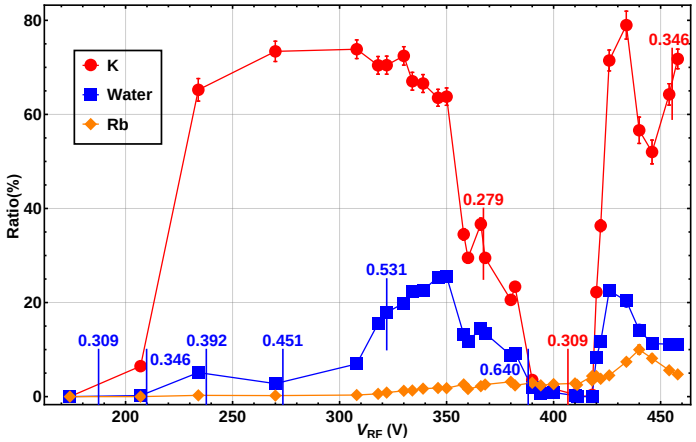

Figure 8: Ratio of the number of counts for a given specie in bunching mode over the number of counts in DC

Lastly, with the RF injection gain setting to 18%, we did scans of RF extraction gain for two modes, DC and bunching. For this scan, we observed large changes in an unexpected fashion of the total counts with the RF gain. However, this phenomenon could be explained by ion motion becoming unstable. The movement of ions within a quadrupole can be studied through the use of the stability parameter q. Theory predicts that in a plausibly stable range of q, there are still unstable points at different values of this parameter[3]. According to those q values, we calculated the corresponding RF amplitudes of water, K, and Rb in our situation and marked them as straight lines in Figure 8. We can see near the red markings, namely unstable settings of RF amplitude for potassium, the ratio of the counts in potassium peaks to total counts changes greatly, which can

explain the peculiar behavior. It would also explain the suppressed amount of water, unaffected $^{39}K^{+}$ for 230V $< V_{RF} <$ 320V. Additionally, it is consistent that $^{85}Rb^{+}$ was not affected by such instability for any RF amplitudes throughout our tests.

4 Conclusion

The testing of the Cooler-Buncher done this summer proved its effectiveness in cooling and bunching ion beams. Through our tests, optimal settings for some key parameters of the cooler-buncher have been found: $V_{trap} = 8$ V, $V_{bunching} = 1.3$ V, $E_{drag} = 0.2$ V/cm, $V_{kick\pm} = 180$ V, $p > 3.5 \times 10^{-2}$ torr, injection RF gain $> 16\%$ and ejection RF amplitude of around 275 V for $^{39}K^{+}$. In the future, four major components of St. Benedict will be combined together to finish the construction, and online commissioning of St. Benedict with ion beams from *TwinSol* will begin. After that, St. Benedict will be used to help test the Standard Model.

5 Acknowledgements

I would like to thank: Professor Brodeur for his help and this opportunity; graduate students Rey Zite, Sam Porter, and Fabio Rivero, and internship student Driss Guillet as well as Dr. Patrick O'Malley for their help and support; alumna of my home university and graduate student of Notre Dame, Biying Liu, for her help before I arrived here; and the Notre Dame REU program, Dr. Garg, and Ms. Amsler for making this summer research possible.

References

[1] A. A. Valverde, M. Brodeur, *et al.*, Hyper. Inter **240**, 38 (2019).

[2] M. Brodeur, T. Ahn, *et al.*, Nucl. Inst. Meth. Phys. Res. B **541**, 79 (2023).

[3] A. Drakoudis, M. Söllner, *et al.*, Int. J. Mass Spectrom **252**, 61 (2006).

Quantifying the Optical Band Gap of $Sn_{1-x}In_xTe$

TRISHA MUSALL

2023 NSF/REU Program
Department of Physics and Astronomy
University of Notre Dame

ADVISOR(S): Prof. Badih Assaf

Abstract

Topological superconductors have gained much excitement as they are highly applicable to fields like quantum computing. $Sn_{1-x}In_xTe$ is one such candidate topological superconductor, with attractive non-toxic, non-radioactive properties. In this project, we quantify the optical band gap, E_o, of $Sn_{1-x}In_xTe$ using Fourier transform infrared spectroscopy and examine how this gap changes with varying indium content ($0 \leq x \leq 0.30$) and temperature. We find that E_o increased with both indium content and temperature. However, this increase in E_o, and consequently in carrier density, is not enough to explain the large increase in previously-obtained Hall densities. As such, this research provides concrete evidence of an indium impurity band that enhances carrier densities, formerly only theorized to exist. This work informs our understanding of the normal state properties of $Sn_{1-x}In_xTe$, which is highly useful in the material's quantum computing applications.

1 Introduction

Band structure — simply defined as the structure of the valence and conduction bands and the energy gap in between them — determines what materials are classified as insulators, semiconductors, and conductors. For one, insulators have a large energy gap between their valence and conduction bands, thus decreasing the likelihood of an electron participating in conduction. Conversely, semiconductors' band gaps are much smaller while conductors do not have a band gap at all. Thus, band structure offers a useful way of identifying a material's conducting properties, which is especially important in discussion of candidate superconductors such as our material of interest, $Sn_{1-x}In_xTe$.

The band gap presents a "forbidden" energy region for electrons: in order for an electron to be excited from the valence band to the conduction band, it must absorb a photon of equal or greater energy than the energy gap, E_g. Any photon of lesser energy than E_g will fail to excite an electron, thus rendering the material optically "transparent" at said photon's energy. As such, by measuring the energy at which light is increasingly absorbed and the material becomes "opaque" — referred to as the absorption edge — one can quantify E_g using optical instruments. Fourier transform infrared spectroscopy (FTIR) is one such tool. One can mark the band gap by passing light of various wavelengths through a sample and analyzing the corresponding transmission spectra.

It is then important to distinguish between the band gap obtained through optical measurements,

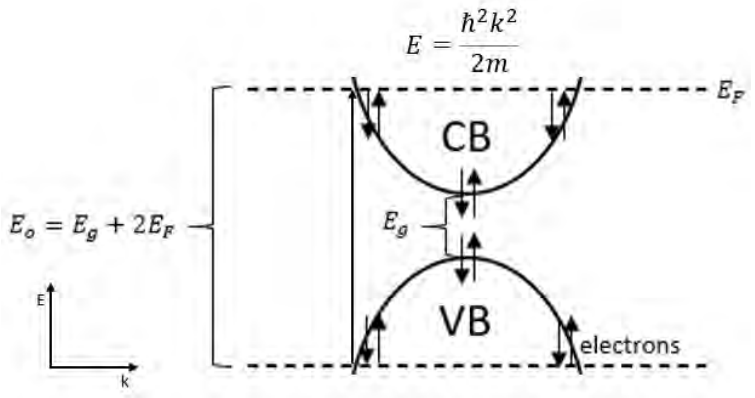

Figure 1: E-k diagram of parabolic band structure, with VB and CB representing the valence and conduction bands, respectively.

E_o, and the true band gap, E_g. There are certain instances where the two values are different. In this work, adding indium to SnTe can increase the number of free electrons, which then occupy states in the valence and conduction bands, as shown in Figure 1 [1]. This effect, called the Moss-Burstein shift, results in a larger value of E_o than E_g. By assuming that the true band gap, E_g, remains constant, we can then use the following relationship to calculate the Fermi energy (energy difference between occupied and unoccupied states), E_F:

$$E_o = E_g + 2E_F \tag{1}$$

For a material with an ellipsoidal Fermi surface such as SnTe, we get two different Fermi wave vectors:

$$k_1 = \sqrt{\frac{2m_t^v E_F}{\hbar^2}} \tag{2}$$

and

$$k_2 = \sqrt{\frac{2m_l^v E_F}{\hbar^2}} \tag{3}$$

where m_t^v and m_l^v refer to the transverse and longitudinal effective masses in the valence band,

respectively. From there, we can calculate the free electron density:

$$n = \frac{k_1 {k_2}^2}{3\pi^2} \tag{4}$$

and thus compare the n values calculated from optical measurements to carrier density values obtained via Hall measurements.

Here, I examine how the optical band gap of candidate topological superconductor $Sn_{1-x}In_xTe$ changes as a function of indium doping content ($0 \leq x \leq 0.30$) and temperature. $Sn_{1-x}In_xTe$, a semiconductor that turns superconducting below critical temperature T_c when alloyed with indium, is both non-toxic and non-radioactive, and thus holds much promise as a topological superconductor. Previously, in order to explain the significant enhancement of charge density as indium content increases [2] [3], an indium impurity band between the valence and conduction bands has been assumed to exist, though not much about the specific role of indium is known. This research — in conjunction with preexisting Hall measurements — further evidences the existence of this impurity band. These studies are important in understanding the changes in the band structure of $Sn_{1-x}In_xTe$; as such changes can drive the superconductivity of $Sn_{1-x}In_xTe$, understanding them is integral in the material's use in potential applications like quantum computing [3].

2 Methods

2.1 Fourier Transform Infrared Spectroscopy

Fourier transform infrared spectroscopy (FTIR) is a common method utilized for quantifying the optical band gap of a material. The instrument works by passing light of various wavelengths through a series of mirrors, one of which is moving (Figure 2) [4]. This moving mirror periodically blocks/transmits each wavelength of light. The light then passes through the sample of interest, and the corresponding absorption/transmission spectrum is inverted via Fourier transform to absorption/transmission as a function of wavenumber (cm^{-1}). By measuring the point at which a

material's transmission drops drastically, or the absorbance edge, one can locate the corresponding wavenumber and thus energy of said point. FTIR proves to be an effective way to estimate the optical band gap.

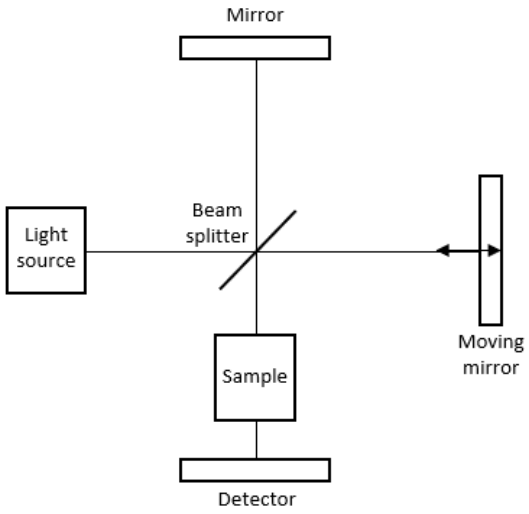

Figure 2: Setup of FTIR.

The setup can then be modified for low temperature experiments by inserting a cryostat into the chamber containing the incident beam, placing the sample of interest inside the cryostat, and cooling the instrument using liquid helium. In this work, we cool to temperatures as low as 4K.

2.2 Relative Transmission and Absorption Edge

The first technique used to evaluate the optical band gap of $Sn_{1-x}In_xTe$ at room temperature was through relative transmission. Given that $Sn_{1-x}In_xTe$ is grown on a substrate of BaF_2, in order to isolate the transmission spectrum of the material itself, one must look at the relative transmission: the transmission of the sample ($Sn_{1-x}In_xTe$ grown on BaF_2) divided by the transmission of the substrate alone (BaF_2).

In an ideal semiconductor, the absorption edge presents itself as a step function. Here, as in Figure 3(a), imperfections in the material cause the edge to take place over some range of wavenumbers. Finding the midpoint of the absorption edge and then the corresponding energy gives an estimation of the optical band gap of the material. The uncertainty value was obtained by taking the first

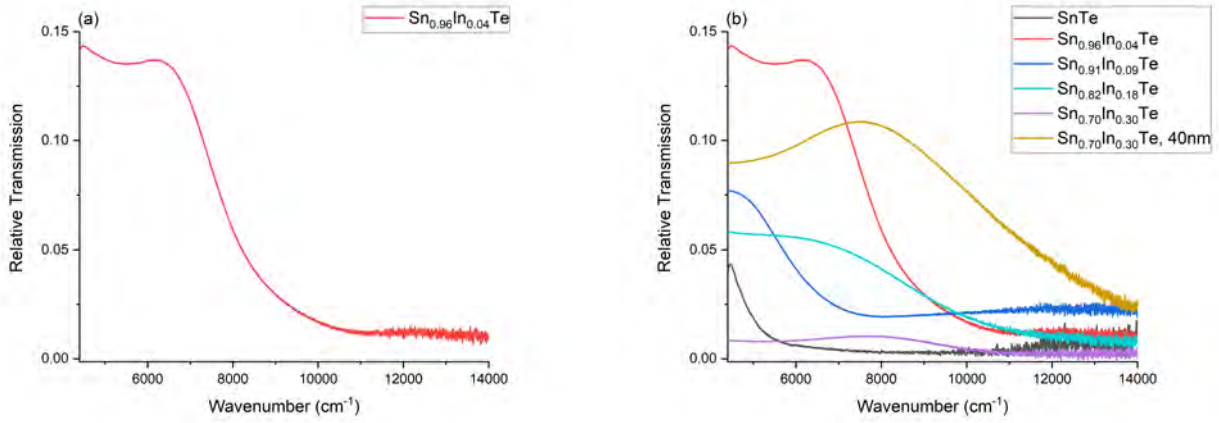

Figure 3: (a) Example absorption edge in relative transmission at room temperature, with a midpoint at 7400 ± 615 cm^{-1}, or 919 ± 76 meV. (b) Relative transmission data for samples of $Sn_{1-x}In_xTe$ at room temperature.

derivative of the absorption edge, applying a Gaussian fit, and taking the standard deviation to be a reflection of the width of the step.

2.3 Tauc Plot

The absorption coefficient, defined as:

$$\alpha = -ln(\frac{T_{sample}}{T_{substrate}}) \tag{5}$$

(where T_{sample} and $T_{substrate}$ are the transmission spectra of the sample and substrate, respectively) is the first step in a second method for finding E_o. For semiconductors with a parabolic dispersion such as SnTe, $\alpha \sim E^{-1/2}$, so plotting $(\alpha E)^2$ vs E and applying a linear fit to the resulting Tauc plot gives an approximation of the optical band gap [5].

It is important to note that the Tauc plot method tends to underestimate the energy gap, specifically at room temperature. We took the mean of two values — the x-intercept of the linear fit and the intercept of the fit with the adjusted baseline, as shown in Figure 4(a) — to be an estimation of the optical band gap at room and low temperature, and took the standard deviation to be the uncertainty value. This takes into account the uncertainty introduced by an unknown background

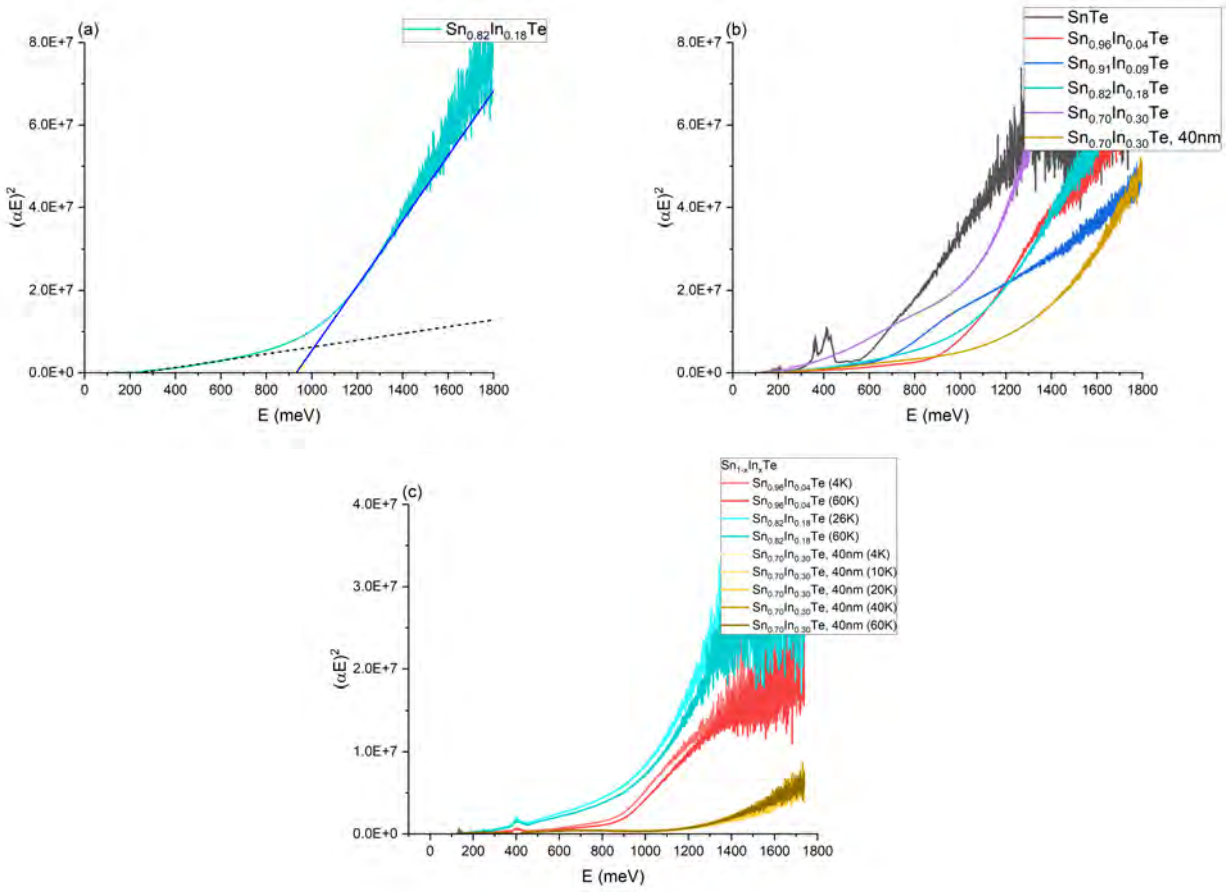

Figure 4: (a) Example Tauc plot. Here, the x-intercept of the top linear fit, shown in blue, gives an optical band gap of 932 $\pm$ 2 meV, while the intercept of the linear fit with the adjusted baseline, shown in black, gives 1013 $\pm$ 3 meV. (b) Tauc plot data for samples of $Sn_{1-x}In_xTe$ at room temperature. (c) Tauc plot data for samples of $Sn_{1-x}In_xTe$ at low temperature.

and changing baseline, as seen in Figures 4(b,c).

3 Results and Discussion

3.1 Indium Content

By varying the indium content x, we examined the effect of indium on the optical band gap of $Sn_{1-x}In_xTe$, as shown in Figure 5(a). With the Tauc plot results specifically, there was an increase in E_o as doping increased. This was the expected result: when indium is introduced into SnTe, more free electrons are added into the system. These free electrons end up occupying states in

the valence and conduction bands, increasing the Fermi energy and the amount of energy needed to excite an electron from band to band. This increase in the optical band gap is thus due to the Moss-Burstein shift.

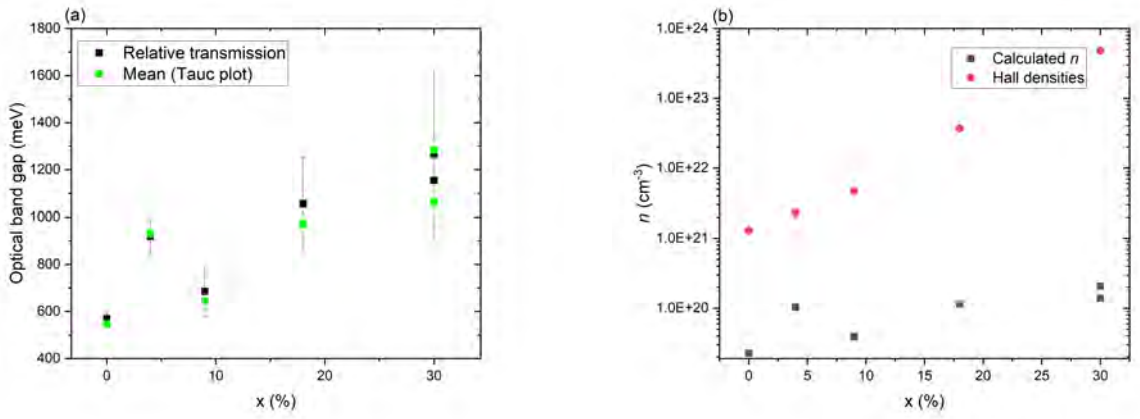

Figure 5: (a) Measured optical band gap of $Sn_{1-x}In_xTe$ as a function of indium content at room temperature. (b) Calculated carrier densities n and carrier densities obtained through Hall measurements.

We then used Equations 1 through 4 to calculate the corresponding carrier density for each sample. We took E_g to be 330 meV, $m_t^v = 0.107m_e$, and $m_l^v = 0.424m_e$, based off literature values for SnTe [6] [7], and compare the carrier densities obtained through our optical measurements to those previously acquired through Hall measurements [3] in Figure 5(b). These calculations operate under the assumption that indium acts as a dopant and does not change the band structure of the material. However, the Hall densities prove to be much higher than the carrier densities calculated here, evidencing that a change in the structure of the valence band — likely an indium impurity band — does indeed occur. This impurity band would give rise to the enhanced Hall densities, and higher values of T_c, previously measured [3].

3.2 Temperature

We then examined the effects of temperature on the optical band gap of samples of indium content $x = 0.04$, 0.18, and 0.30, both at room and low temperature. With the Tauc plot results specifically, we see a slight increase in E_o between low and room temperature values.

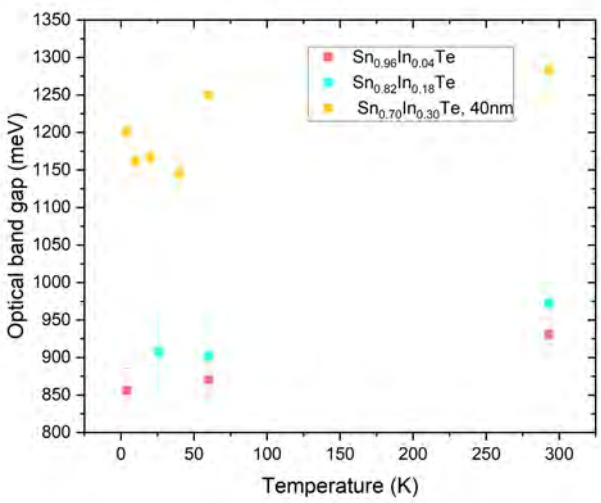

Figure 6: Mean Tauc plot value of optical band gap of $Sn_{1-x}In_xTe$ as a function of temperature.

Most importantly, the same relationship between indium content and optical band gap seen at room temperature, where E_o increases with x, is reflected in the low temperature data. This change in energy gap with indium content is significantly larger than that of the energy gap with temperature, emphasizing the dominant role indium plays in the band structure of $Sn_{1-x}In_xTe$. This further suggests the existence of an indium impurity band.

4 Conclusions

This study offers a look into the changes in the optical band gap of topological superconductor $Sn_{1-x}In_xTe$. We have found that E_o increases as indium content increases, both at room and low temperature, reflecting the Moss-Burstein shift. E_o increases only slightly with increasing temperature, suggesting that any temperature-dependence of the energy gap is dominated by the role of indium. Most importantly, the carrier density calculated from the experimental optical band gap values is much lower than the carrier densities previously obtained through Hall measurements. This implies the existence of an indium impurity band between the valence and conduction bands, which gives rise to the enhanced charge densities seen in the Hall measurements [3]. Previously, the indium impurity band in $Sn_{1-x}In_xTe$ was hypothesized to exist but had not been measured [2].

This research thus provides novel information about the role of indium in $Sn_{1-x}In_xTe$ and its effects on the material's structure and properties.

Acknowledgments

I would like to thank my mentor, Prof. Badih Assaf, and the rest of the Assaf Group for their guidance and aid throughout the experience. Moreover, thank you to Dr. Garg and Kristen Amsler for organizing the REU, my fellow members of the program for their support, and to the NSF PHY-2050527 grant for funding this opportunity.

References

[1] Z. M. Gibbs, A. LaLonde, and G. J. Snyder, New Journal of Physics **15**, 075020 (2013).

[2] A. S. Erickson, *Pairing Mechanisms in Superconductors with Valence-Skipping Dopants*, Ph.D. thesis, Stanford University (2009).

[3] J. Wang, W. Powers, Z. Zhang, M. Smith, B. J. McIntosh, S. K. Bac, L. Riney, M. Zhukovskyi, T. Orlova, L. P. Rokhinson, Y. T. Hsu, X. Liu, and B. A. Assaf, Nano Letters **22**, 792 (2022).

[4] N. Birkner and Q. Wang, Chemistry Libre Texts .

[5] X. Liu, J. Wang, L. Riney, S. K. Bac, D. J. Smith, M. R. McCartney, I. Khan, A. Hoffman, M. Dobrowolska, J. Furdyna, and B. A. Assaf, Journal of Crystal Growth **570**, 126235 (2021).

[6] Y. W. Tung and M. L. Cohen, Physical Review **180**, 823 (1969).

[7] R. L. Bernick and L. Kleinman, Solid State Communications **8**, 569 (1970).

Proton-Emission Resonance Levels in ^{11}B

NICHOLAS RADEN

2023 NSF/REU Program
Department of Physics and Astronomy
University of Notre Dame

ADVISOR(S): Dr. Wanpeng Tan

Abstract

A narrow near-threshold proton resonance in ^{11}B was proposed near E_x=11.44 MeV to explain the branching ratio discrepancy of ^{11}Be→^{10}Be. The proton resonance was thought to enhance the β-delayed proton emission in ^{11}Be and leads to a larger than expected decay branch to ^{10}Be. The reaction ^{7}Li(α,p)^{10}Be was performed using the FN accelerator at ISNAP in the University of Notre Dame to search for the resonance. A range of energies were tested with a focus on the hypothetical excitation value. After the conclusion of the experiment and analysis of the data, there seems to be no resonance level at the indicated value nor any other unknown resonance in the aforementioned energy range though there were unreported triton decays found at higher energies. A more thorough study of the α angular distribution or an approach that would detect a proton resonance width only would be of benefit to this decay. Otherwise, the ^{11}Be→^{10}Be decay would require some form of exotic decay to explain it and with it comes the potential for new physics.

1 Introduction

Proton emission is a form of decay like any other but becomes very interesting with respect to ^{11}B and ^{11}Be. The decay moves a nuclide south on the Chart of Nuclides as it loses a proton. Due to the positioning of ^{11}B on the chart, proton emission causes a decay to a more unstable state, ^{10}Be. The main interest of this decay stems from the β-delayed proton emission of ^{11}Be in which it first undergoes β-decay to ^{11}B which then emits a proton to become ^{10}Be. Since ^{10}Be has a high probability of undergoing β decay, that mechanism is not of much interest to us. The second mechanism of the decay to reach ^{10}Be, however, is what was investigated as there are many curious properties about it.

The most stand-out quality of the β-delayed proton emission of ^{11}Be would be the branching ratio. A branching ratio is essentially the percentage chance that a particle will decay in a certain way. Past experiments have found the branching ratio of ^{11}Be(βp)^{10}Be to be orders of magnitude higher than what theory predicts [1]. This is believed to be because of an unknown resonance level in ^{11}B for proton emission. Should this be the case, there would be an explanation for the branching ratio. But there is a chance that no protons are observed which could point to some other exotic form of decay or an issue with the theory. Should we be unable to explain the amount of ^{10}Be, we

would be led to new physics. In order to attempt to observe this resonance level, a bunched beam of α particles was accelerated onto a thin film of ^{12}C which had natural Lithium deposited onto it.

2 Background

Within nuclear physics are many different forms of decay. A β^- decay is when a neutron becomes a proton while also producing an electron and an anti electron neutrino. This is caused by one of the three quarks within a neutron changing its flavor via the weak force. So after ^{11}Be goes through β-decay, a neutron becomes a proton and ^{11}Be becomes an excited ^{11}B, which is denoted as ^{11}B*.

Another decay is proton emission which is as simple as it sounds. If the nucleus is at a high enough energy, it is capable of emitting a proton as a form of radioactive decay. But due to the strong nuclear force, a certain amount of energy is required to eject the proton unlike other types of decay which can occur at the ground state. So in the β-delayed proton emission, ^{11}Be decays into ^{11}B* which is at an energy level above the proton emission threshold which allows it to decay to ^{10}Be.

The reaction focused on in this study is ^{7}Li(α,p)^{10}Be. Specifically, a bunched beam of α particles, ^{4}He, will be fired onto ^{7}Li in order to produce ^{11}B* so we can check for proton emission. We are searching for a resonance in the energy levels, a level where there is a dramatic increase in the number of decays. The supposed resonance energy level is located around 11.44$\pm$0.04 MeV [2]. And so the beam energy will be tuned to reach this energy level but other known energy levels and branching ratios will be tested as well to verify the process. To find the energy the beam should be fired at, we just use energy and mass conservation using the energy and mass equivalent

$$E_{4He} + E_{CM} + E_{7Li} = E_{11B} + E^*_{11B}$$

$$E_{CM} = E_{11B} + E^*_{11B} - E_{4He} - E_{7Li}$$

$$T_{4He} = E_{CM}\frac{E_{7Li} + E_{4He}}{E_{7Li}}$$

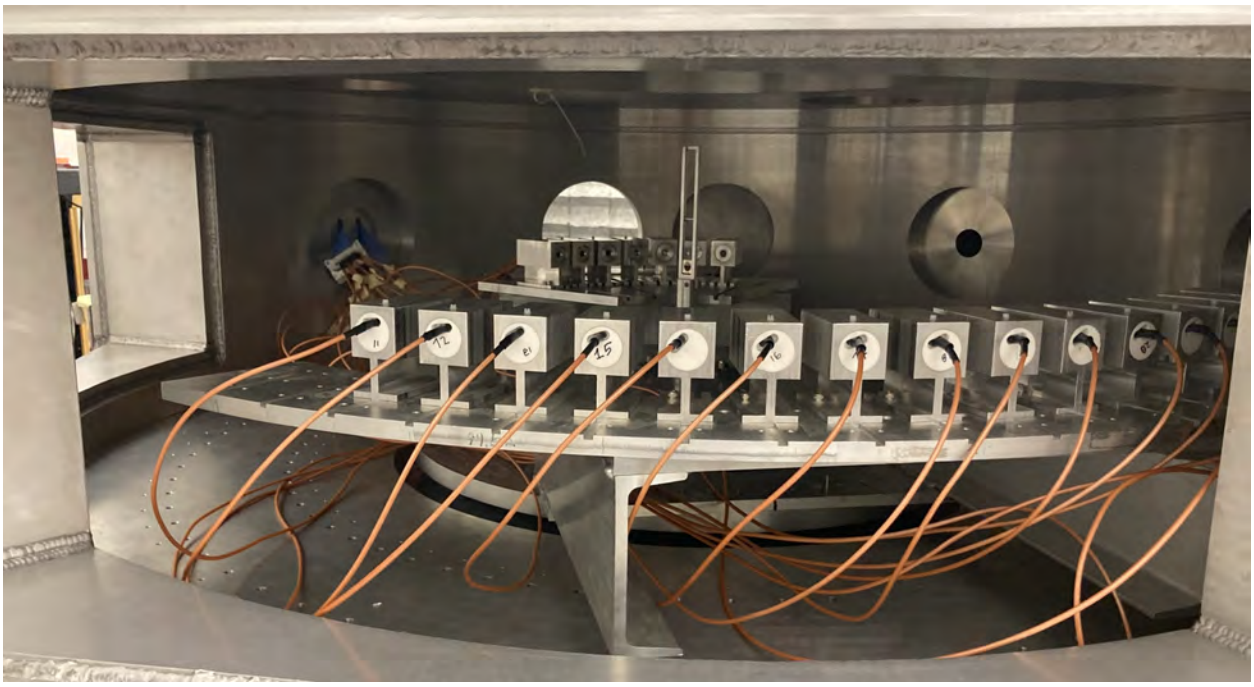

Figure 1: Inside of R2D2 at ISNAP with all 22 silicon detectors and the target ladder in place

where E represents the rest mass of the isotope, E_{cm} is the center of mass energy, T is the kinetic energy and E^* is the excitation energy of $^{11}B^*$. In this case, T_{4He} would be the beam energy as that is the kinetic energy of the α particles being accelerated.

3 Experimental Setup

To examine the proton emission of $^{11}B^*$, a bunched beam of α particles is accelerated onto a thin foil of $^{12}12$ which has ^{7}Li on top of it. For the α source, the HIS (Helium Ion Source) was used to produce the α particles. Bending and focusing corrections are made along the way as the particles travel to the accelerator. They then arrive at the FN Tandem accelerator wherein the energy was varied to test the different excitation levels of ^{11}B. The particles are then accelerated to the target and while travelling, the beam is bunched. Because the beam is bunched, we are capable of time of flight calculations which prior experiments were not capable of.

To make the targets, first a carbon foil with a thickness of 20 $\mu g/cm^2$ was placed on a collimator to act as a backing. Then, natural lithium was evaporated and then deposited onto the

carbon backing. Two different target thickness were made, one being 100 μg/cm^2 and the other 10 μg/cm^2. Because natural lithium and not enriched lithium-7 was used, there was some slight lithium-6 contamination. In addition to the lithium-6 contamination, the targets were not able to enter an evacuated chamber immediately and it took time to evacuate the chamber once they were in. This led to the lithium oxidizing and forming Li_2O on the surface of the target. There was also exposure to moisture in the atmosphere but that was minimized by placing the lithium in a desiccator but there are still possible contaminants.

The scattering itself takes place in a setup known as R2D2. R2D2 is essentially a large vacuum chamber with two concentric tables, one upper and one lower. Both tables can be rotated independent of each other and due to the size of the chamber, it is well suited for measuring time of flight. The lithium targets were placed on the target ladder after the detectors had been setup and calibrated. For the detectors, 22 silicon detectors were used as seen in the figure. 15 were placed in the forward angle from 20 degrees to 90 degrees and 7 were placed in the back angle from 90 degrees to 150 degrees. In order to calibrate, a mixed alpha source of americium-241 and gadolinium-148 was placed in the chamber and multiple runs were performed to get the correct calibration for the DAQ program. For the DAQ a Meystec digital acquisition system was used with an mdpp-16 digitizer.

4 Data and Analysis

For this experiment, there was a total of 48 separate runs but some were at the same energy. There also exist some runs whose purpose was to characterize certain particle identification curves by using the thicker target or a plain carbon backing. By doing this, it is possible to identify the carbon and oxygen curves along with any other products we are not looking for. For the preferred thin targets, 17 runs were had with energies ranging from 6.1 MeV to 4.28 MeV. Larger steps were used at higher energies and smaller steps at lower energies as the low energy range is where the supposed resonance level is. The actual excitation energy of ^{11}B from the reaction ranged from 12.548 to 11.389 MeV.

Seeing as the higher energy levels are well documented and that a thicker target will better show

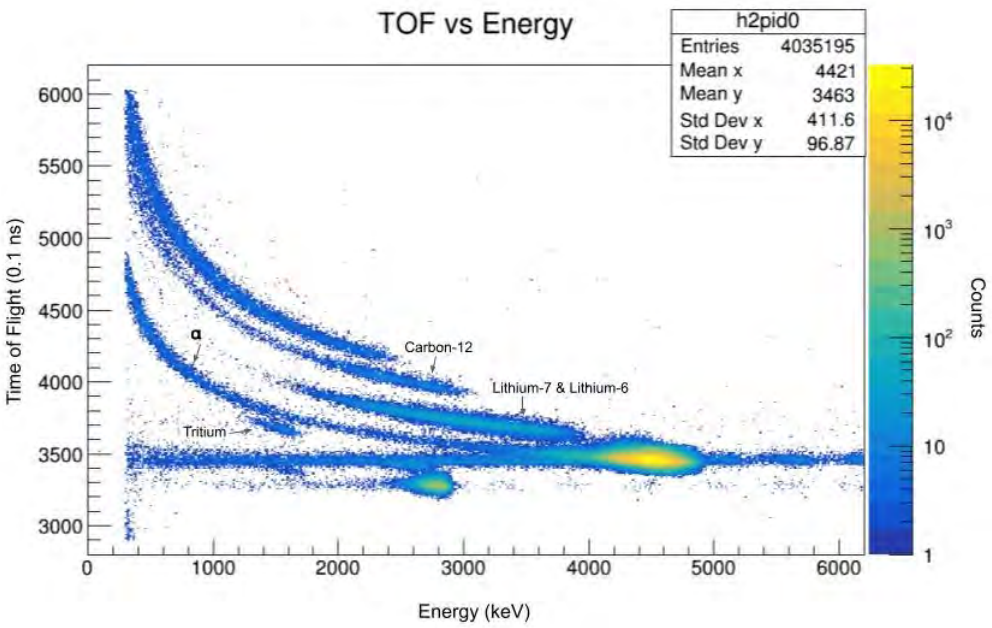

Figure 2: 3D histogram from the 20 degree detector of a run performed at 5.08 MeV

contaminants, that is a good place to set a basis. Looking at the histogram in figure 2, a few decay channels can be observed and confirmed by comparing it with two body relativistic kinematics. The ones of note would be the carbon-12 curve, the lithium-6 and 7 curve, the alpha curve and the tritium curve. At this energy, the alpha trail is too large and covers the proton counts with no easily discernible peak. Thanks to this, it is easier to identify other curves at lower energies and higher angles where there are less counts thereby making it harder to discern from noise.

Now that a baseline has been established using a thicker target, a thinner target at a high energy can be examined as well. Within it, there are less counts making it harder to detect certain nuclides but still possible thanks to the thicker target runs. Of import are the curves marked in figures 3 and 4. It contains about the same visible nuclides as the thick target but now the proton is visible. Due to some noise left the the α particles, a higher angle must be used which does decrease the number of proton counts but does allow us to actually see them. Confirming that those counts are protons is just like the other curves, its energy at this angle is compared to a kinematic curve which is why two different angles are shown. There could be some other nuclide at the same exact energy with a similar enough mass that it could contaminate the counts. But by observing two angles something

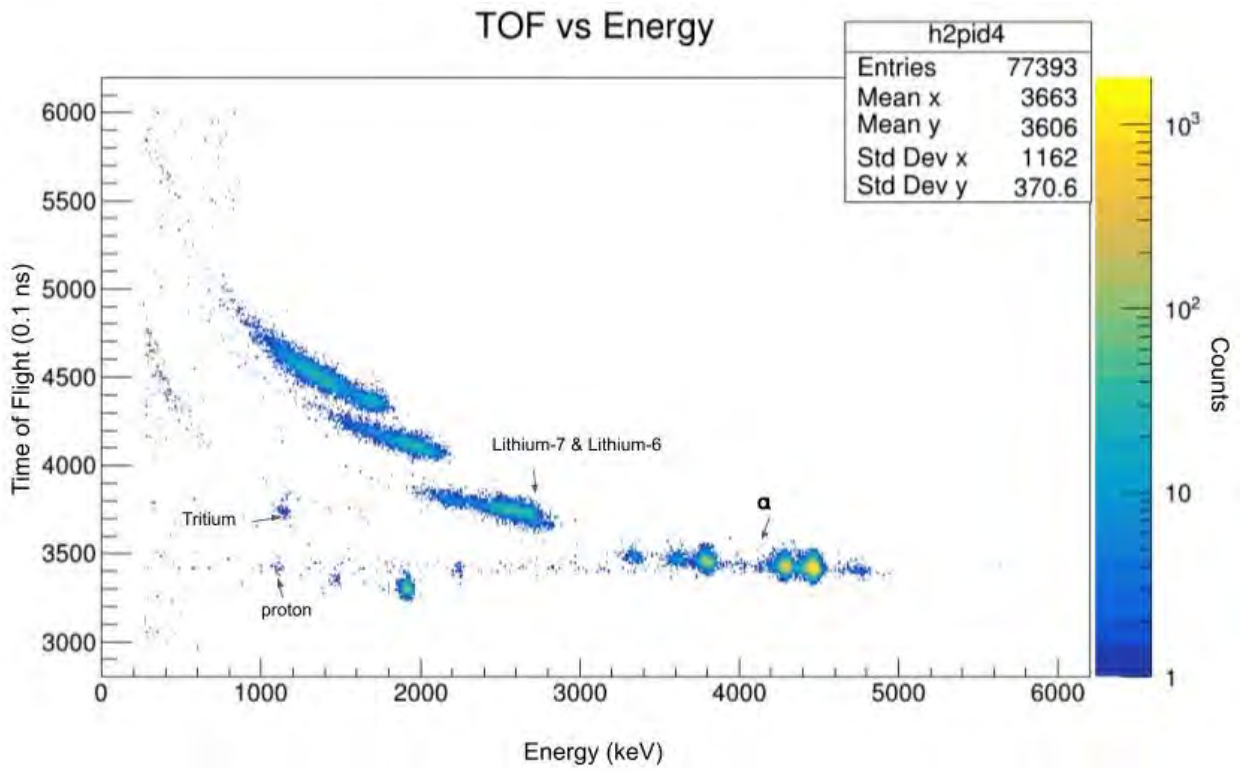

Figure 3: 5.08 MeV run on a thin target measured at 40 degrees

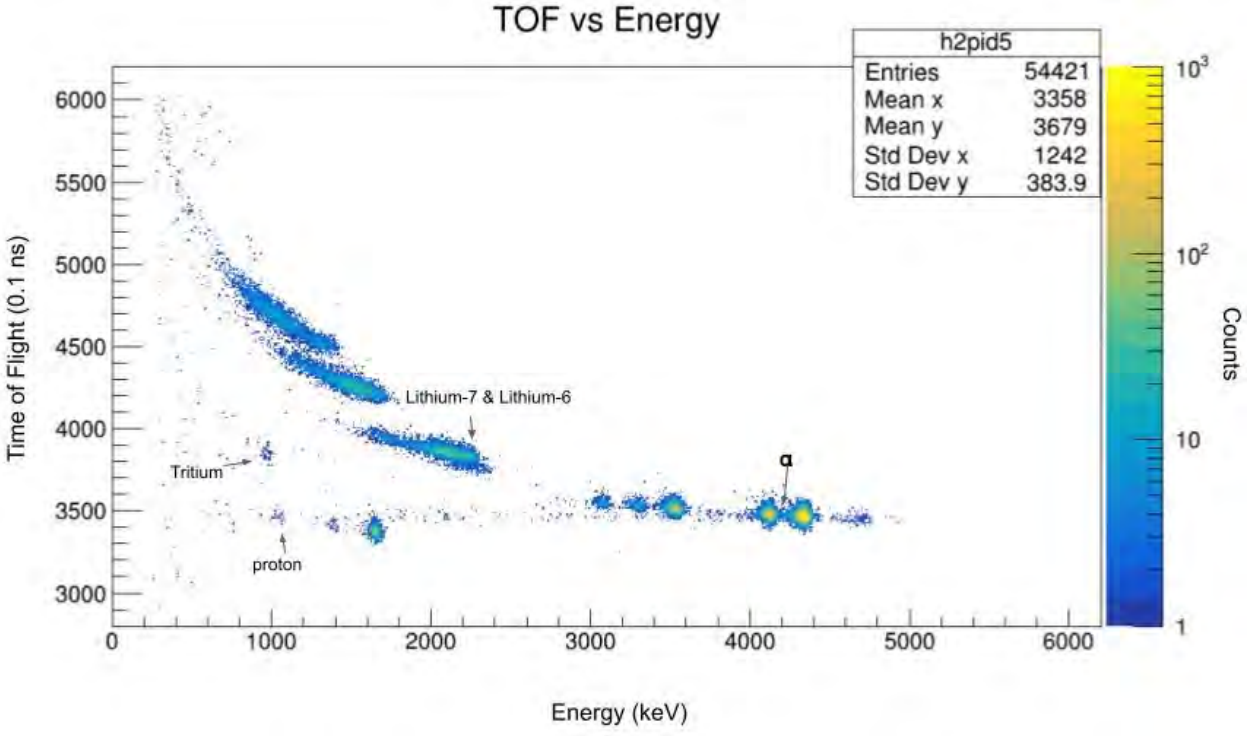

Figure 4: 5.08 MeV run on a thin target measured at 45 degrees

like that is separable.

Even at this high of an energy level, there is a sparse amount of protons detected in comparison to the other decay branches. But should there happen to be a resonance at a lower energy level, the counts should be comparable to that of a higher energy level and should be fairly obvious. That is assuming some form of noise or other nuclide does not cover up the peak. And so the next energy level observed is that of 4.35 MeV which equates to an excited energy level of about 11.434 MeV in ^{11}B.

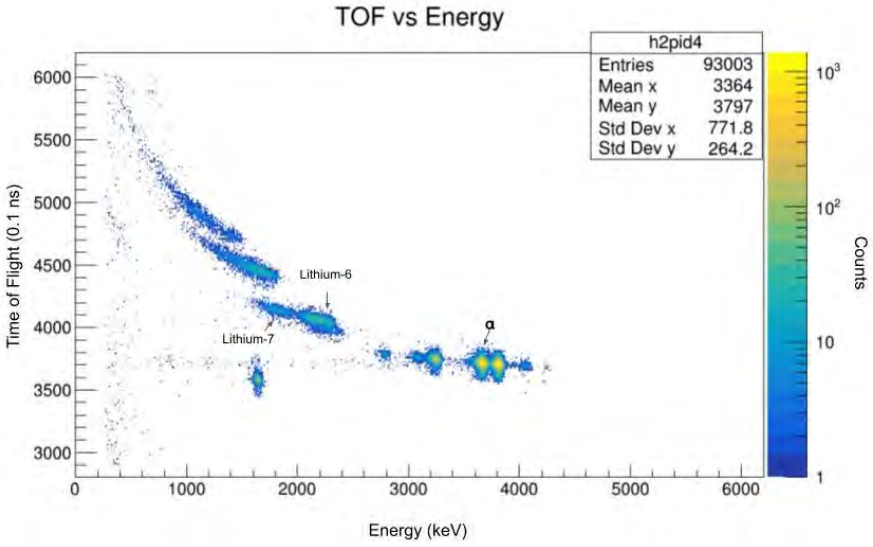

Figure 5: 4.35 MeV run on a thin target measured at 40 degrees

According to two-body kinematic calculations, the proton from the ^{7}Li(α,p)^{10}Be reaction should be located at 0.419 MeV but all we see in that energy range is heaver nuclides. We also do not see any triton decay either at this lower energy. The amount of protons that have theoretically been detected is too small to be able to discern from noise.As reported by Ref [3] there should be a proton emission resonance somewhere in this energy range but we fail to detect a resonance. Should there have been a resonance, a cluster of protons would be visible at 0.419 MeV while being around a similar time of flight as the main α particle cluster. More in depth analysis of the counts is in progress so as to get better confirmation of the lack of a resonance level.

5 Conclusion

At higher energies, known resonances are confirmed. But new evidence shows that the resonance would not be dominated by protons but by tritons produced from the ^{7}Li(α,t)^{8}Be reaction. And as for the lower energies, the energy ranges were scanned carefully to see if there was a resonance level. Initial analysis seems to show no evidence of any resonance in the range of 4.4-4.28 MeV, let alone proton emission . Going with the assumption that there is a resonance in that range, that leaves to options. There is either an alpha width or there is no alpha width.

In the case of an alpha width, there should have been a resonance within this energy range with a strong alpha decay width but we do not see any. This then leads to the idea of a potential resonance with no alpha width and any proton width. In that scenario, it cannot be a cluster but rather a single particle resonance which makes detecting it much harder. So while unlikely, there is a possibility of a single particle resonance within ^{11}B.

Further research could tackle a few different items. One being a careful study of the alpha scattering angle distribution. That would be able to give us evidence of a resonance in a certain energy level. The best way would be to use thinner and more pure ^{7}Li target to get better readings along with smaller energy steps. That way almost all contaminants would be removed from the spectrum and better statistics would be produced. Of course, some other approach could be used that is capable of detecting a proton width only.

Then there is the final possibility of some form of exotic decay and potential new physics. Some studies pointed out certain decays in the past that could explain the amount of ^{10}Be produced. Those being dark neutron decay and n-n' oscillations. Both are under heavy study and could lead to new physics as nothing in the current model predicts either decay.

6 Acknowledgements

I would like to thank Dr. Shelly Lesher for giving me the chance to participate in this REU and Dr. Umesh Garg for running and organizing it. I also want to express my thanks to Dr. Wanpeng Tan

as this project was his idea and I helped with it. Were it not for him, I may not have had a project this summer. Another deserving of thanks would be Kevin Lee, the understanding graduate student that proved to be a lot of help. This experience has given much to think about and will hopefully be a good influence on the choices I will end up making in the near future.

References

[1] Y. Ayyad, B. Olaizola, W. Mittig, G. Potel, V. Zelevinsky, M. Horoi, S. Beceiro-Novo, M. Alcorta, C. Andreoiu, T. Ahn, M. Anholm, L. Atar, A. Babu, D. Bazin, N. Bernier, S. S. Bhattacharjee, M. Bowry, R. Caballero-Folch, M. Cortesi, C. Dalitz, E. Dunling, A. B. Garnsworthy, M. Holl, B. Kootte, K. G. Leach, J. S. Randhawa, Y. Saito, C. Santamaria, P. Šiurytė, C. E. Svensson, R. Umashankar, N. Watwood, and D. Yates, Phys. Rev. Lett. **123**, 082501 (2019).

[2] E. Lopez-Saavedra, S. Almaraz-Calderon, B. W. Asher, L. T. Baby, N. Gerken, K. Hanselman, K. W. Kemper, A. N. Kuchera, A. B. Morelock, J. F. Perello, E. S. Temanson, A. Volya, and I. Wiedenhöver, Phys. Rev. Lett. **129**, 012502 (2022).

[3] Y. Ayyad, W. Mittig, T. Tang, B. Olaizola, G. Potel, N. Rijal, N. Watwood, H. Alvarez-Pol, D. Bazin, M. Caamaño, J. Chen, M. Cortesi, B. Fernández-Domínguez, S. Giraud, P. Gueye, S. Heinitz, R. Jain, B. P. Kay, E. A. Maugeri, B. Monteagudo, F. Ndayisabye, S. N. Paneru, J. Pereira, E. Rubino, C. Santamaria, D. Schumann, J. Surbrook, L. Wagner, J. C. Zamora, and V. Zelevinsky, Phys. Rev. Lett. **129**, 012501 (2022).

Isospin Symmetry Breaking Corrections in the IMSRG and CKM Unitarity Tests of the Standard Model

JONATHAN RIESS

2023 NSF/REU Program
Department of Physics and Astronomy
University of Notre Dame

ADVISOR(S): Prof. Ragnar Stroberg

Abstract

Unitarity of the quark mixing Cabibbo-Kobayashi-Maskawa (CKM) matrix provides one of the stringest tests of the Standard Model of particle physics, with violations of unitarity signaling physics beyond the Standard Model. One way to test CKM unitarity is through nuclear beta decay with so-called superallowed $0^+ \rightarrow 0^+$ Fermi beta decays. Measurements of these transitions have become precise enough that the main source of uncertainty in calculations of elements of the CKM matrix, such as V_{ud}, stems from theoretical corrections. One such contributing correction is encoded in the term δ_c which denotes corrections due to isospin symmetry breaking which are dependent on nuclear structure. Quantifying δ_c can be done using nuclear structure calculations and ab initio nuclear many-body methods such as the In-Medium Renormalisation Group (IMSRG) method. We investigate and report on possible sources of error and uncertainty induced by basis truncation involving IMSRG methods and the nuclear shell model.

1 Introduction

1.1 Isospin Symmetry, CKM Unitarity, and Tests of the Standard Model

In 1932, Heisenberg introduced the concept of isospin because he noticed that the proton and the neutron are very similar in the sense that they are interchangeable with respect to their interactions through the strong nuclear force and their masses. Because of this, protons and neutrons can be thought of as manifestations of the same particle, a nucleon, differing only by a new quantum number called isospin. The name isospin comes from the realisation that this property has a mathematical description similarily to a quantum mechanical version of angular momentum. Thus, we can think of protons as being in the “isospin down" state, while neutrons are in the “isospin up" state[1]. Their exchange can be thought of as a rotation from isospin up to isospin down or vice versa.

Since certain properties of a nucleus remain unchanged with respect to this exchange or rotation of protons and neutrons, we can speak of an isospin symmetry. However, isospin symmetry is not an exact symmetry, but only approximate. This is because protons and neutrons do have individual differences which break this symmetry. For example, under the coulomb interaction, protons are positively charged while neutrons are not. Hence their respective interactions vary.

[1]Specifically, we denote the isospin projection τ_z and write for the proton $\tau_z = -\frac{1}{2}$ and for the neutron $\tau_z = \frac{1}{2}$

Now, the process in which isospin becomes important is in interactions in which particles change isospins. One example of this is through β-decay. There are many types of β-decay, two basic version of which include β^-decay in which a neutron changes into a proton, and β^+ decay in which a proton changes into a neutron. The respective equations for these processes are:

$$\beta^- : n \to p + e^- + \bar{\upsilon}_e \qquad\qquad \beta^+ : p \to n + e^+ + \upsilon_e$$

If we depict these two processes on a more fundamental level in terms of quarks, we can again see that β-decay describes how the flavour of a down quark changes to an up quark, or vice versa. However, this is only a simplified picture. In reality, the up or down quark decays into a superposition of various flavours. For example, the up quar decays into the superposition of a down, strange, and bottom quark. This flavour mixing is encapsulated in the quark flavour mixing CKM matrix:

$$V_{\text{CKM}} = \begin{bmatrix} V_{\text{ud}} & V_{\text{us}} & V_{\text{ub}} \\ V_{\text{cd}} & V_{\text{cs}} & V_{\text{cb}} \\ V_{\text{td}} & V_{\text{ts}} & V_{\text{tb}} \end{bmatrix}$$

The terms $|V_{ij}|^2$ from V_{CKM} are proportional to the probability of transition of a flavour i quark to a flavour j quark.

Since the standard model says that the up quark decays to a superposition of the down, strange, and bottom quark (and can only decay to those three falvours), we naturally should expect that if we sum of the probabilities of transition to either quark falvour, we should get one: $\left|V_{ud}\right|^2 + \left|V_{us}\right|^2 + \left|V_{ub}\right|^2 = 1$. This is related to the idea that the CKM matrix is unitary and thus is called the (top-row) CKM unitarity requirement. Thus, if we want to test the standard model, we could measure each of the terms V_{ud}, V_{us}, V_{ub} and see if their moduli squared add up to 1.

Researchers have indeed done this and come up with the following values: $V_{\text{ud}} = 0.97370 \pm 0.00014$, $V_{\text{us}} = 0.2245 \pm 0.0008$, and $\left|V_{ub}\right|^2 = 1.7 \cdot 10^{-5}$. Note that there are various processed one can use to extract these terms and can therefore arrive at different values for each V_{ij} term[2]. However, if we take "world" averages, we find that[1]: $\left|V_{ud}\right|^2 + \left|V_{us}\right|^2 + \left|V_{ub}\right|^2 = 0.9985 \pm 0.0005$.

[2]For example, the V_{ud} can be determined using superallowed $0^+ \to 0^+$ nuclear beta decays, neutron decays or pion beta decays. The term V_{us} can be found using kaon decays, hyperon decays, or tau decays.

At first, it might not seem like the value of this sum is too far off from 1, however, the difference is significant enough to account for a 2 to 4 sigma anomaly.

This anomly could be a possible hint at physics beyond the standard model. One of the main new-physics explanations[3] is the existence of a new BSM heavy (E6 grand unification)/4th generation quark to which the up quark can decay to. This would account for a new flavour mixing term V_{uD} where D represents the new heavy quark, and if we took into account this new term in the sum above, we would get $|V_{ud}|^2 + |V_{sd}|^2 + |V_{ub}|^2 = 1 - |V_{uD}|^2$. Thus, getting better estimates for the values of V_{ud} for example could help validate such models.

How do we do that? Well, the first step to get the value of V_{ud} is to measure something called the ft values. You can think of these as the strength or rate of the decay or transition. The best process from which to measure these ft values from are the superallowed $0^+ \rightarrow 0^+$ beta decays because we can get the most precise measurements from these processed. Figure 1 shows some of the ft for such superallowed transitions.

Next, we need to take into account that the process that we measure might not be representative of the "mainstream" beta decay event. What we mean with that is that we need to take into account corrections for the fact that there could be other interactions contributing to our measurements. Thus we define something called the corrected ft values, denoted $\mathcal{F}t$ values, where we introduce different categories of corrections $\delta'_R, \delta_{NS}, \delta_C$ as follows:

$$\mathcal{F}t = ft(1 + \delta'_R)(1 + \delta_{\mathrm{NS}} - \delta_C)$$

What these corrections are, I will explain in a second. However, after measuring all these ft values and correcting them to find the $\mathcal{F}t$ values, we can find an average $\mathcal{F}t$

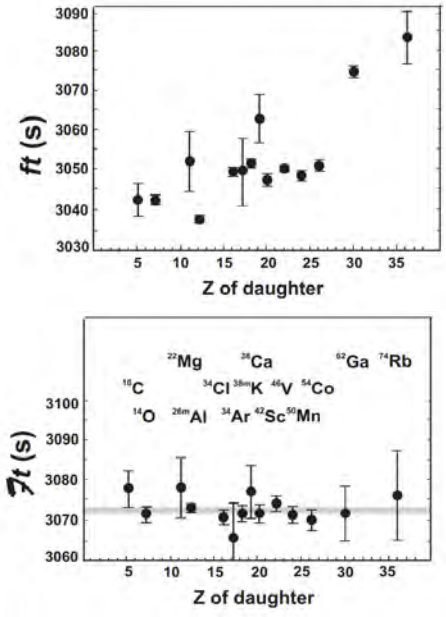

Figure 1: ft and $\mathcal{F}t$ values for certain superallowed nuclei [2]. Average $\mathcal{F}t$ value is the grey line.

[3]Others include: 1) Exotic muon decays such as beyond ordinary muon decays $\mu^+ \rightarrow e^+ \upsilon_e \bar{\upsilon}_\mu$, 2) A new Z boson Z_χ, 3) SUSY, 4) Leptoquarks.

value, which is represented as the grey line in figure 1.

Using this average $\mathcal{F}t$ value, we can then use the formula: $\mathcal{F}t = \frac{K}{2G_F^2|V_{ud}|^2(1+\Delta_R^V)}$ to extract the V_{ud} value since all the other terms are rather well-known constants or can be calculated[4].

Thus, the main challenge when it comes to getting accurate V_{ud} values is not only within the measurement process, but also getting accurate estimates for the correction terms. This is the main goal of the project. Specifically, we are interested in getting an accurate estimate for the correction term δ_c.

Before I explain how to calculate these correction terms, it is important to understand what they represent which can be done with the help of figure 2. From the figure, we can see that the process

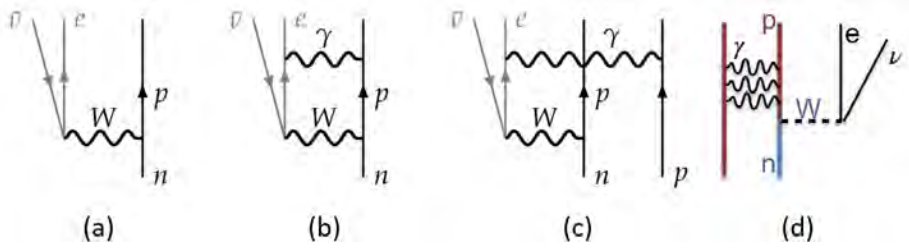

Figure 2: Examples of contributions to correction terms: (a) leading order contribution, (b) radiative correction Δ_R^V & δ_R', (c) nuclear-structure dependent radiative corrections δ_{NS}, (d) isospin symmetry-breaking correction δ_c. Source: [3]

(a) represents the “main-stream" or leading order contribution for beta decay. However, this “main-stream" interaction is not the only one that can occur. For example, the proton can interact with the emitted electrons as seen in (b) or other nucleons in the nuclei can interact with the emitted electrons as seen in (c). These are examples of corrections which would contribute to the radiative corrections $\Delta_R^V, \delta_R', \delta_{\mathrm{NS}}$ since they have to do with interactions with the emitted radiation (electrons). For the δ_c term, we are focused on isospin symmetry breaking corrections which account for the fact that the final state, i.e. the proton in image (d), is not exactly an isospin rotation of the initial state, the neutron, because the Coulomb interaction between the final state proton and other surrounding nucleons in the nuclei breaks the isospin symmetry.

To calculate δ_c, we simply use the formula $\delta_C = 1 - |M_F|^2/2$, where the matrix element

[4]Here G_F is the well-known weak-interaction constant for purely leptonic muon decay, K is a constant, and Δ_R^V is another correction term, the inner or universal electroweak radiatiove corrections to superallowed nuclear beta decays.

$M_F = \langle \Psi_f || \tau || \Psi_i \rangle$ can be calculated using an ab initio nuclear structure calculation method such as IMSRG.

1.2 Ab Initio Approaches to Nuclear Structure Calculations and Nuclear Many-Body IMSRG Methods

In general, there are many methods one can use when doing ab initio calculations in nuclear theory and trying to solve the quantum many-body problem. The method that we will use, as it is particularly appealing for computing corrections such as δ_c, is the IMSRG method since it can be applied to all experimentally studied superallowed nuclei. For a general overview of this method, see ref. [4–6].

However, for a brief discussion of this method, note that we are trying to solve the time-independent Schrödinger equation, $\hat{H}|\psi\rangle = E|\psi\rangle$ which is an eigenvalue problem. If we think of $\hat{H}$ as a matrix, we know from linear algebra that if we diagonalise a matrix $\hat{H}$, we can simply read off the eigenvalues from the diagonal. Hence, our goal is to separate the Hamiltonian $\hat{H}$ into a diagonal part H^{d}, which gives us our solutions, i.e. our eigenvalues, and an off-diagonal part H^{od}, which introduces slight deviances from our solutions, i.e. $\hat{H} = H^{\mathrm{d}} + H^{\mathrm{od}}$. In order to get meaningful results, we try to make H^{od} small, i.e. if we can make the entries in our Hamiltonian depend on a free parameter s : $\hat{H} = H(s) = H^{\mathrm{d}}(s) + H^{\mathrm{od}}(s)$, then we would like for $\lim_{s\to\infty} H^{\mathrm{od}}(s) = \mathbf{0}$ (the matrix with only zeros), and $\lim_{s\to\infty} H^{\mathrm{d}}(s) = H(s)$. Note this is similar to the perturbative expansion $H_{\mathrm{exact}} = H_0 + \lambda H_{\mathrm{int}}$.

In order to "diagonalise" $\hat{H}$, the IMSRG approach is to perform a series of (infinitesimal) unitary transformation U parametrised by a flow parameter s[5]:

$$H(s) = U(s)H(0)U^{\dagger}(s) \tag{1}$$

where $H(s = 0)$ is the starting Hamiltonian and $U(s = 0) = 1$.

[5]Note that this works because a composition of unitary transformations is again a unitary transformation.

1.3 Basis Truncation and Non-Convergence of δ_c Calculations

Because the IMSRG method is an ab initio method, we need to make certain approximations or truncations in order to do our calculations. One of those truncations is a basis truncation. This becomes relevant for example when we are dealing with wavefunctions $|\psi\rangle$ which need to be written in a particular basis $|\psi\rangle = a_1|\phi_1\rangle + a_2|\phi_2\rangle + ...$ such as the Harmonic Oscillator basis. Because these bases have an infinite amount of terms and we are doing calculations using a computer, we need to make a truncation at some point with a cutoff. This cutoff we call $e_{\max} \geq 2n + \ell$ where n and ℓ are the principal and angular momentum quantum number. The way we can think of this $e_{\max}$ is in terms of the nuclear shell model in which the neutrons and protons live in a latter type structure where each rung is a specified energy level with a certain n and ℓ denoted via spectroscopic notation as $1s, 3d$, etc. This is similar to the electron shell model familiar to us from introductory chemistry and can be visualised as follows in figure 3. In this context, $e_{\max}$ becomes a cutoff for which energy levels we consider and which ones we won't. So if we set $e_{\max} = 12$, then we will only consider energy level in the nuclear shell model for which the n and ℓ models sum as $12 \geq 2n + \ell$.

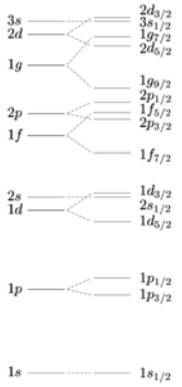

Figure 3: Nuclear Shell Model energy levels with spectrscopic notation.

A way to check if our calculations, for example of δ_c, are still accurate and reliable despite this $e_{\max}$ truncation is by running the calculations for different values of $e_{\max}$ and seeing if the results of those calculation converge to a certain value.

However, if we do this for δ_c, we notice that we get odd behaviour which can be seen in figure 4. Instead of getting convergence when including higher and higher $e_{\max}$ values, we get slow convergence or no convergence at all. In addition, there are a few other peculiarities about these calculations such as a dependence on the reference state used (idealy we would want our calculations to be independent of reference state) and we have large corrections when we include higher n-body terms such as induced two-body terms.

Therefore, the goal of this project is to figure out what is driving this odd behaviour in our calculations, particularily the slow/non convergence of δ_c.

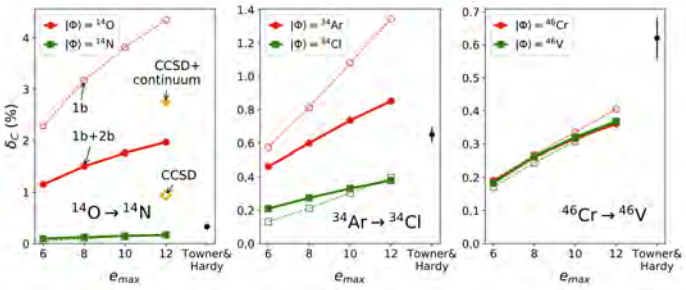

Figure 4: δ_c as a function of $e_{\max}$ [3]

2 Methods

If δ_c is calculated using the formula: $\delta_c = 1 - \frac{|\langle \Psi_f || \tau || \Psi_i \rangle|^2}{2}$, then perhaps we can look at the isospin expectation value $\langle \tau \rangle$ and IMSRG ground state energy as a function of $e_{\max}$ to see if non-convergence stems from them. In order to figure out to what degree spurious isospin breaking plays a role in these calculations, we can use various different potentials when building up the model space of our nuclei. Some of the possible potentials include the Minnesota Potential which is an isospin-conserving potential and is written as the sum of gaussians. It originally came from alpha scattering. We can also include the Coulomb Potential which breaks isospin symmetry. We could also use more realistic potentials which come from Chiral effective field theory, for more details see [7]. For these, we can choose various possibilities such as including only up to 2 body terms or up to 3 body terms. In addition we can make the choice of whether using a potential for NNLO (next-to next-to leading order) or N^{3}LO. The differences between two choices lies in the type of interactions included as seen in the diagrammes shown in the figure below.

In addition, we can also determine if non-convergence is related to mean field wavefunctions of the states used by calculating the wavefunction overlap $\langle \psi_f \psi_i \rangle$. If there is convergence for the mean field wavefunction and overlap for the transition $^{14}O \rightarrow {}^{14}C$ but non-convergence for $^{14}O \rightarrow {}^{14}N$ (note that the ^{14}N would require open shell calculations), this would tell us that other parts of the IMSRG introduce errors and these errors would be due to a corre-

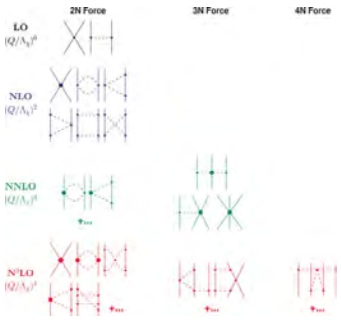

Figure 5: Chiral EFT [7]

lation effect.

3 Results

Running the calculations using IMSRG(2), the following behaviours for the isospin expectation value and IMSRG ground state energy for ^{14}O and ^{22}O were found in 6.

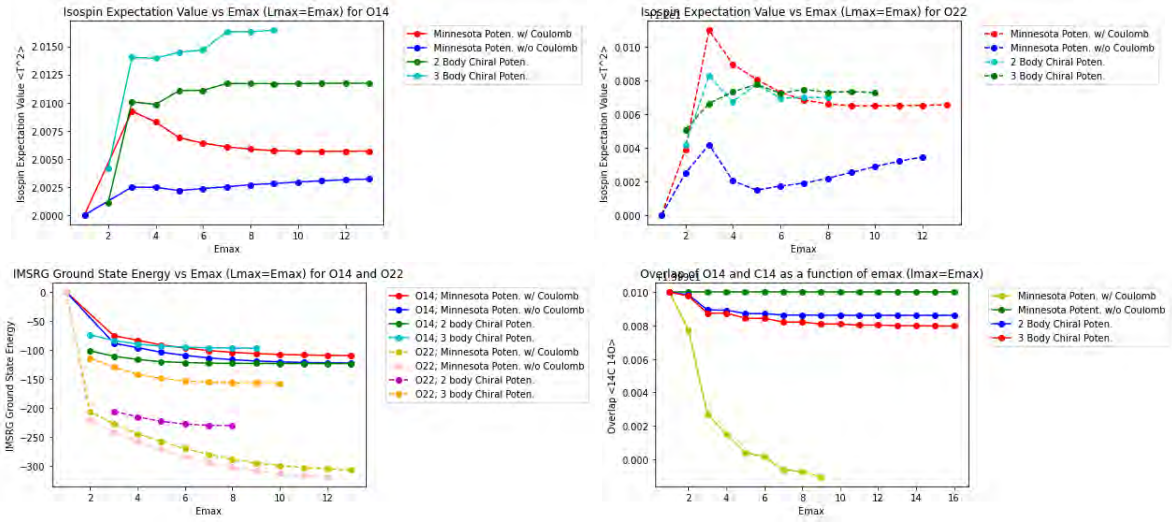

Figure 6: Calculations of the isospin expectation value (top row) and IMSRG ground state energy (bottom left) as a function of $e_{\max}$ for various different potentials and for two nuclei: ^{14}O and ^{22}O. Convergence is generally observed. Wavefunction Overlap for $^{14}O \rightarrow {}^{14}C$ shown bottom right.

Convergence is clearly observed with most calculations being well converged by $e_{\text{emax}} = 12$. Hence, the non/slow convergence cannot stem from the isospin expectation value or ground state energy.

The calculation for the wavefunction overlap of $^{14}O \rightarrow {}^{14}C$ can also be seen in figure 6. However, further research is needed to do the calculations for transitions such as $^{14}O \rightarrow {}^{14}N$ which would require open shell calculations and thus to fully rule out or determine the nature of the contribution to the slow convergence.

4 Conclusion

Running calculations using IMSRG(2) for ^{14}O and ^{22}O with various potentials including the Minnesota potential (with and without Coulomb interactions) and the more realistic chiral effective field theory N^{3}LO potentials with 2 and/or 3 body terms, we report that the slow and non-convergence of the IMSRG calculations of the isospin symmetry breaking correction term δ_c is not due to convergence issues of the expectation value of the isospin operator nor the IMSrg ground state. Future work needs to be done investigating the relationship between the non-convergence of δ_C and the mean-field wavefunctions and their overlap for transitions such as $^{14}O \rightarrow {}^{14}N$. I would like to thank Prof. Storberg, Dr. He, Mr. Farren, and the Notre Dame Physics and Astronomy Department and REU Programme for their help and support.

References

[1] P. Z. et al., Prog. in Theo. and Exp. Phys. 2020, 083C01. (2020).

[2] J. Hardy and I. Towner, PRC **102**, 045501 (2020).

[3] S. R. Stroberg, Particles **4**, 521 (2021).

[4] H. Hergert, S. Bogner, T. Morris, A. Schwenk, and K. Tsukiyama, Physics reports **621**, 165 (2016).

[5] S. R. Stroberg, H. Hergert, S. K. Bogner, and J. D. Holt, Annual Review of Nuclear and Particle Science **69**, 307 (2019).

[6] H. Hergert, Frontiers in Physics **8**, 379 (2020).

[7] R. Machleidta and D. R. Entem, Chiral effective field theory and nuclear forces, arXiv (2011).

Complete Analysis of ^{19}F Energy Levels in 2021 Experiment for ^{15}N$(\alpha,\gamma)^{19}$F Reaction

MELODY SHIMBA

2023 NSF/REU Program
Department of Physics and Astronomy
University of Notre Dame

ADVISOR(S): Prof. Dan Bardayan

Abstract

Following on to a preliminary analysis of $^{15}N(\alpha,\gamma)^{19}F$ performed in 2021, a more complete analysis was required. Studying ^{19}F provides deeper understanding to its mirror nucleus, ^{19}Ne, and gives understanding to novae nucleosynthesis as a result. The analysis of the experiment to confirm the initial conclusions made about ^{19}F from 2021 was completed. This analysis looked at the previously completed experiment in detail to prove the accuracy in the 2021 early conclusions. We found positive correlations between the gamma rays in the experiment and where we expected to see them, thus confirming the work from O'Donnell. The further completeness of the energy levels in ^{19}F will allow for future conclusions to be made about its mirror nucleus ^{19}Ne which impact estimates of ^{18}F synthesis in novae.

1 Introduction

The processes for how astrophysical phenomena- such as novae, occur are not deeply understood. Nuclear reactions are a primary cause, although the catalyst for these reactions is debated among scientists. Studying the interactions can allow scientists to make implications about how novae occur and with what frequency that they do. ^{18}F, which is a strong gamma ray emitter and a potential diagnostic to nova nucleosynthesis after oxygen-neon novae. A reaction to simulate the O-Ne nova is $^{18}F(p,\gamma)^{19}Ne$. This reaction allows scientists to understand how much ^{18}F exists after a nova occurs. However, ^{18}F has a short half-life of about 110 minutes. In addition, ^{19}Ne is an unstable isotope with a half-life of about 18 seconds. This makes both ^{18}F and ^{19}Ne difficult to study. ^{19}Ne has a stable mirror nucleus, however, ^{19}F. Studying ^{19}F can then provide understanding to ^{19}Ne, and in tandem, teach us about the abundances of ^{18}F in neon-type novae [1].

Previous work in 2021 completed the experiment that studied the $^{15}N(\alpha,\gamma)^{19}F$ reaction [2], which in turn can be used to study ^{19}F. Preliminary conclusions were made, however, the full analysis of the data remained incomplete. In order to confirm initial conclusions O'Donnell made, complete analysis of the experiment was required.

2 Background

2.1 Previous Work

A similar experiment had been completed once before, however it only looked between 2.8 - 4.0 MeV [3]. In 2021, the experiment looking at $^{15}N(\alpha,\gamma)^{19}F$ went beyond 4.0 MeV, and analyzed regions up to 7.2 MeV. It was performed on RHINOCEROS, a windowless, differentially pumped, recirculating gas target. [4] The differental pump allowed for the gas target chamber to be held at one pressure, while the beam line itself could be at a different pressure. The pressures of the beam line were changed 158 different times, and each of these contributed to a "run". The recirculating gas target allowed for the expensive gas target, ^{15}N to continuously run without changing the gas. To observe radiation, two types of semiconductor detectors were used: silicon (Si) detectors to measure alpha particles and germanium (Ge) detectors to measure gamma rays.

Five Si detectors in total were used. They were placed at 45, 60, 90, 120, and 135 degrees from the beam line. There were two Ge detectors placed on either side of the target chamber where the beam line passed between them. A tungsten alloy was placed in between to act as a shield with a 1cm slit left to ensure that only a small area of the cross section was observed. Lead blocks were placed around the rest of the detectors to block background.

Of the 158 total runs, only 123 were useable. The remaining 35 runs attempted to change the set up of the runs and yielded data that was not useful for analysis. The early analysis performed by O'Donnell summed 7 of those runs to increase statistics and revealed gamma ray peaks emitted during the reaction. These peaks revealed a previously unknown to ^{19}F state, at 7249 KeV. In addition, O'Donnell studied the energy transition for the 7262 KeV state down to ground state, and was able to estimate the gamma branching ratio impacting $^{18}F(p,\gamma)^{19}Ne$. A further and more complete analysis was necessary for confirmation of the work that was previously done.

2.2 Positron Annihilation

When gamma rays interact in Ge detectors, they can deposit their energy in a number of ways. One is through e^+e^- pair production. When the beam comes in contact with a nucleus, in this case, the helium gas beam with the nitrogen gas target, the high energy gamma ray from $^{15}N(\alpha,\gamma)$ can produce a e^+e^- pair in the Ge detector. The positron annihilates, creating two 511 KeV gamma rays that can escape from the detector. When this happens, the detector then captures lower energy by either 511 KeV or 1022 KeV of energy. The 511 KeV difference is from a single escape peak, and the 1022 KeV difference is from a double escape pair. During the reaction, many peaks in the decay transitions correspond to either a single or double positron annihilation.

2.3 Doppler Shifting

The reaction can occur at any point in the gas target chamber. Depending on where the reaction happens can correspond to a Doppler shift of up or down. When the reaction occurs at an angle before the detectors, then the reaction is upshifted. If the reaction occurs at an angle past the detectors, then it is downshifted. This causes the experimental energies of the peaks to be higher or lower than the expected energies from their expected energies from the National Nuclear Data Center (NNDC) [5].

3 Methods

The analysis set out to do and completed three things:

1. Identify each gamma peak in each run from 0-7700 KeV
2. Find the rough excitation energy expected for $^{15}N(\alpha,\gamma)$ at the center of the target.
3. Identify each gamma peak with a pre-existing decay transition or from the decay transition found by O'Donnell

3.1 Peak Identification

Due to the nature of the data being processed into histograms, we used a program called DAMM.EXE to scrub through each spectra and identify peaks by eye.

3.1.1 DAMM.EXE

DAMM.EXE is a program from Oak Ridge National Lab. It is used by the Institute of Structure and Nuclear Astrophysics (ISNAP) at the University of Notre Dame for reaction analysis. The program takes histogram files and allows for visualization of the counts per energy of the reactions. For this analysis, DAMM.EXE was used to identify the energy of each manually identified peak between a certain region. For this analysis, each region of the spectra was looked at between step sizes of 1000 KeV. See: Figure 1.

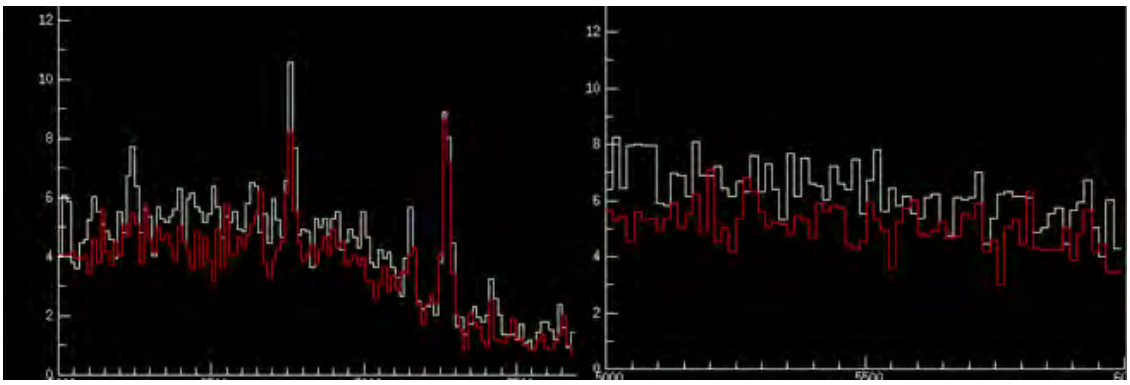

Figure 1: The DAMM.EXE environment for a run over two different regions of the same spectra. The white line is Ge detector 1, the red line is Ge detector 2.

There was not enough information (e.g. the FWHM) of each peak to allow DAMM.EXE to automatically identify/confirm peaks. However, with parameters of physical height of the peak in comparison with the background noise, high counts, and the physical width of the peak, identification became easier over time.

3.2 Alpha Energy at Center of Target and Rough Excitation Energy

The next step was finding the alpha energy at the center of the target (α_x) and rough excitation energy expected to be populated in ^{15}N(α,γ) (rough E$_x$). α_x is the energy of the beam at the center

of the target chamber for each run. The rough excitation energy is generally understood to be the state populated in ^{15}N(α, γ). It is the energy where the gamma rays should be decaying/transitioning from. If, for example, the rough Ex is 7200 KeV, then the corresponding gamma rays should come from transitions around that energy. To find the rough excitation energy, it is the equation for the energy of the center of mass plus a Q value:

$$Ex = \frac{M_{Target}}{M_{Target} + M_{Beam}} E_{Beam} + Q \tag{1}$$

Where the Q value is an energy value determined from the difference between the masses of the nuclei before and after the experiment, multiplied by c^2 to transform it into energy. The value for this experiment was determined to be 4014 KeV. M_{Target} is the mass of the target, M_{Beam} is the mass of the beam, and E_{Beam} is the energy of the beam. In the case of this experiment, the mass of the beam is the mass of alpha particles, $^4He^{2+}$, 4 amu, the mass of the target is the mass of ^{15}N, 15 amu, and the energy of the beam is α_x, which is found using a program called STOPIT.EXE.

3.2.1 STOPIT.EXE

STOPIT.EXE is a program that we used for finding α_x. By inputting the mass of the stopee (i.e. beam), the gas absorber (i.e. target), the initial energy and pressure of the gas for the run, the user can find α_x. The program is generally modeled off of the Bethe-Bloche formula, which is used for calculating energy loss [6]. STOPIT.EXE was created, however, using experimental data that was collected to make it accurate in finding the energy loss of an experiment, as well as returning what energy is remaining. STOPIT.EXE is a significantly more accurate way to find the energy remaining (α_x) than using the Blethe-Bloche formula outright, because of the years of experimental data that was used to create it.

3.3 Transition Identification

Using the transitions on the National Nuclear Data Center (NNDC) website that were experimentally proven for ^{19}F, transitions were identified for the gamma peaks [5]. Once again, by eye, the

closest corresponding energy of the gamma ray with a comparatively high intensity, was found on NNDC. Some observed peaks were actually single and double escape peaks owing to the relatively high energies of the gamma rays. For example, for run 106, a peak with energy of 7262 KeV was found. NNDC determined experimentally that for the transition from 7262 KeV to ground state (0 KeV), there is a high likelihood that a gamma ray of energy 7262 is released. Therefore, the gamma ray has high likelihood of coming from that transition. The next peak found in run 106 is at 6756 KeV. This peak does not have a corresponding transition for NNDC that could explain it better than positron annihilation. The difference between 7262 KeV and 511 KeV is 6751 KeV which is very close to 6756 KeV. The difference in 5 KeV is understood in the Doppler shift, mentioned in the background section. If there were no obvious peak features within a region, then no data was taken, and the next region was immediately examined. See: Figure 2. This process was followed for all of the peaks and 123 runs of the experiment.

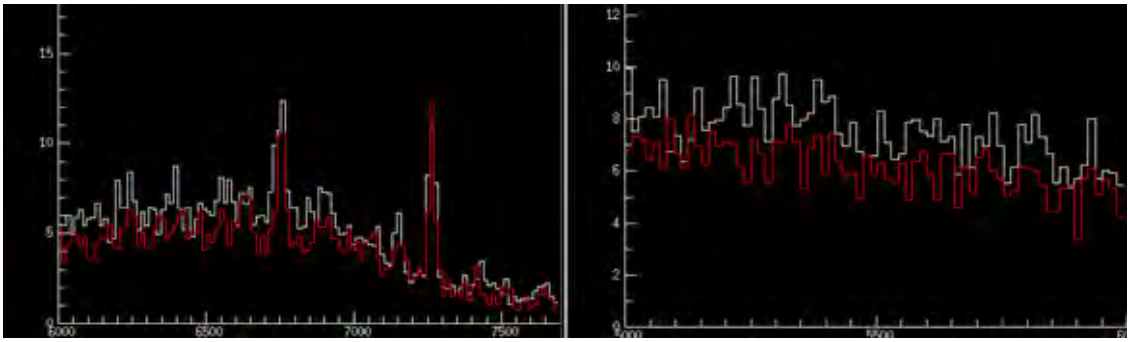

Figure 2: Run 106 with the 511 KeV peak difference (left) alongside noise (right).

4 Results

The analysis revealed two things:

1. A general positive correlation between rough excitation energy and the populated state of energy for the decay transitions

2. Not every run had gamma rays populated in expected energy ranges

Essentially, we would see gamma rays emitted at the energies we expected them to be at. That is a positive correlation for the overall data. Figure three displays the rough excitation energies and the range of states for where the gamma rays populated. Coincidentally, however, there were not always gamma rays picked up by the detector in every run. Many runs contained spectra with only background noise, and no obvious peak emissions. The graph does not include those states where there was only noise present in the run, because no gamma rays were emitted.

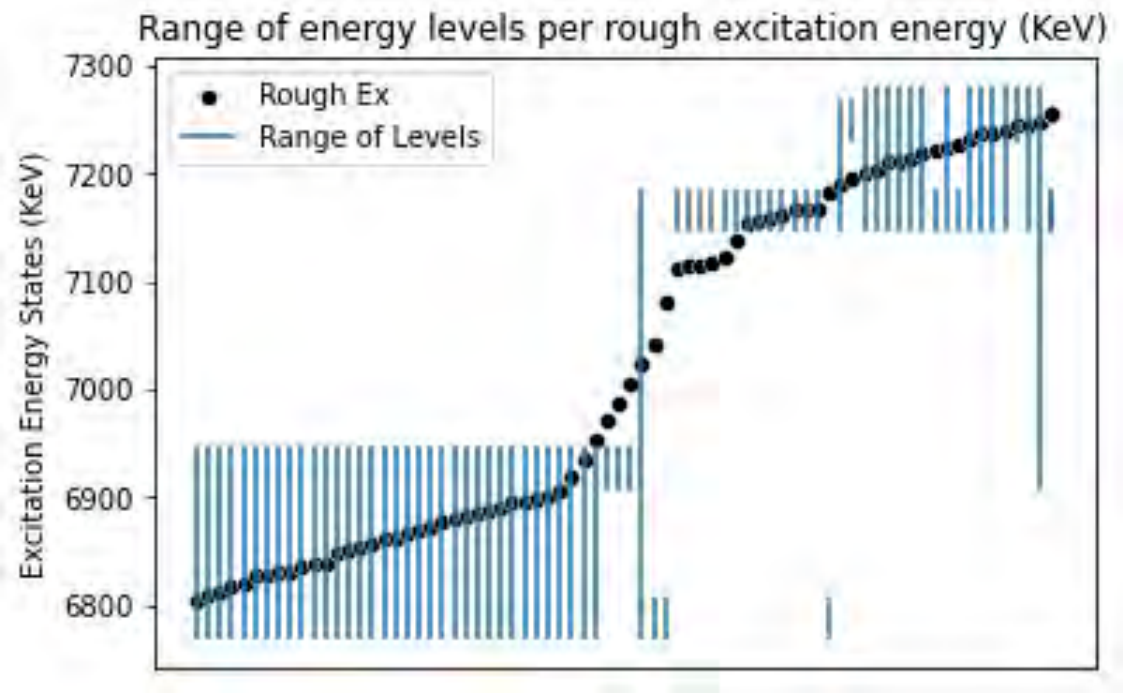

Figure 3: The correlation between the range of energy states and rough excitation energies from the experiment.

The few outliers in the graph indicate that those are runs that can be ruled out from the final astrophysical conclusions made, because they are likely not significant enough to yield important implications. They are likely found due to human error.

5 Conclusion

The complete analysis concluded that the new state and completed state found by O'Donnell are correct for ^{19}F. There was a positive correlation between where we expected to see gamma rays and

where they actually populated from the $^{15}N(\alpha,\gamma)^{19}F$ reaction. The final astrophysical implications are still necessary to make, however. Due to the large nature of the analysis, there are still more steps to be taken in terms of the final astronomical conclusions. A final conclusion and analysis relating ^{19}F back to ^{19}Ne is the necessary next step to make for the overall motivations for the project.

References

[1] D. W. Bardayan, J. C. Blackmon, W. Bradfield-Smith, C. R. Brune, A. E. Champagne, T. Davinson, B. A. Johnson, R. L. Kozub, C. S. Lee, R. Lewis, P. D. Parker, A. C. Shotter, M. S. Smith, D. W. Visser, and P. J. Woods, Phys. Rev. C **63**, 065802 (2001).

[2] G.O'Donnell, Examining the ex= 7262 and 7249 kev states of 19f with the 15n(a,g)19f reaction (2021).

[3] W. Dixon and R. Storey, Nuclear Physics A **284**, 97 (1977).

[4] RHINO, `https://isnap.nd.edu/research/facility/experimental/rhino/`.

[5] M. Wang, G. Audi, A. H. Wapstra, F. G. Kondev, M. MacCormick, X. Xu, and B. Pfeiffer, The ame2012 atomic mass evaluation (ii). tables, graphs and references (2012).

[6] W. R. Leo, Passage of radiation through matter, in *Techniques for Nuclear and Particle Physics Experiments: A How-to Approach* (Springer Berlin Heidelberg, Berlin, Heidelberg, 1994) pp. 17–68.

Exploring the Effects of Plasma Radiation on the pH of Solutions for Potential Medical Applications

Beatriz Silva

2023 NSF/REU Program
Department of Physics and Astronomy
University of Notre Dame

Advisor(s): Dr. Sylwia Ptasińska

Abstract

Despite cancer being the second leading cause of mortality worldwide, current treatments still have limitations, such as drug resistance, cytotoxicity to healthy tissues, and high recurrence rates. Plasma medicine, specifically a low-temperature plasma (LTP), has provided effective cancer therapies in the past few years, with strong effects on cancer cells and inferior side effects on healthy tissues. This study explores how LTP irradiation affects pH in solutions, which is relevant to understanding cancer cell behavior, growth, and spread. Further experiments with one of the amino acids, i.e., glycine, are also conducted to assess how the process is altered in the presence of a biomolecule. It was found that a combination of high voltage, high frequency, and long irradiation times leads to more acid pure water solutions. Additionally, when each irradiation time is analyzed separately, an increase in voltage seems to play a more significant role in lowering the pH of water solutions. Experiments with glycine showed that higher concentrations of the amino acid increase pH stability, while lower concentrations cause similar pH variations as observed in pure solutions.

Introduction

Cancer is characterized by uncontrollable cell growth and spread to other body parts in a process called metastasis. While cancer is the second leading cause of mortality worldwide, all current approaches to prevent and treat this disease have severe limitations. For instance, existing treatments undergo challenges such as drug resistance, pathogenesis complications, cytotoxicity to healthy tissues, inadequate delivery methods to the tumor site, and high recurrence rates. Ideal alternatives and effective cancer therapies should be less-invasive with strong effects on malignant cells and inferior side effects on healthy cells, besides inhibiting the growth of cancer cells via several intracellular mechanisms[1-3].

A novel, feasible approach to overcome such challenges is using a low-temperature plasma (LTP), which has shown positive effects in tumor treatment by killing cancer cells without damaging surrounding tissues[4,5]. Not only is LTP effective in targeting cancer cells, but it also has a significant impact on the pH of aqueous solutions when irradiated under certain voltage and frequency parameters delivered by a plasma source. Previous studies have shown that pH is crucial in cancer growth, division, and spread, as it affects most cellular processes and

microenvironments[6-8]. In particular, low extracellular cancer pH was shown to enhance drug resistance and promote invasive growth and metastases. Conversely, due to the acidic nature of cancer cells, some research suggests using alkaline (basic) pH treatment to reverse the pH gradient back to normal and complement existing therapies[9,10].

In this study, we aim to investigate the effects of plasma irradiation on the pH of solutions under different plasma parametric conditions. The solutions were initially prepared with deionized (DI) water. For the second part of the experiment, the amino acid glycine was diluted in DI water to allow for further observation of how the process was affected by the presence of a biomolecule. By identifying and investigating patterns of pH alterations of plasma-treated solutions, we can develop better strategies for using LTP in cancer treatment, besides predicting possible collateral effects to surrounding tissues and microenvironments that are strongly influenced by extracellular pH.

Methods

For this specific study, two crucial steps are employed: plasma irradiation and pH measurements. Two 500 μL glass containers are fully filled with the desired solution before plasma irradiation and combined in 1.5 mL disposable tubes prior to the pH measurements. For this study, the same amount of deionized water (1 mL) was used for all trials. To observe the relation between pH, plasma, and biomolecules, different glycine concentrations were dissolved in water before filling the glass containers.

Plasma Irradiation

In the plasma source, helium discharge is directed onto the solution for a duration ranging from 0 to 120 seconds, with time intervals of 15 seconds. Three sets of solutions were prepared under

the same conditions of frequency, voltage, irradiation time, and concentrations to allow for greater accuracy when later conducting the pH measurements.

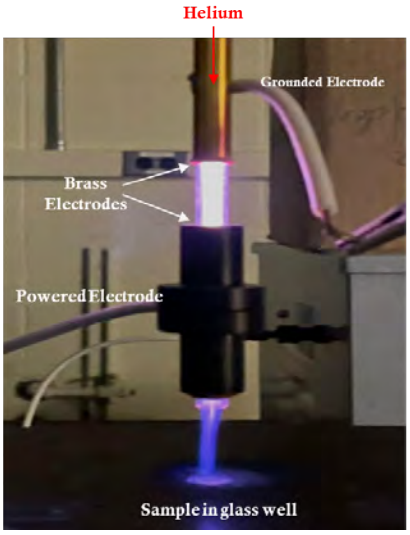

Figure 1. Plasma source scheme used for all experiments. Helium discharge is directed onto the sample in a glass well with different sets of irradiation time, frequency, and voltage.

For pure solutions, our main focus was to study the impact of different voltage and frequency values on the pH of DI water. Four trials for each voltage condition were conducted while maintaining consistent variations in frequency and irradiation time. Specifically, keeping a constant voltage of either 8 kV or 10 kV, the source frequency varied between 1 kHz, 2 kHz, 3 kHz, and 4 kHz. The presence of a magnetic stirrer during the irradiation was tested, as shown in Figure 3, but no relevant effects were observed, which led to the decision not to stir the solution during this step. For glycine solutions, the goal was to observe how different concentrations of biomolecules changed the solution's response to plasma irradiation. To achieve this, two sets of plasma parameters were chosen: 8kV and 1 kHz, and 10 kV and 4 kHz. By using the extreme values of frequency and voltage studied using pure solutions, we assume that the measurements could provide a comprehensive analysis of the effects of the same parametric conditions in the presence of biomolecules. The concentrations of glycine tested were 0.01 M, 0.02 M, 0.1 M, and

0.5 M. However, since the 0.5 M concentration showed significant pH stability, higher concentrations of the amino acid were not included in the tests.

pH Measurements

During each measurement, the pH electrode, which underwent calibration at least every two weeks, was placed into the disposable tube. The electrode was inserted to a depth of approximately 80% of the container, and each prepared solution was measured twice. The pH probe was thoroughly rinsed with pure water and dried with Kimwipes prior to all measurements. The disposable tube was sustained by a support placed on the top of a hotplate stirrer, which remained turned off during the measurements. External interference was not present, and the laboratory's humidity, as it remained relatively stable, was not considered a significant factor.

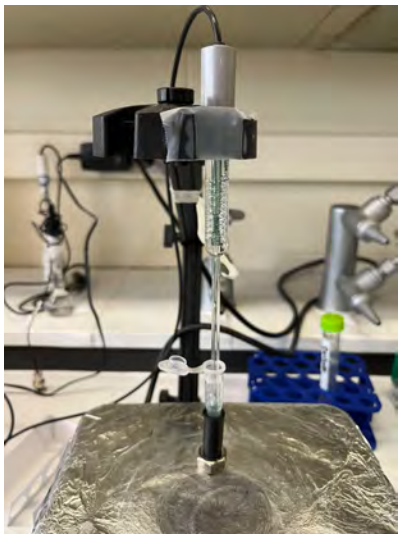

Figure 2. pH electrode and experimental apparatus for pH measurement. pH probe is inserted to a depth of approximately 80% of the disposable tube, and rinsed and dried before each new measurement.

Results

The proposed research aimed to analyze the effects of plasma irradiation on the pH of pure and glycine solutions. To do that, several samples were irradiated under different configurations of frequency and voltage of the plasma source, and amino acid concentration, across a specified

time range. The accuracy of the experiment was obtained by measuring pH of each sample twice, and ensuring that three samples were prepared and treated under the exact same conditions mentioned above.

Stirring Analysis

Initially, a stirring analysis was performed to determine if the employment of a magnetic stirrer would be relevant to the overall results.

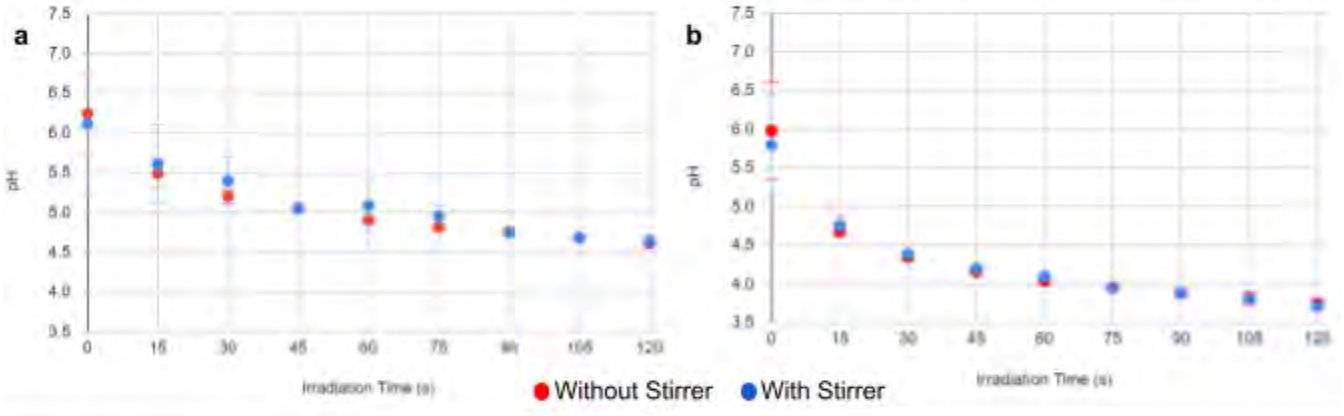

Figure 3. Effects of Stirring on pH of plasma-treated solutions. Plasma parameters:
a) Frequency = 1 kHz, and Voltage = 8 kHz; b) Frequency = 4 kHz, and Voltage = 10 kHz

As seen above, the values were statistically the same, considering the margin of error, and therefore all experiments were conducted without the use of a stirrer. Extreme values of frequency and voltage allowed for a better and broader understanding of stirrer effects on each solution.

Voltage and Frequency Parameters

Next, eight sets of parameters were tested. The color of the plots below are in accordance with the current universal indicator for pH values, in which green represents neutral solutions and yellow stands for more acidic solutions. As seen in Figure 5, a combination of higher voltage (10 kV), higher frequency (4 kHz), and longer irradiation time (120s) resulted in more acid pure

water solutions. Additionally, when each irradiation time is analyzed separately, an increase in voltage seems to play a more significant role in lowering the pH of water solutions, while they are susceptible to smaller changes in pH with the increase of frequency alone.

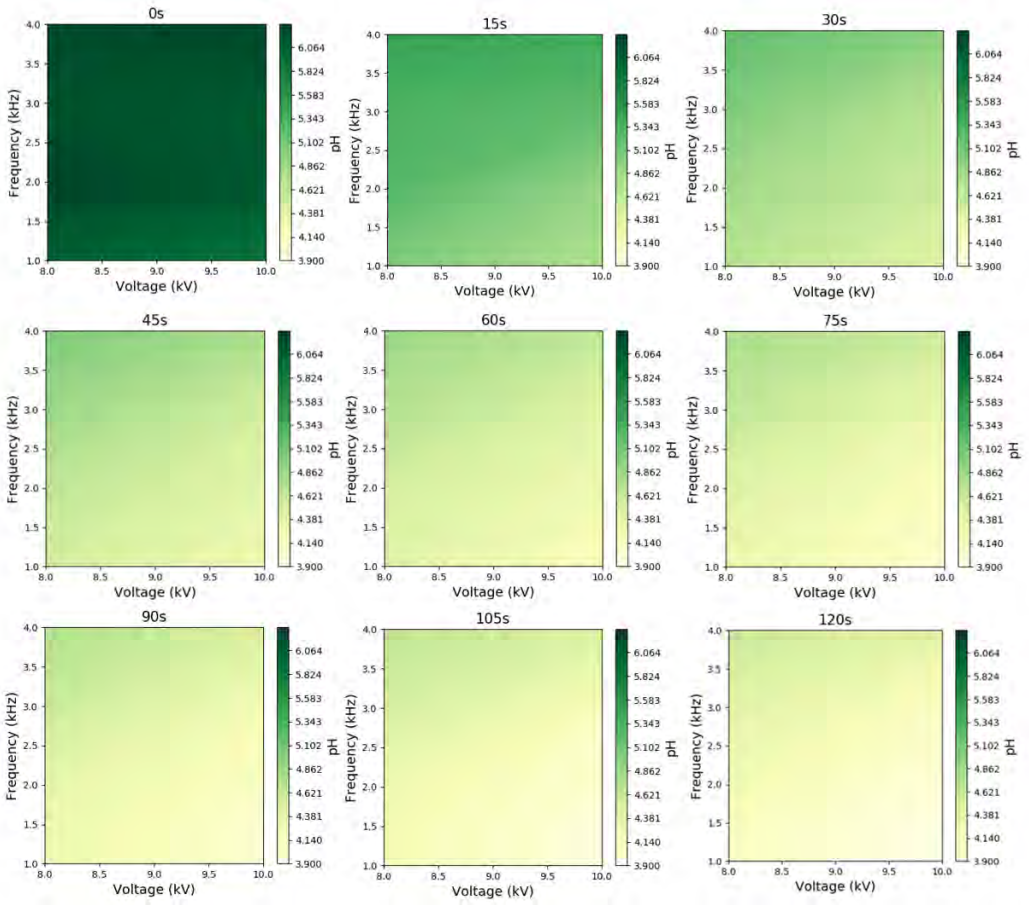

Figure 4: Contour maps of pH changes with respect to irradiation time, voltage, and frequency parameters of plasma irradiation. The combination of higher voltage and frequency, added to longer irradiation time, leads to an increase in solution's acidity.

Amino Acid Concentration

Further experiments were conducted with the simplest amino acid, glycine, to explore the effects of plasma on the pH of solutions containing biomolecules. It was found that greater concentrations of glycine, particularly 0.5 M, significantly increased pH stability, regardless of the chosen parametric conditions delivered by the plasma source. At smaller concentrations,

however, the same pattern of pH variation was observed as in pure solutions. In general, an increase in voltage, frequency, and irradiation exposure time still led to a lower pH for all concentrations observed.

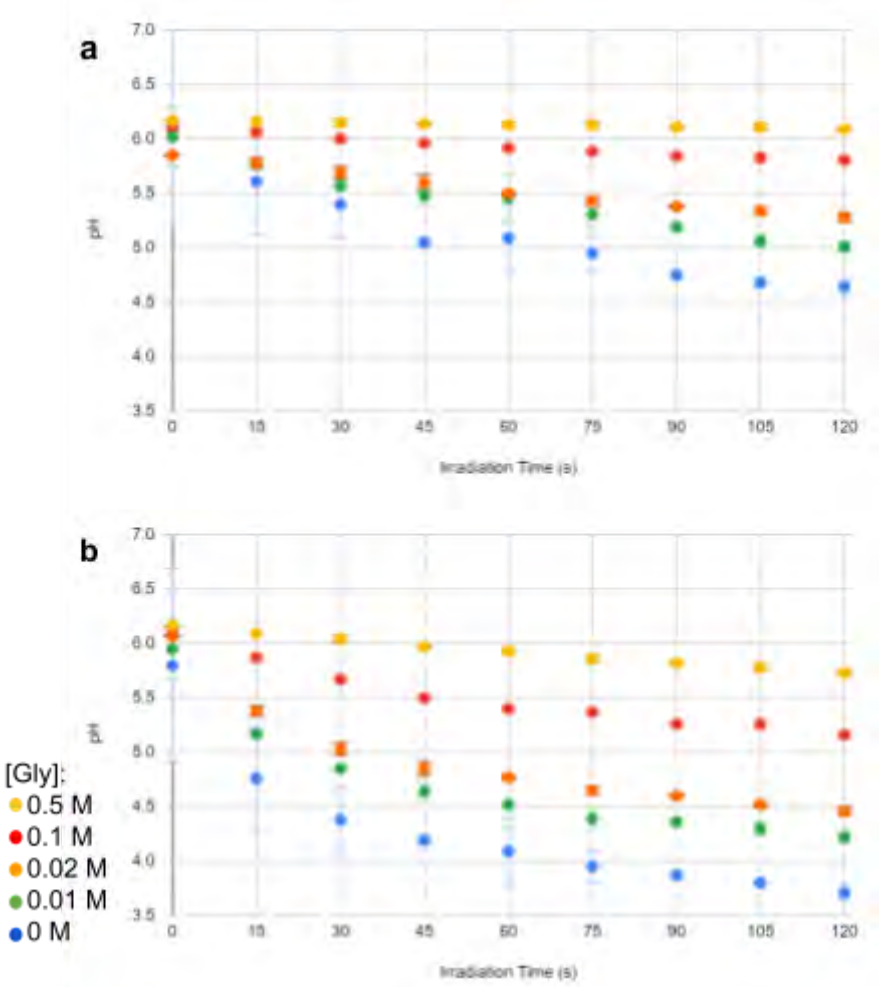

Figure 5: Changes in pH for plasma-treated solutions with different concentrations of glycine. Plasma parameters: a) Frequency: 1 kHz, and Voltage = 8 kHz; b) Frequency = 4 kHz, and Voltage = 10 kHz. Higher concentrations of glycine increase pH stability, while pH variation pattern is similar to pure solutions for lower amino acid concentrations.

Conclusion

As plasma medicine and LTP become more acceptable and effective approaches to treating cancer, it is important to understand the relation between plasma and pH, as well as its interactions determined by the absence or presence of biomolecules vital to the human body. By

testing the effects of plasma radiation with a range of voltage and frequency conditions, this study established that a combination of high voltage, high frequency, and long irradiation times increases the acidity of water solutions. Furthermore, pH alterations are more likely to occur when the voltage delivered by a plasma source is increased. Conversely, pH stability can be restituted by adding high concentrations of the amino acid glycine to pure solutions. Low glycine concentrations resulted in similar patterns of pH variations as observed in pure solutions. Future research into plasma, pH, and biomolecules should focus on determining the causes of the patterns observed and the high stability resulting from adding glycine into the solution. Moreover, while this experiment measured pH changes in pure water and glycine solutions, further studies are required to gain more insight into plasma interactions with different biomolecules to investigate, for instance, collateral effects that such radiation might induce in DNA, surrounding tissues, and other essential amino acids and proteins.

Acknowledgments

I would like to acknowledge and thank Prof. Sylwia Ptasińska, the College of Science, and the Department of Physics and Astronomy of the University of Notre Dame, which made this work possible. I would also like to thank graduate student Cecilia Villavicencio for her guidance and support throughout the experiment. Lastly, I am deeply grateful to my parents for their support, appreciation, and encouragement in all my academic endeavors.

References

[1] Alizadeh, E., S. Ptasińska. “Recent Advances in Plasma-Based Cancer Treatments: Approaching Clinical Translation through an Intracellular View.” *biophysica*, 1(1), 48-72 (2021). https://doi.org/10.3390/biophysica1010005.

[2] von Woedtke, T., et al. “Plasmas for medicine.” *Physics Reports*, 530(4), 291-320 (2013). https://www.sciencedirect.com/science/article/pii/S0370157313001634.

[3] Laroussi, M. “Plasma Medicine: A Brief Introduction.” *Plasma*, 1(1), 47-60 (2018). https://doi.org/10.3390/plasma1010005.

[4] Gao, L., et al. “Applications and challenges of low temperature plasma in pharmaceutical field.” *J Pharm Anal.*, 11(1), 28-36 (2021). https://www.ncbi.nlm.nih.gov/pmc/articles/PMC7930796/.

[5] Sebastian, A., et al. “Revealing low-temperature plasma efficacy through a dose-rate assessment by DNA damage detection combined with machine learning models.” *Sci Rep*, 12, 18353 (2022). https://www.nature.com/articles/s41598-022-21783-3.

[6] Hu, Y., Y. Li. “Effect of Low pH Treatment on Cell Cycle and Cell Growth.” *The FASEB Journal*, 32, 804.49-804.49 (2018). https://faseb.onlinelibrary.wiley.com/doi/abs/10.1096/fasebj.2018.32.1_supplement.804.49.

[7] Omidi, Y., and J. Barar. “Dysregulated pH in Tumor Microenvironment Checkmates Cancer Therapy.” *Bioimpacts*, 3(4), 149-162 (2013). https://www.ncbi.nlm.nih.gov/pmc/articles/PMC3892734/.

[8] Piasentin, N., et al. “The control of acidity in tumor cells: a biophysical model.” *Sci Rep*, 10, 13613 (2020). https://www.nature.com/articles/s41598-020-70396-1.

[9] Lee, Shen-Han, and John R. Griffths. “How and Why Are Cancers Acidic? Carbonic Anhydrase IX and the Homeostatic Control of Tumour Extracellular pH.” *Cancers (Basel)*, 12(6), 1616 (2020). https://www.ncbi.nlm.nih.gov/pmc/articles/PMC7352839/.

[10] Lee, Sungmun, and Aya Shanti. “Effect of Exogenous pH on Cell Growth of Breast Cancer Cells.” *Int J Mol Sci,* 22(18), 9910 (2021). https://pubmed.ncbi.nlm.nih.gov/34576073/.

Calculating X-Ray Yield Predictions of *ex-vacuo* PIXE at 3.9 MeV

KYLE TAFT

2023 NSF/REU Program
Department of Physics and Astronomy
University of Notre Dame

ADVISOR(S): Dr. Graham Peaslee, Anthony Miller

Abstract

Particle-Induced X-ray Emission (PIXE) analysis is an established elemental analysis technique, involving the displacement of inner shell core electrons within target materials to induce X-ray emissions. This paper presents an exploration of PIXE's foundations, methodologies, and validation. The investigation encompasses crucial aspects, including background subtraction techniques, quantification of X-ray counts in spectra, and the intricate process of yield calculation. Empirical validation is realized through a comparative analysis of bromine and zinc gypsum puck standard samples, evaluating measured data against calculated yields. Notably, an unexpected disparity in the calculated yield prompts further inquiries. This study unveils PIXE's remarkable potential while beckoning further investigations, ultimately underscoring its significance as a potent tool for elemental analysis.

1 Introduction

Particle-Induced X-ray Emission (PIXE) analysis is a powerful technique utilized to understand the elemental composition of materials by exploiting the production of characteristic X-rays through the displacement of inner shell core electrons. High-energy incident particles, notably protons, interact with the target material's atoms, leading to the ejection of inner shell electrons from their stable energy levels, specifically within the K and L shells. The specific experiment at hand works with a beam of 3.9 MeV protons bombarding the target in an ex-vacuo manner. We perform this analysis out of vacuum to greatly speed up the experimental process.

This paper delves into the intricate facets of PIXE analysis, encompassing its foundational principles, methodologies, and empirical validation. To understand the process of this analysis, the subsequent sections focus on the theoretical background, the used background subtraction techniques, and the intricate procedure for quantifying X-ray counts in spectra. Subsequently, the study delves into the heart of the PIXE technique—the yield calculation— working through a explanation of the intricate variables and mechanisms that culminate in a meaningful quantification of X-ray emissions.

2 Background

In Particle-Induced X-ray Emission (PIXE) analysis, X-ray production originates from the displacement of inner shell core electrons within the target material. High-energy incident particles, such as protons, interact with the atoms of the target material, leading to the ejection of inner shell electrons from their stable energy levels. Specifically, the inner shell electrons from the K shell or the L shell are displaced during this process.

2.1 Auger Electrons

One notable outcome of the inner shell electron displacement is the emission of Auger electrons. The Auger effect involves the cascade process where an outer shell electron fills the vacancy created in the inner shell. As a result of this transition, Auger electrons are emitted from the atom. Although these Auger electrons do not directly contribute to PIXE analysis, they can be significant in terms of background contamination. If Auger electrons escape from the target material and interact with the detector or surrounding materials, they may introduce unwanted signals, complicating the accurate determination of X-ray intensities.

2.2 Characteristic X-rays

Another crucial X-ray production mechanism is the generation of characteristic X-rays. After an inner shell electron is displaced, an electron from a higher energy level may transition to fill the vacancy. This process results in the emission of characteristic X-rays, which possess distinct energies corresponding to the energy difference between the involved electron energy levels. Various characteristic X-ray transitions are of particular interest. For example, filling the vacancy in the K shell results in K-alpha and K-beta X-rays. The K-alpha X-rays are emitted when the electron transitions from the L shell to the K shell, while the K-beta X-rays occur during the transition from the M shell to the K shell. Each element has specific energy values of X-rays released during these specified electron transitions. This allows for the ability to precisely identify the elements in the target material based on detection of the unique X-rays.

3 Methods

3.1 Background Subtraction

Background subtraction is a fundamental technique in spectra analysis to mitigate the influence of unwanted contaminants inherent to data collection and experimental procedures. A thorough comprehension of the underlying background aids in refining the measurements, facilitating a more accurate and precise analysis. In the context of PIXE, several extensively studied sources contribute to background contamination, with electron bremsstrahlung being the primary contributor.

Bremsstrahlung, a German term denoting "braking radiation," arises from the deceleration of charged particles, particularly electrons, during their ejection from target atoms. When these electrons are expelled, a portion of their kinetic energy is converted into radiating X-rays, which the detector cannot readily differentiate from the characteristic X-rays originating from PIXE. This continuous electron bremsstrahlung background poses a significant challenge in PIXE analysis. To address this issue, a well-established approach involves employing a cubic spline function with nodes placed at local minima [1]. By fitting this cubic spline function to the measured data, the continuous background resulting from electron bremsstrahlung can be effectively modeled and subsequently subtracted from the spectra. The need for accurate background subtraction in PIXE analysis cannot be overstated, as it substantially impacts the result of the elemental quantification process.

3.2 Quantifying Counts in Spectra

In the analysis of given spectra, it becomes imperative to determine the number of counts associated with energy peaks of interest. Due to factors in the nature of the experiment, the counts recorded for each characteristic X-ray follow roughly a normal distribution in energy about the energy of interest. The key objective is to ascertain the total number of counts for each energy region of interest. The integral, or area under the curve, of the peaks is employed as the

fundamental approach to quantify these counts.

Numerous methodologies exist for calculating these integrals, and this paper adopts the utilization of fitting Gaussian distributions to characterize each of the peaks. This choice offers distinct advantages, especially when dealing with overlapping peaks, where there may not be a clear and separate full Gaussian shape, complicating visual differentiation. Nevertheless, by fitting Gaussian distributions to the peaks, it becomes possible to discriminate one peak from another, leveraging the expected Gaussian shape. The process involves employing the simple Gaussian equation (1) to be centered about each specific energy of interest. Where A is the amplitude of the peak, x_0 is the mean of the peak, and σ is the standard deviation. The Gaussian distributions are fitted using an optimization code, which seeks to minimize the distance between the fitted Gaussian functions and the actual data Fig. 1. This optimization process enables accurate determination of the parameters for each Gaussian peak, yielding reliable counts for the energy regions of interest through taking the integral of the curve.

By adopting this fitting and integration approach, the paper ensures a robust and precise estimation of the counts associated with different energies in the collected spectra. This methodology enhances the resolution of overlapping peaks and facilitates an accurate determination of element concentrations.

$$G(x) = Ae^{-(x-x_0)^2/2\sigma^2} \tag{1}$$

3.3 Yield Calculation

The yield calculation represents a crucial step in our analytical process, wherein we determine the expected number of X-rays to be detected from a given element and its specific transition, considering the experimental setup's numerous influencing factors [2]. This comprehensive calculation involves multiple variables, which collectively contribute to a equation enabling the determination of the yield (2).

The key variables considered include the number of incident protons bombarding the target

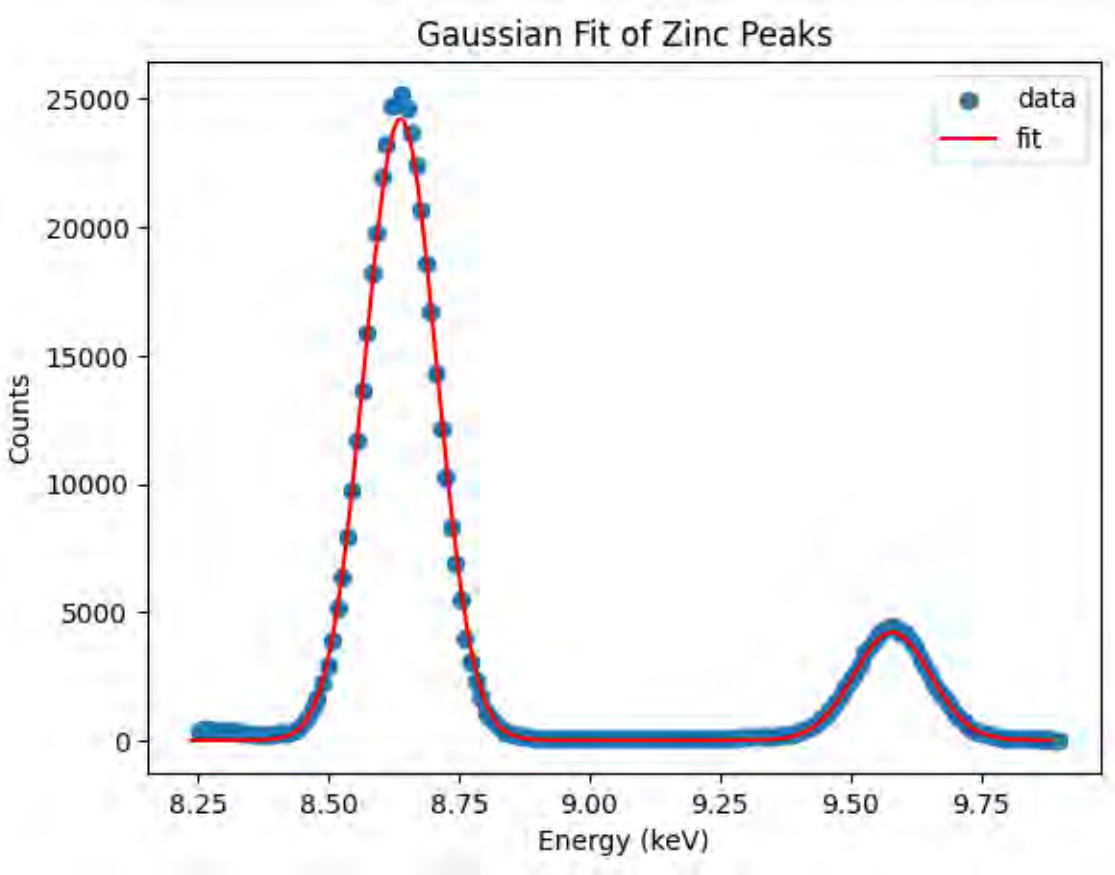

Figure 1: This figure demonstrates an examples of the multiple Gaussian fitting of two zinc peaks of a spectrum.

material, denoted as N_p, concentration of the specific element of interest present in the material, represented by C_z, and the X-ray fluorescence efficiency of the material, which quantifies the ratio of Auger emissions to the detectable X-ray fluorescence. The fluorescent rate is denoted as ω_Z. Furthermore, the line intensity ratio plays a significant role in our calculation. This ratio accounts for the variations in X-ray transitions, such as K-alpha and K-beta, resulting from displacements in the K shell and subsequent filling from the L shell and M shell, respectively. The line intensity ratio is denoted as b_Z.

In addition to these factors, we must incorporate the detector efficiency, ϵ_Z, and geometry, G, which accounts for the detector's capability to capture the emitted X-rays. Additionally, we consider the X-ray transmission through air, denoted as t_Z, to account for potential attenuation effects.

The integrative aspect of the calculation involves an integral term, encompassing the entrance energy and exit energy of the protons as bounds, multiplied by the cross section and the transmission factor. Moreover, we incorporate the stopping power and the material density, denoted as $\Lambda(E)$ and ρ, respectively.

It is important to acknowledge that many of these essential variables can be obtained from existing literature sources or simulated through appropriate models. These referenced sources would provide the necessary data and values to perform the yield calculation accurately and comprehensively [3–6].

By encompassing all these critical parameters in our yield equation, we ensure a rigorous and systematic approach to quantify the expected X-ray counts for specific elements and their transitions. This comprehensive calculation underscores the reliability and precision of our PIXE analysis, facilitating its wide-ranging applications in diverse scientific investigations.

$$Y(Z) = \frac{N_{av}\omega_Z b_Z t_Z \epsilon_Z^i G}{A_Z} N_p C_Z \int_{E_0}^{E_f} \frac{\sigma_Z(E) T_Z(E)}{\Lambda(E)} \, \mathrm{d}E \tag{2}$$

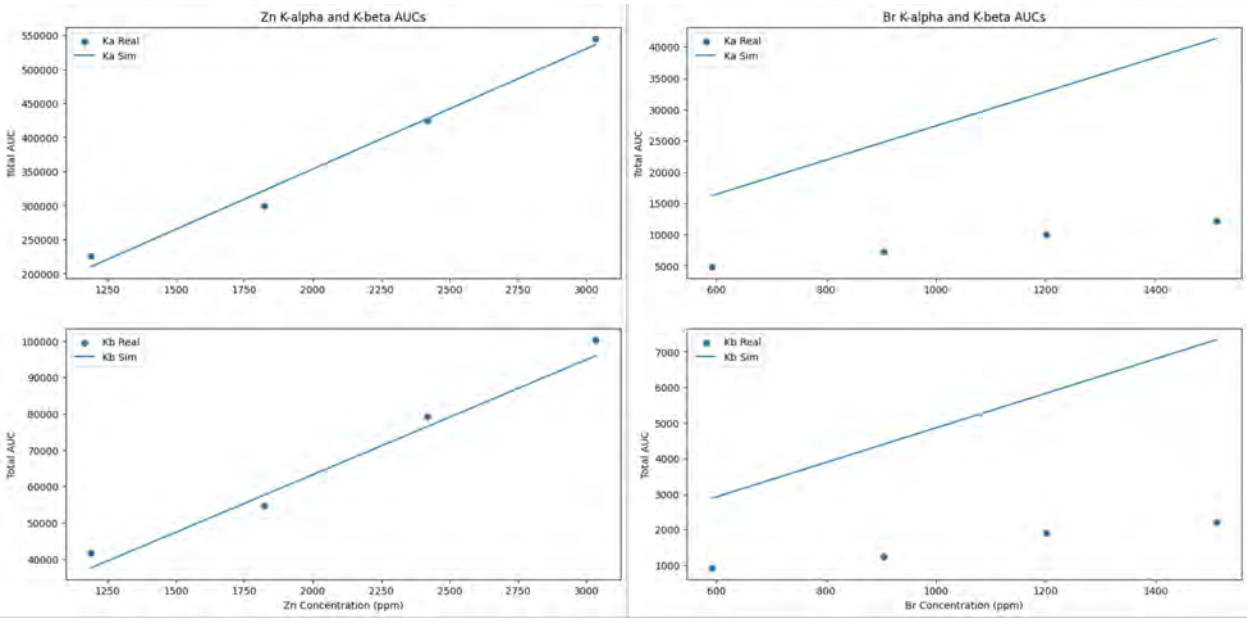

Figure 2: This figure visualizes the calculated yields against the empirically found counts of each energy's peak. The slopes are calibrated to zinc's K-alpha.

4 Results

Utilizing empirical data derived from puck standards containing known concentrations of bromine and zinc, a comparative analysis was conducted between experimental measurements and calculated yield values. The comparison hinged on comparing the empirical areas under the curves (AUCs) quantities with calculated yields.

The results are presented through four graphs 2. Two separate graphs were generated for each element showing the K-alpha and K-beta transitions specific to the respective element.

A critical element of the analysis was the implementation of scaling the calculation for zinc's K-alpha data. This calibration takes into consideration unconsidered values such as geometric considerations, detector efficiency, and any other systematic offsets due to the experiment.

Additionally, AUCs of sulfur were used to normalize the data points to one another to offset the fluctuations in beam position and current that occurs through a day of accelerator running.

5 Conclusion

The outcome unveiled a notable divergence that is particularly evident in the analysis of bromine. Surprisingly, an unanticipated disparity in the slope emerged, indicating an approximate threefold discrepancy compared to the calculated projection. This intriguing observation highlights an unexplained divergence that warrants further investigation and analysis.

Some notable areas of investigation to be further pursued are in the experimental setup, creation and calculation of the puck's concentrations, unaccounted for factors in the yield equation, or a fallacy in the techniques displayed in this paper.

References

[1] L. Yi, Z. Liu, K. Wang, M. Chen, S. Peng, W. Zhao, J. He, and G. Zhao, Nuclear Instruments and Methods in Physics Research Section A: Accelerators, Spectrometers, Detectors and Associated Equipment **775**, 12 (2015).

[2] S. A. E. Johansson and J. L. Campbell, Pixe: A novel technique for elemental analysis (Wiley, New York, 1988).

[3] H. Paul and J. Sacher, Atomic Data and Nuclear Data Tables **42**, 105 (1989).

[4] M. Batič, M. G. Pia, and S. J. Cipolla, Computer Physics Communications **183**, 398 (2012).

[5] J. H. Hubbell and S. M. Seltzer, NIST Standard Reference Database **126**, https://dx.doi.org/10.18434/T4D01F (1990).

[6] I. Han, M. Şahin, L. Demir, and Y. Şahin, Applied Radiation and Isotopes **65**, 669 (2007).

Resolution Testing of the Notre Dame Enge Split-Pole Spectrograph Focal Plane Detector

ALEXEI TEMIDIS

2023 NSF/REU Program
Department of Physics and Astronomy
University of Notre Dame

ADVISOR(S): Dr. Dan Bardayan

Abstract

Study of nuclear structure for astrophysics demands high precision to indirectly determine certain nuclear reaction rates, because uncertain measurements cause imprecise calculations of these reaction rates. Notre Dame has acquired an Enge split-pole spectrograph which can be used to precisely measure nuclear level energies by magnetically separating and focusing particles onto the focal plane detector based on their momentum. This high-precision spectrometer provides a means to ascertain astrophysical reaction rates, providing a deeper understanding of nuclear processes in astrophysical environments. To fully harness this machine's capabilities, the current commissioning phase is focused on ensuring precise position measurements from the focal plane detector which requires determining inherent resolution of the electronics by analyzing histograms of pulser data. Future tests include using a collimated alpha source to provide a more realistic determination of the detector's resolution. Presently, the analysis of the Notre Dame spectrograph's test results is in progress.

1 Introduction

Over the past century, nuclear physics has been closely associated with Dr. Julius Robert Oppenheimer and The Manhattan Project. This connection with large-scale nuclear weapons has led to a common misconception that nuclear physics isn't concerned with precision. In reality, precision is vital in this field, especially when dealing with the production and handling of such devices, as any errors could have severe consequences. Nuclear physics, however, is a much broader field than simply the development of atomic warheads. The field studies many different aspects of nuclear reactions: byproducts, reaction rates, the theory behind it all, etc. Nuclear astrophysics studies stellar evolution and nucleosynthesis from thousands or even millions of light years away. Medical nuclear physicists develop machines to scan for diseases in our own bodies such as the MRI. To study such precise reactions, nuclear physicists need incredibly precise machinery that can measure to within their specified tolerances. This summer, I have been working on rehabilitating a precision instrument, the Enge split-pole spectrograph, for use at the University of Notre Dame's Nuclear Science Lab.

2 Background

Max Planck and Niels Bohr are renowned as the fathers of quantum mechanics due to their groundbreaking theory of quantized energy. Rather than considering energy as a continuous variable, they proposed that it exists in predetermined values, appearing in discrete "packets" known as quanta. This concept was extended by Einstein, who postulated that even electromagnetic radiation, such as light, can be quantized into particles called photons. To put it simply, this transition from continuous to discrete energy levels is what we refer to as the quantization of energy.

In contemporary understanding, we have come to recognize that excited nuclei exhibit the same quantized energy levels as electrons do, governed by the principles of quantum mechanics. The location and excitation energies of these states vary among different atoms, depending on their internal structure. Measuring these energy levels has proven to be highly valuable, as it allows us to determine essential nuclear properties, such as the identity of the nucleus and, indirectly, the reaction rate that created it. However, it is essential to remember that these processes occur on the atomic level, which is incredibly small. Hence, the instruments used to measure these variables must be exceedingly precise, as uncertainties in measurements can lead to inaccurate calculations.

In spectrograph technology, increasing precision typically involves reducing beam spot size, target thickness, or the solid angle of acceptance. Yet, such methods also reduce the rate of data accumulation. In 1966, Harald A. Enge, a pioneering nuclear physicist at MIT, introduced a revolutionary spectrograph that successfully increased resolving power without compromising data collection capability [1]. He aptly named this innovation the "split pole magnetic spectrograph for precision nuclear spectroscopy," later referred to as the "Enge split pole spectrograph." Presently, the University of Notre Dame is in the process of recommissioning one of these machines. [2]

3 Detector Operation

When a charged particle moves through a magnetic field, it undergoes a force that acts perpendicular to its motion, causing it to follow a circular trajectory. This circular path is determined by

three factors: the strength of the magnetic field, the particle's charge, and its momentum. This relationship can be described by the equation:

$$\rho = \frac{p}{Bq} \tag{1}$$

Here, ρ represents the bending radius, p is the momentum of the particle, B is the strength of the magnetic field, and q denotes the charge of the particle [3].

The Enge split pole spectrograph capitalizes on this property to effectively separate particles with varying energy levels. These particles exhibit different bending radii due to their distinct momenta. By using two separate magnetic fields, the spectrograph separates and then refocuses the particles, allowing the focal plane detector to accurately measure their energy based on their bending radii.

To determine the bending radius, the spectrograph records the location at which the particle intercepts the detector and registers a pulse via the electronics. This bending radius information is essential for accurately analyzing the particle's energy within the Enge split pole spectrograph.

4 Resolution Testing

Currently, during the commissioning phase of Notre Dame's Enge split pole spectrograph, the focus is on assessing the precision of the focal plane detector's position measurements. This crucial step involves conducting tests to ascertain the machine's resolution capabilities under both ideal and realistic conditions. Two specific tests have been performed this summer as part of the commissioning process: pulser tests and collimated alpha tests. These tests are designed to provide valuable insights into the performance and accuracy of the focal plane detector.

4.1 Pulser Tests

Pulser tests are conducted to assess the intrinsic resolution of the electronics within the Enge split pole spectrograph. These tests simulate an ideal scenario where a signal is sent individually through

various positions on the delay line, allowing us to gauge the detector's accuracy in placing the signal. During these tests, we collected data from multiple runs, analyzing how precisely the measurements can be made when a signal aligns precisely with a single position on the detector.

Our qualitative analysis of the pulser test results showed promising outcomes. However, it's important to note that we did not conduct a quantitative analysis to obtain specific numerical values for the detector's resolution. Despite this, the qualitative findings indicate that the instrument's ability to pinpoint signals with high precision is encouraging.

4.2 Alpha Tests

Alpha tests were conducted to simulate a more realistic operational scenario for the detector. To approximate such conditions, a temporary collimator was constructed using PVC pipe pieces and washers, mounted onto the detector with 80-20 pieces. The spectrograph was set up as it would be during an actual beam run. The alpha source was placed within the collimator, and the chamber was sealed and evacuated to approximately 10E-3 Torr. Subsequently, the cathode and anode were charged, the chamber was filled with P10 gas, and data acquisition was initiated using the pacman data acquisition manager.

However, upon analyzing the data from the alpha tests, the results did not meet the anticipated expectations. Ideally, the histograms should have displayed a peak corresponding to the position of the alpha source. Although a peak was observed, it did not shift when the source's position was changed. Additionally, excessive noise in the data hindered the identification of meaningful results. The cause of this noise was suspected to be sparking inside the chamber. It was observed that our detector experienced significant sparking at 1050v, while another collaborating laboratory achieved minimal sparking at 1700v, even though both were running in similar environments. Two potential solutions were suggested to address this problem: switching to a different gas or addressing the Frisch grid.

During the initial construction of the Frisch grid, an electrically conductive epoxy was used, resulting in sharp corners and edges that were not sanded down before installation. These sharp

edges might be a primary cause of the sparking. The proposed solution involves disassembling a significant portion of the detector to access the Frisch grid for sanding and inspection to detect any other impurities. However, this task was not carried out during this summer's commissioning phase.

5 Foil Window

The detector's ion chamber comprises openings covered by aluminized mylar foil windows, which serve as barriers to contain the gas while allowing light ions to pass through to the detector itself. Constructing these windows is a challenging task with a relatively low success rate. Here is my procedure for constructing such a window:

1. **Preparing the Surface:** Ensure that the surface where the foil will be attached is smooth and free of any gashes or imperfections. To achieve this, wet sand the surface using ethyl alcohol, starting from 240 grit and gradually progressing up to 600 grit until the surface is deemed acceptable.

2. **Cleaning the Surface:** Thoroughly clean the entire piece to remove any dust resulting from the sanding process.

3. **Cutting and Aligning the Foil:** Cut the aluminized mylar foil to the required size. Use temporary tape to attach the foil to a dummy piece, which will aid in aligning the foil during the process.

4. **Preparing the Epoxy:** Mix the epoxy as directed on the instruction label.

5. **Applying the Epoxy:** Evenly spread the epoxy on the prepared surface.

6. **Placing the Foil:** Carefully flip the dummy piece onto the epoxy so that only the foil makes contact with the epoxy. To prevent any spilled epoxy from binding the foil to the dummy piece, place paper towels between the foil and the dummy piece.

7. **Ensuring Proper Bonding:** During the first attempt, there may have been creases and folds in the contact surfaces between the foil and the metal. If this occurs, it is advisable to restart the process. Remove and re-sand the piece, then repeat the steps outlined above. This time, tape the foil onto the window itself, essentially making the window its own piece to cure. Smooth out any creases or imperfections that appear during the process.

8. **Applying Even Pressure:** Once satisfied with the foil's positioning, place the dummy piece back onto the window to ensure even pressure with all points of contact.

By following this procedure and taking care to eliminate creases and imperfections, you increase the chances of successfully constructing a functioning aluminized mylar foil window for the detector's ion chamber.

6 Conclusion

In conclusion, the efforts dedicated to the Enge split pole spectrograph this summer have been instrumental in laying the groundwork for its full operational potential. The progress made during this period serves as a small but crucial stepping stone toward achieving its intended functionality.

Looking ahead, the next critical steps involve conducting calibration and comprehensive testing with a ^{13}C beam, characterized with well-defined properties. These crucial tests will be instrumental in fine-tuning the spectrograph's performance and ensuring its optimal operation for future experiments.

Notably, Scott Carmichael's upcoming study on the reaction rates of specific processes within core collapsing supernovae holds great promise. In particular, his focus on investigating the ^{58}Ni(^{3}He,t)^{58}Cu reaction is poised to yield valuable insights into the mechanisms underlying these fascinating astrophysical phenomena.

By building upon the work accomplished this summer, the Enge split pole spectrograph at Notre Dame is poised to make significant contributions to nuclear physics research, deepen our understanding of nuclear reactions, and shed light on the complex dynamics of astrophysical phe-

nomena. As the journey toward achieving full operational capability continues, the Enge stands as a testament to the dedication and ingenuity of the researchers involved in this ambitious endeavor. With each milestone achieved, we inch closer to unlocking the mysteries of the universe and making meaningful contributions to the field of nuclear science.

References

[1] J. E. Spencer and E. H. A., Nuclear Instruments and Methods **49** (1967).

[2] D. W. Bardayan, P. D. O'Malley, D. Robertson, E. Stech, and M. Wiescher, AIP Conference Proceedings **2160**, 070008 (2019), https://pubs.aip.org/aip/acp/article-pdf/doi/10.1063/1.5127731/14196625/070008_1_online.pdf .

[3] S. Carmichael, (2023).